UNIVERSITY OF LEEDS

A Spectroscopic Study Into Accretion In Herbig Ae/Be Stars.

John Robert Fairlamb

School of Physics and Astronomy

University of Leeds

Submitted in accordance with
the requirements for the degree of

Doctor of Philosophy

March 2015

Preface

Within this thesis, some of the chapters contain work presented in the following jointly authored publications:

I. “Spectroscopy and linear spectropolarimetry of the early Herbig Be stars PDS 27 and PDS 37” – K. M. Ababakr, **J. R. Fairlamb**, R. D. Oudmaijer, M. E. van den Ancker, 2015, MNRAS, submitted.

II. “X-Shooter spectroscopic survey of Herbig Ae/Be stars I: Stellar parameters and accretion rates” – **J. R. Fairlamb**, R. D. Oudmaijer, I. Mendigutía, J. D. Ilee, M. E. van den Ancker, 2015, MNRAS, submitted.

III. “ Stellar Parameters and Accretion Rate of the Transition Disk Star HD 142527 from X-Shooter ” – I. Mendigutía, **J. R. Fairlamb**, B. Montesinos, R. D. Oudmaijer, J. Najita, S. D. Brittain, M. E. van den Ancker, 2014, ApJ, 790, 21.

IV. “Investigating the inner discs of Herbig Ae/Be stars with CO bandhead and Brγ emission” – J. D. Ilee, **J. R. Fairlamb**, R. D. Oudmaijer, I. Mendigutía, M. E. van den Ancker, S. Kraus, H. E. Wheelright, 2015, MNRAS, 445, 3723.

Paper I is included in a small section in Chapter 2. The paper involves a dedicated procedure for obtaining stellar parameters in the stars PDS 27 and PDS 37. The methods and work presented in these sections of the paper were performed and written by the second author J. R. Fairlamb. Other sections of the paper were either jointly written between the primary author, K. M. Ababakr, and the secondary author, or they were the sole work of K. M. Ababakr; as such, these particular sections are not included in this thesis.

Paper II forms the basis of Chapter 2 and 3. The paper details the derivation of stellar parameters for a large sample of HAeBe stars, and it analyses the mass accretion rate using the UV-excess. The work was carried out by the primary author, J. R. Fairlamb, and the text was also written by the primary author. The co-authors provided comments on various drafts of the paper which the primary author has incorporated in the final paper.

Paper III is a dedicated study of the Herbig Ae star HD 142527. The secondary author, J. R. Fairlamb, wrote the section involving accretion derived from the Balmer excess and performed the relevant work behind the values listed. The techniques in this paper are similar to the ones presented in Chapter 3, but the methodology and stellar parameters used are slightly different.

Paper IV contains Brγ line strengths and luminosities. These values are also present in Chapter 4. Their determinations involved some of the stellar parameter given in Chapter 2. All of these values were determined by the second author, J. R. Fairlamb, with the relevant sections in the paper regarding the values also written by the second author. The remainder of the paper was written by the primary author, J. D. Ilee, and is not included in this thesis.

Acknowledgements

Firstly, my thanks go out to my supervisor René Oudmaijer, whose knowledge has helped me immensely, but perhaps more importantly his constant enthusiasm has kept me motivated throughout. My thanks are extended to the rest of my academic peers here in Leeds for providing valuable insights and discussions. In particular, thanks go to Ignacio Mendigutia and John Ilee who have greatly helped in my studies, both academically in the office, and non-academically in the "executive office".

Next, thanks are required for all of my fellow PhD students, every one of whom have provided great conversation and good times over the many years. Special thanks go to my office mates Nichol Cunningham and Tom Douglas for all the chin-wag sessions, and of course for putting up with me during these final months. Special thanks are due for Jacob Close and Karim Ababakr for including me in their entertaining and constant bickering (and also for being great climbing buddies).

Outside of the office my thanks go to my friends, both near and far, for always having encouraged me and being there for me when I need

to chill out. Special thanks go to my fellow monster hunters, and beer hunters, James Banning and Oscar Shefik for *forcing* me to play so many videogames and boardgames in my free time here in Leeds.

Super special thanks go to my wonderful fiancée Gemma, who has allowed me to drag her away from Scotland to keep me company here. My thanks are for you always being there to talk to and laugh with at any hour, I couldn't ask for a more wonderful partner.

Lastly, important extra special thanks go to my parents who have provided me with support both emotionally and financially, not just throughout my PhD but throughout the whole of my life too. Without your never-ending encouragement and support I wouldn't be where I am today.

Thanks.

Abstract

This thesis presents a spectroscopic study of the stellar properties, accretion rates, and emission lines of 91 Herbig Ae/Be stars.

Medium resolution spectra and optical photometry are used to spectrally type a sample of 91 Herbig Ae/Be stars in a homogeneous fashion. Stellar parameters of temperature, surface gravity, mass, radius, luminosity, distance, age, and reddening are determined using the above in combination with pre-main sequence tracks. The temperatures are in agreement with previous assessments, while new distance and mass estimates for some objects constitute a large improvement.

Measurements of the UV-excess across the Balmer jump region are made, and they are modelled within the context of magnetospheric accretion. Accretion rates are derived from the fitting. Seven Herbig Be stars could not be fitted within this context, suggesting a possible breakdown of magnetospheric accretion towards the higher mass Herbig Ae/Be stars. Different relationships between accretion rate and age are observed for the cases of Herbig Ae stars and Herbig Be stars; this is suspected to be an evolutionary effect of both the star approaching the main sequence and the pre-main sequence lifetime of the star itself.

Line luminosities are measured for 32 different emission lines ranging from ~ 4000–21700 Å. All lines are observed to be correlated with the accretion luminosity, providing multiple new accretion diagnostics. The mean power-law relationship between accretion luminosity and line luminosity is observed to be the same between HAeBes and CTTs, within the errors. However, a line by line comparison between the two, demonstrates deviation in 80% of comparable lines. This deviation appears greatest in the Herbig Be regime. Further investigation is required into the line profiles and current scatter observed in relationships for different classes of pre-main sequence stars.

Abbreviations

BL	Boundary Layer
CMF	Core Mass Function
CTTs	Classical T Tauri stars
ESO	European Southern Observatory
EW	Equivalent Width
GMC	Giant Molecular Cloud
HAe	Herbig Ae
HAeBe	Herbig Ae/Be
HBe	Herbig Be
HR	Hertzsprung-Russell
IMF	Initial Mass Function
IR	Infrared
ISM	Interstellar Medium
KH	Kelvin-Helmholtz
MA	Magnetospheric Accretion
MYSO	Massive Young Stellar Object
NIR	Near Infrared
PAH	Polycyclic Aromatic Hydrocarbon
PDS	Pico dos Dias Survey
PMS	Pre-Main Sequence
SED	Spectral Energy Distribution

SNR	Singal-to-Noise Ratio
TTs	T Tauri stars
UVB	Ultra-Violet and Blue
UV	Ultra-Violet
VIS	Visible
YSO	Young Stellar Object
ZAMS	Zero Age Main Sequence
2MASS	2 Micron All Sky Survey

Contents

List of Figures

LIST OF FIGURES

List of Tables

Chapter 1

Introduction

Star formation is a broad and complex area of astrophysics which spans many large scales in size, mass, and density from giant molecular clouds all the way down to solar scale pre-main sequence stars. The aim of this chapter is to provide an overview of star formation by detailing both our current understanding and the challenges awaiting us in this exciting field of research.

1.1 Clouds, Filaments, and Cores

In order to understand the smallest scales of star formation, that is, of young stars, it is important to understand the environments from which they are born. After all, it is the properties of the molecular clouds, their filaments, and the dense cores within them, that dictate what kind of stars can form in them.

1.1.1 Giant Molecular Clouds

Giant Molecular clouds, GMCs, as the name suggests, are clouds of molecular gas located within the interstellar medium, ISM. Hydrogen is known to be the most abundant element in the universe, and as such molecular clouds are mostly comprised of molecular hydrogen; this has been inferred through H I measurements from as far back as 1970 (Carruthers 1970). However, molecular hydrogen is difficult to detect due to it not having a dipole moment, and no emission lines in the radio-band. Instead, a molecule is needed which can be excited at the same low temperatures, of 5-15 K, and densities, of $N \sim 100\ \mathrm{cm}^{-3}$, seen in molecular clouds (Solomon *et al.* 1987). Carbon Monoxide serves as such a tracer; with the first detections being picked up 45 years ago by (Wilson *et al.* 1970). The conversion factor between CO and H_2 is generally seen to be constant throughout our galaxy, though different conversion factors could alter findings in anomalous regions or other galaxies (Shetty *et al.* 2011; Narayanan *et al.* 2011, 2012).

Using this tracer it has been observed that GMCs span a mass range of 10^3–$10^{6.5}\ \mathrm{M}_\odot$, with an approximately constant surface mass density of $170\ \mathrm{M}_\odot \mathrm{pc}^{-2}$ (Solomon *et al.* 1979, 1987). Smaller molecular clouds have been observed, which are commonly referred to as Bok Gloubles. These clouds are generally located in the less dense regions of the galaxy, such as at high galactic latitudes (Magnani *et al.* 1985), and further out in the galactic disc (Brand & Wouterloot 1995; Heyer *et al.* 2001). The largest GMCs, however, are primarily observed in denser regions of the galaxy, like the central molecular zone and spiral arms (Oka *et al.* 2001). A maximum mass of $10^{6.5}\ \mathrm{M}_\odot$ has been observed in both the Milky Way and the Large Magellanic Cloud, while the distribution of GMC masses obey various power-laws as a function of galactic radius (Rosolowsky 2005).

Going back to the main topic of star formation, it is not just the formation of the actual stars which is uncertain; GMC formation is still a hot topic under debate. In order for them to form, a stage is required where the atomic gas distributed throughout the ISM must be brought together into denser regions, as this is essential for the formation of H_2 and CO molecules (Hollenbach & McKee 1979; van Dishoeck & Black 1988). One theory of GMC formation is through cloud-cloud collisions, where GMCs are created through the collision of smaller molecular clouds (Oort 1954; Field & Saslaw 1965). One issue with this is the time required for enough collisions of smaller clouds to create a GMC before the clouds are dispersed, but recent observations of increased molecular cloud density in the spiral arms (Colombo *et al.* 2014) could allow more collisions between clouds due to their closer proximity; this has been shown to be acceptable by modelling too (Dobbs & Pringle 2013).

Another method of GMC formation is that of converging flows from stellar feedback, where the clouds are formed from material being swept up by supernova shock-waves or expanding H II regions (McCray & Kafatos 1987; Bania & Lyon 1980; Koyama & Inutsuka 2000). Recently, observations have been made of increased molecular cloud production at the edges of galactic supershells by Dawson *et al.* (2011), which supports the colliding flow theory.

Gravitational instabilities are another mechanism of GMC formation, which was postulated long ago as a consequence of perturbations in the galactic disc (Toomre 1964; Goldreich & Lynden-Bell 1965; Roberts 1969; Elmegreen 1979). In this scenario a cloud of gas will collapse gravitationally if the gravitational force can overcome the opposing gas pressure.

In all of the above approaches there will always be a magnetic field present in the GMC. It is suspected that this global magnetic field can actually aid star formation in GMCs, through possible magnetic instabilities (Parker 1966; Mouschovias 1974). However, it may also serve as a hindrance to star formation by supporting the cloud against collapse (Mouschovias & Spitzer 1976; Nakano & Nakamura 1978). Magnetic support is feasible provided the cloud mass remains below a critical mass of $M_{\rm crit} = \Phi/(4\pi^2 {\rm G})^{1/2}$, where Φ is the magnetic flux. Such support may be overcome through ambipolar diffusion (Mouschovias 1987; Lizano & Shu 1989). This is where neutral material crosses the magnetic field lines, thereby removing a portion of the magnetic flux relative to the mass. Lately is has been observed, on average, that GMCs appear to be supercritical with a ratio of GMC cloud mass to critical mass of $M_{\rm GMC}/M_{\rm CR} \sim 2 - 3$, which allows the clouds to overcome magnetic support and collapse (Crutcher 2012). Magnetic fields have also been shown in simulations to play a role in the orientation of the dense filamentary substructures, which form within GMCs from the collapsing material; they are seen to be perpendicular to the magnetic field if its strength is large enough (Van Loo *et al.* 2013).

1.1.2 Filaments

It is not only the creation of GMCs that is complex; their internal structures are too. They appear to contain a filamentary structure of higher density regions within them. This is thought to be produced through a combination of colliding flows, turbulence, gravitational forces and magnetic forces (their exact influence shall be discussed below). Filaments are typically at least ∼1–10 pc in length,

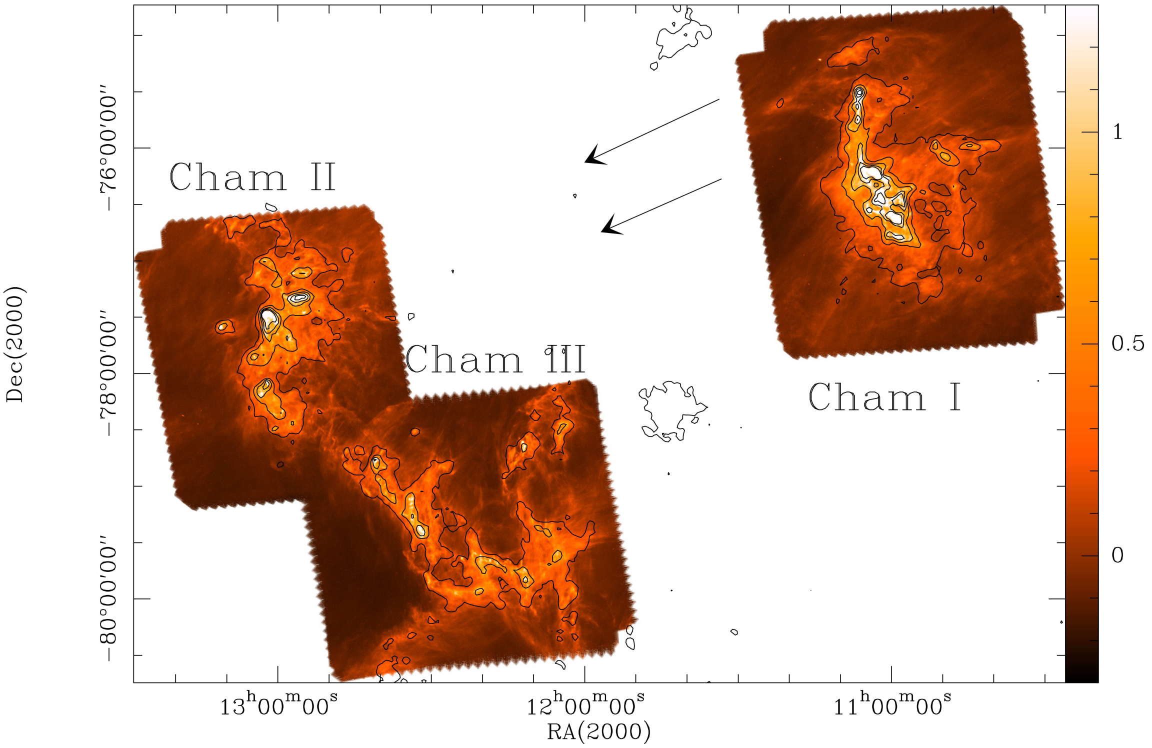

Figure 1.1: The Chameleon GMC is shown above, in 250 μm, for three separate regions within. All of these regions display a filamentary structure. This figure is taken from Alves de Oliveira *et al.* (2014, and references therein). The main filament of Cham I is seen as perpendicular to the magnetic field orientation, which is represented by two arrows, as determined by Whittet *et al.* (1994); McGregor *et al.* (1994). Some striation features are seen to be aligned with this magnetic field in Cham I too.

and are seen to be even larger in IRDCs (Jackson *et al.* 2010; Beuther *et al.* 2011). Recent observations from the *Herschel* survey show that this filamentary structure is present all throughout the cold ISM (Pilbratt *et al.* 2010; André *et al.* 2010; Men'shchikov *et al.* 2010). It has also been shown that the radial profiles of all filaments, in the Gould belt clouds, are ∼0.1 pc (Arzoumanian *et al.* 2011) for both active star forming regions (Bontemps *et al.* 2010), and regions with nearly no star formation (Ward-Thompson *et al.* 2010). This width is approximately two times less than the sonic scale below which interstellar turbulence becomes subsonic in diffuse gas. This lends support to the argument of large-scale turbulence dissipation inducing filaments. It is possible that this is a lower limit to the applicability of Larson's law, which is a power-law relationship between the observed line width of a cloud and its size (Larson 1981).

A *hub* filament structure has been observed in the Pipe nebula of merging filaments, which are suspected to have formed due to feedback from the nearby Sco OB association (Peretto *et al.* 2012). This hub is likely dominated by the largest filament present, with the smaller filaments feeding into it (Hill *et al.* 2011; Hennemann *et al.* 2012). Merging filaments have also been observed in the colder and denser IRDCs (Henshaw *et al.* 2013), where the radial profiles are again observed to be ~ 0.1 pc (Kainulainen & Tan 2013). At the intersections between the merging filaments the column densities are seen to be higher, due to them containing embedded dense cores; these are possible sites of clustered star formation (Myers 2011). The cores have a density structure similar to a Bonnor-Ebert sphere (Johnstone *et al.* 2000; Alves *et al.* 2001; Tafalla *et al.* 2004).

1.1.3 Cores

The work of Polychroni *et al.* (2013) has shown that not all cores are associated with filaments; approximately 29% of the cores they analysed are not associated, and they are also less dense. The increased density of the associated cores is possibly a consequence of the associated-cores being fed by the filaments (Smith *et al.* 2011). This is supported by the observations of Peretto *et al.* (2013), where a candidate O-type star progenitor core is seen to still be gaining material from the filament in which it is embedded. The dense cores seen within filaments are suspected to form after material in the filament has reached a critical density and collapses down (Molinari *et al.* 2010). Currently local collapse of filaments is favoured over the theory of global collapse (Banerjee *et al.* 2006; Pon *et al.* 2011).

Dense cores are the final sites of star formation from which stars will be born. The stars which arise from multiple dense cores, a cluster, will follow a given mass distribution, referred to as the Initial Mass Function (IMF). The IMF was originally described as a power law by Salpeter (1955), where solar-like stars are seen to be more plentiful than larger stars. Modifications have been made since then to account for the small numbers of very low mass stars, and brown dwarfs, observed as zero mass is approached (Miller & Scalo 1979; Kroupa 2001; Chabrier 2003; Maschberger 2013). This turn-off point is taken to be $\sim$0.1–1 $M_{\odot}$.

It has been observed that the numbers of dense cores, and their masses, follow a Core Mass Function, CMF (Motte *et al.* 1998; Testi & Sargent 1998; Johnstone *et al.* 2000; Könyves *et al.* 2010). The CMF is comparable to the IMF, in the sense that both of them follow a power law as a function of mass, with a turn off point towards lower masses. Compared to the IMF, the CMF is shifted by a factor of three towards higher masses - a reflection of the efficiencies (or rather inefficiencies) present in core collapse.

The conversion from the CMF to the IMF is a complicated situation to analyse due to the larger uncertainties concerning the mass of dense cores. These uncertainties arise from the difficulty in identifying cores by their density gradient and separating it from the background; a cut-off density must be chosen. Another uncertainty is due to cores being extended structures, where multiple cores could be identified as a single one (Pineda *et al.* 2009; Reid *et al.* 2010); for the IMF the stars are mostly clear and luminous points. The translation from CMF to

IMF may also be affected by fragmentation of cores into multiple systems (Bate *et al.* 2003; Goodwin *et al.* 2008).

1.1.4 Core Collapse

To form stars, the dense cores must become gravitationally unstable in order for it to collapse (Klessen *et al.* 2000; Clark & Bonnell 2005). Such instabilities occur when the local density increases, which could be attributed to turbulence within the GMC (McKee & Ostriker 2007). Another way to look at gravitational stability, and local density enhancement, is by considering the Jeans Mass, $\mathrm{M}_{\mathrm{Jeans}}$. This is the critical mass required for a sphere of gas, solely supported by thermal pressure, to undergo gravitational collapse:

$$M_{\mathrm{Jeans}} = \left(\frac{5k_bT}{\mathrm{G}\mu m_H}\right)^{\frac{3}{2}} \left(\frac{3}{4\pi\rho}\right)^{\frac{1}{2}} \tag{1.1}$$

where M_{Jeans} is the Jeans Mass, k_b is the Boltzmann constant, T is the thermal temperature, G is the gravitational constant, m_H is the mass of a hydrogen atom, and ρ is the density. This equation highlights the importance of having a high density region in order for gravity to overcome thermal pressure and subsequently collapse. Provided M_{Jeans} is exceeded, the collapse occurs close to the free-fall time with inner regions collapsing faster than the outer regions (Shu 1977; Larson 1969). During collapse the density is ever increasing and the release of gravitational potential energy heats the collapsing material. If the material remains optically thin then it can radiate this heat away, which can result in further fragmentation via the Jeans mass equation.

A point will occur during the collapse of cores where the density at the centre of collapse has increased to the point where the material is no longer optically thin. This results in an increased temperature within as the radiation cannot escape. The increased thermal pressure will halt the collapse, and forms a hydrostatic core. A description of the processes after this point is given by Masunaga *et al.* (1998) where material outside of this core will continue to fall onto the core but is decelerated as it reaches the surface. This material will compress the core, while the outer layer can still cool by radiation. Compression will cause the temperature inside the core to continue rising, to the point where hydrogen dissociates. From this point material will free-fall onto the surface; this is known as the accretion phase.

The M_{Jeans} situation and free-fall of material are idealised cases, with many factors currently omitted. In particular the discussion so far has not included the effects of rotation and the restrictions it places on formation in regards to angular momentum conservation. The effects of rotation present at the dense core level would result in larger than observed rotational velocities upon collapse to a stellar size object of many orders of magnitude. Angular momentum must be conserved, so there must be mechanisms present which lower it during collapse. One such method is magnetic braking. This occurs when the rotation of the cloud twists the frozen in field line, which results in an increase in local magnetic tension. This tension exerts a braking torque on the cloud, which works to counteract the spin and lowers specific angular momentum. (Mestel & Spitzer 1956; Mouschovias & Paleologou 1979; Nakano 1989). This, theoretically, can reduce the angular momentum by more than two orders of magnitude (Mouschovias & Paleologou 1979). Recent observations by Girart *et al.* (2009) of a massive, hot, molecular core have shown signatures of magnetic breaking. The field lines threading the core are observed to be deformed towards the centre, producing an hourglass shaped field structure, while it is also seen to be simultaneously contracting and rotating.

Another possible method of shedding angular momentum is through the process of accretion discs and outflows. Depending upon the orientation of the magnetic field the resulting outflows may be magnetically driven (Blandford & Payne 1982), or centrifugally driven (Pudritz & Norman 1983). Observations of outflows from T Tauri stars have been seen to be rotating, which supports outflows as a method of dispersing angular momentum (Bacciotti *et al.* 2002). While in the accretion disc, momentum can be transferred outwards in the disc via torque due to gravitational instabilities, turbulence, or shearing in flow instabilities (Pringle 1981; Balbus & Hawley 1991; Papaloizou & Lin 1995)

Outflows form a strong source of feedback within cores and clouds, but they are not the only one. Another is from H_{II} fronts and shocks produced by already formed OB stars (Elmegreen & Lada 1977). These shocks can compress the molecular gas and cause collapse to form an additional set of stars i.e. star formation progresses in a sequential manner. Evidence of a sequential nature of formation is presented by Beccari *et al.* (2010) through the analysis of the $H\alpha$ line in the NGC 3603 cluster. Based on this line the authors find that 1/3 of the sample have an age $> 10\,\mathrm{Myr}$, while 2/3 have an age between 1 to $10\,\mathrm{Myr}$ with a median of $3\,\mathrm{Myr}$. This is suggestive of sequential star formation, as the star formation rate is increasing with time: initially, the first stars are born, they provide positive feedback, then the next generation of star formation will contain more stars.

Alternatively, recent simulations have shown that when feedback sources are combined with magnetic fields, the fragmentation of cores can also be inhibited (Price & Bate 2007; Commerçon *et al.* 2011; Myers *et al.* 2013). Observations by Palau *et al.* (2013) of 18 regions with embedded cores found that 50% of the cores showed evidence of fragmentation and 30% showed no signs of fragmentation. Additionally, theoretical work by Commerçon *et al.* (2011) suggests that magnetic fields can also inhibit fragmentation, while the cores in which turbulence is dominant show higher fragmentation. The suppression of fragmentation would suggest that the collapsing material will form just one star, often referred to as monolithic collapse or core accretion. This has been proposed as a theory for forming the most massive stars, up to $\sim 100\,\mathrm{M}_{\odot}$, from very dense cores (McKee & Tan 2002, 2003). Observations by Zhang *et al.* (2013) of a heavily embedded, massive protostar have been modelled successfully within this core accretion scenario.

An alternative formation scenario for high mass stars is through competitive accretion (Bonnell *et al.* 1997; Bonnell & Bate 2002). In this scenario the largest stars form in the centre of the cluster, as the majority of the surrounding gas is fed towards them due to their position at the centre of the gravitational potential well. In the Orion molecular cloud it has been observed that the most massive stars are clustered in the centre of the region, along with the stellar number density being of the order 2×10^4 pc^{-3} (Hillenbrand & Hartmann 1998). The formation of high mass stars in clusters is supported by observations that only 4% of O-field stars appear to have an origin outside of stellar clusters (de Wit *et al.* 2005).

1.2 Young Stellar Objects

Since this discussion now centres around Young Stellar Objects, YSOs, forming in clusters, it is important to discuss the various types of stars which exist at this stage, along with how they change on their evolution towards the main sequence.

The different stages of YSO evolution are summarised in Figure 1.2. The figure shows the SED of the four main stages, along with a graphic visualisation of their general appearance. The top image is the earliest stage of evolution, referred to as Class 0. Their SED peaks at sub-mm wavelengths, and this allowed them to be first observed through sub-mm observations by Andre *et al.* (1993). Since then, more class 0 protostars have been identified, and are seen to always be associated with high density regions (Sadavoy *et al.* 2014). The remaining three stages are shown successively underneath. These three classes were initially identified before the class 0 stage was introduced by (Lada 1987), who grouped YSOs into 3 classes based on their spectral index:

$$\alpha = \frac{\mathrm{d}\,\log\lambda F_\lambda}{\mathrm{d}\,\log\lambda} \tag{1.2}$$

Class 0 stars were not part of this initial classification by (Lada 1987), as they had not been observed yet, though they are now classified as having a spectral index of $\alpha > 3$. This high spectral index reflects their deeply embedded nature. They have been observed to have very strong molecular outflows, which are ∼10 times greater than those in class I sources (Bontemps *et al.* 1996).

In the Class I stage the molecular outflows are now seen to be much weaker than in Class 0 stars. The molecular outflow so far has helped in dispersing the surrounding envelope. Some of the envelope will have accreted onto the

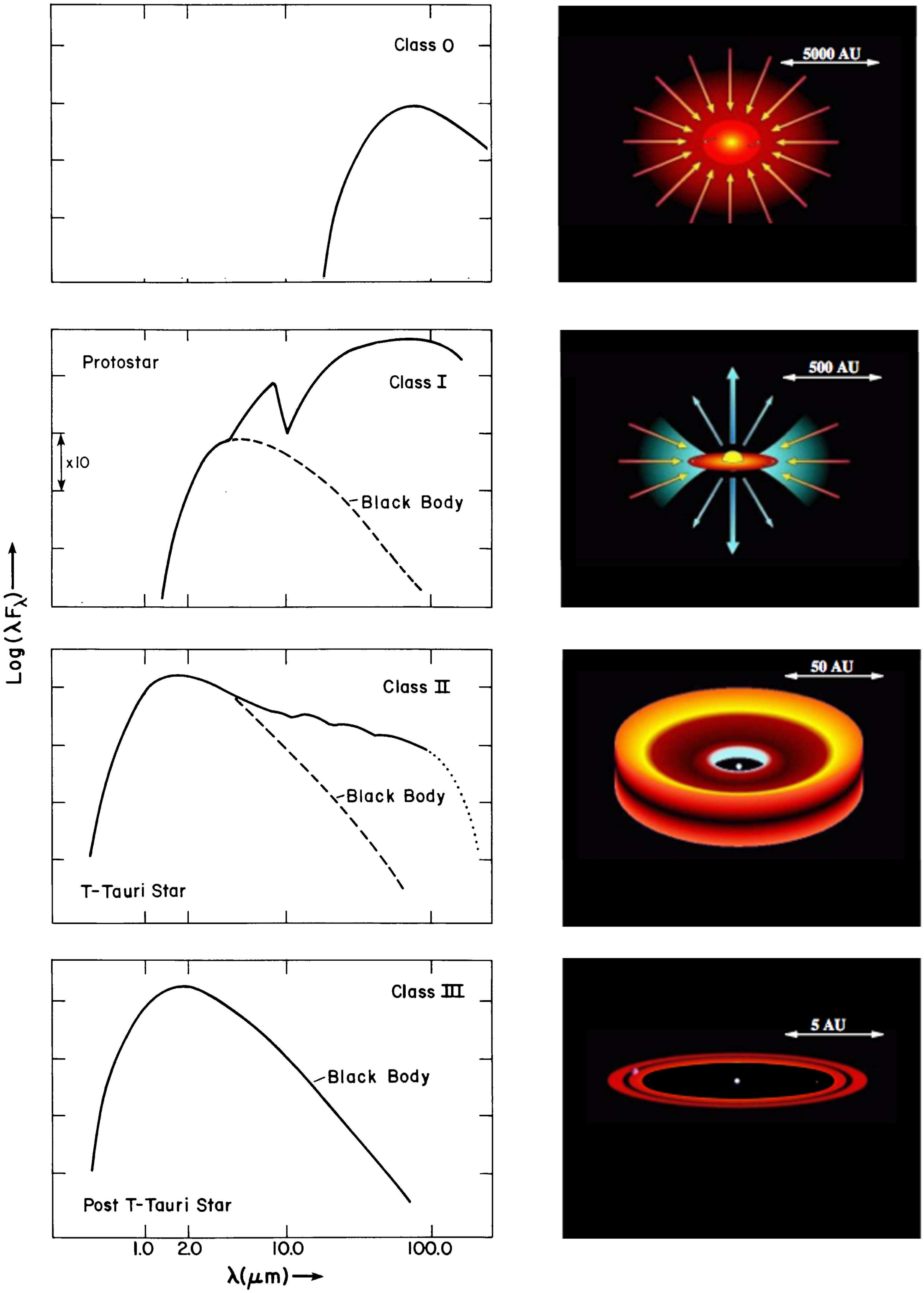

Figure 1.2: The four different classes of PMS evolution are show above, with the SEDs of each class on the left, and a graphic visualisation of each class on the right. The properties of each class are provided in the text. The figure is adapted from the works of Lada (1987) and Isella (2006).

circumstellar disc in order to drive the outflow too. Their spectral slope is defined as $0 < \alpha \leq 3$.

In the Class II stage the central star can now be seen, and the class is defined as having a spectral index of $-2 < \alpha \leq 0$. The blackbody contribution of the central star can now be seen along with the IR excess from the circumstellar disc, which is comprised of gas and dust (Sargent & Beckwith 1987). Stars belonging to this class are the Classical T Tauri stars and the Herbig Ae/Be stars.

Class III objects are the very final stages of star formation with the main star being either on the main sequence or just before it. Their spectral index is $-3 < \alpha \leq -2$, which is predominately a blackbody function of the central star and only small amount of IR excess from the now mostly dispersed circumstellar disc.

1.2.1 T Tauri Stars

The T Tauri stars, TTs, form the Class II-III category of objects between 0.1–2.0 $\mathrm{M}_{\odot}$, making them the progenitors of stars like our own Sun. They were identified 70 years ago by Joy (1945), who recognised them as a distinct class of variable stars with various low excitation emission lines, like H I, Fe II, and Ca II, present in their spectra. Since their discovery they have been divided into two separate groups. The first group are the ones identified by Joy (1945), which are referred to as the Classical T Tauri stars, (CTTs). They are seen to have an IR-excess, emission lines, and often a UV-excess; these are class II YSOs. The other group of TTs was originally recognised though X-ray detections by Feigelson & Kriss (1981), and they were later named Weak T Tauri stars, (WTTs). This is because they are seen to have weaker emission lines than CTTs (the equivalent width of Hα $<$ 10 Å), virtually no-IR excess, no UV-excess, and little variability (see Bertout 1989, for a review). Due to these properties they are said to belong to Class III YSOs. Therefore, there appears to be a trend that the WTTs are further in their evolution than CTTs, as they are beginning to display properties more typical of main sequence stars.

With a circumstellar disc and a UV-excess present in CTTs, it was suspected that they undergo accretion from the disc onto the star. Originally, it was thought that a boundary-layer model of the disc reaching directly onto the star could explain this excess (Bertout *et al.* 1988), but this has lost favour in the past 20 years due to other explanations. Now, the general consensus is that the UV-excess is caused as a consequence of magnetospheric accretion, MA (Ghosh & Lamb 1979; Uchida & Shibata 1985; Koenigl 1991; Shu *et al.* 1994; Calvet & Gullbring 1998). A full discussion of MA shall be provided in Chapter 3.3. To summarise, the magnetic field of the star truncates the inner disc at a radius from the star, which is determined by the magnetic field strength. From this radius the material will be channelled along the field lines onto the star. The channelled material, or accretion column, will shock the photosphere upon impact, releasing soft x-rays which are thermally reprocessed, and observable as the UV-excess. Support for this is given by: detections of strong-magnetic fields, which can channel the material (Johns-Krull *et al.* 1999a,b; Johns-Krull 2007; Donati *et al.* 2007); observed UV excesses and absorption line veiling (Basri & Batalha 1990; Valenti *et al.* 1993; Hartigan *et al.* 1995; Gullbring *et al.* 1998; Calvet & Gullbring 1998; Gullbring *et al.* 2000; Ingleby *et al.* 2013); and observed line profiles, who's origins are consistent with arising from an accretion column (Muzerolle *et al.*

1998a, 2001; Kurosawa *et al.* 2011).

The derived accretion rates of CTTs, from the UV-excess and veiling, are observed to be correlated with emission line strength. In particular, relationships have been established between the line luminosities and the accretion luminosity for multiple lines (Muzerolle *et al.* 1998b; Natta *et al.* 2004; Muzerolle *et al.* 2005; Natta *et al.* 2006; Herczeg & Hillenbrand 2008; Dahm 2008; Ingleby *et al.* 2013; Alcalá *et al.* 2014). These relationships have been further extended to apply to low mass brown dwarfs (Natta *et al.* 2004), and also towards more massive intermediate mass T Tauri stars of 1.5-2.5 $\mathrm{M}_{\odot}$(Calvet *et al.* 2004). This is now bordering on the Herbig Ae/Be mass range, so this raises a question: to what extent do the line luminosity to accretion luminosity relationships hold? That is, do they hold for more massive stars?

1.2.2 Massive Young Stellar Objects

At the other end of the YSO mass spectrum are the Massive Young Stellar objects, which are the progenitors of massive O and B type stars. They are considered to have a mass greater than 8 $\mathrm{M}_{\odot}$. As discussed earlier, their formation is highly associated with the densest clouds; as such, they are predominately located towards the galactic centre (Lumsden *et al.* 2013), and in the spiral arms (Urquhart *et al.* 2011). One of the biggest problems in observing these stars is that they are very rare (compared to low mass YSOs), and are heavily extinct; typical levels of reddening are observed to have $A_V > 10$ (Mottram *et al.* 2011). The reasons for their high extinction can be understood by first considering their formation from a dense core. Namely, by adopting a spherical cloud of gas and considering the free-fall time-scale:

$$\tau_{ff} = \left(\frac{3\pi}{32G\rho}\right)^{\frac{1}{2}} \tag{1.3}$$

τ_{ff} dictates the time required for an isothermal sphere to collapse under gravity unopposed e.g. a typical dense core with a number density of n=10^4 cm^{-3} finds τ_{ff} to be of the order 0.5 Myr. During contraction gravitational potential energy is converted into heat and radiated away. Therefore, the other time-scale to consider is the thermal time-scale, often referred to as the Kelvin-Helmholtz time-scale:

$$\tau_{\mathrm{KH}} = \frac{\mathrm{G}M^2}{RL} \tag{1.4}$$

where G is the gravitational constant, M is the mass of star, R is its radius, and L is its luminosity. Typically, main sequence values are adopted here as they provide the longest allowable time-scale. The transition to high mass stars is defined at $\sim$8 M$_{\odot}$, as this is where $\tau_{\mathrm{KH}} \approx \tau_{ff}$. For increasingly massive stars, τ_{KH} becomes much shorter than τ_{ff}. This is responsible for their high A_V values, mentioned earlier, as the star can reach high luminosities before all the surrounding material has settled onto it or been dispersed. The result is that the star can obtain high enough temperatures to begin main sequence burning while still accreting (Palla & Stahler 1993). This poses the problem of a high radiation pressure, which could potentially overcome the accretion, causing it to halt (Kahn 1974). It has been suggested theoretically that this can be overcome with accretion from a disc (Krumholz & McKee 2005). Lately, observations of massive disc candidates are beginning to support this via observations of rotating discs (Sánchez-Monge *et al.* 2013; Cesaroni *et al.* 2014; Beltrán *et al.* 2014).

Overall, the combination of their short time-scales and scarcity makes understanding high mass star formation a complex task, with many open questions still on the table. More observations are required to confirm disc accretion in MYSOs, and this remains difficult due to their fast evolution: the class I-III phases are skipped entirely, which means their processes of formation could be dramatically different. Therefore, to understand what could be happening close to this mass range, observations of slightly less massive stars, which are optically visible and do display the class I-III phases, may provide clues towards MYSO formation. The class of stars that meet this criteria are the Herbig Ae/Be stars.

1.2.3 Herbig Ae/Be Stars

The focus of this thesis is directed toward the Herbig Ae/Be class of stars. They form the important intermediate mass range of YSOs, of 2–10 $M_{\odot}$, between the CTTs and the MYSOs; forming a bridge between the two. Here I summarise our understanding of HAeBe stars, including the latest breakthroughs on these stars, and the future challenges which await.

This class of stars was originally identified by George Herbig in his seminal paper: Herbig (1960). The aim of his work was to find the young pre-main sequence stars which are the higher mass analogues to the now well established CTTs. In order to do this the stars had to meet the following criteria: "spectral type A or earlier with emission lines; lies in an obscured region; and the star illuminates fairly bright nebulosity in its immediate vicinity". The first criteria is the defining point of these stars, while the other two are used to reduced the contamination of the sample by stars which are not of PMS nature e.g. planetary nebulae appear nebulous but are generally not seen in obscured regions, as their birthing molecular cloud has long since dispersed. The criteria for HAeBe stars have been relaxed in more recent surveys attempting to find candidate HAeBe stars (Finkenzeller & Mundt 1984; Thé *et al.* 1994; Vieira *et al.* 2003). These studies have often drawn upon other indicators, associated with young stars, in order to find more targets. The presence of an IR-excess has often been utilised to identify these stars. The IR-excess is now known to be a key characteristic of class II stars, but their presence was not known when HAeBes were initially identified. Since then, the presence of a circumstellar disc around HAeBes has been confirmed through direct optical observations (McCaughrean & O'dell 1996; Grady *et al.* 2001), via sub-mm observations (Mannings & Sargent 1997), and also from polarised light, which is scattered off of the disc (Vink *et al.* 2002, 2005). These observations match well with the circumstellar disc being the origin of the IR-excess (van den Ancker *et al.* 2000; Meeus *et al.* 2001).

The HAeBes have been also been classified into two different subgroups based on the behaviour of this IR-excess (Meeus *et al.* 2001). For Group I stars, their inner disc is expected to be optically thick and shields the rest of the disc; the resulting disc emission can be modelled by a power law. The HAeBes in Group II require an additional blackbody component on top of a power law in order to reproduce their observed IR-excess. The additional blackbody component is suspected to be caused by the flared outer disc - the consequence of an optically thin inner disc allowing the outer disc to be exposed directly to stellar radiation. For the HAeBes with flared outer discs, the emission of ro-vibrational CO from the disc has been seen to reach as far in as $\approx$ 10 au from the star, while non-flared discs show CO extending to distances within 1 au of the star (van der

Plas *et al.* 2009, 2015; Ilee *et al.* 2014). It is suspected that these differences may be evolutionary, with the flared discs being more evolved transitional discs containing disc gaps. Such gaps have been observed by Maaskant *et al.* (2013) to only be present in Group I HAeBes. Poly-cyclic aromatic hydrocarbons, PAH, have been proposed to be good tracers of the gas flow across the gaps, while their luminosities could suggest that lower-mass discs have larger gaps (Maaskant *et al.* 2014).

The gaps present could also mark the onset of disc dispersal (see Alexander *et al.* 2014, for a review), with one of the likeliest mechanisms being through photo-evaporation (Hollenbach *et al.* 1994). This is suspected to be a likely candidate for explaining WTTs, which may also be applicable to HAeBes. However, there is currently no defined analogue of WTTs in HAeBes, although as we accrue additional information about transitional disc HAeBes perhaps an analogous class will be found. The shorter PMS stage experienced by HAeBes, over TTs, is likely the main reason as to why the number of transitional HAeBes is so few, as it requires an adequate amount of time for disc dispersal.

Returning to the case of gaps seen in some HAeBe discs, one explanation is that they could be caused by dynamical clearing of orbiting planets (Alexander & Armitage 2009; Dodson-Robinson & Salyk 2011). This possibility has grown stronger with recent observations of planetary candidates around the two HAeBe stars HD 142527 and HD 100546 (Quanz *et al.* 2013; Brittain *et al.* 2013; Currie *et al.* 2014; Close *et al.* 2014). In particular, the observations of the HD 142527 system by Close *et al.* (2014), detect Hα emission from the location of the planetary candidate. Hα is a known tracer of accretion; the strength of the line, in this case, suggests that the planetary candidate is still undergoing formation at a rate of $\sim 5.9\times10^{-10}\,\mathrm{M_\odot\,yr^{-1}}$. This is in agreement with CO streams accreting from the outer to inner disc at a rate of 7×10^{-9} to $2\times10^{-7}\,\mathrm{M_\odot\,yr^{-1}}$ (Casassus *et al.* 2013); the streams allow the inner gas disc to maintain its accretion rate of $\sim 0.7-2\times10^{-7}\,\mathrm{M_\odot\,yr^{-1}}$ (Garcia Lopez *et al.* 2006; Mendigutía *et al.* 2014). These two HAeBes are select cases, both of which are fairly cool Herbig Ae stars. As such, they may be expected to behave more similarly to low mass stars, and do not represent the HAeBes as a whole.

One of the largest questions at present concerning accretion in HAeBes is: does magnetospheric accretion govern the accretion process for HAeBe stars? The application of MA to HAeBes has been shown to work theoretically by Muzerolle *et al.* (2004); the authors demonstrated a case of modelling MA in the Herbig Ae star UX Ori. Since then, multiple works have determined accretion rates from the the measured UV-excess within the context of MA (Donehew & Brittain 2011; Mendigutía *et al.* 2011a; Pogodin *et al.* 2012; Mendigutía *et al.* 2013, 2014). However, the application of MA could not reproduce the UV-excess in all HAeBes. Additionally, correlations between the line luminosity and the accretion luminosity have been suggested to breakdown for Herbig Be stars by Donehew & Brittain (2011). On the contrary, Mendigutía *et al.* (2011a) have observed the relationships to remain similar to the ones seen in CTTs. Therefore, more observations are required to pass judgement on the matter.

One aspect which would greatly help to recognise if MA is possible in HAeBes would be the presence, or firm absence, of a magnetic field. After all, for MA to be applicable the central star requires a magnetic field with sufficient strength to truncate the disc; for CTTs this strength is of the order of kilo-Gauss strengths (Ghosh & Lamb 1979; Koenigl 1991; Shu *et al.* 1994; Johns-Krull 2007; Bouvier *et al.* 2007). Within the theory of MA, the HAeBes would require a much weaker dipole magnetic field of only a few hundred gauss, or even less for more complicated fields, for MA disc accretion to occur (Wade *et al.* 2007; Cauley & Johns-Krull 2014). There have only been a few detections of magnetic fields in HAeBes so far, and they show strengths greater than a few hundred gauss (Wade *et al.* 2005; Catala *et al.* 2007; Hubrig *et al.* 2009). The largest survey into magnetic fields of HAeBes was performed recently by Alecian *et al.* (2013), and yields clear detections in only 5 stars out of 70. This may give the impression that MA is not possible in HAeBes, but in actuality the minimum strengths required for MA in HAeBes remain below the current detection limits. This means that MA controlled accretion in HAeBes is still a possibility, which requires further investigation.

1.3 Thesis Intentions

This introduction has discussed a general overview of star formation, culminating in the present problems regarding the observability of MYSOs and the prospect of HAeBes as a bridge towards their understanding.

This thesis details the spectroscopic investigation into 91 Herbig Ae/Be stars - the largest spectroscopic analysis of HAeBes to date. The goals regarding this data set are broken down into the following chapters:

Chapter 2 is dedicated to the stellar properties of the HAeBe sample itself. Many of the HAeBes in this sample are poorly understood, with little information known about them, while others have conflicting stellar parameters listed throughout the literature. Using optical spectra, a homogeneous approach to spectral typing the entire sample is undertaken. This provides the ground work for obtaining accretion rates, line luminosities, and statistics related to stellar properties.

Chapter 3 is focused on the accretion rate determinations. UV-excesses are measured from the spectra and modelled within the context of magnetospheric accretion. Combined with the stellar parameters from Chapter 2 accretion rates can be determined for all of the detected UV-excesses. Trends in the sample of accretion versus various stellar parameters can then be assessed, along with the applicability of MA being present in HAeBes.

Chapter 4 features the emission lines. They span the entirety of the hydrogen Balmer series, in the optical, through to the Brγ line at $2.1661\,\mu$m. This allows a full assessment of line strengths, profiles, and luminosities for a wealth of suspected emitting regions. The emission lines are analysed with regards to the stellar parameters and the mass accretion rates established in Chapters 1 & 2. Comparisons are also dawn against the CTTs in order to assess any changes as a function of mass and age.

Chapter 5 features the conclusions of this study, including a discussion of its implications and future work to be undertaken.

Chapter 2

Spectral Typing of Herbig Ae/Be Stars

2.1 Introduction

The broad mass range spanned by HAeBes, of 2–10 $\mathrm{M}_\odot$, covers a temperature scale of $\sim$6000–35000 K, and a luminosity scale that spans many orders of magnitude from $\sim$10–10000 $\mathrm{L}_\odot$. According to theoretical PMS tracks, this corresponds to the 2 $\mathrm{M}_\odot$ HAeBes reaching the main sequence after $\sim$10 Myr (Bressan *et al.* 2012). Their PMS nature is a key feature of HAeBes, which was initially suspected by their discoverer George Herbig, and was later confirmed by Strom *et al.* (1972), who observed the HAeBes to have lower surface gravities than MS stars. This allows them to have a wide range of properties, as an observed cool star may actually be very bloated, very massive, and still in the early stages of contraction.

Accurate knowledge of stellar parameters is essential for any work involving modelling the circumstellar environments around the central star, as the star's properties play a large role in determining the energy input. They are also critical for accretion rate determinations, which rely on the measurement of excess flux over the photospheric component (this forms the key focus of Chapter 3).

Many scientific papers have been dedicated to such a pursuit. One of the first major works involving spectral typing HAeBes in a homogeneous fashion was by Mora *et al.* (2001). They looked at 70 suspected PMS stars, and were able to spectrally type 30 HAeBe stars into classical MK-spectral types based on comparisons with spectral standard stars. The next major study by Hernández *et al.* (2004), was dedicated to determining temperatures in HAeBe stars though the analysis of ratios between multiple absorption features in the spectra. Further stellar parameters were derived through adopting distances to the stars. This method proved successful for 58 of their 75 stars, while the remainder were contaminated by emission lines.

More recently the work by Montesinos *et al.* (2009) demonstrated a method of spectral typing and deriving additional stellar parameters, which is distance independent; this was successfully applied to 19 HAeBe stars. Their method involved SED modelling in order to obtain a temperature for the stars, and then used high resolution optical spectra to characterise the surface gravity and metalicity of each star.

These approaches to spectral typing have many benefits, but they all suffer from a few drawbacks when the goal is to obtain many stellar parameters. In particular the cases which rely on previously determined distances to calculate luminosities are limited straight away by the distance, which may be incorrect as they are often based on prior assumptions about the star's parameters. The last approach, by Montesinos *et al.* (2009), is most favourable as it does not rely upon distances, and an estimate of the surface gravity is obtained. The surface gravity is a crucial parameter for directly calculating accretion rates. Its value can alter dramatically depending upon the method used. Therefore, when considering a large set of HAeBes in a statistical manner, it is important that the parameters of all stars are determined consistently and are not biased towards the method of calculation.

I present in this chapter a homogeneous approach to determining stellar parameters in a sample of 91 HAeBe stars. The main goals are to provide a set of parameters which are both consistent for each star, and between the entire sample. A temperature, mass, radius, distance, surface gravity, luminosity, and the reddening towards each star will be calculated. These determinations will be performed by combining the powerful X-Shooter spectra with previous photometry. This lays the ground work for the later chapters in this thesis which will discuss more of the statistics in regards to accretion rates and circumstellar activity.

The chapter is broken up as follows. Section 2.2 provides details on the selected sample and important details on data reduction. Section 2.3 details the exact methods for determination of all stellar parameters. Section 2.4 analyses these results in regards to previous literature values. Section 2.5 provides information on some of the exceptional objects observed, with Section 2.5.1 giving a detailed look at two particularly interesting stars. Section 2.6 forms the discussion of the results. Finally, Section 2.7 provides the conclusions of this chapter.

2.2 Observations and Data Reduction

Table 2.1: Column 1 shows the target names, columns 2 and 3 are RA and DEC, column 4 gives the observation date, columns 5-7 give the exposure times for each arm, column 8 is the number of Detector Integration Times for the NIR arm, and finally columns 9-11 give the Signal-to-Noise Ratio in each arm.

Name	RA	DEC	Obs Date	Exposure Time (s)				SNR		
	(J2000)		(yyyy/mm/dd)	UVB	VIS	NIR	NDIT	UVB	VIS	NIR
UX Ori	05:04:29.9	-03:47:16.8	2009-10-05	360	360	20	18	42	256	119
PDS 174	05:06:55.4	-03:21:16.0	2009-10-05	1200	1200	120	2	127	64	105
V1012 Ori	05:11:36.5	-02:22:51.1	2009-10-05	1000	1000	80	12	128	157	164
HD 34282	05:16:00.4	-09:48:38.5	2009-12-06	120	120	40	3	171	216	100
HD 287823	05:24:08.1	02:27:44.4	2009-12-06	120	120	60	2	100	171	110
HD 287841	05:24:42.8	01:43:45.4	2009-12-06	360	360	60	6	78	200	67
HD 290409	05:27:05.3	00:25:04.9	2010-01-02	120	120	60	2	195	157	83
HD 35929	05:27:42.6	-08:19:40.8	2009-12-17	80	80	20	8	36	125	70
HD 290500	05:29:48.0	-00:23:45.8	2009-12-17	600	600	300	2	208	342	72
HD 244314	05:30:18.9	11:20:18.2	2010-01-02	120	120	60	2	64	140	123
HK Ori	05:31:28.1	12:09:07.6	2009-12-17	1000	1000	80	12	49	120	87
HD 244604	05:31:57.3	11:17:38.8	2009-12-17	120	120	20	8	76	170	89
UY Ori	05:32:00.4	-04:55:54.6	2009-12-26	1200	1200	300	1	228	327	66
HD 245185	05:35:09.7	10:01:49.9	2009-12-17	120	120	60	2	240	171	152
T Ori	05:35:50.6	-05:28:36.9	2009-12-17	200	200	10	5	155	198	116
V380 Ori	05:36:25.5	-06:42:58.9	2009-12-17	640	640	6	20	9	178	92
HD 37258	05:36:59.1	-06:09:17.9	2010-01-02	120	120	40	3	62	220	72
HD 290770	05:37:02.5	-01:37:21.3	2009-12-26	120	120	30	4	260	243	154
BF Ori	05:37:13.2	-06:35:03.3	2010-01-02	360	360	40	9	25	185	99
HD 37357	05:37:47.2	-06:42:31.7	2010-02-05	80	80	40	4	123	208	86
HD 290764	05:38:05.3	-01:15:22.2	2009-12-26	240	240	30	8	61	200	100
HD 37411	05:38:14.6	-05:25:14.4	2010-02-05	200	200	60	3	214	183	120
V599 Ori	05:38:58.4	-07:16:49.2	2010-01-06	1440	1440	20	10	61	150	79

Continued on next page

Table 2.1 – continued from previous page

Name	RA	DEC	Obs Date	Exposure Time (s)				SNR		
	(J2000)		(yyyy/mm/dd)	UVB	VIS	NIR	NDIT	UVB	VIS	NIR
V350 Ori	05:40:11.9	-09:42:12.2	2010-02-05	600	600	100	6	77	260	69
HD 250550	06:01:59.9	16:30:53.4	2010-01-02	120	120	12	10	104	218	126
V791 Mon	06:02:15.0	-10:01:01.4	2010-02-24	360	360	60	6	67	343	92
PDS 124	06:06:58.5	-05:55:09.2	2010-02-10	1200	1200	300	1	189	63	81
LkHa 339	06:10:57.7	-06:14:41.8	2010-01-17	1200	1200	240	5	122	63	109
VY Mon	06:31:06.8	10:26:02.9	2010-02-08	1200	1200	12	20	11	49	37
R Mon	06:39:10.0	08:44:08.2	2010-02-01	1200	1200	12	20	11	49	129
V590 Mon	06:40:44.7	09:47:59.7	2010-02-01	1200	1200	200	6	143	165	117
PDS 24	06:48:41.8	-16:48:06.0	2009-12-16	1200	1200	360	3	145	48	64
PDS 130	06:49:58.7	-07:38:52.1	2009-12-16	1200	1200	240	5	124	122	54
PDS 229N	06:55:40.1	-03:09:53.1	2010-02-10	1200	1200	400	3	111	105	125
GU CMa	07:01:49.6	-11:18:03.9	2009-12-16	24	24	4	6	127	180	46
HT CMa	07:02:42.7	-11:26:12.3	2010-01-30	1200	1200	120	10	200	246	110
Z CMa	07:03:43.2	-11:33:06.7	2010-02-24	600	120	13.3	20	28	87	80
HU CMa	07:04:06.8	-11:26:08.0	2010-01-17	1200	1200	200	6	186	216	132
HD 53367	07:04:25.6	-10:27:15.8	2010-02-24	24	24	4	6	62	166	121
PDS 241	07:08:38.8	-04:19:07.0	2009-12-21	1200	1200	400	3	227	295	129
NX Pup	07:19:28.4	-44:35:08.8	2010-02-01	480	480	4	20	44	191	54
PDS 27	07:19:36.1	-17:39:17.9	2010-02-24	1200	1200	12	20	9	118	63
PDS 133	07:25:05.1	-25:45:49.1	2010-02-24	1200	1200	160	2	3	22	35
HD 59319	07:28:36.9	-21:57:48.4	2010-02-24	80	80	40	4	265	14	131
	PDS 134	07:32:26.8	-21:55:35.3	2010-02-24	1200	1200	600	2	197	210
80										
HD 68695	08:11:44.3	-44:05:07.5	2009-12-21	160	160	60	3	160	180	85
HD 72106	08:29:35.0	-38:36:18.5	2009-12-19	80	80	40	4	49	136	88
TYC 8581-2002-1	08:44:23.5	-59:56:55.8	2009-12-21	600	600	200	3	181	205	89

Continued on next page

Table 2.1 – continued from previous page

Name	RA	DEC	Obs Date	Exposure Time (s)				SNR		
	(J2000)		(yyyy/mm/dd)	UVB	VIS	NIR	NDIT	UVB	VIS	NIR
PDS 33	08:48:45.4	-40:48:20.1	2009-12-21	1200	1200	600	2	278	181	62
HD 76534	08:55:08.8	-43:27:57.3	2010-01-30	120	180	60	3	149	254	63
PDS 281	08:55:45.9	-44:25:11.4	2009-12-21	120	120	30	4	193	175	58
PDS 286	09:05:59.9	-47:18:55.2	2009-12-21	1200	1200	12	20	96	204	106
PDS 297	09:42:40.0	-56:15:32.2	2010-01-04	1200	1200	300	2	211	210	55
HD 85567	09:50:28.3	-60:57:59.5	2010-03-06	120	180	8	20	141	183	147
HD 87403	10:02:51.3	-59:16:52.7	2010-03-06	120	120	60	2	136	137	152
PDS 37	10:10:00.3	-57:02:04.4	2010-03-31	1200	1200	18	15	18	182	109
HD 305298	10:33:05.0	-60:19:48.6	2010-03-31	360	360	180	2	155	209	94
HD 94509	10:53:27.2	-58:25:21.4	2010-02-05	160	160	60	3	12	163	119
HD 95881	11:01:57.1	-71:30:46.9	2010-01-04	120	180	8	20	56	223	105
HD 96042	11:03:40.6	-59:25:55.9	2010-02-05	80	80	40	4	97	107	48
HD 97048	11:08:03.0	-77:39:16.0	2010-02-05	180	180	8	20	208	254	137
HD 98922	11:22:31.5	-53:22:09.0	2010-03-30	36	36	6	20	85	196	76
HD 100453	11:33:05.3	-54:19:26.1	2010-03-29	120	180	8	20	36	111	75
HD 100546	11:33:25.1	-70:11:39.6	2010-03-30	36	36	2	20	284	207	94
HD 101412	11:39:44.3	-60:10:25.1	2010-03-30	120	120	40	3	90	125	117
PDS 344	11:40:32.8	-64:32:03.0	2010-03-31	1200	1200	600	2	236	190	101
HD 104237	12:00:04.8	-78:11:31.9	2010-03-30	36	36	6	20	25	88	81
V1028 Cen	13:01:17.6	-48:53:17.0	2010-03-29	360	360	40	9	101	165	113
PDS 361S	13:03:21.6	-62:13:23.5	2010-03-31	1200	1200	600	2	118	193	96
HD 114981	13:14:40.4	-38:39:05.0	2010-03-29	36	36	6	6	251	185	97
PDS 364	13:20:03.5	-62:23:51.7	2010-03-31	1200	1200	360	3	130	117	107
PDS 69	13:57:44.0	-39:58:47.0	2010-03-29	120	120	20	6	44	66	76
DG Cir	15:03:23.4	-63:22:57.2	2010-03-31	1440	1440	40	20	14	103	124
HD 132947	15:04:56.2	-63:07:50.0	2010-03-12	160	160	60	3	231	263	150

Continued on next page

Table 2.1 – continued from previous page

Name	RA	DEC	Obs Date	Exposure Time (s)				SNR		
	(J2000)		(yyyy/mm/dd)	UVB	VIS	NIR	NDIT	UVB	VIS	NIR
HD 135344B	15:15:48.2	-37:09:16.7	2010-03-31	40	40	8	6	42	115	93
HD 139614	15:40:46.3	-42:29:51.4	2010-03-28	80	80	20	8	35	140	98
PDS 144S	15:49:15.4	-26:00:52.8	2010-03-31	1200	1200	25	10	49	127	71
HD 141569	15:49:57.8	-03:55:18.6	2010-03-28	24	24	4	6	177	151	74
HD 141926	15:54:21.5	-55:19:41.3	2010-03-12	120	120	12	10	66	199	81
HD 142666	15:56:40.2	-22:01:39.5	2010-03-28	180	180	8	20	53	126	78
HD 142527	15:56:41.8	-42:19:21.0	2010-04-01	40	40	4	20	23	88	81
HD 144432	16:06:57.8	-27:43:07.4	2010-03-12	120	180	8	20	54	126	111
HD 144668	16:08:34.0	-39:06:19.4	2010-03-30	36	36	6	20	96	190	142
HD 145718	16:13:11.4	-22:29:08.3	2010-03-29	120	120	12	10	84	165	84
PDS 415N	16:18:37.4	-24:05:22.0	2010-03-31	1200	1200	50	5	13	66	37
HD 150193	16:40:17.7	-23:53:47.0	2010-03-30	300	180	8	20	100	152	129
AK Sco	16:54:45.0	-36:53:17.1	2009-10-05	80	80	20	8	26	91	55
PDS 431	16:54:58.9	-43:21:47.7	2010-04-01	1200	1200	600	2	173	172	83
KK Oph	17:10:07.9	-27:15:18.6	2010-03-26	800	800	12	20	57	275	63
HD 163296	17:56:21.4	-21:57:21.7	2009-10-05	36	36	2	20	87	241	78
MWC 297	18:27:39.7	-03:49:53.1	2009-10-06	1200	40	39.9	20	162	96	58

Table 2.2: Photometry, temperatures, and distances from the literature.

Name	U (mag)	B (mag)	V (mag)	R (mag)	I (mag)	Phot Ref	Teff (K)	Teff Ref	D (pc)	D ref
UX Ori	10.94	10.71	10.34	10.12	9.88	a	8410	i	340	ap
PDS 174	13.54	13.65	12.84	12.18	11.42	b	18700	b	340	ap
V1012 Ori	12.62	12.46	12.04	11.61	11.25	c	8600	c	340	ap
HD 34282	10.15	10.05	9.89	9.81	9.71	a	8720	i	340	ap
HD 287823	9.98	9.90	9.68	9.59	9.48	b	8720	j	340	ap
HD 287841	10.63	10.50	10.21	10.06	9.89	a	8990	i	340	ap
HD 290409	10.20	10.11	10.02	9.96	9.89	b	10500	b	340	ap
HD 35929	8.71	8.53	8.12	7.87	7.61	a	6870	k	360	aq
HD 290500	11.41	11.35	11.04	-	-	d	8970	b	470	ap
HD 244314	10.42	10.30	10.10	9.96	9.80	b	8720	l	440	ap
HK Ori	11.72	11.79	11.41	11.05	10.66	a	8460	m	440	ap
HD 244604	9.68	9.57	9.38	9.27	9.12	a	8720	l	440	ap
UY Ori	13.38	13.16	12.79	12.56	12.19	b	10500	b	510	ap
HD 245185	10.02	10.00	9.91	9.87	9.82	a	9520	l	440	ap
T Ori	11.38	10.98	10.43	10.10	9.63	a	8660	i	510	ap
V380 Ori	10.80	11.04	10.53	10.11	9.50	a	9230	n	510	ap
HD 37258	9.84	9.80	9.67	9.59	9.49	a	8970	o	510	ap
HD 290770	9.18	9.30	9.27	9.23	9.18	b	10500	b	470	ap
BF Ori	10.34	10.05	9.82	9.68	9.48	a	8990	i	510	ap
HD 37357	9.00	8.95	8.84	8.79	8.72	a	9230	l	510	ap
HD 290764	10.29	10.20	9.88	9.68	9.44	b	7200	b	470	ap
HD 37411	10.07	9.95	9.82	9.72	9.58	a	9100	l	510	ap
V599 Ori	17.07	15.41	13.76	12.69	11.55	a	7200	b	510	ap
V350 Ori	11.39	11.15	10.82	10.62	10.34	a	8990	i	510	ap
HD 250550	9.34	9.61	9.54	9.32	9.54	e	10750	l	280	ar
V791 Mon	10.31	10.68	10.38	10.12	9.87	b	18700	p	1100	as
PDS 124	13.15	12.97	12.44	12.15	11.81	b	9520	b	830	w
LkHa 339	14.59	14.24	13.47	12.80	11.93	a	9230	q	830	w
VY Mon	15.28	14.56	12.97	11.82	10.60	a	8200	i	800	at
R Mon	12.17	12.53	11.93	11.41	10.87	a	12400	i	800	at
V590 Mon	12.52	12.75	12.60	12.42	12.12	a	13000	r	800	at
PDS 24	13.94	13.62	13.26	12.98	12.69	b	10500	b	590	ap
PDS 130	14.42	14.06	13.40	12.96	12.44	b	10500	b	830	w
PDS 229N	13.82	13.70	13.13	12.74	12.24	b	9520	b	830	w
GU CMa	5.88	6.56	6.54	6.47	6.37	a	25000	s	1050	au
HT CMa	12.55	12.29	11.87	11.38	11.87	e	9520	q	1050	au
Z CMa	11.20	10.50	9.25	8.40	7.65	f	30000	f	1050	au

Continued on next page

Table 2.2 – continued from previous page

Name	U (mag)	B (mag)	V (mag)	R (mag)	I (mag)	Phot Ref	Teff (K)	Teff Ref	D (pc)	D ref
HU CMa	11.72	11.84	11.55	11.32	11.16	a	11900	q	1050	au
HD 53367	6.80	7.37	6.95	6.67	6.30	a	29500	s	1050	au
PDS 241	12.33	12.71	12.06	11.45	11.11	b	30000	b	7000	av
NX Pup	9.93	9.96	9.63	9.38	9.07	a	7290	t	410	ap
PDS 27	14.61	14.32	13.00	12.00	10.98	b	22000	u	-	u
PDS 133	13.57	13.61	13.13	12.79	12.50	b	14000	b	2500	b
HD 59319	7.86	8.23	8.31	8.34	8.42	a	11900	v	-	-
PDS 134	12.50	12.61	12.20	11.92	11.65	b	14000	b	-	-
HD 68695	10.00	9.92	9.82	9.76	9.66	b	9520	w	410	ap
HD 72106	8.39	8.50	8.50	8.49	8.49	b	9810	x	370	ap
TYC*	12.18	11.94	11.48	11.19	10.95	b	† 8200	b	145	ap
PDS 33	12.85	12.63	12.34	12.16	11.97	b	9520	b	370	ap
HD 76534	7.68	8.18	8.07	7.97	7.84	a	20350	y	370	ap
PDS 281	9.43	9.46	8.87	8.50	8.08	b	17050	b	370	ap
PDS 286	14.39	13.91	12.15	10.91	9.76	b	30000	b	370	ap
PDS 297	12.50	12.34	12.03	11.83	11.59	b	7850	b	145	ap
HD 85567	8.11	8.65	8.51	8.33	8.08	a	12450	z	650	aq
HD 87403	9.28	9.31	9.26	9.22	9.16	b	10100	aa	145	ap
PDS 37	15.56	15.06	13.54	12.38	11.21	b	22000	u	-	u
HD 305298	10.36	11.07	10.86	10.66	10.47	b	36900	ab	-	-
HD 94509	9.01	9.15	9.12	9.10	9.10	a	9730	ac	-	-
HD 95881	8.53	8.36	8.19	-	-	g	8990	ad	118	ap
HD 96042	7.89	8.60	8.47	8.36	8.23	b	25400	ad	-	-
HD 97048	8.96	8.80	8.44	8.20	7.95	a	10010	ae	160	aq
HD 98922	6.74	6.82	6.77	6.69	6.61	a	10500	w	850	aq
HD 100453	8.10	8.07	7.78	7.60	7.42	b	7390	aa	122	aq
HD 100546	6.60	6.70	6.69	6.67	6.66	a	10500	af	97	aq
HD 101412	9.57	9.42	9.24	9.13	9.00	b	10010	aa	118	ap
PDS 344	13.09	13.40	13.15	12.95	12.77	b	15400	b	-	-
HD 104237	6.64	6.73	6.52	6.38	6.23	a	8410	z	115	aq
V1028 Cen	10.39	10.70	10.61	10.48	10.33	a	14100	z	130	aq
PDS 361S	13.10	13.35	12.85	12.49	12.09	b	18700	b	-	-
HD 114981	6.55	7.13	7.23	7.27	7.33	b	†15400	b	550	aq
PDS 364	13.85	13.93	13.46	13.05	12.63	b	11900	ag	118	ap
PDS 69	9.92	10.12	9.80	9.50	9.12	b	17050	ah	630	ah
DG Cir	15.96	15.87	14.75	13.96	13.06	a	15000	ai	700	aw
HD 132947	8.87	8.96	8.91	8.89	8.89	a	10500	af	-	-
HD 135344B	9.14	9.14	8.63	8.16	7.83	h	6590	aj	140	ap
HD 139614	8.67	8.64	8.40	8.26	8.11	b	7850	aj	140	ap

Continued on next page

Table 2.2 – continued from previous page

Name	U (mag)	B (mag)	V (mag)	R (mag)	I (mag)	Phot Ref	Teff (K)	Teff Ref	D (pc)	D ref
PDS 144S	13.59	13.28	12.79	12.49	12.16	b	8200	b	145	ap
HD 141569	7.23	7.20	7.10	7.03	6.95	a	9520	aj	116	aq
HD 141926	8.72	9.20	8.64	8.21	7.77	b	20300	b	-	-
HD 142666	9.42	9.17	8.67	8.35	8.01	b	7580	aj	145	ap
HD 142527	9.20	9.15	8.27	-	-	g	6260	ak	230	ak
HD 144432	8.64	8.53	8.17	7.94	7.72	a	7350	i	160	aq
HD 144668	7.28	7.11	6.78	6.57	6.38	a	7930	al	160	aq
HD 145718	10.00	9.62	9.10	8.79	8.45	b	8200	ag	117	aq
PDS 415N	13.43	12.96	12.04	11.47	10.85	b	7200	b	120	ax
HD 150193	9.69	9.33	8.80	8.41	7.97	a	10010	af	120	ax
AK Sco	9.56	9.53	8.90	8.54	8.18	a	6450	am	103	aq
PDS 431	14.20	13.99	13.42	13.02	12.59	b	9520	b	145	ap
KK Oph	13.17	12.97	12.36	11.83	11.03	a	8030	an	145	ap
HD 163296	7.00	6.96	6.85	6.80	6.71	a	8720	l	119	aq
MWC 297	14.94	14.27	12.03	10.18	8.80	a	23700	ao	250	ao

† These two stars are listed as objects QT3 (TYC 8581-2002-1) and QT4 (HD 114981) in the first Table of Vieira *et al.* (2003). However, their places appear swapped in the second table by these authors. This suspicion is supported by additional photometry of HD 114981 and by the authors observed temperatures and the temperatures derived in this work. Based on this we have switched the photometry from Vieira *et al.* (2003) around for these two stars.

* The name has been shortend, the fullname is TYC 8581-2002-1

References: (a) de Winter *et al.* (2001), (b) Vieira *et al.* (2003), (c) Miroshnichenko *et al.* (1999), (d) Guetter (1979), (e) Herbst & Shevchenko (1999), (f) van den Ancker *et al.* (2004), (g) Malfait *et al.* (1998), (h) Coulson & Walther (1995), (i) Mora *et al.* (2001), (j) Hernández *et al.* (2005), (k) Miroshnichenko *et al.* (2004), (l) Gray & Corbally (1998), (m) Baines *et al.* (2004), (n) Finkenzeller & Mundt (1984), (o) Gray & Corbally (1993), (p) Cidale *et al.* (2001), (q) Hernández *et al.* (2004), (r) Pérez *et al.* (2008), (s) Tjin A Djie *et al.* (2001), (t) Finkenzeller (1985), (u) Ababakr *et al.* (2015, submitted), (v) Houk & Smith-Moore (1988), (w) Herbst & Racine (1976), (x) Houk (1982), (y) Valenti *et al.* (2000), (z) van den Ancker *et al.* (1998), (aa) Guimarães *et al.* (2006), (ab) Graham (1970), (ac) Stephenson & Sanduleak (1971), (ad) Houk & Cowley (1975), (ae) Whittet *et al.* (1987), (af) Levenhagen & Leister (2006), (ag) Carmona *et al.* (2010), (ah) Reipurth & Zinnecker (1993), (ai) Gahm & Malmort (1980), (aj) Dunkin *et al.* (1997), (ak) Fukagawa *et al.* (2006), (al) Tjin A Djie *et al.* (1989), (am) Andersen *et al.* (1989), (an) Herbig (2005), (ao) Drew *et al.* (1997), (ap) de Zeeuw *et al.* (1999), (aq) van Leeuwen (2007), (ar) Canto *et al.* (1984), (as) Hilton & Lahulla (1995), (at) Dahm & Simon (2005), (au) Shevchenko *et al.* (1999), (av) Avedisova (2000), (aw) Franco (1990), (ax) Loinard *et al.* (2008).

2.2.1 X-Shooter Spectrograph and Target Selection

Observations were performed over a period of 6 months between October 2009 and April 2010 using the X-Shooter echelle spectrograph – mounted at the VLT, Cerro Paranal, Chile (Vernet *et al.* 2011). X-Shooter provides spectra covering a large wavelength range of 3000–23000 Å. The wavelength coverage is simultaneous and is split across three arms: the UVB arm, 3000–5600 Å; the VIS arm, 5500–10200 Å; and the NIR arm, 10200-24800 Å. The smallest slit widths available of 0.5", 0.4" and 0.4" were used to provide the highest possible spectral resolutions of R $\sim$ 10000, 18000 and 10500 for the respective UVB, VIS and NIR arms. In total 91 science targets were observed in nodding mode using an ABBA sequence. Table 2.2 includes details of the RA and DEC, exposure times, and the signal-to-noise in each arm, for each target. The SNR is calculated by analysing a 30 Å region of spectra centred about the wavelengths of 4600, 6750, and 16265 Å for the UVB, VIS, and NIR arm respectively. These regions were chosen as they are generally the flattest continuum regions in each star. Although emission lines, and absorption lines of cooler objects, can artificially lower the measured SNR, for a fair treatment we stick with the above regions to provide a rough guide to the quality of each spectrum.

The targets were selected from the catalogues of Thé *et al.* (1994), and Vieira *et al.* (2003). 51 targets were selected from Thé *et al.* (1994), and 40 from the Vieira *et al.* (2003) catalogue, bringing the total number of targets to 91. The observations cover around 70% of the southern HAeBes identified by Thé *et al.* (1994), and about 50% of the targets observed by Vieira *et al.* (2003). It should be noted that many of these stars are HAeBe candidate stars; particularly the

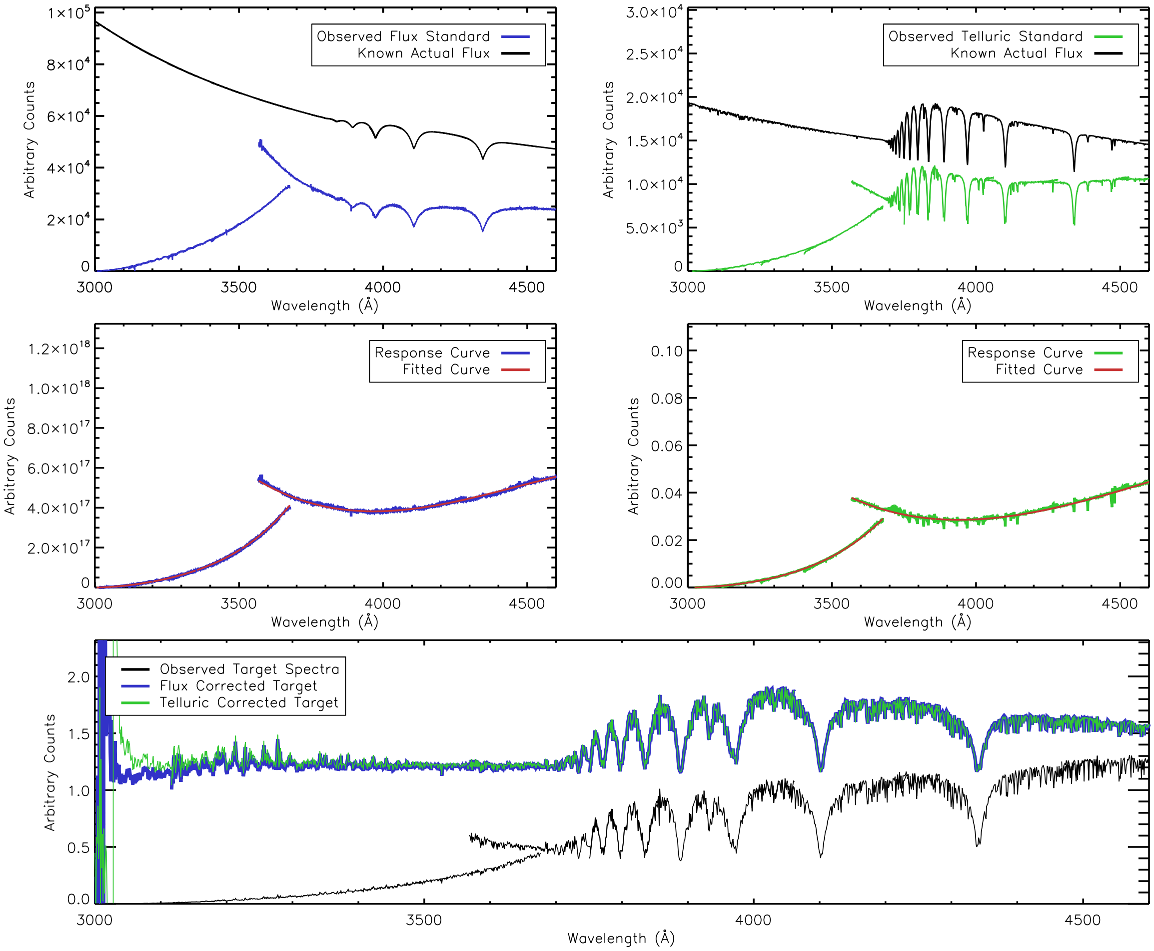

Figure 2.1: Shown above are the two different cases of correcting target spectra via either: a flux standard - shown on the left; or a telluric standard - shown on the right. The top-left panel shows the observed flux standard (blue) and the expected spectra of the flux standard (black). Similarly the top-right panel shows the observed telluric standard (green) and its expected spectra (black). The middle two panels show a division of the observed standard stars (blue and green) by their expected spectra from the top panels, and a two part curve (red) is also shown as a fit to this division. The very bottom panel shows the result of applying the two fits from the middle panel to the target spectra (black). It can be seen that the two methods of correction are equivalent. All spectra have been arbitrarily scaled in order to be visible on each plot.

ones from the Pico dos Dias Survey (PDS) by (Vieira *et al.* 2003). Therefore, there may be a few stars which have been misclassified as HAeBes, such as regular Be stars, or even post-AGB stars. For many of the targets little information is known about them, particularly in regards to multiplicity (see Duchêne 2015, for a review). It is known that HAeBes have high binary fractions (Baines *et al.* 2006; Wheelwright *et al.* 2010), and as a consequence, any close separation binaries will contribute towards observed spectra. In this work our focus is on the UV and optical portions of the spectra, where we assume that the primary star, the HAeBe target, provides the largest contribution to the brightness. Contributions from secondary stars will be more numerous for the observed literature photometry, as they use larger slit widths/apertures. Photometry of all the targets is sourced from the literature, and is provided in Table 2.2 along with previous estimates of the temperature of each star.

Telluric standards were observed either just before or after each science exposure. They were observed in stare mode for short exposures, ∼10 s, due to their brightness. Flux standard stars were observed on approximately half of the evenings in offset mode, which allows accurate sky subtraction to be performed.

2.2.2 Data Reduction

All data were reduced automatically by ESO, following standard procedures of the X-Shooter pipeline v0.9.7 (Modigliani *et al.* 2010). A random number of targets were quality checked by the primary investigator of the original observing proposal (René Oudmaijer), who found the reduction to be of good quality. Only one aspect is not included in the standard procedures and that is flux calibration.

However, for the work presented in this thesis absolute flux calibration of the spectra is not required. Only an accurate determination of the spectral shape is needed in the UVB arm; specifically across the Balmer Jump region where the difference between the U-band and B-band is required in order to measure any excess UV-emission (these measurements will be performed in Chapter 3). Flux calibrations of the other arms are not required as interest lies solely in the strengths of the spectral lines in those arms, which only need knowledge of the continuum around the lines along with existing broadband photometry (measurement and analysis of the spectral lines is deferred to Chapter 4).

Ordinarily, to obtain the correct SED of the spectra flux calibrations are performed using the observed flux standards of each night. However, as mentioned, flux standards were not observed on all evenings. A solution to this is to instead use the telluric standards, for which there is at least one per target, as a means of correction. This will ensure a uniform treatment to all of the targets, although caution should be noted of using stars which are not dedicated flux standards for calibration. To mitigate any problems that could arise from this, consistency checks are made against the flux standards for the nights where they are available and will be discussed at the end of this section. For this method of spectral shape calibration accurate knowledge of the spectral type of each telluric is required. To ensure a homogeneous reduction I adopted my own spectral typing of each telluric in this work. This helps to minimise any reduction errors, and will also allow us to place a systematic error on this reduction method. Full details of the spectral typing, along with a discussion of how they compare with literature values, will be provided in Section 2.3. Once the spectral type is determined, the observed telluric spectra are divided through by a model atmosphere of the same spectral type in order to obtain an instrumental *response* curve. The model atmospheres adopted here, and throughout this work, are sets of Kurucz-Castelli models (Kurucz 1993; Castelli & Kurucz 2004) computed by Munari *et al.* (2005), due to their small dispersion of 1 Å over the UVB wavelength range (these will be referred to as KC-models hereafter). The resulting response curve from this division is then fit with two curves: one for the echelle orders < 3600 Å and another for the orders > 3600 Å. This is because the response at ~ 3600 Å is not the same between the two over-lapping echelle orders. Figure 2.1 shows the procedure of the above method for a target observed by both a flux standard and a telluric standard; it highlights the two different response curves in the U-band region in the middle panels. The figure also shows the consistency check comparing the flux standard reduction, on the left, to the telluric standard reduction, on the right. The final panel of the figure demonstrates the similarity of the results with a difference of $< 3\%$ across the spectra. Larger deviations are seen between the two spectra close to 3000 Å due to low levels of counts. This region is not used in this work and can be disregarded. The same method is performed on other stars for which both a telluric and flux standard are available, and the maximum deviation seen is only 5% across the spectra. Overall, it can be seen that this method of using the telluric standards for instrumental response correction provides a satisfactory SED calibration of the data; as such it is performed on all targets.

2.3 Distance and Stellar Parameters Determinations

Determining accurate stellar parameters is crucial for extracting an accretion rate, and for obtaining further information about the age, evolution, and ongoing processes in the environment around HAeBe stars. Many stars in this sample have had their stellar parameters determined previously, but this has often been done in smaller sub-sets using a variety of methods. For this reason a full treatment of determining stellar parameters is performed on the entire sample, in a nearly homogeneous fashion, to provide better consistency between the stars.

The determination of parameters is summarised in Figure 2.2 as a three step process, consisting of:

1. Spectral typing is performed using the X-Shooter spectra to provide accurate limits on the effective surface temperature, T_{eff}, and also on the surface gravity, log(g), where possible.

2. KC-models and the photometry are used to assess the reddening, A_V, and to obtain a distance/radius ratio, $D/R_\star$, for each target.

3. Finally, PMS evolutionary tracks are used to infer a mass, $M_\star$, and age (and other parameters if not yet determined).

These separate stages of the stellar parameter determination process are now given in detail.

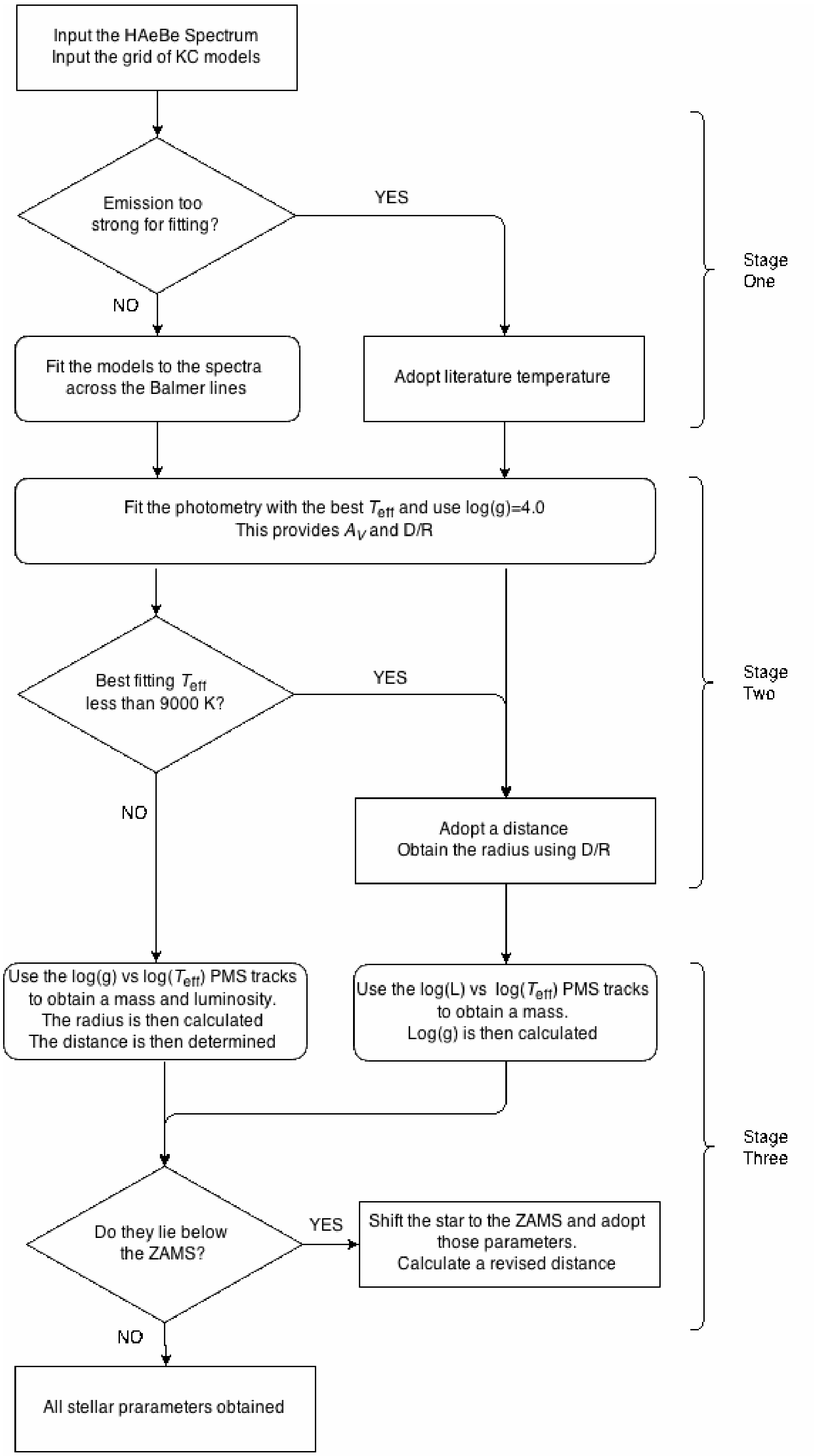

Figure 2.2: This flowchart provides a visual overview of the stellar parameter determination process. It covers the different situations which can occur for each star during each stage. Thorough details of each step and stage in the flowchart are provided in the text.

2.3.1 Temperature and Surface Gravity Determination

The first stage takes advantage of the large wavelength coverage and medium spectral resolution of X-Shooter to perform spectral typing; allowing the narrowing down of the possible T_{eff} and log(g) values for each target. This is done by following a similar method to Montesinos *et al.* (2009), of spectral typing using the wings of the hydrogen Balmer series. These lines are favoured due to their sensitivity to changes in both T_{eff} and log(g). Specifically, the Hβ, Hδ, and Hϵ lines are used as they have the largest intrinsic absorption of the series, after the Hα line. Hα is not used for spectral typing as it is often seen in emission, and is both the strongest and broadest of the Balmer series in HAeBes; this could affect the derived parameters. Therefore, fitting is performed on the other lines in the series.

To perform the fitting, each line is first normalised based on the continuum either side of the line. They are then compared against a grid of KC-model spectra, which have also been normalised in the same way using the same regions either side of the line. The resolution of the grid is set to be in steps of 250 K for T_{eff} and 0.1 dex for log(g). The fit of the synthetic spectra to the observed spectra is judged using the wings of each line, and continuum features, where the intensity is greater than 0.8. This avoids the problems of both emission and rotational broadening in the line, which affect the central parts of the underlying absorption the most. Figure 2.3 gives four examples of this fitting, highlighting the power for obtaining an accurate T_{eff} and log(g), where many errors are as small as the chosen step size. However, despite this reliable technique, issues arise for situations. The first, is that there is a non-linear relationship between the Balmer line width and the surface gravity for objects where $T_{\rm eff} < 9000\,{\rm K}$ (Guimarães *et al.* 2006). This produces a degeneracy in the fitting below this temperature, and for this reason log(g) is not constrained using the spectra for those objects. The second issue concerns objects which display extreme emission lines; where the line strength is exceptionally strong across the Balmer series to the point where the width of the lines eclipse even the broad photospheric absorption wings. Extremely strong P-Cygni, or inverse P-Cygni, profiles can also affect the line shape in the wings. An example of extreme emission is shown in the bottom-right panel of Figure 2.3, where none of the intrinsic photospheric absorption can be seen due to the emission. P-Cygni absorption is also present in this example, further complicating any possible analysis of the wings. Objects like the example just given, for which both $T_{\rm eff}$ and log(g) cannot be constrained, will be treated separately on an individual basis, and are detailed in Section 2.5. The objects for which $T_{\rm eff}$ has been constrained can have all of their parameters determined in the next two steps.

For the telluric standards the same steps above are applied. This is because they are well-behaved stars for which a $T_{\rm eff}$ and log(g) determination is straight forward. These parameters are required for the data reduction discussed previously in Section 2.2.2.

2.3.2 Photometry Fitting

The second step of this process takes two directions: One for the case in which $T_{\rm eff}$ and log(g) were determined, and the other for when only $T_{\rm eff}$ could be determined. In both cases, fitting spectra of model atmospheres based on the param-

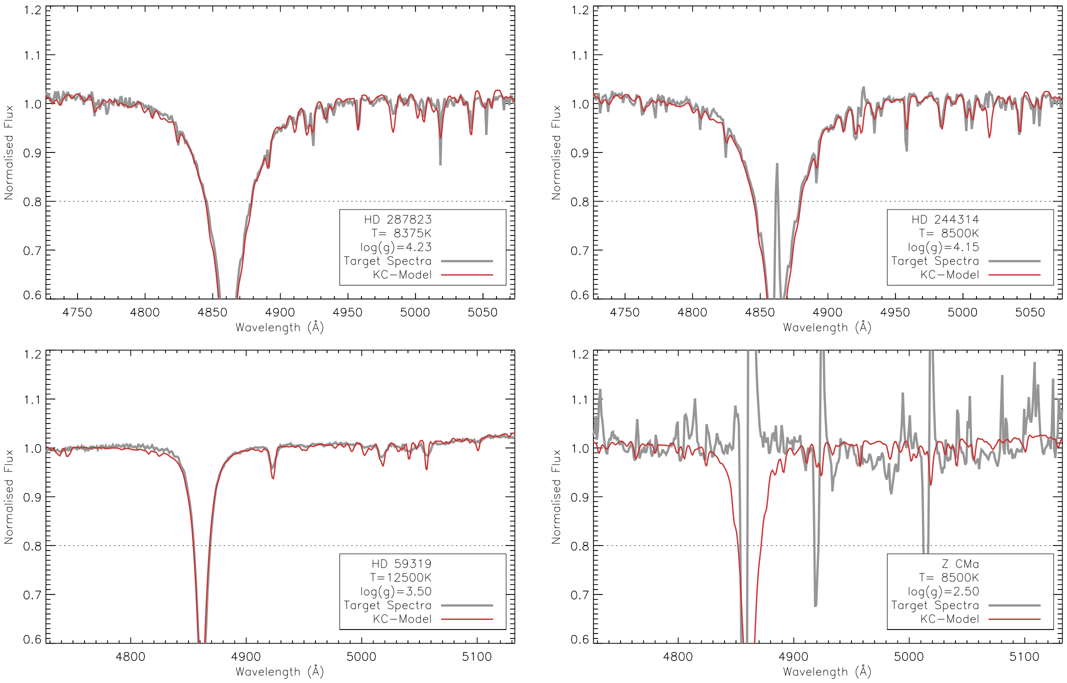

Figure 2.3: Examples of spectral typing for four targets are presented here. Each panel shows both the target spectra (grey), and a KC-model which denotes a good fit (red). The parameters for the KC-model are given for each fit. Also plotted is a dashed line, at 0.8 of the normalised intensity, which is used as a cut-off in the fitting. The two panels on the left show the cases for straight forward fit where there is no obvious emission. The figure in the top-right is a case where there is clear emission present; a good fit is still achieved. The bottom-right panel gives an example of one of the few objects which cannot be spectrally typed in this way due to extremely strong emission; this exceptional object, and others, are presented in detail in Chapter 2.5.

eters determined in the previous step, to the observed optical photometry will be performed. The fitting will provide a level of reddening, A_V, to each star, and a scaling factor, $D/R_\star$, due to the fitting of surface flux models to observed photometry.

To perform the fitting only the $BVRI$ points are used; the U-band can be influenced heavily by the Balmer Excess, and no photometry long-wards of the I-band is used due to the possible influence of the IR-excess (which itself would require dedicated modelling). The B-band may also be affected by an extremely large flux excess. These cases are rare, and the change in the B-band magnitude would not significantly affect the fitting as the excess energy follows a similar SED shape (the fitting is far more sensitive to the input temperature). Another point to consider when looking at optical photometry is the effects of variability, as this has been observed in numerous HAeBes (de Winter *et al.* 2001; Oudmaijer *et al.* 2001; Mendigutía *et al.* 2011b; Pogodin *et al.* 2012; Mendigutía *et al.* 2013). However, variability information is not present for all of the targets, but we estimate that the calculated parameters will not be affected significantly if the photometric variation is less than 0.2 mag. Variability has indeed been observed to be less than 0.1 mag in 43% of HAeBes, from a sample of 117 stars, by de Winter *et al.* (2001). In all cases where there are multiple photometric values to choose from, the ones at maximum brightness are chosen; this best reflects the scenario in which viewing is mostly of the stellar photosphere. So, an assumption is adopted here that the photometry we use is predominately photospheric and not highly variable.

In order to fit the photometry, a unique grid of KC-models is set up based on the limits derived in step 1 for each star; the grid follows the same step sizes used in the previous step. Log(g) does not have a significant effect on the fitting to the photometry, as the SED shape is overwhelmingly dominated by the temperature. This allows a log(g)=4.0 to be adopted for the stars in which log(g) could not be determined previously; the actual log(g) value will be determined in the next step for these stars.

The models are reddened until a best fit to the photometry is achieved; the best fit being when the reddened SED shape of the model is in-line with the

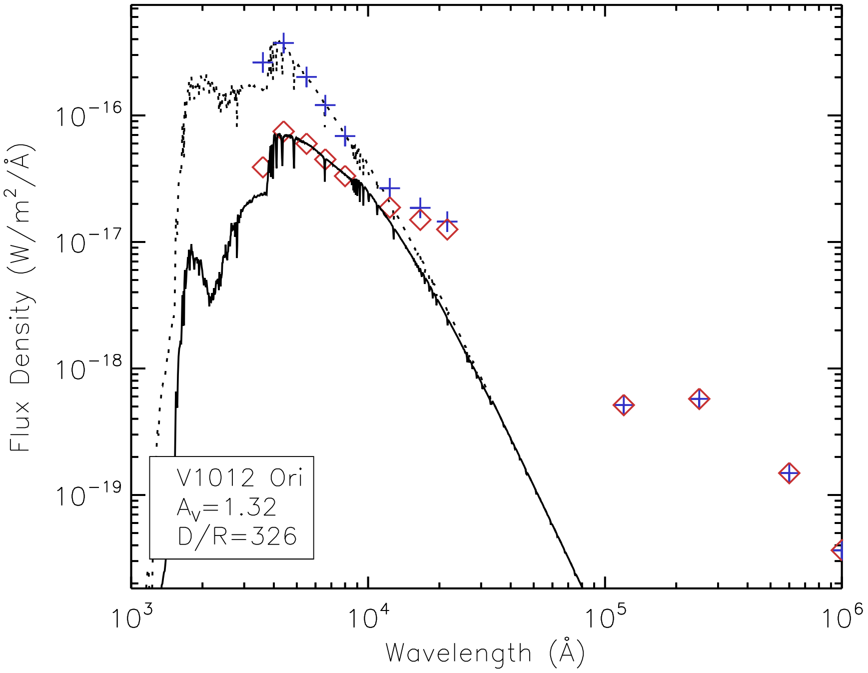

Figure 2.4: Here is an example of step 2 in the stellar parameter determinations (see Section 2.3.2), where a reddened KC-model (black) is fitted to the observed photometry (red diamonds). The opposite is also shown, of dereddened photometry (blue plus signs) and a KC-model (dashed line). The level of reddening, A_V, is displayed in the figure. The fit provides a ratio between the distance to the star and its radius, $D/R_\star$, as this is required to scale the model to fit the photometry. Also visible in this plot is how the dereddened U-band magnitude is higher than the KC-model used, a possible indication of Balmer Excess. A clear IR excess can also been seen, starting at around the J-band; a typical feature of PMS stars.

photometry. Dereddening is performed using the reddening law of Cardelli *et al.* (1989), with a standard total-to-selective extinction, R_V, of 3.1 used in all cases. The implications of this choice will be discussed at the end of Section 2.4. The models are normalised to the V-band point by a scaling factor, which is $(D/R_\star)^2$. This scaling factor arises from fitting models which are in units of surface flux to the observed photometry. An advantage of knowing this scaling factor is that it allows either distance or radius to be determined provided the other is known. Figure 2.4 shows an example of the above fitting for the case of V1012 Ori, along with a dereddened version of the photometry and the model spectra. This object is shown as it demonstrates a clear IR-excess, a noticeable A_V, and a U-band magnitude slightly higher than the KC-model spectra, reflecting a possible Balmer Excess.

At this stage the techniques diverge between the stars for which a log(g) was determined, and for the ones in which it could not be done. For the former no further action is taken in this step. For the latter a distance is adopted to the star based upon the location of the star on the sky and its possible associations with nearby star forming regions. By adopting a distance to these stars a radius can be determined from the scaling factor. Then, combining this radius with the temperature, the luminosity is calculated by a black-body relationship of $L_\star = 4\pi R_\star^2 \sigma T_{\rm eff}^4$ (this calculation is equivalent to the sum of the flux under the KC-model multiplied by $4\pi D^2$). The stars for which this process is performed on are noted in the final column of Table 2.4, along with the distance adopted for them.

2.3.3 Mass, Age, Radius, and log(g) Determination

In this third and final step, the remaining stellar parameters are now determined through the use of PMS tracks. The PARSEC tracks of Bressan *et al.* (2012) are used for the majority of this step as they cover a mass range of 0.1–12M$_\odot$, which encompasses all of the theoretical HAeBe mass range. Additionally, two tracks from Bernasconi & Maeder (1996) are used for objects greater than 12 M$_\odot$. Each track is of a fixed mass, with no accretion contribution, which evolves over time in $T_{\rm eff}$ and $L_\star$ as the star contracts. As $T_{\rm eff}$ and $L_\star$ change, so do $R_\star$ and log(g) as

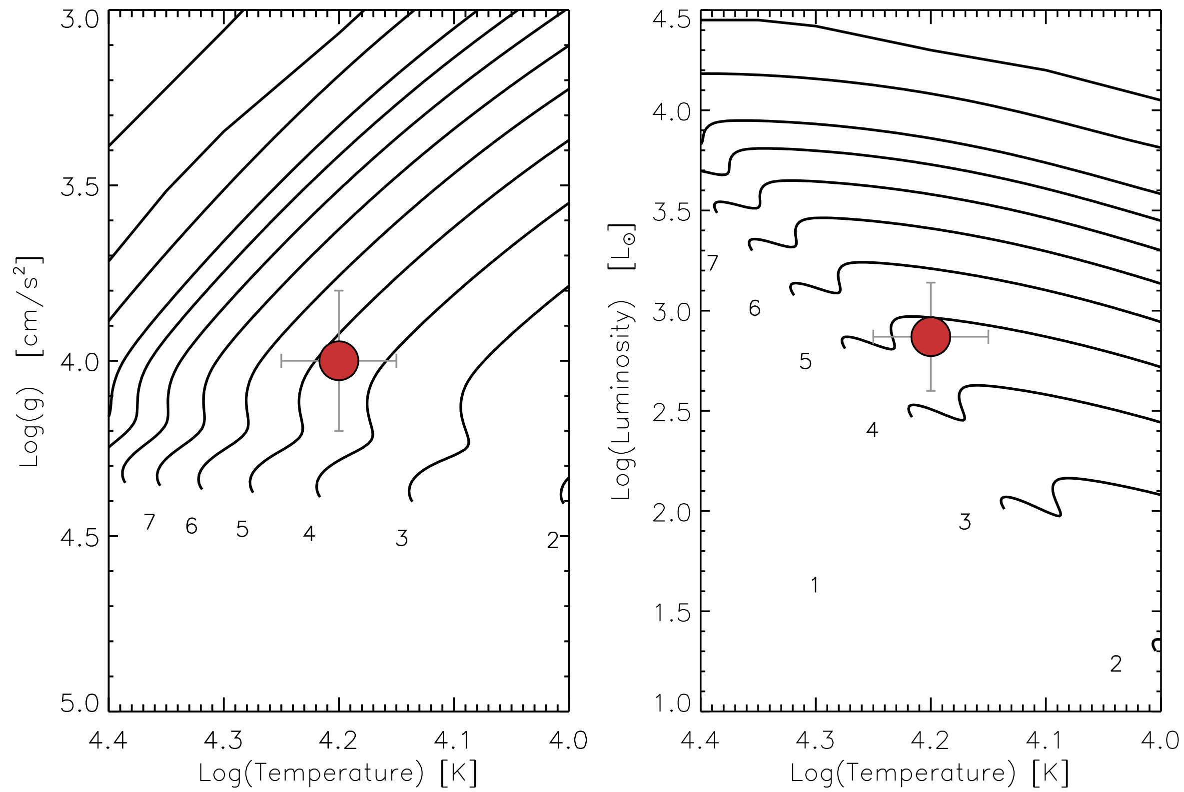

Figure 2.5: This plot demonstrates how the PMS tracks are used to obtain further stellar parameters. Depending upon previous information a star with either be plot on the log(g) vs. log($T_{\rm eff}$) plot, on the left hand side, or on the HR-diagram plot, shown on the right. An example point is plotted, showing how one plot maps to the other; this property allows other parameters to be determined.

a consequence. This allows each star to be plotted on either an $L_\star$ vs. $T_{\rm eff}$ set of tracks, for the stars where $L_\star$ is known from the adopted distance; or on a log(g) vs. $T_{\rm eff}$ set of tracks, for the stars where both log(g) and $T_{\rm eff}$ were determined from the spectra. These plots, along with an example point are, shown in Figure 2.5. From the figure it can be seen how one panel maps to the other. A mass and age are extracted from the PMS tracks for all of the stars, regardless of which panel they are plotted on. If log(g) could not be previously determined for a star, then it is now calculated using this mass and the radius from the previous step.

For the majority of the stars, where log(g) was determined, a luminosity, mass, and age are all extracted from the tracks. These can then be used to obtain a radius from the temperature and luminosity, or the mass and log(g); both choices are equivalent. Then, using the $D/R_\star$ factor a distance can be determined.

However, not all cases allow for the parameters to be extracted from the tracks. These few cases are where the stars are located below the zero-age main sequence (ZAMS). For nearly all of these stars it is a consequence of the adopted literature distances used. The distances provide small radii, from the $D/R_\star$ ratio, which can be deemed too small as they are less than the expected radius of a ZAMS star of the same temperature. Previously, for these stars, an assumption had been made that the stars were associated with a star-forming region. It is now more probable from the spectral typing and position of the stars in relation to the PMS tracks, that some of the distances chosen are not valid i.e. the star is not associated with the chosen region. Instead, the spectrally determined T_{eff} should be favoured as it is directly observed from the spectra, and more likely to be correct compared to the distance. So, a solution to this problem is to calculate new distances to these outlier targets using T_{eff} and $D/R_\star$; distances which provide more sensible radii. To do this, the problem stars are moved to the ZAMS point appropriate for their derived temperature. This point provides new determinations of $L_\star$, $R_\star$, $M_\star$, and an age; these are effectively lower limits if the ZAMS point is assumed to be correct. With this new ZAMS radius, a revised distance is calculated from $D/R_\star$. All objects affected by these ZAMS changes are noted in the the final column of Table 2.4. At this point all basic stellar parameters, relevant to this work, have now been determined.

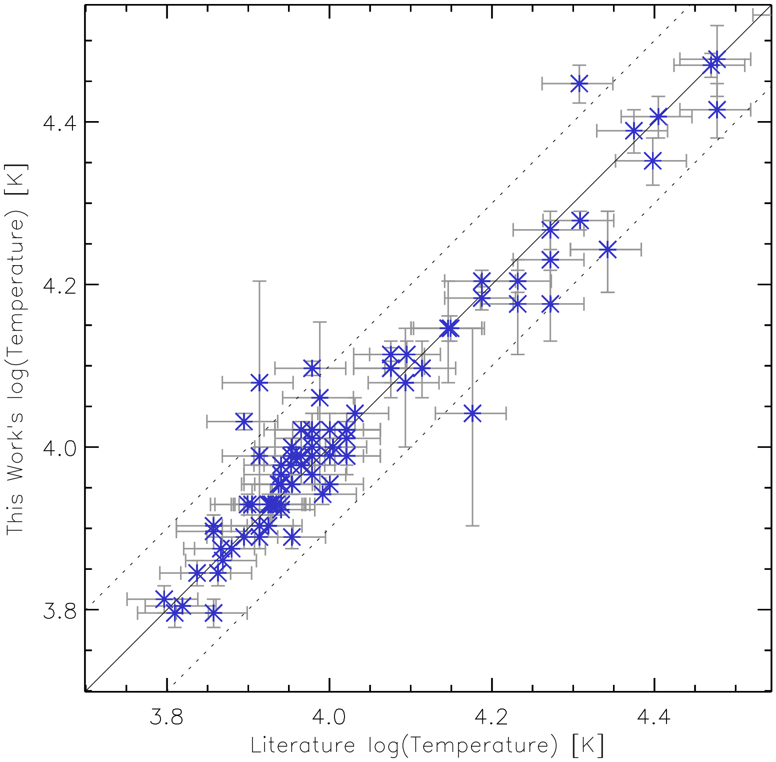

Figure 2.6: The temperatures derived in this work are compared to past literature estimates here. The solid black line is the expected line of correlation and the dashed lines are a 0.1 dex deviation from this. The standard deviation between the two is 0.02, with a mean offset of 0.03 towards this work. The dashed lines encompass 3σ, demonstrating that the two samples are well correlated. The literature temperatures and references used are provided in Table 2.2.

2.4 Literature Comparisons

The approach adopted for determining the stellar parameters, in Section 2.3, is now assessed through comparisons with the literature. The first check to be done is of the temperature, which is the most important parameter. Figure 2.6 compares the temperatures derived in this work against previous estimates from the literature, where references are given in Table 2.2. The majority of the

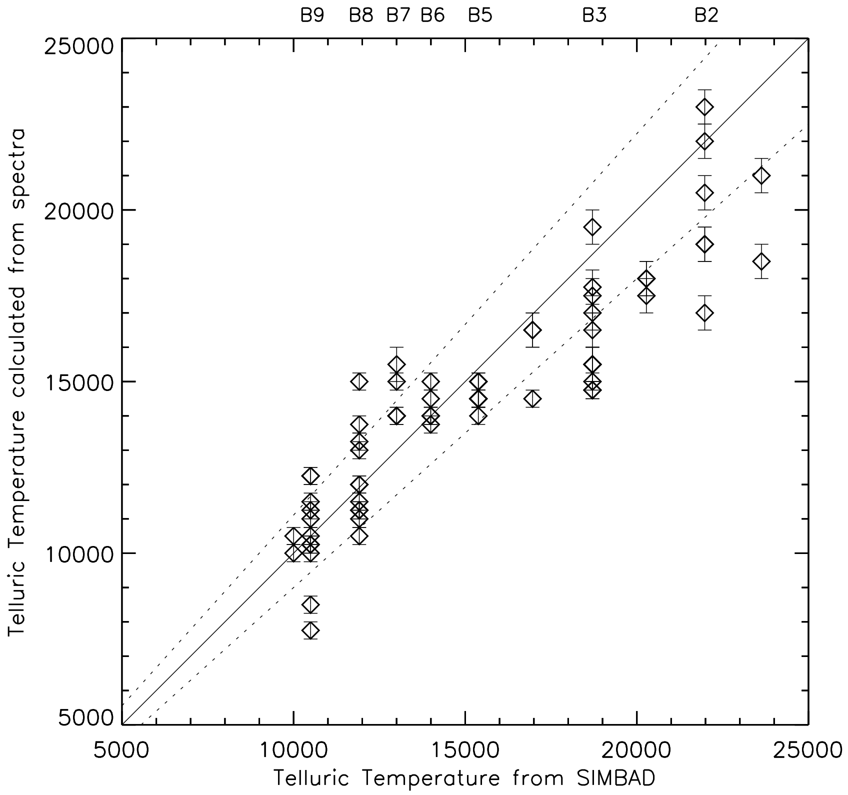

Figure 2.7: The temperature of the telluric standards, derived in this work, are plotted against their temperatures, as taken from the literature. The black solid line shows the 1:1 match between the two, while the dashed lines display a temperature error based on the distance between subclasses. The telluric standards are also labelled by their spectral types in columns.

literature provide spectral types rather than a precise temperature for each star. These are converted using the values provided in Kenyon & Hartmann (1995), and an error of 10% is assigned for each spectral class. The figure shows over 95% of the stars are in agreement, within the errors. The temperature determinations in this work have been based on some of the best spectra available for these objects which helps keep errors to a minimum. The temperatures derived for the telluric standards are also compared against past literature values in Figure

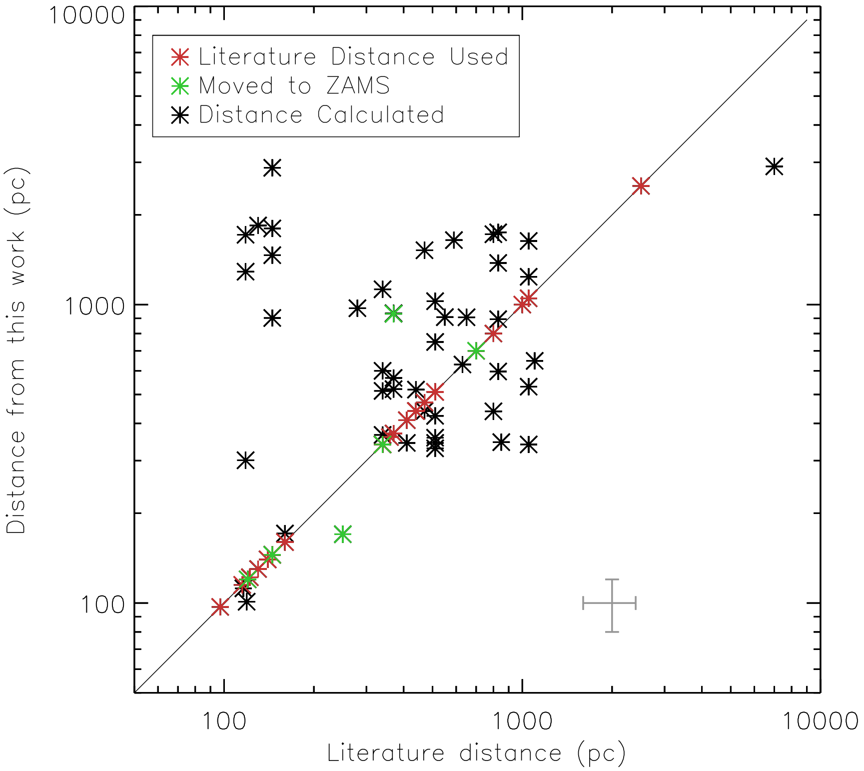

Figure 2.8: Objects in which a literature distance was adopted are marked in red. The few cases in which stars did not fall on the PMS tracks, and were subsequently moved to the ZAMS, are marked in green. All other stars, for which a log(g) and $T_{\rm eff}$ could be determined, are plotted in black. The black solid line is the line of correlation. A typical error bar of 20% is displayed in grey in the bottom right corner. A group of outliers can be seen towards the top left, which will be discussed in the text.

2.7. The literature temperatures were calculated using the spectral types given on SIMBAD [1]. The spectral types are primarily from the Michigan Sky Survey. The figure shows a general agreement between this work and the literature. The spectra used in this work are of significantly better resolution than used in the Michigan Sky Survey, allowing more precise temperature determinations.

---

[1] The SIMBAD database is operated at CDS, Strasbourg, France: `http://simbad.u-strasbg.fr/simbad/`

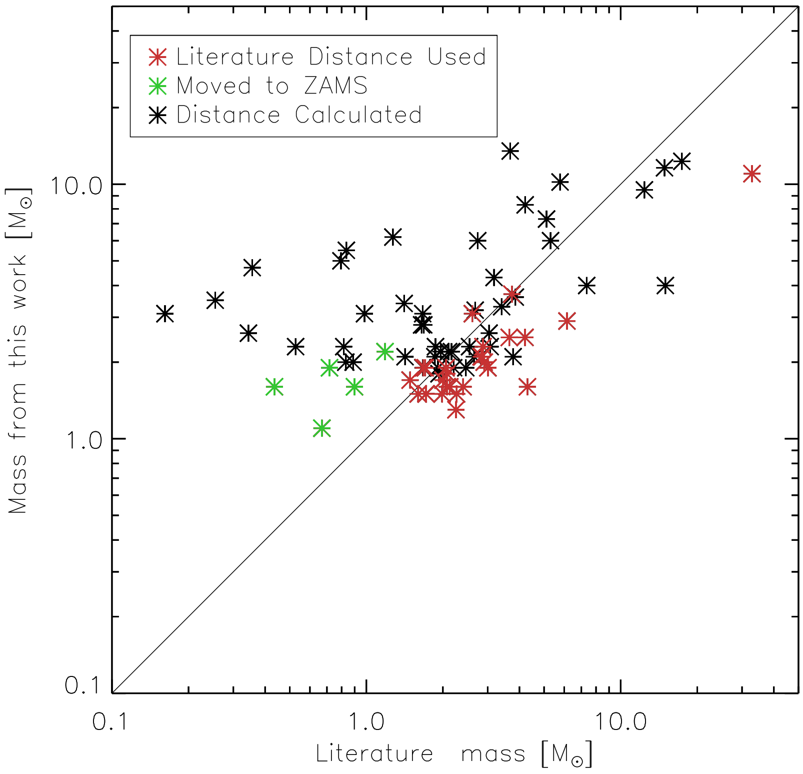

Figure 2.9: The mass determined from the PMS tracks is plotted against the mass derived using previous literature. A word of caution should be noted here as the literature values were calculated based on the spectral type listed.

The above points serve as a justification for the homogeneous approach to determining temperatures and their use here, for both the target stars and the telluric standards.

The method adopted here to obtain stellar parameters is distance independent, provided that log(g) can be determined from the spectra. As such, the distances derived in this work are compared against the previous literature distances in Figure 2.8 (when available and listed in Table 2.2). In the figure the stars for which log(g) could not be determined are plotted in red, as they required a literature distance to be adopted. Out of these stars, a few had to have their distances revised; otherwise, they would lie below the ZAMS. These stars are plotted in green. Many of the other stars are clustered between 300–1000 pc, where an error of ∼20% brings them in-line with the literature. Not all stars are in agreement though. In particular, there is a group of stars in the literature which are suspected to have distances of ∼100 pc, but this work calculates the distances to be closer to ∼1–2 kpc. An explanation for the discrepancies can be attributed to the adopted literature distances being assigned using the location of the stars on the sky and their possible associations with OB regions (de Zeeuw *et al.* 1999). If the original associations are used then the resulting radii of stars would have to be very small to match the observed photometry and spectroscopically determined temperature. In some cases the radii would be $< 1\,\mathrm{R}_\odot$, while the temperature of the stars is greater than 10000 K. This is not physical for such hot stars, particularly when they are suspected to be of a PMS nature. Therefore, the distances based on associations may not be correct, which would explain the discrepancies in Figure 2.8. Further support is lent to the larger derived distances being correct through measurement of the DIBs in the spectra. In most of these stars, the strength of the DIBs would suggest an $A_V-0.5$–2.0 mag (Jenniskens & Desert 1994). In general, the extinction due to dust in the ISM follows a trend of $\sim$ 1.8 mag/ kpc (Whittet 2003), which would indeed agree with the larger distances determined in this work.

Comparisons are now extended further by looking at the mass of the stars. The literature masses are calculated using the photometry, temperatures, and distances provided in Table 2.2 and the tables of intrinsic stellar properties from Kenyon & Hartmann (1995). This allows A_V to be determined for each star based on its temperature and corresponding intrinsic $B - V$ colour index. The reddening is used to correct the visual magnitude, which can be combined with the distance to determine and absolute magnitude. This can be used with a bolometric correction, based on the temperature, to obtain the bolometric magnitude; which gives a bolometric luminosity. Then by using the temperature with this luminosity a radius is calculated. At this point, only one step remains to obtain a mass. This could be inferred from the luminosity, but preference is taken for a more accurate approach of using the surface gravity, log(g). This selection is based on the luminosity class of the star i.e. supergiant, giant, dwarf (van den Ancker, private communication). Combining log(g) with the radius allows the mass to be determined. This process is done for each star in the literature for which there was a previous distance estimate. The resulting comparison shows how all the values determined in this work fall roughly between $\sim$1–10 $M_{\odot}$, while the literature masses have a much larger scatter which goes nearly as low as 0.1 $M_{\odot}$. This, in the same manner as the distance discrepancies, can be attributed to the adopted distances being incorrect for those stars; as the same distance associations have been used in the mass calculation. A further factor which complicates the comparison is the adopted log(g) for the literature values, which by definition affects the output mass when changed.

As mentioned in Section 2.3.2 an $R_V = 3.1$ was adopted for determining the reddening and the D/R ratios. This value of R_V has been shown to provide acceptable fits to a set of HAeBes when considering both photometry and spectra (Montesinos *et al.* 2009). However, it has been suggested that higher R_V values, closer to 5.0, may be more appropriate for some HAeBes due to the large amount of circumstellar material around them which contributes to the reddening (Hernández *et al.* 2004; Manoj *et al.* 2006). For the majority of stars in this sample the colour excess is low, mean E(B-V)$\sim$ 0.4. This means that the choice of R$_V$ will have little impact on the reddening calculated at each magnitude. Indeed, many of the stars are calculated to have an A_V close to zero when using R$_V$ = 3.1, this will remain the same for stars with an R$_V$ = 5.0. The stars which will be affected the most are the ones with the highest reddening. To keep the treatment of stars homogeneous a single value of R$_V$ has been adopted of 3.1. However, if an R$_V$ of 5.0 was adopted then the knock-on effects to the stellar parameters, and eventually mass accretion rates, will be minor; since the observed and intrinsic B-V colours remain the same the colour excess will be the same in both cases, and the A_V must therefore change. The result of this change is that the D/R ratio will be slightly lower, resulting in a smaller distance calculated towards the star. However, other stellar parameters will be virtually unchanged since the change in distance, which would mean a higher luminosity, is accounted for by the increased extinction. Any changes in the distance due to the adopted R$_V$ values are less than the error associated with the distance. In general, the choice of R$_V$ has a minimal effect on the parameters determined.

Overall, the spectral typing of the temperatures in this work agree with the literature. However, the distances and masses obtained do not always agree. Since the literature distances were often based on associations, it is more reasonable to trust the distances calculated in this work as these are derived directly through observations of the spectra.

Table 2.3: Details of the derived stellar parameters. Stars for which a distance estimate from the literature is used, or if the star was moved to the ZAMS, are noted in the final column (Column 10).

Name	$T_{\rm eff}$ (K)	log(g) [cm/s^2]	log($L_\star$) [L$_\odot$]	$M_\star$ (M$_\odot$)	$R_\star$ (R$_\odot$)	A_V (mag)	Age (Myr)	Distance (pc)	Notes
UX Ori	8500 ± 250	$3.90^{+0.25}_{-0.25}$	$1.54^{+0.38}_{-0.33}$	$2.1^{+0.7}_{-0.3}$	$2.7^{+0.4}_{-0.2}$	$0.48^{+0.07}_{-0.03}$	$4.24^{+3.24}_{-2.35}$	600^{+96}_{-50}	
PDS 174	17000 ± 2000	$4.10^{+0.40}_{-0.40}$	$2.91^{+0.56}_{-0.56}$	$5.0^{+2.3}_{-2.3}$	$3.3^{+0.7}_{-0.7}$	$3.51^{+0.07}_{-0.07}$	$0.60^{+0.43}_{-0.43}$	1126^{+238}_{-237}	
V1012 Ori	8500 ± 250	$4.38^{+0.15}_{-0.15}$	$0.94^{+0.28}_{-0.37}$	$1.6^{+0.3}_{-0.3}$	$1.4^{+0.4}_{-0.4}$	$1.32^{+0.02}_{-0.04}$	$15.16^{+7.58}_{-7.58}$	445^{+137}_{-130}	† *
HD 34282	9500 ± 250	$4.40^{+0.15}_{-0.15}$	$1.17^{+0.28}_{-0.36}$	$1.9^{+0.4}_{-0.4}$	$1.4^{+0.4}_{-0.4}$	$0.01^{+0.02}_{-0.00}$	$10.00^{+5.00}_{-5.00}$	366^{+111}_{-109}	
HD 287823	8375 ± 125	$4.23^{+0.11}_{-0.15}$	$1.09^{+0.17}_{-0.20}$	$1.7^{+0.1}_{-0.1}$	$1.7^{+0.3}_{-0.3}$	$0.00^{+0.05}_{-0.00}$	$9.01^{+4.11}_{-2.28}$	340^{+68}_{-68}	† a
HD 287841	7750 ± 250	$4.27^{+0.12}_{-0.12}$	$0.87^{+0.17}_{-0.21}$	$1.5^{+0.1}_{-0.1}$	$1.5^{+0.2}_{-0.2}$	$0.00^{+0.05}_{-0.00}$	$14.07^{+4.10}_{-4.10}$	340^{+68}_{-68}	† a
HD 290409	9750 ± 500	$4.25^{+0.25}_{-0.25}$	$1.42^{+0.29}_{-0.29}$	$2.1^{+0.2}_{-0.2}$	$1.8^{+0.1}_{-0.1}$	$0.00^{+0.05}_{-0.00}$	$5.50^{+2.03}_{-2.03}$	514^{+36}_{-29}	
HD 35929	7000 ± 250	$3.47^{+0.11}_{-0.11}$	$1.76^{+0.17}_{-0.21}$	$2.9^{+0.4}_{-0.4}$	$5.2^{+0.7}_{-0.8}$	$0.00^{+0.05}_{-0.00}$	$1.65^{+0.81}_{-0.55}$	360^{+72}_{-72}	† b
HD 290500	9500 ± 500	$3.80^{+0.40}_{-0.40}$	$1.94^{+0.61}_{-0.53}$	$2.8^{+1.8}_{-0.7}$	$3.5^{+1.0}_{-0.5}$	$0.00^{+0.05}_{-0.00}$	$2.26^{+3.39}_{-1.72}$	1522^{+436}_{-211}	
HD 244314	8500 ± 250	$4.15^{+0.11}_{-0.15}$	$1.21^{+0.18}_{-0.23}$	$1.8^{+0.1}_{-0.1}$	$1.9^{+0.3}_{-0.3}$	$0.10^{+0.02}_{-0.05}$	$7.52^{+1.97}_{-1.96}$	440^{+88}_{-88}	† a
HK Ori	8500 ± 500	$4.22^{+0.13}_{-0.13}$	$1.13^{+0.24}_{-0.27}$	$1.7^{+0.2}_{-0.2}$	$1.7^{+0.3}_{-0.3}$	$1.21^{+0.12}_{-0.14}$	$8.73^{+2.73}_{-2.73}$	440^{+88}_{-88}	† a
HD 244604	9000 ± 250	$3.99^{+0.15}_{-0.13}$	$1.54^{+0.18}_{-0.23}$	$2.1^{+0.3}_{-0.2}$	$2.4^{+0.4}_{-0.5}$	$0.14^{+0.00}_{-0.04}$	$4.56^{+1.53}_{-1.32}$	440^{+88}_{-88}	† a
UY Ori	9750 ± 250	$4.30^{+0.20}_{-0.20}$	$1.36^{+0.23}_{-0.23}$	$2.0^{+0.1}_{-0.1}$	$1.7^{+0.1}_{-0.1}$	$1.11^{+0.02}_{-0.00}$	$6.35^{+1.84}_{-1.84}$	1027^{+38}_{-35}	
HD 245185	10000 ± 500	$4.25^{+0.25}_{-0.25}$	$1.49^{+0.29}_{-0.29}$	$2.2^{+0.2}_{-0.2}$	$1.8^{+0.1}_{-0.1}$	$0.00^{+0.05}_{-0.00}$	$4.91^{+1.70}_{-1.70}$	519^{+34}_{-28}	
T Ori	9000 ± 500	$3.60^{+0.30}_{-0.30}$	$2.12^{+0.47}_{-0.46}$	$3.3^{+1.5}_{-1.0}$	$4.8^{+1.0}_{-0.8}$	$1.50^{+0.08}_{-0.05}$	$1.35^{+2.27}_{-0.93}$	750^{+159}_{-123}	
V380 Ori	9750 ± 750	$4.00^{+0.35}_{-0.35}$	$1.71^{+0.52}_{-0.26}$	$2.3^{+1.1}_{-0.2}$	$2.5^{+0.5}_{-0.1}$	$2.21^{+0.05}_{-0.07}$	$3.73^{+2.46}_{-2.49}$	330^{+73}_{-17}	
HD 37258	9750 ± 500	$4.25^{+0.25}_{-0.25}$	$1.42^{+0.29}_{-0.29}$	$2.1^{+0.2}_{-0.2}$	$1.8^{+0.1}_{-0.1}$	$0.06^{+0.05}_{-0.04}$	$5.50^{+2.03}_{-2.03}$	424^{+25}_{-22}	
HD 290770	10500 ± 250	$4.20^{+0.30}_{-0.30}$	$1.64^{+0.38}_{-0.38}$	$2.3^{+0.5}_{-0.5}$	$2.0^{+0.2}_{-0.2}$	$0.00^{+0.05}_{-0.00}$	$4.16^{+1.89}_{-1.89}$	440^{+43}_{-41}	
BF Ori	9000 ± 250	$3.97^{+0.15}_{-0.13}$	$1.57^{+0.19}_{-0.22}$	$2.1^{+0.3}_{-0.2}$	$2.5^{+0.4}_{-0.5}$	$0.33^{+0.03}_{-0.02}$	$4.34^{+1.55}_{-1.32}$	510^{+102}_{-102}	† a

Continued on next page

Table 2.3 – continued from previous page

Name	$T_{\rm eff}$ (K)	log(g) [cm/s^2]	log($L_\star$) [L$_\odot$]	$M_\star$ (M$_\odot$)	$R_\star$ (R$_\odot$)	A_V (mag)	Age (Myr)	Distance (pc)	Notes
HD 37357	9500 ± 250	$4.10^{+0.10}_{-0.10}$	$1.52^{+0.13}_{-0.11}$	$2.1^{+0.1}_{-0.1}$	$2.1^{+0.1}_{-0.0}$	$0.00^{+0.05}_{-0.00}$	$4.93^{+0.87}_{-0.87}$	344^{+15}_{-4}	
HD 290764	7875 ± 375	$3.90^{+0.17}_{-0.15}$	$1.36^{+0.22}_{-0.26}$	$1.9^{+0.4}_{-0.2}$	$2.6^{+0.5}_{-0.5}$	$0.16^{+0.12}_{-0.14}$	$5.25^{+2.58}_{-1.90}$	470^{+94}_{-94}	† a
HD 37411	9750 ± 250	$4.35^{+0.15}_{-0.15}$	$1.28^{+0.28}_{-0.36}$	$1.9^{+0.4}_{-0.4}$	$1.5^{+0.5}_{-0.5}$	$0.21^{+0.01}_{-0.00}$	$9.00^{+4.50}_{-4.50}$	358^{+109}_{-107}	
V599 Ori	8000 ± 250	$3.72^{+0.13}_{-0.12}$	$1.68^{+0.19}_{-0.23}$	$2.5^{+0.4}_{-0.4}$	$3.6^{+0.6}_{-0.7}$	$4.65^{+0.06}_{-0.07}$	$2.82^{+1.40}_{-1.00}$	510^{+102}_{-102}	† a
V350 Ori	9000 ± 250	$4.18^{+0.11}_{-0.16}$	$1.31^{+0.19}_{-0.22}$	$1.9^{+0.1}_{-0.1}$	$1.9^{+0.3}_{-0.3}$	$0.69^{+0.02}_{-0.03}$	$6.41^{+1.97}_{-1.67}$	510^{+102}_{-102}	† a
HD 250550	11000 ± 500	$3.80^{+0.40}_{-0.40}$	$2.28^{+0.61}_{-0.53}$	$3.4^{+2.1}_{-0.9}$	$3.8^{+1.0}_{-0.5}$	$0.00^{+0.05}_{-0.00}$	$1.42^{+2.21}_{-1.09}$	973^{+267}_{-136}	
V791 Mon	15000 ± 1500	$4.30^{+0.16}_{-0.16}$	$2.35^{+0.40}_{-0.51}$	$3.6^{+0.7}_{-0.7}$	$2.2^{+0.7}_{-0.7}$	$1.17^{+0.06}_{-0.04}$	$1.80^{+0.90}_{-0.90}$	648^{+204}_{-184}	
PDS 124	10250 ± 250	$4.30^{+0.20}_{-0.20}$	$1.47^{+0.23}_{-0.23}$	$2.2^{+0.2}_{-0.2}$	$1.7^{+0.1}_{-0.1}$	$1.23^{+0.03}_{-0.00}$	$5.48^{+1.64}_{-1.64}$	894^{+34}_{-33}	
LkHa 339	10500 ± 250	$4.20^{+0.20}_{-0.20}$	$1.64^{+0.24}_{-0.24}$	$2.3^{+0.2}_{-0.2}$	$2.0^{+0.1}_{-0.1}$	$3.54^{+0.01}_{-0.01}$	$4.16^{+1.18}_{-1.18}$	597^{+27}_{-25}	
VY Mon	12000 ± 4000	$3.75^{+0.50}_{-0.50}$	$2.56^{+0.77}_{-0.65}$	$4.0^{+3.7}_{-1.3}$	$4.4^{+1.6}_{-0.7}$	$5.68^{+0.17}_{-0.45}$	$0.89^{+2.61}_{-0.80}$	439^{+181}_{-113}	
R Mon	12000 ± 2000	$4.00^{+0.11}_{-0.24}$	$2.19^{+0.34}_{-0.40}$	$3.1^{+0.8}_{-0.6}$	$2.9^{+0.3}_{-0.3}$	$2.42^{+0.08}_{-0.13}$	$1.92^{+1.23}_{-0.89}$	800^{+160}_{-160}	† c
V590 Mon	12500 ± 1000	$4.20^{+0.30}_{-0.30}$	$2.06^{+0.37}_{-0.37}$	$3.1^{+0.6}_{-0.6}$	$2.3^{+0.2}_{-0.2}$	$1.03^{+0.04}_{-0.05}$	$2.19^{+1.00}_{-1.00}$	1722^{+171}_{-160}	
PDS 24	10500 ± 500	$4.20^{+0.30}_{-0.30}$	$1.64^{+0.38}_{-0.38}$	$2.3^{+0.5}_{-0.5}$	$2.0^{+0.2}_{-0.2}$	$1.11^{+0.04}_{-0.03}$	$4.16^{+1.91}_{-1.91}$	1646^{+162}_{-157}	
PDS 130	10500 ± 250	$3.90^{+0.20}_{-0.20}$	$2.02^{+0.30}_{-0.27}$	$2.8^{+0.7}_{-0.4}$	$3.1^{+0.4}_{-0.2}$	$2.07^{+0.01}_{-0.00}$	$2.25^{+1.32}_{-1.07}$	1748^{+216}_{-129}	
PDS 229N	12500 ± 250	$4.20^{+0.20}_{-0.20}$	$2.06^{+0.23}_{-0.23}$	$3.1^{+0.2}_{-0.2}$	$2.3^{+0.1}_{-0.1}$	$2.03^{+0.01}_{-0.01}$	$2.19^{+0.63}_{-0.63}$	1379^{+57}_{-56}	
GU CMa	22500 ± 1500	$3.90^{+0.40}_{-0.40}$	$3.87^{+0.62}_{-0.62}$	$9.5^{+6.8}_{-6.8}$	$5.7^{+1.7}_{-1.7}$	$0.57^{+0.03}_{-0.02}$	$0.11^{+0.10}_{-0.10}$	531^{+163}_{-163}	
HT CMa	10500 ± 500	$4.00^{+0.20}_{-0.20}$	$1.88^{+0.29}_{-0.24}$	$2.6^{+0.6}_{-0.2}$	$2.6^{+0.3}_{-0.1}$	$0.23^{+0.05}_{-0.02}$	$2.96^{+1.19}_{-1.32}$	1634^{+187}_{-72}	
Z CMa	8500 ± 500	$2.53^{+0.17}_{-0.17}$	$3.62^{+0.24}_{-0.28}$	$11.0^{+1.7}_{-1.7}$	$29.8^{+5.2}_{-5.3}$	$3.37^{+0.12}_{-0.16}$	$0.03^{+0.02}_{-0.02}$	1050^{+210}_{-210}	† d
HU CMa	13000 ± 250	$4.20^{+0.20}_{-0.20}$	$2.16^{+0.23}_{-0.23}$	$3.2^{+0.2}_{-0.2}$	$2.4^{+0.1}_{-0.1}$	$0.80^{+0.02}_{-0.01}$	$1.88^{+0.52}_{-0.52}$	1240^{+47}_{-46}	
HD 53367	29500 ± 1000	$4.25^{+0.25}_{-0.25}$	$4.11^{+0.37}_{-0.37}$	$12.3^{+4.2}_{-4.2}$	$4.3^{+0.7}_{-0.7}$	$1.88^{+0.02}_{-0.01}$	$0.08^{+0.08}_{-0.08}$	340^{+53}_{-54}	
PDS 241	26000 ± 1500	$4.00^{+0.30}_{-0.30}$	$4.11^{+0.46}_{-0.46}$	$11.6^{+5.5}_{-5.5}$	$5.6^{+1.2}_{-1.2}$	$2.60^{+0.04}_{-0.01}$	$0.08^{+0.07}_{-0.07}$	2907^{+614}_{-617}	

Continued on next page

Table 2.3 – continued from previous page

Name	T_{eff} (K)	log(g) [cm/s^2]	log($L_\star$) [L$_\odot$]	$M_\star$ (M$_\odot$)	$R_\star$ (R$_\odot$)	A_V (mag)	Age (Myr)	Distance (pc)	Notes
NX Pup	7000 ± 250	$3.78^{+0.13}_{-0.13}$	$1.28^{+0.20}_{-0.21}$	$1.9^{+0.3}_{-0.3}$	$3.0^{+0.5}_{-0.5}$	$0.00^{+0.07}_{-0.00}$	$4.92^{+2.37}_{-1.67}$	410^{+82}_{-82}	† a
PDS 27	17500 ± 3000	$3.16^{+0.27}_{-0.27}$	$4.39^{+0.40}_{-0.40}$	$15.3^{+5.4}_{-4.4}$	$17.0^{+4.0}_{-4.0}$	$5.03^{+0.14}_{-0.14}$	$0.10^{+0.10}_{-0.10}$	3170^{+660}_{-620}	† e
PDS 133	14000 ± 2000	$4.08^{+0.12}_{-0.11}$	$2.46^{+0.33}_{-0.38}$	$3.7^{+0.9}_{-0.7}$	$2.9^{+0.4}_{-0.4}$	$1.43^{+0.09}_{-0.10}$	$1.27^{+0.94}_{-0.56}$	2500^{+500}_{-500}	† f
HD 59319	12500 ± 500	$3.50^{+0.20}_{-0.20}$	$3.03^{+0.31}_{-0.30}$	$5.7^{+1.6}_{-1.2}$	$7.0^{+0.9}_{-0.8}$	$0.00^{+0.05}_{-0.00}$	$0.32^{+0.34}_{-0.17}$	1218^{+162}_{-137}	
PDS 134	14000 ± 500	$3.40^{+0.30}_{-0.30}$	$3.45^{+0.46}_{-0.45}$	$7.6^{+3.5}_{-2.3}$	$9.1^{+1.9}_{-1.5}$	$1.22^{+0.03}_{-0.02}$	$0.15^{+0.28}_{-0.10}$	5687^{+1178}_{-931}	
HD 68695	9250 ± 250	$4.40^{+0.15}_{-0.15}$	$1.11^{+0.28}_{-0.37}$	$1.8^{+0.4}_{-0.4}$	$1.4^{+0.4}_{-0.4}$	$0.00^{+0.05}_{-0.00}$	$10.00^{+5.00}_{-5.00}$	344^{+106}_{-103}	
HD 72106	8750 ± 250	$3.89^{+0.13}_{-0.12}$	$1.63^{+0.18}_{-0.21}$	$2.3^{+0.3}_{-0.3}$	$2.8^{+0.5}_{-0.5}$	$0.00^{+0.05}_{-0.00}$	$3.76^{+1.47}_{-1.18}$	370^{+74}_{-74}	† a
TYC 8581-2002-1	9750 ± 250	$4.00^{+0.10}_{-0.10}$	$1.71^{+0.14}_{-0.12}$	$2.3^{+0.2}_{-0.1}$	$2.5^{+0.1}_{-0.1}$	$0.94^{+0.04}_{-0.00}$	$3.73^{+0.78}_{-0.89}$	902^{+47}_{-25}	
PDS 33	9750 ± 250	$4.40^{+0.15}_{-0.15}$	$1.23^{+0.27}_{-0.36}$	$1.9^{+0.4}_{-0.4}$	$1.4^{+0.4}_{-0.4}$	$0.52^{+0.04}_{-0.00}$	$9.00^{+4.50}_{-4.50}$	932^{+282}_{-279}	∗
HD 76534	19000 ± 500	$4.10^{+0.20}_{-0.20}$	$3.18^{+0.26}_{-0.20}$	$6.0^{+0.9}_{-0.6}$	$3.6^{+0.3}_{-0.2}$	$0.62^{+0.02}_{-0.01}$	$0.37^{+0.19}_{-0.14}$	568^{+43}_{-29}	
PDS 281	16000 ± 1500	$3.50^{+0.30}_{-0.30}$	$3.62^{+0.47}_{-0.45}$	$8.3^{+4.0}_{-2.5}$	$8.5^{+1.8}_{-1.4}$	$1.89^{+0.07}_{-0.10}$	$0.12^{+0.23}_{-0.09}$	936^{+207}_{-168}	
PDS 286	30000 ± 3000	$4.25^{+0.16}_{-0.16}$	$4.18^{+0.41}_{-0.52}$	$13.5^{+2.7}_{-2.7}$	$4.6^{+1.5}_{-1.5}$	$6.27^{+0.05}_{-0.04}$	$0.10^{+0.05}_{-0.05}$	521^{+167}_{-146}	
PDS 297	10750 ± 250	$4.00^{+0.20}_{-0.20}$	$1.93^{+0.29}_{-0.24}$	$2.6^{+0.6}_{-0.2}$	$2.7^{+0.3}_{-0.1}$	$0.81^{+0.01}_{-0.02}$	$2.77^{+1.12}_{-1.22}$	1465^{+166}_{-59}	
HD 85567	13000 ± 500	$3.50^{+0.30}_{-0.30}$	$3.13^{+0.46}_{-0.45}$	$6.0^{+2.7}_{-1.8}$	$7.2^{+1.5}_{-1.2}$	$0.89^{+0.03}_{-0.02}$	$0.27^{+0.52}_{-0.18}$	907^{+183}_{-146}	
HD 87403	10000 ± 250	$3.30^{+0.10}_{-0.10}$	$2.83^{+0.15}_{-0.15}$	$5.5^{+0.7}_{-0.6}$	$8.7^{+0.6}_{-0.5}$	$0.00^{+0.05}_{-0.00}$	$0.32^{+0.15}_{-0.10}$	1801^{+125}_{-109}	
PDS 37	17500 ± 3500	$2.94^{+0.35}_{-0.35}$	$4.75^{+0.39}_{-0.39}$	$21.1^{+11.0}_{-5.3}$	$25.8^{+5.0}_{-5.0}$	$5.81^{+0.13}_{-0.13}$	$0.10^{+0.10}_{-0.10}$	4310^{+670}_{-670}	† e
HD 305298	34000 ± 1000	$4.31^{+0.16}_{-0.16}$	$4.46^{+0.23}_{-0.41}$	$15.7^{+3.1}_{-3.1}$	$4.6^{+1.4}_{-1.4}$	$1.30^{+0.00}_{-0.02}$	$0.02^{+0.01}_{-0.01}$	3366^{+1010}_{-979}	∗
HD 94509	11500 ± 1000	$2.90^{+0.40}_{-0.40}$	$3.76^{+0.65}_{-0.62}$	$10.8^{+9.0}_{-4.3}$	$19.2^{+6.8}_{-4.3}$	$0.00^{+0.05}_{-0.00}$	$0.05^{+0.16}_{-0.05}$	4384^{+1585}_{-1009}	
HD 95881	10000 ± 250	$3.20^{+0.10}_{-0.10}$	$2.98^{+0.15}_{-0.15}$	$6.2^{+0.8}_{-0.7}$	$10.3^{+0.7}_{-0.6}$	$0.00^{+0.05}_{-0.00}$	$0.21^{+0.10}_{-0.07}$	1290^{+90}_{-78}	
HD 96042	25500 ± 1500	$3.80^{+0.20}_{-0.20}$	$4.36^{+0.33}_{-0.29}$	$14.0^{+5.1}_{-2.8}$	$7.8^{+1.3}_{-0.8}$	$0.78^{+0.03}_{-0.01}$	$0.02^{+0.05}_{-0.02}$	1792^{+302}_{-197}	
HD 97048	10500 ± 500	$4.30^{+0.20}_{-0.20}$	$1.52^{+0.23}_{-0.23}$	$2.2^{+0.2}_{-0.2}$	$1.7^{+0.1}_{-0.1}$	$0.90^{+0.05}_{-0.02}$	$5.12^{+1.52}_{-1.52}$	171^{+7}_{-7}	

Continued on next page

Table 2.3 – continued from previous page

Name	T_{eff} (K)	log(g) [cm/s^2]	$\log(L_\star)$ [L$_\odot$]	$M_\star$ (M$_\odot$)	$R_\star$ (R$_\odot$)	A_V (mag)	Age (Myr)	Distance (pc)	Notes
HD 98922	10500 ± 250	$3.60^{+0.10}_{-0.10}$	$2.48^{+0.15}_{-0.15}$	$4.0^{+0.5}_{-0.5}$	$5.2^{+0.3}_{-0.3}$	$0.09^{+0.01}_{-0.00}$	$0.84^{+0.35}_{-0.26}$	346^{+22}_{-20}	
HD 100453	7250 ± 250	$4.08^{+0.15}_{-0.13}$	$0.93^{+0.17}_{-0.21}$	$1.5^{+0.2}_{-0.1}$	$1.9^{+0.3}_{-0.3}$	$0.00^{+0.05}_{-0.00}$	$9.97^{+6.29}_{-2.79}$	122^{+24}_{-25}	† b
HD 100546	9750 ± 500	$4.34^{+0.06}_{-0.06}$	$1.29^{+0.14}_{-0.14}$	$1.9^{+0.1}_{-0.1}$	$1.5^{+0.1}_{-0.1}$	$0.00^{+0.05}_{-0.00}$	$7.02^{+1.49}_{-1.49}$	97^{+10}_{-10}	† b
HD 101412	9750 ± 250	$4.30^{+0.20}_{-0.20}$	$1.36^{+0.23}_{-0.23}$	$2.0^{+0.1}_{-0.1}$	$1.7^{+0.1}_{-0.1}$	$0.21^{+0.03}_{-0.00}$	$6.35^{+1.84}_{-1.84}$	301^{+11}_{-10}	
PDS 344	15250 ± 500	$4.30^{+0.20}_{-0.20}$	$2.39^{+0.25}_{-0.25}$	$3.7^{+0.5}_{-0.5}$	$2.3^{+0.1}_{-0.1}$	$0.86^{+0.01}_{-0.02}$	$1.48^{+0.52}_{-0.52}$	2756^{+172}_{-165}	
HD 104237	8000 ± 250	$3.89^{+0.12}_{-0.12}$	$1.41^{+0.17}_{-0.21}$	$2.0^{+0.3}_{-0.2}$	$2.6^{+0.4}_{-0.4}$	$0.00^{+0.05}_{-0.00}$	$4.92^{+1.87}_{-1.46}$	115^{+23}_{-23}	† b
V1028 Cen	14000 ± 500	$3.80^{+0.30}_{-0.30}$	$2.85^{+0.45}_{-0.41}$	$4.7^{+2.0}_{-1.0}$	$4.5^{+0.9}_{-0.5}$	$0.57^{+0.01}_{-0.03}$	$0.59^{+0.69}_{-0.39}$	1843^{+355}_{-215}	
PDS 361S	18500 ± 1000	$3.80^{+0.30}_{-0.30}$	$3.53^{+0.46}_{-0.41}$	$7.4^{+3.2}_{-1.7}$	$5.7^{+1.1}_{-0.7}$	$1.90^{+0.04}_{-0.01}$	$0.19^{+0.23}_{-0.12}$	4385^{+872}_{-541}	
HD 114981	16000 ± 500	$3.60^{+0.20}_{-0.20}$	$3.47^{+0.30}_{-0.30}$	$7.3^{+2.0}_{-1.5}$	$7.1^{+0.9}_{-0.8}$	$0.00^{+0.05}_{-0.00}$	$0.18^{+0.17}_{-0.09}$	908^{+118}_{-99}	
PDS 364	12500 ± 1000	$4.20^{+0.20}_{-0.20}$	$2.06^{+0.23}_{-0.23}$	$3.1^{+0.2}_{-0.2}$	$2.3^{+0.1}_{-0.1}$	$1.87^{+0.05}_{-0.03}$	$2.19^{+0.58}_{-0.58}$	1715^{+97}_{-91}	
PDS 69	15000 ± 2000	$4.00^{+0.35}_{-0.35}$	$2.72^{+0.52}_{-0.76}$	$4.3^{+2.0}_{-1.5}$	$3.4^{+0.7}_{-0.6}$	$1.60^{+0.07}_{-0.07}$	$0.84^{+2.02}_{-0.62}$	630^{+141}_{-126}	
DG Cir	11000 ± 3000	$4.41^{+0.18}_{-0.18}$	$1.49^{+0.68}_{-0.93}$	$2.2^{+0.4}_{-0.4}$	$1.5^{+0.5}_{-0.5}$	$3.94^{+0.13}_{-0.54}$	$5.95^{+2.97}_{-2.97}$	713^{+250}_{-184}	† *
HD 132947	10250 ± 250	$3.90^{+0.10}_{-0.10}$	$1.97^{+0.15}_{-0.14}$	$2.7^{+0.3}_{-0.3}$	$3.1^{+0.2}_{-0.1}$	$0.00^{+0.05}_{-0.00}$	$2.44^{+0.77}_{-0.65}$	565^{+35}_{-26}	
HD 135344B	6375 ± 125	$3.94^{+0.12}_{-0.12}$	$0.85^{+0.18}_{-0.22}$	$1.5^{+0.2}_{-0.2}$	$2.2^{+0.4}_{-0.4}$	$0.23^{+0.05}_{-0.06}$	$7.99^{+3.24}_{-2.34}$	140^{+28}_{-28}	† a
HD 139614	7750 ± 250	$4.31^{+0.12}_{-0.12}$	$0.82^{+0.17}_{-0.21}$	$1.5^{+0.1}_{-0.1}$	$1.4^{+0.2}_{-0.2}$	$0.00^{+0.05}_{-0.00}$	$15.64^{+4.29}_{-4.29}$	140^{+28}_{-28}	† a
PDS 144S	7750 ± 250	$4.13^{+0.14}_{-0.16}$	$1.02^{+0.20}_{-0.23}$	$1.6^{+0.2}_{-0.1}$	$1.8^{+0.3}_{-0.3}$	$0.57^{+0.07}_{-0.08}$	$9.45^{+4.81}_{-2.88}$	1000^{+200}_{-200}	† f
HD 141569	9750 ± 250	$4.35^{+0.15}_{-0.15}$	$1.28^{+0.28}_{-0.37}$	$1.9^{+0.4}_{-0.4}$	$1.5^{+0.5}_{-0.5}$	$0.01^{+0.01}_{-0.00}$	$9.00^{+4.50}_{-4.50}$	112^{+34}_{-33}	
HD 141926	28000 ± 1500	$3.75^{+0.25}_{-0.25}$	$4.70^{+0.26}_{-0.37}$	$19.4^{+4.5}_{-5.0}$	$9.7^{+1.1}_{-1.3}$	$2.40^{+0.03}_{-0.04}$	$0.00^{+0.03}_{-0.00}$	1254^{+143}_{-175}	
HD 142666	7500 ± 250	$4.13^{+0.11}_{-0.16}$	$0.96^{+0.20}_{-0.24}$	$1.6^{+0.2}_{-0.1}$	$1.8^{+0.3}_{-0.3}$	$0.50^{+0.08}_{-0.09}$	$10.43^{+6.21}_{-3.34}$	145^{+29}_{-29}	† a
HD 142527	6500 ± 250	$3.93^{+0.08}_{-0.08}$	$0.90^{+0.12}_{-0.13}$	$1.6^{+0.1}_{-0.1}$	$2.2^{+0.1}_{-0.2}$	$0.00^{+0.05}_{-0.00}$	$8.08^{+1.94}_{-1.63}$	140^{+20}_{-20}	† g
HD 144432	7500 ± 250	$4.05^{+0.17}_{-0.14}$	$1.04^{+0.19}_{-0.21}$	$1.6^{+0.2}_{-0.1}$	$2.0^{+0.3}_{-0.3}$	$0.00^{+0.06}_{-0.00}$	$8.72^{+4.81}_{-2.50}$	160^{+32}_{-32}	† b

Continued on next page

Table 2.3 – continued from previous page

Name	T_{eff} (K)	log(g) [cm/s^2]	log($L_\star$) [L$_\odot$]	$M_\star$ (M$_\odot$)	$R_\star$ (R$_\odot$)	A_V (mag)	Age (Myr)	Distance (pc)	Notes
HD 144668	8500 ± 250	$3.75^{+0.13}_{-0.12}$	$1.76^{+0.19}_{-0.22}$	$2.5^{+0.4}_{-0.4}$	$3.5^{+0.6}_{-0.6}$	$0.33^{+0.05}_{-0.04}$	$2.70^{+1.32}_{-0.93}$	160^{+32}_{-32}	† b
HD 145718	8000 ± 250	$4.37^{+0.15}_{-0.15}$	$0.82^{+0.29}_{-0.37}$	$1.5^{+0.3}_{-0.3}$	$1.3^{+0.4}_{-0.4}$	$0.74^{+0.06}_{-0.05}$	$19.54^{+9.77}_{-9.77}$	134^{+41}_{-39}	† ∗
PDS 415N	6250 ± 250	$4.47^{+0.15}_{-0.15}$	$0.13^{+0.30}_{-0.39}$	$1.1^{+0.2}_{-0.2}$	$1.0^{+0.3}_{-0.3}$	$1.11^{+0.11}_{-0.15}$	$336.02^{+168.01}_{-168.01}$	197^{+60}_{-58}	† ∗
HD 150193	9000 ± 250	$4.27^{+0.17}_{-0.17}$	$1.21^{+0.19}_{-0.23}$	$1.9^{+0.1}_{-0.1}$	$1.7^{+0.3}_{-0.3}$	$1.55^{+0.02}_{-0.04}$	$7.22^{+1.89}_{-1.89}$	120^{+24}_{-24}	† h
AK Sco	6250 ± 250	$4.26^{+0.10}_{-0.10}$	$0.38^{+0.18}_{-0.20}$	$1.2^{+0.1}_{-0.1}$	$1.3^{+0.2}_{-0.2}$	$0.00^{+0.05}_{-0.00}$	$17.71^{+4.71}_{-3.42}$	103^{+20}_{-21}	† b
PDS 431	10500 ± 500	$3.70^{+0.20}_{-0.20}$	$2.32^{+0.31}_{-0.30}$	$3.5^{+1.0}_{-0.7}$	$4.4^{+0.6}_{-0.5}$	$1.76^{+0.03}_{-0.03}$	$1.19^{+1.07}_{-0.61}$	2875^{+384}_{-316}	
KK Oph	8500 ± 500	$4.38^{+0.15}_{-0.15}$	$0.94^{+0.33}_{-0.43}$	$1.6^{+0.3}_{-0.3}$	$1.4^{+0.4}_{-0.4}$	$2.70^{+0.10}_{-0.15}$	$15.16^{+7.58}_{-7.58}$	279^{+86}_{-81}	† ∗
HD 163296	9250 ± 250	$4.30^{+0.20}_{-0.20}$	$1.23^{+0.23}_{-0.23}$	$1.9^{+0.1}_{-0.1}$	$1.6^{+0.0}_{-0.0}$	$0.00^{+0.05}_{-0.00}$	$7.56^{+2.17}_{-2.17}$	101^{+4}_{-3}	
MWC 297	24500 ± 1500	$4.00^{+0.30}_{-0.30}$	$3.95^{+0.46}_{-0.46}$	$10.2^{+4.6}_{-4.6}$	$5.3^{+1.1}_{-1.1}$	$8.47^{+0.04}_{-0.03}$	$0.10^{+0.08}_{-0.08}$	170^{+34}_{-34}	

† – A literature distance is initially adopted to these stars, as log(g) cannot be determined from the spectra. ∗ – Stars which have been placed on the ZAMS. References: (a) de Zeeuw *et al.* (1999), (b) van Leeuwen (2007), (c) Dahm & Simon (2005), (d) Shevchenko *et al.* (1999), (e) Ababakr *et al.* (2015, submitted), (f) Vieira *et al.* (2003), (g) Fukagawa *et al.* (2006), (h) Loinard *et al.* (2008).

2.5 Exceptional Stars

Before moving onto the discussion, it is important to note that there are a small minority of stars which could not be assigned a temperature from the spectra alone (see Section 2.3.1). Figure 2.10 displays the Hβ line profile for these stars. The large amount of emission and P-Cygni absorption in all of these stars makes spectral typing using this line impossible. For these stars a different approach must be taken, on an individual basis, in order to assign a temperature. This is done by drawing upon as many literature sources on these objects as possible. There are 7 objects from the entire sample which require this treatment. The stars, and steps taken, are detailed below:

VY Mon – This star is included here because it has the worst SNR of the sample. This makes accurate spectral typing difficult, but a cautious estimate of around 12000 K can be made for the temperature. This agrees with past literature estimates of 8200-12000 K (Mora *et al.* 2001; Manoj *et al.* 2006). A generous error of 4000 K is adopted due to the poor SNR.

R Mon – In the spectra of R Mon all lines are seen in emission or as P-Cygni profiles, making any temperature estimate impossible from spectra alone. The temperature has been previously listed as around 12000 K in past works (Mora *et al.* 2001; Manoj *et al.* 2006). Since this is the only temperature estimate available, and with no other indicators present, this temperature is adopted.

Z CMa – As with R Mon, this star has many P-Cygni lines and emission lines in its spectra, but lacks absorption features for spectral typing. In the literature this star is seen to have the largest spread in listed temperatures; ranging

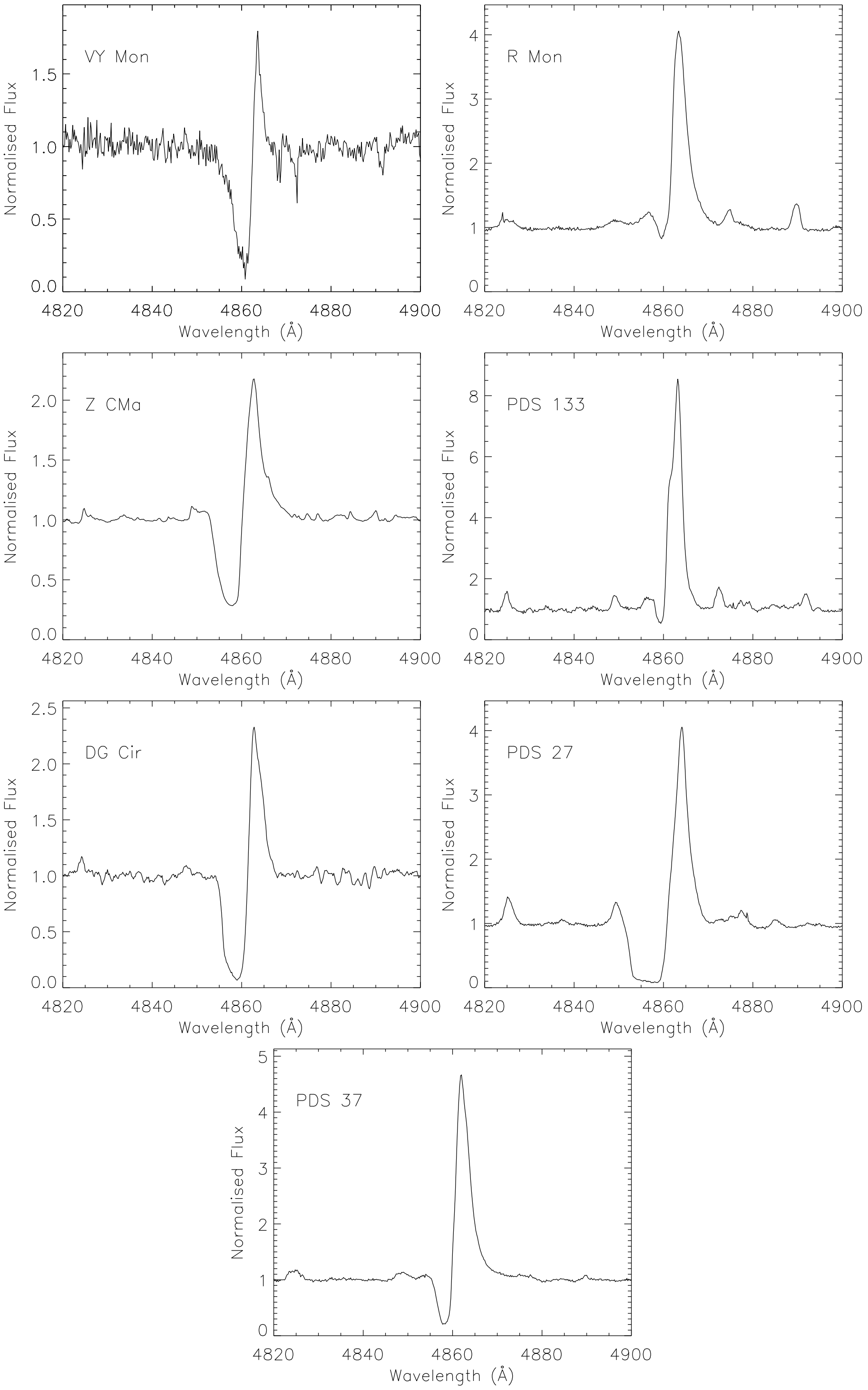

Figure 2.10: The Hβ line profiles of the stars which have strong emission lines, and could not be spectral typed are displayed in this figure. Each plot is labelled with the star's name.

from 30000 K (van den Ancker *et al.* 2004; Manoj *et al.* 2006), down to 11500 K (Donehew & Brittain 2011), and even as low as 8500 K (Hinkley *et al.* 2013). The temperature from Hinkley *et al.* (2013) is adopted as their work spatially resolves the Herbig star in this system from its FU Or-like companion. The companion may have affected previous determinations. In addition to this, they provide SED fitting to the observed photometry to determine the temperature; making this the most robust measurement for Z CMa.

PDS 133 – Another star devoid of any photospheric absorption in its spectra, and which has extremely strong emission lines (the equivalent width of Hα is ~ -100 Å). Previously, the star has been listed in the literature as having $T_{\rm eff}$ =14000 K by Vieira *et al.* (2003), who estimated the temperature photometrically. As this is the only estimation in the literature, it is adopted here.

DG Cir – A star with reasonably strong emission; the Balmer series are seen as P-Cygni profiles. A broad spectral type of class B has previously been assigned to this star by Sanduleak & Stephenson (1973) and Vieira *et al.* (2003). Gahm & Malmort (1980) do not give a spectral type but note its similarities to V380 Ori; which has been spectral typed here. A small region of possible absorption lines can be seen around 5200 Å, but they appear blended with emission lines making an exact temperature determination difficult. Based on these features I agree with a B spectral type, and would narrow this to a late-B type star of ∼11000 K, due to the similarities with V380 Ori. A generous error of 3000 K is adopted.

2.5.1 PDS 27 & PDS 37

There are a further two exceptional stars to still discuss; PDS 27 and PDS 37. These have been chosen for further investigation as they are poorly understood stars which appear spectrally similar. They are both HAeBe candidate stars which have formed the focus of a recent study by Ababakr *et al.* (2015, submitted). They were identified as candidate HAeBes in the Pico dos Dias Survey due to Hα emission and photometric colours, as detailed in the paper by (Vieira *et al.* 2003). Based on the observed photometry, those authors estimated the stars to be early-B type stars of $\sim$ 20000 K, with PDS 27 estimated to be at a distance of 1100 pc, and PDS 37 at 720 pc.

The suspected early-type of these stars places them as objects of particular interest, as the number of early B-type HBes is far smaller that the number of late-type HBes. However, their spectral type, or rather temperature, cannot be confirmed using the techniques in Section 2.3.1 due to both stars displaying strong P-Cygni profiles across the lines used. The only other absorption lines seen, which are not P-Cygni shaped, come from the Helium I lines. These lines are displayed in Figure 2.11, where they are seen to be variable, and therefore may only provide a limited estimate on the temperature. If the origin of the He I lines is assumed to be photospheric, then the greatest absorption strength would peak at around 21000 K. However, the observed strength is greater than predicted by model stellar atmospheres for both stars. The lines are also asymmetric, with blue shifted absorption extending to $\sim$-450 km s^{-1}, which is approximately the same as observed in the hydrogen lines. Therefore, it is possible that the absorption seen in the helium lines is coming from a strong wind. Strong winds have been

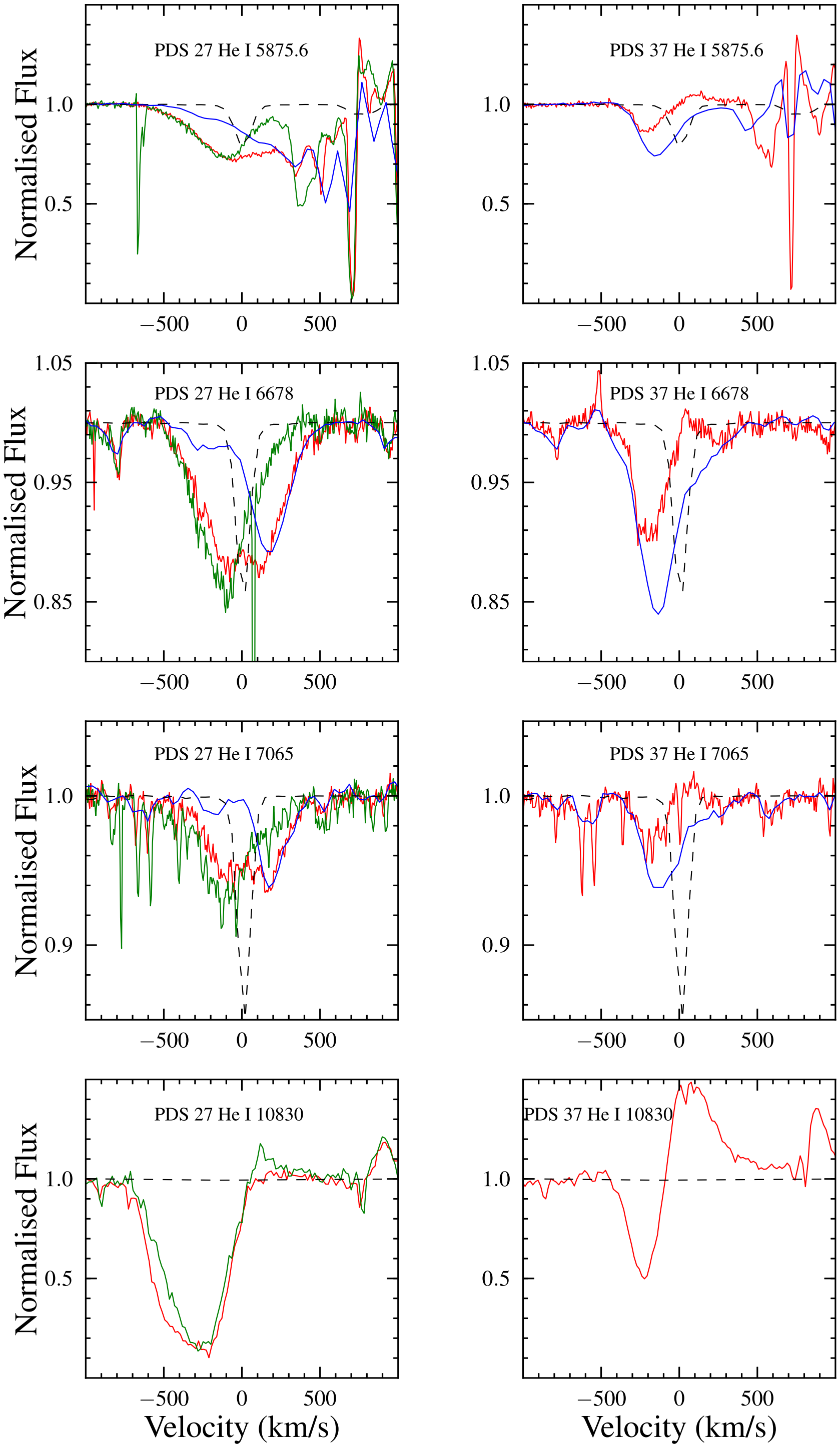

Figure 2.11: The He I lines for each of the stars are displayed here with PDS 27 on the right hand side, and PDS 37 on the left hand side. The red spectra are the X-shooter data, while the blue is additional FORS spectra (PDS 27 also has a second X-shooter observation, shown in blue). Variability can be seen between all the epochs in both stars. The lines are seen to be particularly strong in comparison to a Kurucz model with a temperature of 21000 K, with zero rotation and displayed as a black dashed line. This figure is also contained in Ababakr *et al.* (2015, submitted).

observed in T Tauri stars using the He I 10830 Å line, although such strong and broad absorption is not expected in CTTs at higher energy transitions of He I, like the 6678 Å and 7065 Å lines, by either theory (Kurosawa *et al.* 2011) or observations (Beristain *et al.* 2001). This suggests that the stars would be much hotter than CTTs.

A lower limit can be placed on the temperature using the observed photometric colours. Vieira *et al.* (2003) measure $(B-V)_{obs} = 1.32$ for PDS 27 and $(B-V)_{obs} = 1.52$ for PDS 37. In order to obtain the intrinsic colour index the observed photometry needs to be corrected for reddening. This can be estimated through measurements of the diffuse interstellar bands, (DIBs). Their strength is directly proportional to the amount of interstellar dust along the line of sight to a star. However, the DIBs are thought to only trace dust within the ISM, and cannot provide an estimate of the circumstellar dust, or rather its contribution to the reddening. Therefore, they can only provide a lower limit to the reddening, and hence a lower limit to the $(B-V)$ correction. The colour excesses measured from the DIBs are 1.20 ± 0.16 for PDS 27 and 0.98 ± 0.37 for PDS 37. The lowest, or rather bluest, $(B-V)_{int}$ determined from subtracting the DIBs contribution is found to be -0.04 in PDS 27 and 0.15 in PDS 37. This places the lower limit on PDS 27 as a B9 star with a temperature of 10000 K, and PDS 37 as an A5 star with a temperature of 8000 K.

An upper limit can be placed on the temperature based on the observed size of the Balmer jump. This is because the Balmer jump decreases in size with increasing temperature (for temperatures greater than $\sim$ 9000 K, where the Balmer jump is at maximum). Therefore, the observed size of the jump places an upper limit on the photospheric temperature. It does not provide a lower limit

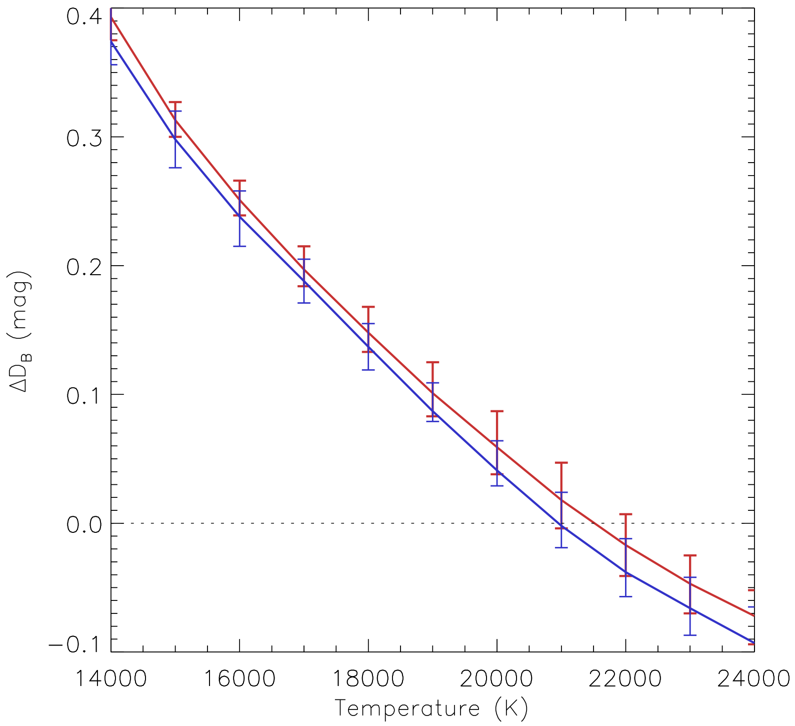

Figure 2.12: The difference between the Balmer jump measured in the target stars to the expected Balmer jump is plotted as a function of temperature. PDS 27 is shown in red; PDS 37 in blue. At ∼21000 K the limit is reached where the observed size of the Balmer jump is the same as the expected Balmer jump for that temperature. For temperatures greater than this the observed jump would be larger than expected, which is unphysical. The errors are based on the uncertainties in the distance.

though, as a small jump can be achieved by cooler stars combined with a source of excess flux i.e due to accretion. Such a contribution cannot be ruled out if these stars are thought to be PMS stars. Figure 2.12 shows the observed excesses, for a range of temperatures, measured over the Balmer jump region. This provides an upper limit of 21000 K in both stars.

In addition, N I emission lines are observed at 8629 Å and 8683 Å in both objects. These lines have a high excitation energy (∼10 eV), and have only been observed in B-type HAeBes, predominately in early B-types (Hamann & Persson

1992b). Based on the presence of these lines it is reasonable to assume that both of the stars are more likely to be early B-type than late B-type. Therefore, a revised lower limit of the temperature of PDS 27 and 37 is made of 14000 K.

Based on the three above arguments, which combine knowledge of photometry and spectra, it is plausible that the range in temperature is 14000–21000 K. Therefore, a temperature of 17500 ± 3500 K is adopted for both objects.

Both of the objects are in the same situation as the stars for which no log(g) determination could be made; like them a distance must be adopted in order to determine a luminosity and derive the other stellar parameters. In this work the distance shall be determined using a galactic rotation curve combined with the measured velocity of the stars. The galactic rotation curve by Reid *et al.* (2009) is used.

The velocities of the stars are measured from the centre of various symmetric emission lines, and also as the central point of double-peaked lines. The corrected V_{LSR} is observed to be $12.6 \pm 7.0\,\mathrm{km\,s^{-1}}$ for PDS 37, which yields a distance of 4.64 (+0.46,-0.59) kpc. The V_{LSR} of PDS 27 is uncertain, as additional spectra from FORS2 shows that it is variable by $\sim 20\,\mathrm{km\,s^{-1}}$. For this reason it is not used here. Instead, the velocities of the parental cloud, in which the stars lie, is considered through the use of molecular observations. The ^{13}CO(2-1) and NH_3(1,1) transitions, from Urquhart *et al.* (2011), have velocities of $43.5\,\mathrm{km\,s^{-1}}$ for PDS 27 and $5.4\,\mathrm{km\,s^{-1}}$ for PDS 37; these yield distances of 3.2 ± 0.6 kpc for PDS 27 and 3.7 ± 1.0 kpc for PDS 37. For PDS 37 this agrees with the spectral line observations, indicating that it does trace the systemic velocity, and provides weight for using the molecular line for PDS 27 too. For the final distance adopted to PDS 27 is the molecular observation, while for PDS 37 an average of the measurements used, providing a distance of 4.31 ± 0.67 kpc. A consitancy check is performed by calculating the kinematic distance based on the measured velocity of the DIBs. The derived distances from the DIBs are less than the calculated distances to the star. This is as expected as they trace the material between us and the star.

The luminosity of both stars is then determined from the steps described in Section 2.3.2, where the use of photometry provides the $D/R_\star$ ratio from which the radius is determined by using the above distances. This is combined with the temperature to provide the luminosity. The remaining stellar parameters are determined using the PMS tracks, as described in Section 2.3.3, all of which are detailed in Table 2.4.

2.6 HR-diagram Location and Evolutionary Discussion

2.6.1 HR-diagram Location

Using the spectra, log(g) could be determined for the majority of the sample in addition to $T_{\rm eff}$. For these stars, the stellar parameters were determined using PMS tracks. Their placement on these tracks confirms the young nature of these stars and is shown in Figure 2.13, in the left hand panel; the right hand panel shows the corresponding HR-diagram. The 8 stars of the sample which required revised distances to be calculated to them (see Section 2.3.3) are not included here as their placement is artificial when compared to the other stars. A large proportion of the sample are clustered between 2–3 $M_\odot$, which is likely caused

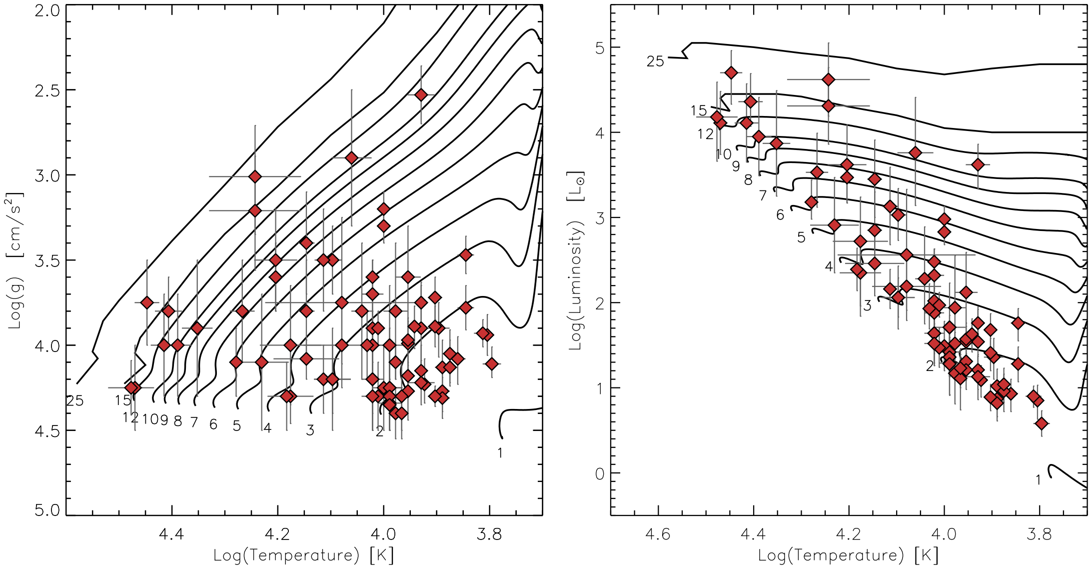

Figure 2.13: The left panel shows all the stars for which log(g) and T_{eff} could be determined from the spectra. These are translated into an HR-diagram in the right hand panel. The PMS evolutionary mass tracks of Bressan *et al.* (2012) and Bernasconi & Maeder (1996) are also plotted as solid black lines and labelled according to mass. Stars which were moved onto the ZAMS are not included in this plot.

by a combination of two effects. The first being that lower mass sources are more numerous, as described by the initial mass function, IMF, (Salpeter 1955). The range of masses determined in this work agrees fairly well with a typical Salpeter-IMF distribution, particularly when considering the selection criteria (the criteria skews our sample towards high mass objects, as these are the ones of greater interest in this work). Table 2.4 shows the comparison of the mass distribution in this work versus the distribution given in Zinnecker & Yorke (2007) for a typical IMF function.

The second aspect, which may be contributing to the clustering, is a visibility effect due to low mass stars being more evolved and less extinct than younger high mass stars (as predicted by a comparison between the Kelvin-Helmholtz

Table 2.4: Compares the number of HAeBes found in different mass bins with the theoretical IMF distribution

Mass Bin	Theoretical	This Work
1–2 $M_\odot$	99	31[†]
2–4 $M_\odot$	39	36
4–8 $M_\odot$	15	11
8–16 $M_\odot$	6	11
> 16 $M_\odot$	4	2

[†] This sample is focused on HAeBes and does not represent the 1–2 $M_\odot$ bin well, as HAeBes are generally more massive.

time-scale and the free-fall time-scale). This second point is supported by the A_V values measured in this sample where, in general, the lower mass objects tend to have lower A_V values. However, it should be noted that a high A_V does not automatically mean that the object has a high mass, as many low mass stars of young ages also have high extinction values (e.g. V599 Ori has an $A_V = 4.65$, but only has $T_{\rm eff} = 8000$ K and $M_\star = 2.5$ M$_\odot$).

Figure 2.13 also shows that the stars appear to be split into three groups: some very high mass HBes with >9 M$_\odot$; some intermediate mass HAeBes with a mass ∼3–7 M$_\odot$; and the largest group of HAeBes with a mass of ∼1–3 M$_\odot$. Curiously, very few stars are seen around ∼8 M$_\odot$. This is most likely just a coincidence due to low number statistics. However, for the most part the highest mass HAeBes do have high levels of extinction, which may result in less detections. Another point to note is that clustering of the stars could be attributed to the stars actually belonging to the same cluster. The star forming regions in which some of the HAeBes in this work appear to be associated with are the Orion-OB1, Mon-OB1, CMa-R1, and Sco-OB2 regions (de Zeeuw *et al.* 1999; Shevchenko *et al.* 1999;

Dahm & Simon 2005; van Leeuwen 2007). Since the regions are located at fixed distances, clustering of luminosities will occur if the stars are of similar spectral type. It is worth noting that the number of stars in each mass bin of a cluster is governed by the initial mass of the cloud in which they form. By looking at just a few star forming regions we naturally get clusters of similar mass stars in each one; resulting in clustered regions in an HR-diagram. However, only a small number of distances are adopted from the literature as an input parameter in this work, and they are drawn from various catalogues and regions on the sky. The spread on the HR-diagram can simply be attributed to, relatively, low number statistics.

2.6.2 Age

Next, the age of the stars is investigated. Figure 2.14 shows age against temperature. It can be seen, in general, that the highest temperature objects are also the youngest. This reflects the PMS evolution of the hotter stars being shorter, such that they can only been seen at small ages. Likewise, the cooler stars can be seen at larger ages. However, it should be noted that some cool stars can also be quite young; as evidenced by a few HAeBes in the figure. This is because they are likely massive stars that are still undergoing contraction, hence young, and will move towards hotter temperatures. Such an evolution is rapid, and slow towards the main sequence. A best fit to the data in the figure is found of $\log(t) \propto -3.26 \times \log(T_{\rm eff})$, where t is the age in Myr. Given that the evolution of PMS stars results in them getting hotter with time, this should be not be taken as a relationship for determining one from the other. Instead, it roughly

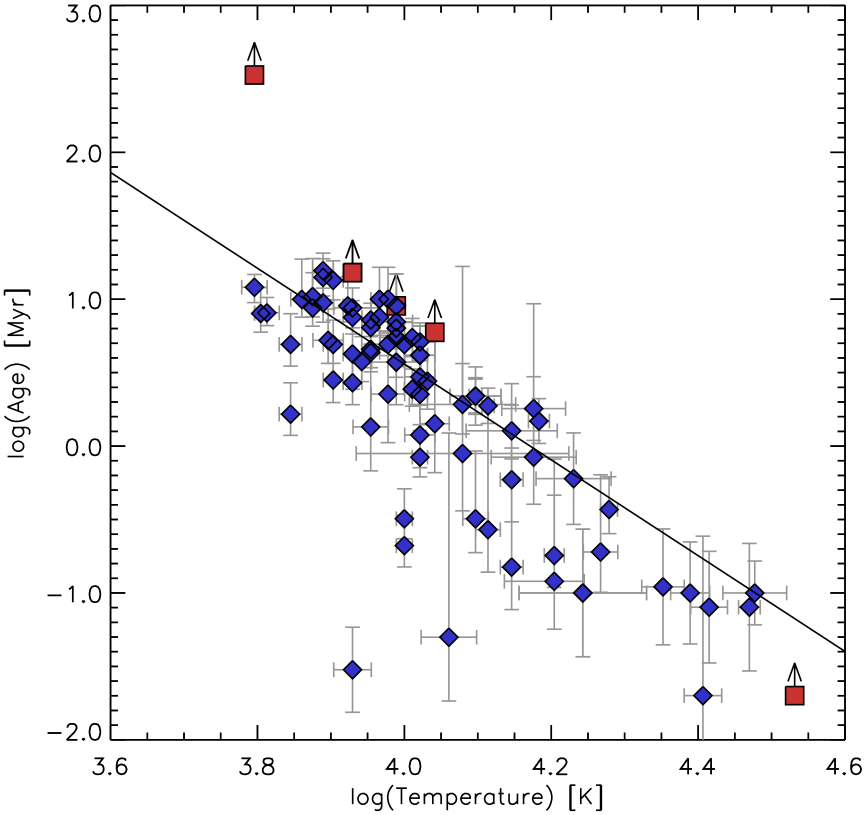

Figure 2.14: Here the age, as determined from the PMS tracks, is plotted against the temperature of the star. The plot shows how the older stars are always the cooler stars i.e. the ones with a lower mass and evolve towards the main sequence slower than their high mass counter parts as expected. However, all of the hottest objects, $T_{\rm eff} > 20000\,{\rm K}$, are seen to be the youngest ones, $t < 0.5\,{\rm Myr}$. Some cool and young stars are also present, which are likely to be in the early stages of their PMS evolution. A best fit to the data in the figure is plotted of $\log(t) \propto -3.26 \times \log(T_{\rm eff})$

describes the upper limit to the age of the stars for a given temperature. It is worth stressing that the HBes can only be seen at early ages when it comes to looking at HAeBes statistically. The HBes will always be much younger than the majority of HAes, but they may also be much closer to the main sequence. Overall, caution must be exercised in drawing conclusions from age comparisons due to the various evolutionary stages involved.

2.7 Conclusions

To conclude, presented in this chapter is the largest spectroscopic survey of HAeBes to date, which is dedicated to obtaining stellar parameters. They are obtained through a thorough process of spectral typing using the Balmer series (which peaks in aborption for the HAeBes). Determinations of the temperature and surface gravity have been made for the majority of the sample in a homogeneous fashion. Combined with photometry and theoretical PMS tracks these have allowed the determination of stellar radius, mass, luminosity, the distance, the A_V, and age; in a consistent manner.

The observed temperatures are found to be agreement with the literature. However, the derived distances do not always agree with literature distances which are based on associations with star-forming regions. The distances determined in this work are supported by measurements of diffuse interstellar bands and provide more sensible stellar parameters than the distances from the associations. Therefore, revised distances have also been determined in this chapter.

Overall, this chapter has demonstrated a homogeneous method of determining stellar parameters, which are consistent with past values. The methods involved have also allowed improvements to be made in regards to distance determinations. All of the derived parameters set the ground work for not just the next chapters in this thesis, but for future statistical work on HAeBes too.

Chapter 3

Accretion Rate Determinations From UV-Excess Measurements

3.1 Introduction

Currently, Herbig Ae/Be stars are thought to share many properties with CTTs. Both have been observed to have circumstellar discs; both have been observed to have numerous emission lines in their spectra; both are known to have lower surface gravities than main sequence stars; and both have been observed to have a UV-excess. However, despite the similarities many questions remain in regards to the HAeBes: Are the discs similar between the two groups? Is the origin of the emission lines in CTTs the same as in HAeBes? Is the UV-excess in HAeBes caused by Magnetospheric accretion?

Lately, more and more has been learnt about the discs around HAeBes. In particular the HAeBes are known to form two different groups based on their emitted IR-excess from the disc (Meeus *et al.* 2001), where it is thought that

CO from the disc can still reach to within 1 au of the star in some of these HAeBes (van der Plas *et al.* 2009, 2015; Ilee *et al.* 2014). Even observable gaps, and possible planets, have been observed within these discs (Quanz *et al.* 2013; Brittain *et al.* 2013; Currie *et al.* 2014; Close *et al.* 2014). This leads to the question of the role accretion plays in their discs. This has large implications on PMS systems, influencing the achievable mass of planets forming within the disc, the final mass of the star, and the time-scales on which they evolve. Planets under formation require mass to be fed onto them, while the numerous emission lines and observed UV-excess require a source of energy (Garrison 1978; Mendigutía *et al.* 2011a; Donehew & Brittain 2011).

The consensus at present in CTTs is that their observed UV-excess can be explained within the context of magnetospheric accretion (Calvet & Gullbring 1998). Support of this explanation has grown stronger through observations of the UV-excess matching the theory (Gullbring *et al.* 1998, 2000; Ingleby *et al.* 2013), while observed line profiles have also been seen to fit within this context too (Muzerolle *et al.* 1998a, 2001; Kurosawa *et al.* 2011). Under this paradigm the disc material is truncated by the magnetic field lines from the star, and from here the material is funnelled via the field lines, in free-fall, onto the star. The accreted material shocks the photosphere, which causes X-ray emission. The majority of that emission is then absorbed by the surroundings, heating them, and is re-emitted at longer wavelengths. This gives rise to an observable UV-excess (Calvet & Gullbring 1998). Therefore, measurement of the UV-excess can be directly related to mass accretion from the disc to the star.

However, for MA to be applicable the star must have a magnetic field with sufficient strength to truncate the disc; for CTTs this is of the order of kilo-Gauss strengths (Ghosh & Lamb 1979; Koenigl 1991; Shu *et al.* 1994; Johns-Krull 2007; Bouvier *et al.* 2007). For MS stars magnetic fields due to convection are not predicted to exist for stars with $T_{\text{eff}} > 8300\,\text{K}$ (Simon *et al.* 2002). This may also be true for PMS stars. To date, there have only been a few detections of magnetic fields in HAeBes (Wade *et al.* 2005; Catala *et al.* 2007; Hubrig *et al.* 2009). The largest survey into the magnetic fields of HAeBes was performed recently by Alecian *et al.* (2013), and yields clear detections of only 5 stars out of 70. Out of these detections it remains unclear if these magnetic fields are due to fossil fields, where the present day magnetic field is a remnant of the larger scale cloud from which the star has formed; or if it is a dynamo-induced magnetic field due to convective motions within the star (Charbonneau & MacGregor 2001).

When applying the theory of MA (Koenigl 1991; Shu *et al.* 1994) to HAeBes, a weak dipole magnetic field of only a few hundred gauss, or even less, is needed for MA to occur (Wade *et al.* 2007; Cauley & Johns-Krull 2014). These strengths are below current detection limits; this means that MA controlled accretion in HAeBes is still a possibility.

The main focus of this chapter is to provide the largest survey on direct accretion tracers in HAeBes to date. To do this, measurements of the UV excess shall be made and fitted within the context of MA shock modelling. This method of accretion-shock modelling has been successfully adapted and applied to small sets of HAeBes in recent years (Muzerolle *et al.* 2004; Donehew & Brittain 2011; Mendigutía *et al.* 2011a; Pogodin *et al.* 2012; Mendigutía *et al.* 2013, 2014). However, the number of HBes analysed in previous works are often small, particularly for early-type HBes, and needs to be tested further.

The overall aim of this chapter is to provide a quantitative look into the accretion rate of HAeBes, with a particular emphasis on how it varies as a function of stellar parameters. An assessment of the applicability of using MA to find the accretion rate shall also be performed. To do this, the HAeBe sample presented in Chapter 2 will be analysed. This chapter is broken down as follows: Section 3.2 will detail the measurements of the Balmer excess. Section 3.3 will detail the application of MA to the measurements, and the derivation of the accretion rates. Section 3.4 will discuss the findings and how they compare with the stellar parameters obtained in Chapter 2. Finally, Section 3.5 will provide the conclusions of this chapter.

3.2 Balmer Excess

The UV-excess can be determined by measuring the Balmer Excess, ΔD_B, which is defined as the difference between the observed flux and the expected intrinsic photospheric flux as measured across the Balmer Jump region (this region spans the wavelength range where the hydrogen Balmer series reaches its recombination limit $\sim$ 3680–3640 Å). ΔD_B is often more visible in low temperature stars due to their cooler photospheres, as the excess is easily noticeable on top of it. This UV-excess has been measured in both brown dwarfs (Herczeg & Hillenbrand 2008; Herczeg *et al.* 2009; Rigliaco *et al.* 2012) and CTTs (Calvet *et al.* 2004; Gullbring *et al.* 2000; Calvet *et al.* 2004; Ingleby *et al.* 2013). From these past studies the current consensus to the origin of the excess is magnetospheric accretion. It has also been shown, in small samples, that an observable ΔD_B in HAeBes stars can be explained within the same context (Muzerolle *et al.* 2004; Donehew & Brittain 2011; Mendigutía *et al.* 2011a; Pogodin *et al.* 2012). We aim to further our understanding of accretion in HAeBes by testing accretion within the context of MA to a large sample of HAeBes; this includes numerous HBe stars for which little investigation has been done.

In order to test many stars, measurements must be acquired first. To do this a definition of the Balmer excess, which will be used here, is required:

$$\Delta D_B = (U - B)_0 - (U - B)_{\mathrm{dered}} \tag{3.1}$$

where, $(U - B)_0$ is the intrinsic colour of the target and $(U - B)_{\mathrm{dered}}$ is the dereddened observed colour index. This definition has been used in many works, where it has also been modified depending on the type of data involved (Garrison 1978; Donehew & Brittain 2011; Mendigutía *et al.* 2013). Since the equation is based on photometry, and the sample data is spectroscopic, a modification of the above equation will be used for measurement. The spectra will allow a more accurate determination of ΔD_B. Detailed below are two of the best methods of measuring ΔD_B involving spectra.

3.2.1 Method 1 – SED Matching: Single Point Measurement

The first approach to measuring ΔD_B uses the spectral region of the the UVB arm from 3500–4600 Å, and adopts the same techniques of Donehew & Brittain (2011). This method requires the spectra of the target to be compared against the spectra of a star with the same spectral type. The KC-models mentioned in Chapter 2 earlier are used again here as the intrinsic stellar spectra. Following the spectral shape calibration in Section 2.2, the spectrum of each target shows

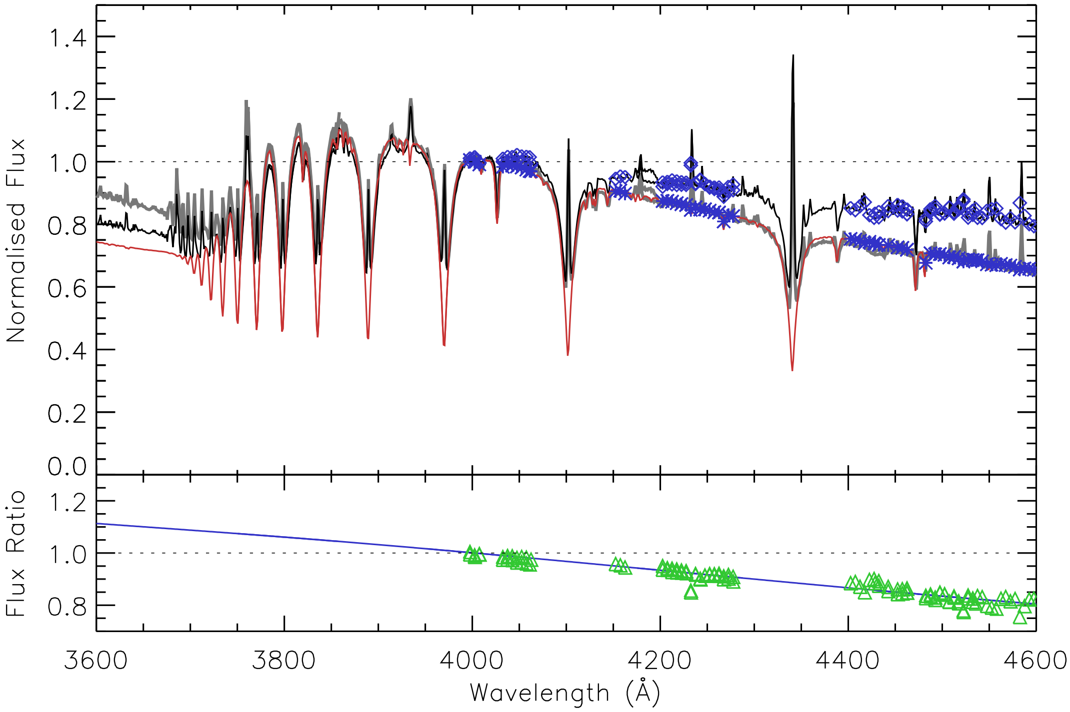

Figure 3.1: An example of the method 1 technique for the measurement of ΔD_B where the target spectrum is normalised to match the model spectrum between 4000–4600 Å is shown. The top pannel shows the target spectra (black), a KC-model of the corresponding spectral type (red), and the result (grey), all normalised to 4000 Å. Continuum areas are selected in each spectrum (shown in blue) between 4000–4600 Å. The bottom panel shows the ratios of these continuum points (green); they are fitted by a reddening law and extrapolated to 3600 Å. This level of reddening correction is then applied to the original spectra (the result is plotted in grey in the top panel). The SED of the model and the corrected spectra are now exactly the same between 4000-4600 Å, allowing measurement of the Balmer Excess to be performed around the 3600 Å region.

the correct, observed SED shape. This allows both the target and model spectra to be normalised to 4000 Å, while preserving their SED. Next, a correction for reddening present in the observed spectra is performed. To do this, the difference between the measured continuum of the target and the model between 4000–4600 Å is fitted by a reddening law (the reddening law of Cardelli *et al.* (1989) is used here). This also provides a best-fit A_V value. Extinction correction is applied to the whole spectrum, while keeping the 4000 Å point as a pivot; since the spectrum was normalised to this point. The result of this method is that the SED of the target is adjusted in such a way that the slope between the intrinsic model and the target spectrum now match between 4000–4600 Å. The success of this normalisation is not dependent upon the amount of extinction towards the star (Muzerolle *et al.* 2004; Donehew & Brittain 2011). Fig 3.1 shows the application of this SED slope matching technique along with an example output.

To perform the measurement of ΔD_B attention must be drawn back to Equation 3.1, where the magnitudes are now converted into a flux:

$$\Delta D_B = -2.5 \log \left(\frac{F_U^{\mathrm{phot}}}{F_B^{\mathrm{phot}}} \right) + 2.5 \mathrm{log} \left(\frac{F_U^{\mathrm{dered}}}{F_B^{\mathrm{dered}}} \right) \tag{3.2}$$

where F is the flux, with subscripts denoting the corresponding wavelength region, and the superscripts are: the intrinsic flux, denoted as 'phot'; and the dereddened flux, denoted as 'dered'. Now, consider the fact that the observed, dereddened flux includes an accretion contribution; such that $F_U^{\mathrm{dered}} = F_U^{\mathrm{phot}} + F_U^{\mathrm{acc}}$, which allows the above equation to be written as:

$$\Delta D_B = 2.5 \log \left(\frac{F_U^{\mathrm{phot}} + F_U^{\mathrm{acc}}}{F_B^{\mathrm{phot}} + F_B^{\mathrm{acc}}} \times \frac{F_B^{\mathrm{phot}}}{F_U^{\mathrm{phot}}} \right) \tag{3.3}$$

This equation can be reduced through the use of a normalisation factor α^{norm}, such that $(F_B^{\mathrm{phot}} + F_B^{\mathrm{acc}}) \times \alpha^{\mathrm{norm}} = F_B^{\mathrm{phot,norm}}$. This normalisation across the B-band is performed automatically by matching the SED of the target to the intrinsic SED. This gives us the final form of the ΔD_B equation:

$$\Delta D_B = 2.5 \log \left(\frac{F_U^{\mathrm{phot,norm}} + F_U^{\mathrm{acc,norm}}}{F_U^{\mathrm{phot}}} \right) \tag{3.4}$$

By these definitions, the $F_U^{\mathrm{phot,norm}} + F_U^{\mathrm{acc,norm}}$ is just the flux observed from the target spectra and F_U^{phot} is taken from a KC-model of the same spectral type. Since the spectrum obtained is of medium resolution we adopt a narrower range than a typical broadband filter to represent the U-band magnitude. This also gives us better precision in measurements. The wavelength region of measurement is 3500–3680 Å. This is chosen as it is beyond the Balmer recombination limit. However, two of the echelle orders of X-Shooter overlap in this region, and the SNR in an echelle order decreases as wavelength decreases. Therefore, to minimise errors the 3500–3600 Å region from echelle order 21 and the 3600–3680 Å region from echelle order 20 are measured and combined to give the most accurate result.

3.2.2 Method 2 – B-Band Normalised, Multi-point Measurements

An alternate method of measuring ΔD_B is given by Mendigutía *et al.* (2013), which also does not require the reddening towards a star to be known. An example of this method is shown in Figure 3.2, where it is seen to cover a larger wavelength range than method 1; as this method requires measurements of both the U-band and V-band points. These two points are measured from the observed spectra and a KC-model of the same spectral type (the same model as in method 1), after normalisation to the B-band. Rather than correcting for

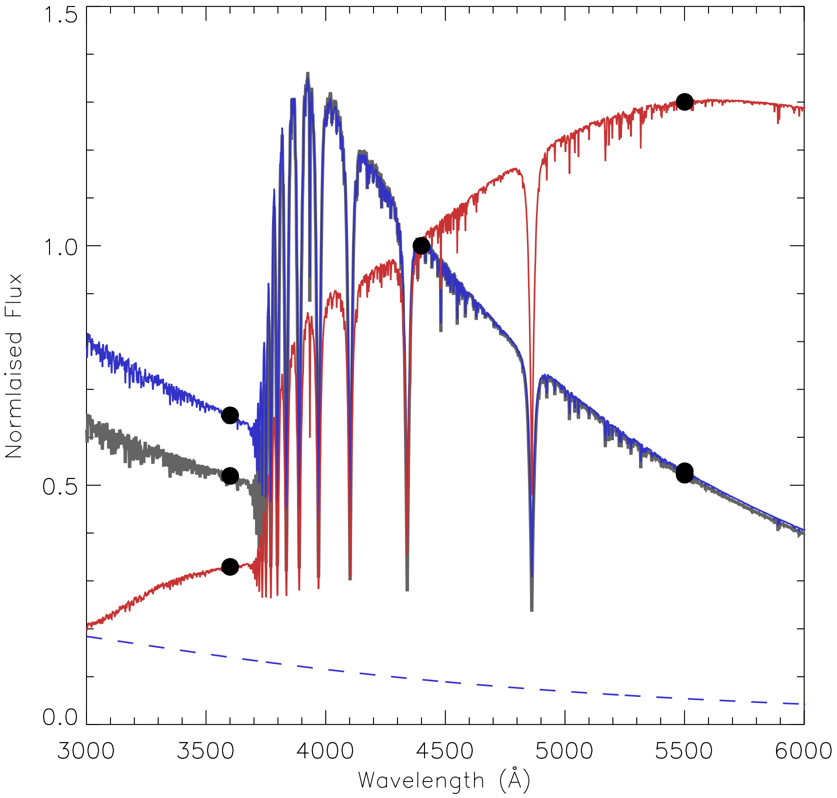

Figure 3.2: An example of the method 2 measurement of ΔD_B is shown here. A model atmosphere for a star where $T_{\rm eff}$ = 10000 K, log(g)=4.14, $M_\star = 2.0\,{\rm M}_\odot$, and $R_\star = 2.0\,{\rm R}_\odot$is shown in grey. The UV-excess is displayed as the blue dashed line; calculated using $\dot{M}_{\rm acc}$= $10^{-6.5}\,{\rm M}_\odot\,{\rm yr}^{-1}$. The expected observation, the model plus the excess, is shown in blue. Also shown is an example of a more realistic case in which reddening in involved, here $A_V = 3.0$ is applied. All of the spectra have been normalised to 4400 Å, as this is required for measurements to be made; this is marked by a black dot. The remaining black dots mark the points at which the Balmer excess will be measured.

A_V, as in the previous method, reddening independence is achieved by expanding Equation 3.1 and substituting in an expression for each reddening component: $A_\lambda = A_V(k_\lambda/k_V)$, where A_λ and A_V are the extinction at any given wavelength and in the V-band, respectively. Similarly, k_λ and k_V are the opacities for any given wavelength and the V-band, respectively. Applying the expression for A_V to Equation 3.1 gives:

$$\Delta D_B = (U-B)^{\mathrm{int}} - (U-B)^{\mathrm{obs}} + A_V\left(\frac{k_U}{k_V} - \frac{k_B}{k_V}\right) \tag{3.5}$$

The superscript ‘int’ refers to the intrinsic magnitudes (from a KC-model in this case) while the superscript ‘obs’ refers to the observed magnitudes (from the observed spectra). The values of the opacities are determined by the reddening law adopted; the reddening law of Cardelli *et al.* (1989) is used here with a standard total-to-selective extinction factor of R_V=3.1. This gives $k_U/k_V = 1.57$ and $k_B/k_V = 1.33$. To remove the A_V term the relationship between A_V and colour excess needs to be used: $A_V = \mathrm{R}_V E(B-V)$. At this point it should be noted that the method is now reddening independent, since A_V has been removed, but remains dependent on the reddening law adopted, as this determines the opacity ratios. This new form for the Balmer Excess is:

$$\begin{aligned}\Delta D_B = {} & (U-B)^{\mathrm{int}} - (U-B)^{\mathrm{obs}} + \\ & \mathrm{R}_V\left(\frac{k_U}{k_V} - \frac{k_B}{k_V}\right)\left[(B-V)^{\mathrm{obs}} - (B-V)^{\mathrm{int}}\right]\end{aligned} \tag{3.6}$$

which can be expressed in terms of flux, instead of magnitudes, as follows:

$$\Delta D_B = 2.5\log\left(\frac{F_U^{\mathrm{obs}}\alpha^{\mathrm{norm}}F_B^{\mathrm{phot}}}{F_B^{\mathrm{obs}}\alpha^{\mathrm{norm}}F_U^{\mathrm{phot}}}\right) + \\ 2.5\,\mathrm{R}_V\left(\frac{k_U}{k_V}-\frac{k_B}{k_V}\right)\log\left(\frac{F_V^{\mathrm{obs}}\alpha^{\mathrm{norm}}F_B^{\mathrm{phot}}}{F_B^{\mathrm{obs}}\alpha^{\mathrm{norm}}F_V^{\mathrm{phot}}}\right) \tag{3.7}$$

where α^{norm} is a normalising factor for the B-band, as seen in method 1, but the normalisation is instead performed such that the spectra will be unity at 4400 Å. This allows the equation to reduce to its final form:

$$\Delta D_B = 2.5\log\left(\frac{F_U^{\mathrm{obs,norm}}}{F_U^{\mathrm{phot}}}\right) + 2.5\,\mathrm{R}_V\left(\frac{k_U}{k_V}-\frac{k_B}{k_V}\right)\log\left(\frac{F_V^{\mathrm{obs,norm}}}{F_V^{\mathrm{phot}}}\right) \tag{3.8}$$

in this form it can be seen that only four points need measuring to obtain ΔD_B, as demonstrated in Figure 3.2; two from the target spectra, two from the model.

3.2.3 Comparisons and Checks

The two methods used are similar but have some subtle differences. One, is that the central wavelength for the B-band normalisation is different between the two; it is centred at 4000 Å for method 1, and is centred at 4400 Å for method 2. The next difference is that method one performs a reddening correction using a section of the observed spectrum and relies on matching this to a stellar model. On the other-hand, method 2 makes an automatic reddening correction by incorporating the adopted reddening law into the equation for ΔD_B, which corrects it within the equation based on the law chosen. Method two also applies this over a much larger spectral region to method 1. Both approaches have also been adapted from

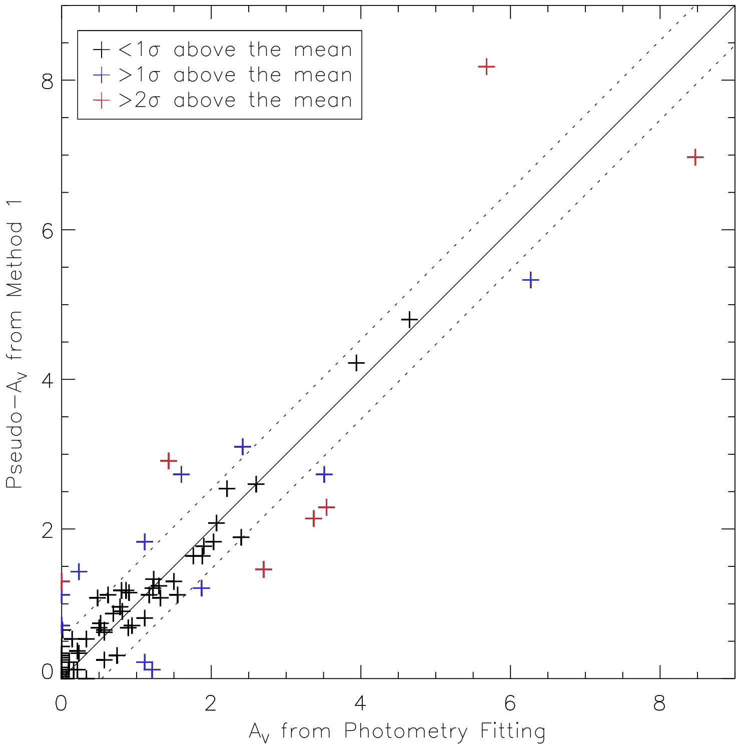

Figure 3.3: This shows a comparison of a pseudo-A_V, extracted from the method 1 measurement of ΔD_B based on how much the SED was adjusted, against the A_V determined from the photometry fitting in Section 2.3.2. The solid black line is the 1:1 ratio line, while the dashed lines are 1σ deviations from this, of 0.60 mag. Only 8% of the targets are outside 2σ; these ones often have the largest A_V values (these will be discussed in the text). Errors in the photometric A_V are typically 0.05–0.15 (about the size of the points), they are detailed in Table 2.4.

a definition which was originally based on broadband photometry too. Therefore, some checks need to be made to see whether both approaches are comparable to each other.

The first check is between how the A_V values determined in Section 2.3, compare with the A_V values extracted from method 1; as the fitting between 4000–4600 Å can be used to infer an A_V value. Figure 3.3 displays this comparison. In the figure the standard deviation between the two is found to be 0.60 mag, and is represented by the dashed black lines. Within this 1σ interval 79% of the sample are included. This helps to highlight that the majority of the sample are tightly correlated, while the outliers are more extreme and actually skew the standard deviation. There are 7 stars showing differences greater than 2σ from the mean. One of these is VY Mon, which has the lowest SNR of the objects in the blue because it is very extinct. This makes the SED adjustment more difficult and less accurate. The other outliers often have large A_V and/or large ΔD_B values. This is not entirely unexpected as a significant excess can affect the SED shape of the spectra, which would complicate both photometry fitting and the SED adjustments performed. For HAeBes in general this is less likely, as they are already very hot and the UV-excesses need to be very strong to significantly affect the SED. One source of discrepancy may be due to the $BVRI$ points being coarse and measuring the flux over a large region, while the spectral method covers a narrow wavelength range of 4000 – 4600 Å, with a greater accuracy in that region. The photometry used is also not simultaneous with the spectra; variability could therefore also play a role in the differences. Ultimately, this scatter is quite low with very few outliers; this is acceptable considering the above factors and the standard reddening law adopted in both cases.

The next check is to see how ΔD_B varies between the two methods of measurement; Figure 3.4 shows the comparison. The standard deviation between the two methods is 0.04 mag. Since the original ΔD_B equation, Equation 3.1, can be seen to contain a dereddened term, the differences can be partly attributed to how the reddening corrections are made in each case. Another source of discrepancy is that the measurement and normalisation regions used are different.

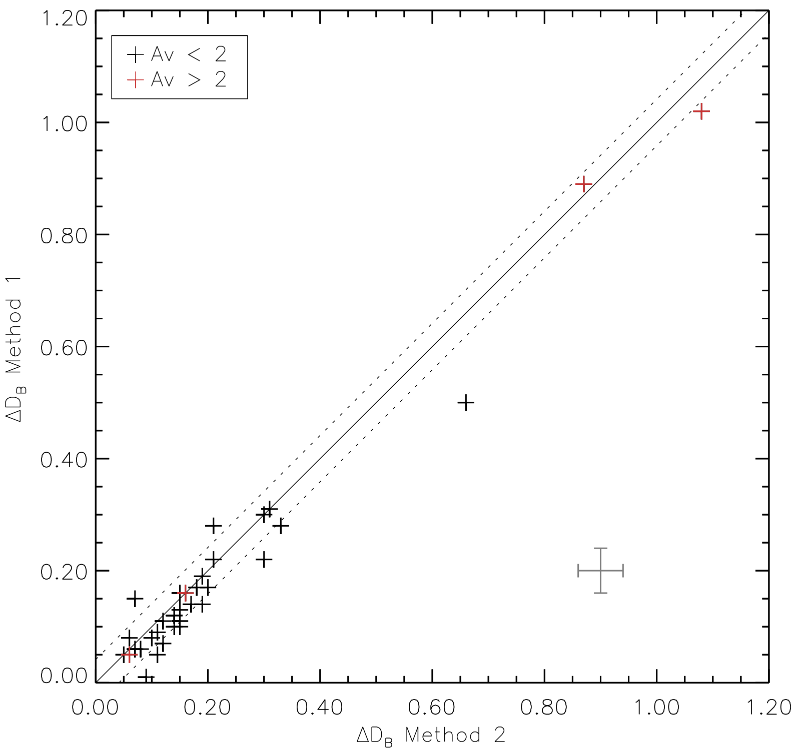

Figure 3.4: A comparison is made between the two different methods of measuring ΔD_B (detailed in Section 3.2.1 & 3.2.2). A line of expected 1:1 correlation is shown (solid black), along with deviations of 0.04 mag from the correlation (dashed lines). A few outliers can be seen, often they are ones with higher levels of extinction; these are discussed in the text. For clarity individual error bars are not plotted due to the tightness of the points. Instead, a typical error bar of 0.04 mag is plotted in the bottom right corner. The actual errors range between 0.04–0.10 mag, and are provided in Table 3.1.

Emission lines in any of these regions could change the result.

The first approach in method 1 covers a small wavelength range of 3600 – 4600 Å, of which only the 4000 – 4600 Å region is used for the reddening correction. This means that the first approach is not particularly sensitive to a given reddening law due to the small wavelength range it covers, and can be deemed reddening independent for low levels of extinction, $A_V < 10$, provided that the

SED is not significantly affected by accretion between 4000 – 4600 Å. On the other hand, the second method relies more upon the adopted reddening law than method 1 because it covers a larger wavelength region of 3600 – 5500 Å. Depending on the R_V selected the resulting opacity ratios, seen in Equation 3.6, can change substantially, which in turn alters the measured ΔD_B. Changing R_V in method 1 does not noticeably affect ΔD_B as it is always the SED profiles which are being matched. Through this matching, the A_V used will change to retain the SED shape; this keeps ΔD_B approximately the same, for low A_V values, as the wavelength region analysed is small. Returning to the figure, a few outliers can be seen between the two methods; the majority of these are objects with high extinction, or which were identified as having a discrepant A_V between the photometric method and the spectral method in which they were determined. Overall, consistency is shown between the methods employed here. Most of the values obtained lie within the errors of each other (see Table 3.1) or they are deviant by an amount which can be attributed to statistical scatter. Based on the above analysis, we deem the methods equivalent. Therefore, in each case an average of the two will be taken for the final result; unless one method has a lower measurement error, which can occur depending on emission lines in both the measurement and normalisation regions, then that method will be favoured over the other. The ΔD_B value for each star along with the errors and method(s) used to obtain it, are detailed in Table 3.1. It should be noted that clear excesses are visible in the spectra (in all cases which are not upper limits), but measurement of the detected excess is complicated by absorption and emission throughout. The errors assigned to ΔD_B also appear large when compared with the value of ΔD_B itself. The enhanced errors are mostly due to taking the logarithm of a

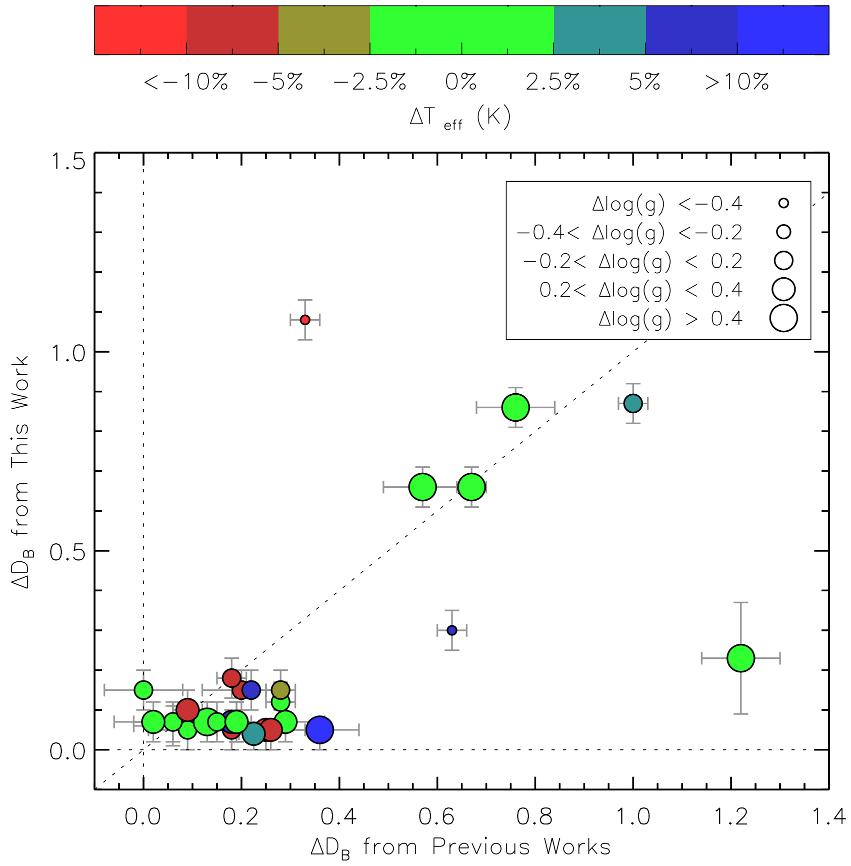

Figure 3.5: A comparison is drawn here between the final ΔD_B measured in this work versus the ΔD_B measured by other authors in the literature (Donehew & Brittain 2011; Mendigutía *et al.* 2011a; Pogodin *et al.* 2012). The difference in temperature between the two sources is calculated as a percentage of the total stellar temperature (cooler temperatures than the literature are red, while hotter ones are blue). The size of each symbol reflects the difference in log(g) measured. Overall the largest deviations in ΔD_B are for the objects with the greatest differences in stellar parameters. Photometric variability may also have an effect.

ratio (see Equation 3.4); where an error of 1% in the continuum detection can then translate to more than a 30% error in ΔD_B, as it is the difference between the observed and intrinsic being measured.

As a consistency check, a comparison of the ΔD_B values determined in this work versus previous values published in the literature is shown in Figure 3.5. The majority of the measurements are clustered at values < 0.4 mag, with past literature values showing a slightly larger spread in ΔD_B than our sample. The main source of deviation between this work and the literature is due to the T_{eff} and log(g) parameters used for each star; as these differ so will the intrinsic spectra against which ΔD_B is measured. The figures shows this clearly with a number of objects having deviant ΔD_B and stellar parameters, where the largest variations in ΔD_B are indeed the stars with the largest deviations in T_{eff} and log(g). Another source which may add to the discrepancies is genuine variability of the star and its accretion rate. Overall, the majority of sources share common values, within the errors, and the majority of discrepancies can be explained by the adoption of different stellar parameters.

3.3 Accretion Rates

Accretion rates are an important parameter of pre-main sequence stars. They provide an insight into how the stars are evolving, along with the impact this will have on disc-star interactions, and which may even have repercussions on planet formation. In this section the measured ΔD_B is used to calculate $\dot{M}_{\text{acc}}$ using accretion shock-modelling within the context of magnetospheric accretion.

3.3.1 Magnetospheric Modelling

The context of MA is adopted in order to test its applicability to a wide sample of HAeBes. The main assumption here is that the excess flux visible over the Balmer Jump region is produced by shocked emission from an in-falling accretion column.

Table 3.1: Table of Accretion Rates. Column 1 gives the target name. Columns 2-4 give the measured Balmer Excess, filling factor and derived accretion rate; ΔD_B errors are rounded to the closest 0.01 and include all systematic errors. Column 5 details by which method the values were obtained. Column 6 gives the accretion luminosity. Finally, column 7 notes which stars can be modelled by MA.

Name	ΔD_B (mag)	f (%)	$\log(\dot{M}_{\rm acc})$ [$\mathrm{M}_\odot$/yr]	Method(s) Used	$\log(L_{\rm acc})$ [$\mathrm{L}_\odot$]	Achievable by MA
UX Ori	$\leq$ 0.04	$\leq$ 0.7	$\leq$ -7.26	Method 1 & 2	$\leq$ 0.13	y
PDS 174	$\leq$ 0.02	$\leq$ 2.8	$\leq$ -6.76	Method 2	$\leq$ 0.92	y
V1012 Ori	$0.19^{+0.05}_{-0.05}$	$4.4^{+1.0}_{-0.9}$	$-7.20^{+0.21}_{-0.28}$	Method 1 & 2	$0.35^{+0.26}_{-0.32}$	y
HD 34282	$0.06^{+0.05}_{-0.05}$	$1.7^{+0.9}_{-0.8}$	$-7.69^{+0.28}_{-0.59}$	Method 1	$-0.06^{+0.32}_{-0.61}$	y
HD 287823	$0.15^{+0.05}_{-0.05}$	$3.0^{+0.7}_{-0.7}$	$-7.13^{+0.18}_{-0.23}$	Method 1 & 2	$0.37^{+0.20}_{-0.24}$	y
HD 287841	$\leq$ 0.05	$\leq$ 0.8	$\leq$ -7.82	Method 1 & 2	$\leq$ -0.32	y
HD 290409	$\leq$ 0.07	$\leq$ 2.1	$\leq$ -7.31	Method 1 & 2	$\leq$ 0.25	y
HD 35929	$0.10^{+0.05}_{-0.05}$	$1.0^{+0.4}_{-0.3}$	$-6.37^{+0.18}_{-0.26}$	Method 1 & 2	$0.87^{+0.20}_{-0.28}$	y
HD 290500	$0.21^{+0.05}_{-0.05}$	$6.1^{+1.7}_{-1.5}$	$-6.11^{+0.17}_{-0.17}$	Method 1 & 2	$1.29^{+0.35}_{-0.21}$	y
HD 244314	$0.12^{+0.05}_{-0.05}$	$2.4^{+0.7}_{-0.7}$	$-7.12^{+0.20}_{-0.25}$	Method 1 & 2	$0.35^{+0.21}_{-0.26}$	y
HK Ori	$0.66^{+0.05}_{-0.05}$	$27.7^{+6.0}_{-3.8}$	$-6.17^{+0.17}_{-0.16}$	Method 1 & 2	$1.33^{+0.19}_{-0.18}$	y
HD 244604	$0.05^{+0.05}_{-0.05}$	$1.1^{+0.7}_{-0.1}$	$-7.22^{+0.26}_{-0.32}$	Method 1	$0.22^{+0.28}_{-0.34}$	y
UY Ori	$\leq$ 0.02	$\leq$ 0.6	$\leq$ -7.92	Method 1 & 2	$\leq$ -0.35	y
HD 245185	$\leq$ 0.07	$\leq$ 2.3	$\leq$ -7.29	Method 1 & 2	$\leq$ 0.29	y
T Ori	$\leq$ 0.05	$\leq$ 1.0	$\leq$ -6.54	Method 1 & 2	$\leq$ 0.79	y
V380 Ori	$0.87^{+0.05}_{-0.05}$	$80.3^{+19.7}_{-21.9}$	$-5.34^{+0.10}_{-0.15}$	Method 1 & 2	$2.12^{+0.31}_{-0.16}$	y
HD 37258	$0.14^{+0.05}_{-0.05}$	$4.5^{+1.5}_{-1.3}$	$-6.98^{+0.14}_{-0.17}$	Method 1 & 2	$0.58^{+0.15}_{-0.18}$	y
HD 290770	$0.15^{+0.05}_{-0.05}$	$6.2^{+1.6}_{-1.5}$	$-6.74^{+0.12}_{-0.14}$	Method 1 & 2	$0.82^{+0.16}_{-0.17}$	y
BF Ori	$0.15^{+0.05}_{-0.05}$	$3.6^{+0.9}_{-0.9}$	$-6.65^{+0.17}_{-0.25}$	Method 2	$0.77^{+0.19}_{-0.27}$	y
HD 37357	$0.30^{+0.05}_{-0.05}$	$10.1^{+1.7}_{-1.5}$	$-6.42^{+0.09}_{-0.06}$	Method 1 & 2	$1.08^{+0.09}_{-0.06}$	y
HD 290764	$0.21^{+0.05}_{-0.05}$	$3.5^{+0.8}_{-0.7}$	$-6.56^{+0.17}_{-0.22}$	Method 1 & 2	$0.80^{+0.21}_{-0.24}$	y
HD 37411	$0.15^{+0.05}_{-0.05}$	$4.9^{+1.3}_{-1.2}$	$-7.13^{+0.24}_{-0.34}$	Method 1 & 2	$0.47^{+0.29}_{-0.38}$	y
V599 Ori	$\leq$ 0.01	$\leq$ 0.1	$\leq$ -7.67	Method 2	$\leq$ -0.33	y
V350 Ori	$0.15^{+0.05}_{-0.05}$	$3.7^{+1.0}_{-0.9}$	$-6.95^{+0.18}_{-0.23}$	Method 1 & 2	$0.55^{+0.19}_{-0.24}$	y
HD 250550	$0.30^{+0.05}_{-0.05}$	$17.1^{+4.3}_{-3.1}$	$-5.63^{+0.14}_{-0.11}$	Method 1 & 2	$1.82^{+0.32}_{-0.17}$	y
V791 Mon	$0.19^{+0.05}_{-0.05}$	$27.5^{+10.2}_{-8.0}$	$-6.16^{+0.28}_{-0.35}$	Method 1 & 2	$1.55^{+0.32}_{-0.39}$	y
PDS 124	$0.11^{+0.05}_{-0.05}$	$4.1^{+1.3}_{-1.2}$	$-7.11^{+0.13}_{-0.19}$	Method 2	$0.50^{+0.14}_{-0.20}$	y
LkHa 339	$0.13^{+0.05}_{-0.05}$	$5.3^{+1.5}_{-2.1}$	$-6.81^{+0.12}_{-0.22}$	Method 2	$0.75^{+0.13}_{-0.22}$	y
VY Mon	$0.23^{+0.14}_{-0.14}$	$17.5^{+22.7}_{-13.0}$	$-5.50^{+0.42}_{-0.64}$	Method 1 & 2	$1.96^{+0.60}_{-0.66}$	y
R Mon	$0.86^{+0.05}_{-0.05}$	-	-	Method 1 & 2	-	n
V590 Mon	-	-	-	-	-	-
PDS 24	$\leq$ 0.05	$\leq$ 1.9	$\leq$ -7.25	Method 2	$\leq$ 0.31	y

Continued on the next page

Table 3.1 – Continued from previous page

Name	ΔD_B (mag)	f (%)	$\log(\dot{M}_{\rm acc})$ [$M_\odot$/yr]	Method(s) Used	$\log(L_{\rm acc})$ [$L_\odot$]	Achievable by MA
PDS 130	$0.16^{+0.05}_{-0.05}$	$6.6^{+1.6}_{-1.5}$	$-6.23^{+0.12}_{-0.13}$	Method 1 & 2	$1.22^{+0.17}_{-0.15}$	y
PDS 229N	$0.09^{+0.05}_{-0.05}$	$6.4^{+2.4}_{-3.6}$	$-6.67^{+0.14}_{-0.36}$	Method 2	$0.96^{+0.14}_{-0.36}$	y
GU CMa	$0.14^{+0.05}_{-0.05}$	$60.3^{+33.4}_{-18.5}$	$-5.00^{+0.23}_{-0.13}$	Method 1 & 2	$2.72^{+0.41}_{-0.36}$	y
HT CMa	$0.11^{+0.05}_{-0.05}$	$4.3^{+1.5}_{-1.4}$	$-6.61^{+0.16}_{-0.19}$	Method 1 & 2	$0.89^{+0.20}_{-0.19}$	y
Z CMa	$1.08^{+0.05}_{-0.05}$	$48.0^{+17.0}_{-9.4}$	$-3.01^{+0.20}_{-0.19}$	Method 1 & 2	$4.05^{+0.22}_{-0.22}$	y
HU CMa	$0.14^{+0.05}_{-0.05}$	$12.2^{+3.4}_{-4.9}$	$-6.35^{+0.11}_{-0.22}$	Method 1 & 2	$1.27^{+0.11}_{-0.22}$	y
HD 53367	$0.10^{+0.05}_{-0.05}$	-	-	Method 1 & 2	-	n
PDS 241	$0.05^{+0.05}_{-0.05}$	$21.6^{+20.3}_{-1.3}$	$-5.56^{+0.29}_{-0.06}$	Method 1 & 2	$2.25^{+0.37}_{-0.23}$	y
NX Pup	$0.08^{+0.05}_{-0.05}$	$0.9^{+0.4}_{-0.3}$	$-6.96^{+0.21}_{-0.33}$	Method 2	$0.34^{+0.23}_{-0.34}$	y
PDS 27	$0.15^{+0.06}_{-0.06}$	$46.7^{+33.1}_{-21.2}$	$-4.07^{+0.34}_{-0.45}$	Method 1 & 2	$3.43^{+0.41}_{-0.49}$	y
PDS 133	$1.26^{+0.05}_{-0.05}$	-	-	Method 1 & 2	-	n
HD 59319	$0.05^{+0.05}_{-0.05}$	$3.4^{+2.3}_{-0.4}$	$-5.76^{+0.22}_{-0.11}$	Method 1 & 2	$1.65^{+0.26}_{-0.15}$	y
PDS 134	$\leq$ 0.03	$\leq$ 3.0	≤ -5.60	Method 2	$\leq$ 1.82	y
HD 68695	$0.05^{+0.05}_{-0.05}$	$1.3^{+0.8}_{-0.1}$	$-7.78^{+0.30}_{-0.38}$	Method 2	$-0.17^{+0.34}_{-0.41}$	y
HD 72106	$0.31^{+0.05}_{-0.05}$	$7.7^{+1.4}_{-1.3}$	$-6.21^{+0.15}_{-0.18}$	Method 1 & 2	$1.20^{+0.18}_{-0.20}$	y
TYC 8581-2002-1	$0.15^{+0.05}_{-0.05}$	$4.6^{+1.2}_{-1.0}$	$-6.58^{+0.10}_{-0.13}$	Method 1 & 2	$0.88^{+0.11}_{-0.13}$	y
PDS 33	$\leq$ 0.04	$\leq$ 1.2	≤ -7.84	Method 1 & 2	≤ -0.21	y
HD 76534	$\leq$ 0.01	$\leq$ 1.7	≤ -6.95	Method 1 & 2	$\leq$ 0.77	y
PDS 281	-	-	-	-	-	-
PDS 286	$0.07^{+0.05}_{-0.05}$	$64.6^{+35.4}_{-39.6}$	$-5.41^{+0.20}_{-0.69}$	Method 1 & 2	$2.55^{+0.62}_{-0.71}$	y
PDS 297	$\leq$ 0.01	$\leq$ 0.4	≤ -7.60	Method 2	≤ -0.12	y
HD 85567	$0.55^{+0.05}_{-0.05}$	-	-	Method 1 & 2	-	n
HD 87403	$0.05^{+0.05}_{-0.05}$	$1.5^{+0.9}_{-0.2}$	$-5.82^{+0.20}_{-0.07}$	Method 2	$1.48^{+0.21}_{-0.09}$	y
PDS 37	$0.09^{+0.16}_{-0.08}$	$24.3^{+73.3}_{-15.1}$	$-4.00^{+0.61}_{-0.81}$	Method 1	$3.46^{+0.64}_{-0.83}$	y
HD 305298	$0.06^{+0.05}_{-0.05}$	-	-	Method 2	-	n
HD 94509	-	-	-	-	-	-
HD 95881	$\leq$ 0.05	$\leq$ 1.5	≤ -5.65	Method 1 & 2	$\leq$ 1.63	y
HD 96042	$0.12^{+0.05}_{-0.05}$	$94.4^{+5.6}_{-38.5}$	$-4.57^{+0.03}_{-0.28}$	Method 1 & 2	$3.18^{+0.32}_{-0.30}$	y
HD 97048	$\leq$ 0.01	$\leq$ 0.4	$-\leq -8.16$	Method 2	$\leq$ -0.55	y
HD 98922	$\leq$ 0.01	$\leq$ 0.4	≤ -6.97	Method 2	$\leq$ 0.41	y
HD 100453	$\leq$ 0.01	$\leq$ 0.1	≤ -8.31	Method 1 & 2	≤ -0.92	y
HD 100546	$0.18^{+0.05}_{-0.05}$	$6.1^{+1.6}_{-1.5}$	$-7.04^{+0.13}_{-0.15}$	Method 1 & 2	$0.56^{+0.14}_{-0.15}$	y
HD 101412	$\leq$ 0.04	$\leq$ 1.2	≤ -7.61	Method 1 & 2	≤ -0.04	y
PDS 344	$\leq$ 0.03	$\leq$ 3.5	≤ -7.02	Method 1 & 2	$\leq$ 0.68	y
HD 104237	$0.17^{+0.05}_{-0.05}$	$2.8^{+0.7}_{-0.6}$	$-6.68^{+0.15}_{-0.20}$	Method 1 & 2	$0.70^{+0.18}_{-0.22}$	y
V1028 Cen	$0.10^{+0.05}_{-0.05}$	$10.6^{+3.7}_{-3.3}$	$-5.76^{+0.16}_{-0.22}$	Method 1	$1.76^{+0.26}_{-0.24}$	y

Continued on the next page

Table 3.1 – Continued from previous page

Name	ΔD_B (mag)	f (%)	$\log(\dot{M}_{\rm acc})$ [$M_\odot$/yr]	Method(s) Used	$\log(L_{\rm acc})$ [$L_\odot$]	Achievable by MA
PDS 361S	$0.12^{+0.05}_{-0.05}$	$26.2^{+9.9}_{-7.7}$	$-5.26^{+0.17}_{-0.20}$	Method 1 & 2	$2.35^{+0.27}_{-0.23}$	y
HD 114981	$\leq$ 0.06	$\leq$ 8.1	$\leq$ -5.48	Method 1 & 2	$\leq$ 2.03	y
PDS 364	$0.28^{+0.05}_{-0.05}$	$26.8^{+8.4}_{-6.4}$	$-6.05^{+0.13}_{-0.12}$	Method 1 & 2	$1.58^{+0.13}_{-0.12}$	y
PDS 69	$0.31^{+0.05}_{-0.05}$	$62.8^{+29.8}_{-20.8}$	$-5.32^{+0.21}_{-0.21}$	Method 1 & 2	$2.28^{+0.30}_{-0.27}$	y
DG Cir	$0.79^{+0.05}_{-0.05}$	-	-	Method 1 & 2	-	n
HD 132947	$0.06^{+0.05}_{-0.05}$	$2.1^{+1.0}_{-1.0}$	$-6.71^{+0.17}_{-0.42}$	Method 1 & 2	$0.73^{+0.18}_{-0.42}$	y
HD 135344B	$0.07^{+0.05}_{-0.05}$	$0.7^{+0.3}_{-0.3}$	$-7.37^{+0.24}_{-0.41}$	Method 1 & 2	$-0.04^{+0.26}_{-0.42}$	y
HD 139614	$0.09^{+0.05}_{-0.05}$	$1.5^{+0.6}_{-0.5}$	$-7.63^{+0.20}_{-0.30}$	Method 1	$-0.10^{+0.21}_{-0.31}$	y
PDS 144S	$\leq$ 0.01	$\leq$ 0.1	$\leq$ -8.35	Method 1	$\leq$ -0.90	y
HD 141569	$0.05^{+0.05}_{-0.05}$	$1.5^{+0.9}_{-0.1}$	$-7.65^{+0.33}_{-0.47}$	Method 1	$-0.05^{+0.37}_{-0.50}$	y
HD 141926	$0.20^{+0.05}_{-0.05}$	-	-	Method 1 & 2	-	n
HD 142666	$\leq$ 0.01	$\leq$ 0.1	$\leq$ -8.38	Method 1 & 2	$\leq$ -0.93	y
HD 142527	$0.06^{+0.05}_{-0.05}$	$0.6^{+0.3}_{-0.3}$	$-7.45^{+0.19}_{-0.48}$	Method 1	$-0.09^{+0.19}_{-0.48}$	y
HD 144432	$0.07^{+0.05}_{-0.05}$	$1.0^{+0.5}_{-0.4}$	$-7.38^{+0.22}_{-0.40}$	Method 1 & 2	$0.02^{+0.24}_{-0.41}$	y
HD 144668	$0.20^{+0.05}_{-0.05}$	$3.9^{+0.9}_{-0.8}$	$-6.25^{+0.16}_{-0.19}$	Method 1 & 2	$1.10^{+0.19}_{-0.22}$	y
HD 145718	$\leq$ 0.01	$\leq$ 0.2	$\leq$ -8.51	Method 1	$\leq$ -1.01	y
PDS 415N	$\leq$ 0.04	$\leq$ 0.5	$\leq$ -8.45	Method 1 & 2	$\leq$ -0.91	y
HD 150193	$0.07^{+0.05}_{-0.05}$	$1.6^{+0.8}_{-0.7}$	$-7.45^{+0.25}_{-0.43}$	Method 2	$0.10^{+0.26}_{-0.44}$	y
AK Sco	$\leq$ 0.04	$\leq$ 0.4	$\leq$ -7.90	Method 1	$\leq$ -0.52	y
PDS 431	$0.11^{+0.05}_{-0.05}$	$4.3^{+1.5}_{-1.4}$	$-6.06^{+0.16}_{-0.22}$	Method 1 & 2	$1.34^{+0.21}_{-0.24}$	y
KK Oph	$\leq$ 0.05	$\leq$ 1.0	$\leq$ -7.84	Method 2	$\leq$ -0.29	y
HD 163296	$0.07^{+0.05}_{-0.05}$	$1.8^{+0.8}_{-0.8}$	$-7.49^{+0.14}_{-0.30}$	Method 2	$0.08^{+0.14}_{-0.30}$	y
MWC 297	$0.11^{+0.08}_{-0.08}$	$56.3^{+43.7}_{-26.5}$	$-5.16^{+0.25}_{-0.43}$	Method 1 & 2	$2.62^{+0.40}_{-0.48}$	y

A detailed description of the magnetospherically driven accretion column and shock-modelling is given by Calvet & Gullbring (1998, hereafter CG98), while a description of its application to HAeBe stars is given in Muzerolle *et al.* (2004) and Mendigutía *et al.* (2011a). Here, the key points of those papers are summarised and details of how MA can work in regards this sample:

Firstly, the magnetic field lines of the star interact with the disc and truncate it at R_i, the truncation radius. It is generally accepted that the truncation radius is close to, or inside, the co-rotation radius, R_{cor}, (Koenigl 1991; Shu *et al.* 1994, CG98). At the truncation radius material is funnelled by the field lines and falls at speeds close to free-fall towards the stellar surface; where it shocks the photosphere upon impact. The velocity of the infalling material, v_s, is given as:

$$v_s = \left(\frac{2\mathrm{G}M_\star}{R_\star}\right)^{1/2}\left(1 - \frac{R_\star}{R_i}\right)^{1/2} \tag{3.9}$$

The velocity can be related to the accretion rate via the density. This can be done by considering a slice though an accretion column, where $\dot{M}_{\mathrm{acc}}$ is a measure of rate at which material passes through it; therefore, there is a dependency on time and quantity of the matter i.e a relationship to velocity and density. As mentioned, the accretion column will cover a given area of the star. Therefore, the density can be expressed as:

$$\rho = \frac{\dot{M}_{\mathrm{acc}}}{A v_s} \tag{3.10}$$

where A is the area of the star covered by the accretion column, defined as $A = f4\pi R_\star^2$, and f is a filling factor such that $f = 0.1$ would be 10% surface coverage. The filling factor is required as we consider the accretion to be funnelled though a column, rather than being evenly distributed over the entire stellar surface. Putting this in terms of energy, the total inward flux of energy of the accretion column is:

$$\mathscr{F} = (1/2)\rho v_s^3 \tag{3.11}$$

this can be substituted into Equations 3.9 and 3.10, as this energy is carried into the column and must be re-emitted back out of the star (see CG98 for details on this energy balance). This means the total luminosity from the accretion column, as given in CG98, can be written as:

$$L_{\rm col} = (\mathscr{F} + F_*)A = \zeta\left(\frac{G\dot{M}_{\rm acc}M_\star}{R_\star}\right) + F_\star A = \zeta L_{\rm acc} + F_\star A \tag{3.12}$$

where $F_\star$ is the intrinsic flux of the stellar photosphere, $L_{\rm acc}$ is the accretion luminosity, and $\zeta = 1 - (R_\star/R_i)$. The accretion luminosity is defined as $L_{\rm acc} = G\dot{M}_{\rm acc}M_\star/R_\star$. For this work R_i is chosen to be 2.5 $R_\star$, as this has been shown to be an appropriate value which is often less than $R_{\rm cor}$ (Muzerolle *et al.* 2004; Mendigutía *et al.* 2011a). $R_{\rm cor}$ can be smaller than the adopted 2.5 $R_\star$, as can be the case for fast rotators, but this will not affect the derived accretion rate significantly e.g. for a very small R_i=1.5 $\mathrm{R}_\odot$ the resulting accretion rate would be less than a factor of two different from one where R_i =2.5 $\mathrm{R}_\odot$.

As shown in Mendigutía *et al.* (2011a), the column luminosity is $L_{\rm col} = F_{\rm col}A$, where $F_{\rm col}$ is the flux produced by the accretion column. This total amount of flux can be expressed as a blackbody function, where $F_{\rm col} = \sigma T_{\rm col}^4$. Similarly the same can be done for the photosphere, $F_* = \sigma T_*^4$. This results in $\sigma T_{\rm col}^4 = \mathscr{F} + \sigma T_\star^4$.

At this point the unknowns are f, $\mathscr{F}$, $T_{\rm col}$, and $\dot{M}_{\rm acc}$. $T_{\rm col}$ has just been shown to be governed by the amount of energy flowing onto the photosphere, $\mathscr{F}$, and by the temperature of the photosphere itself, $T_\star$. For each star $T_{\rm col}$ is determined using the temperatures derived in chapter 2. $\mathscr{F}$ is fixed to 10^{12} erg cm^{-2} Å^{-1}, as this has been shown to provide appropriate filling factors of $\leq$ 0.15 in the majority of cases in HAeBes studied so far (Muzerolle *et al.* 2004; Mendigutía *et al.* 2011a). Values less than this can be ruled out as they will not provide strong enough heating for the hotspot to be visible in a HAeBe star (Calvet &

Gullbring 1998; Muzerolle *et al.* 2004). This leaves only f and $\dot{M}_{\rm acc}$ remaining. $\dot{M}_{\rm acc}$ can be determined from ΔD_B by making use of the equations above; for which there is a unique ΔD_B vs. $\dot{M}_{\rm acc}$ combination for each star due to its stellar parameters. To obtain this curve, $\dot{M}_{\rm acc}$ values are tested between 10^{-3}–$10^{-10}{\rm M}_{\odot}{\rm yr}^{-1}$. With $\mathscr{F}$ fixed, and all the other stellar parameters known, the filling factor corresponding to each $\dot{M}_{\rm acc}$ value is found through the following equation (which is a rearrangement of the $2^{\rm nd}$ and $3^{\rm rd}$ terms in Equation 3.12):

$$f = \zeta \left(\frac{G\dot{M}_{\rm acc}M_{\star}}{R_{\star}} \right) \frac{1}{4\pi R_{\star}^{2}\mathscr{F}} \tag{3.13}$$

From this equation it is apparent how f, $\mathscr{F}$, and $\dot{M}_{\rm acc}$ are linking to each other. Therefore, a larger value than 10^{12} erg cm^{-2} Å^{-1} adopted for $\mathscr{F}$ would result in a lower filling factor, while the accretion rate would remain the same. This means that any change in $\mathscr{F}$ will not affect the accretion rate calculations, but it will instead influence the filling factors calculated. For this reason the filling factors obtained should be treated cautiously throughout. A greater $\mathscr{F}$ value has not been tested in previous theoretical models, and some of the assumptions made thus far may no longer hold and cannot be fully tested in this approach. The $T_{\rm col}$ determined previously is used to make a black-body, which represents the accretion hotspot, and multiplying this by f gives the excess flux. The excess flux is then combined with a KC-model, determined using the relevant stellar parameters. From this ΔD_B can be measured. This is repeated for all $\dot{M}_{\rm acc}$ and f combinations. The result provides a unique ΔD_B vs. $\dot{M}_{\rm acc}$ curve, which the accretion rate can be read off of.

Figure 3.6 gives the ΔD_B vs. $\dot{M}_{\rm acc}$ curves for a series of different tempera-

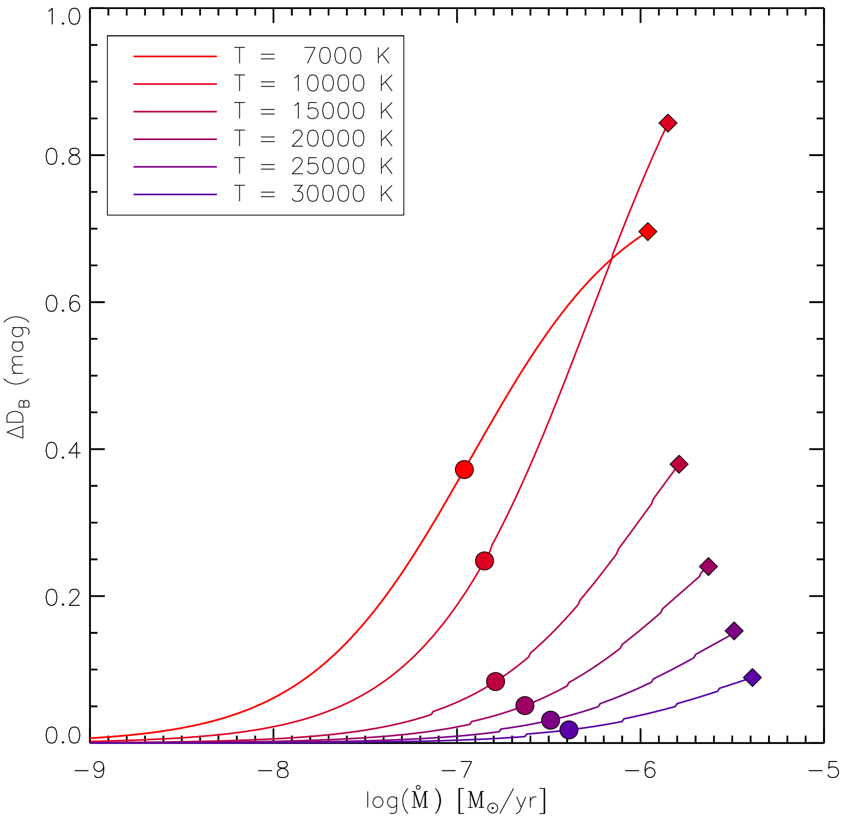

Figure 3.6: Shown here are the relationships between ΔD_B and $\dot{M}_{\rm acc}$ for a series different temperature stars (labelled in the legend). It is apparent from the plot that the same ΔD_B value would result in a higher accretion rate when measured in a hot star than in a cool star. The filled circles display the point at which f =0.1, where the accretion column covers 10% of the surface. Similarly, the filled diamonds are where f =1.0 (full coverage).

ture stars (for simplicity in the figure their other parameters are taken from the ZAMS). The figure demonstrates that the same ΔD_B, measured in two different temperature stars, can refer to differing accretion rates. Also, the T=10000 K curve is seen to reach the highest ΔD_B value, as the size of the Balmer Jump peaks at around this temperature.

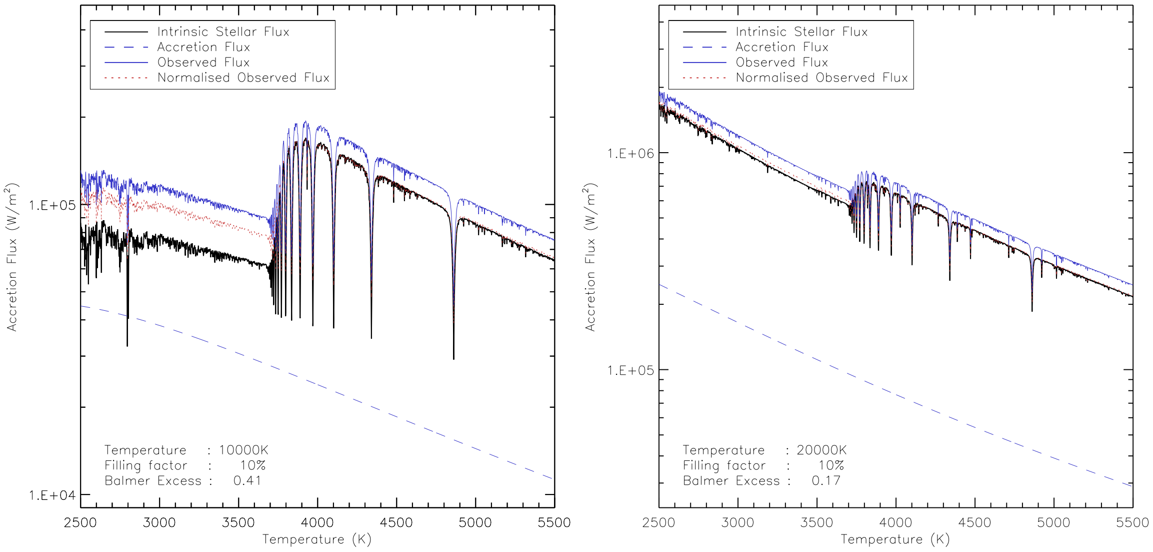

Figure 3.7: Shows KC-model atmospheres (black) for a 10000K star, on the left, and a 20000K star, on the right. In both cases $\mathscr{F}$=10^{12} erg cm^{-2} Å^{-1} and log($\dot{M}_{\rm acc}$)=-6.5. These allow the accretion flux (blue, dashed) to be calculated. Adding this flux to the intrinsic photosphere provides the observed spectra (blue, solid). Also shown is the result normalised to 4000 Å (red, dashed), in order to measure ΔD_B via method 1. The resulting ΔD_B values are given in the plot, demonstrating how they vary depending on the temperature of the star.

Figure 3.7 demonstrates the same concept, of ΔD_B vs. $\dot{M}_{\rm acc}$ changing as a function of temperature, as shown by the curves in Figure 3.6; except, this figure also highlights how the excess flux impacts the appearance of the spectra too. There are two cases in the figure, one for a star of 10000 K, and the other for a star of 20000 K. It can be seen for $\dot{M}_{\rm acc} = 10^{-6.5}\,{\rm M}_\odot\,{\rm yr}^{-1}$ that the resulting ΔD_B changes from 0.41 for the 10000 K star, to only 0.17 for the 20000 K star. This is why the calculation of separate ΔD_B vs. $\dot{M}_{\rm acc}$ curves, for each star, are crucial. It also demonstrates that the SED shape is not significantly affected by the excess longwards of 4000 Å, which means that the approach of methods 1 and 2 remain valid. Table 3.1 contains the $\dot{M}_{\rm acc}$ values calculated using an individual curve for each star.

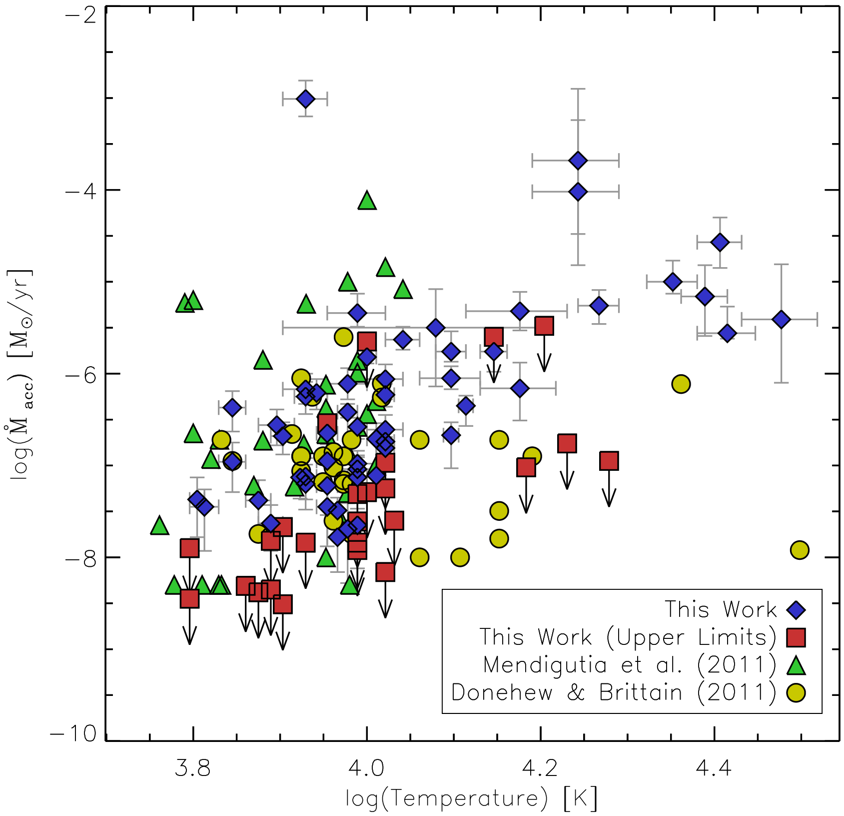

Figure 3.8: $\dot{M}_{\rm acc}$ versus $T_{\rm eff}$ is shown for each object, along with literature values for a comparison. In general it can be seen that $\dot{M}_{\rm acc}$ increases with temperature, with a scatter of 2-3 orders of magnitude in $\dot{M}_{\rm acc}$ throughout.

3.3.2 Literature Comparisons

Comparisons of $\dot{M}_{\rm acc}$ derived in this work are made against previous detections in HAeBes and CTTs. In the first comparison, Figure 3.8 places this sample against other stars from the literature in which $\dot{M}_{\rm acc}$ has also been determined directly using ΔD_B. For the HAes, ∼10000 K and lower, the range in this work appears similar to past works with $\dot{M}_{\rm acc}$ spanning from anywhere between 10^{-8}–10^{-5} M$_\odot$yr^{-1}, with the exception of one star at $\sim 10^{-3}$ M$_\odot$yr^{-1} (Z CMa, which is likely a young HBe star based on its mass of $11\,\mathrm{M_\odot}$). The HBes closest to the HAes show a similar range in magnitude of 10^{-7}–10^{-4} $\mathrm{M_\odot yr^{-1}}$. The range then decreases once the temperature has increased beyond 20000 K, where $\dot{M}_{\rm acc}$ spans 10^{-6}–10^{-4} $\mathrm{M_\odot yr^{-1}}$. This narrower range can be partially attributed to a detection effect since, as the temperature of the star increases the observable ΔD_B will decrease. Therefore, if the temperature of the star is very high then low accretion rates will be undetectable via the Balmer Excess method, as supported by the ΔD_B vs. $\log(\dot{M}_{\rm acc})$ curves in Figure 3.6. Returning to Figure 3.8, comparisons are also drawn against previously published accretion rates. The Mendigutía *et al.* (2011a) sample has a scatter mostly comparable to this work except, there are some stars in their sample which have accretion rates about an order of magnitude higher than our findings. The exact reason for the discrepancies is unknown, but it is likely to be a combination of the two different types of dataset, spectra and photometry, and the different methods of measurement used because of this i.e. the photometric method requires dereddening to be performed prior to measurement of ΔD_B. Variability also plays a role.

Comparing our results with the work of Donehew & Brittain (2011) we find a systematically higher accretion rate for objects greater than 10000 K, the HBes, of around 1–2 orders of magnitude. This can be attributed to their calculation of $\dot{M}_{\rm acc}$ from a single ΔD_B vs. $\dot{M}_{\rm acc}$ relationship for all of their objects. Whereas in this work, the relationship between the two has been calculated on an individual basis for each star, based on its stellar parameters (see Figure 3.6). Therefore, they are not directly comparable.

A comparison is also made against the literature of $\dot{M}_{\rm acc}$ vs. $M_\star$ in Figure 3.9. This comparison also looks at how the results compare to the HAeBes from

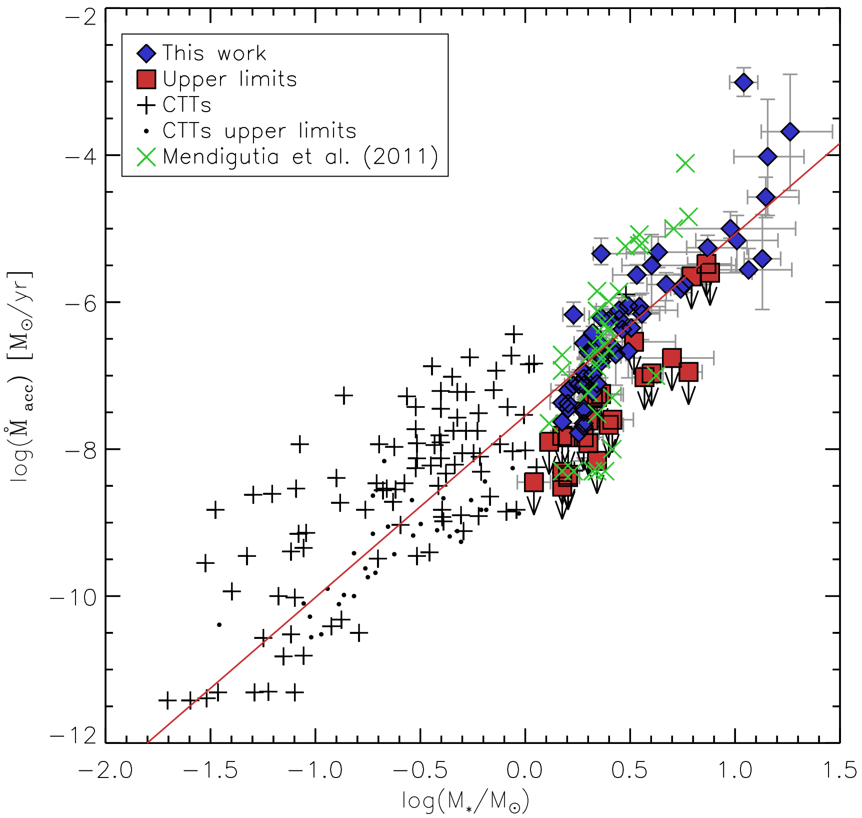

Figure 3.9: $\dot{M}_{\mathrm{acc}}$ versus $M_\star$ is shown for each star, where detected, along with additional HAeBe sources from Mendigutía *et al.* (2011a), and CTTs from Natta *et al.* (2006). A red solid line fit to all of the points, excluding upper limits, is shown of $M_\star \propto \dot{M}_{\mathrm{acc}}^{2.47\pm0.07}$.

Mendigutía *et al.* (2011a), along with a look at lower luminosity CTTs from Natta *et al.* (2006). A trend is seen of increasing accretion rate with increasing stellar mass; the fit shown in the figure gives $\dot{M}_{\mathrm{acc}} \propto M_\star^{2.47\pm0.07}$. The values for the HAeBes obtained in this work show agreement with the values obtained from Mendigutía *et al.* (2011a).

Figure 3.10 shows a similar relationship of how L_{acc} changes as a function of $L_\star$. Again, comparisons are made against HAeBes and CTTs from the literature.

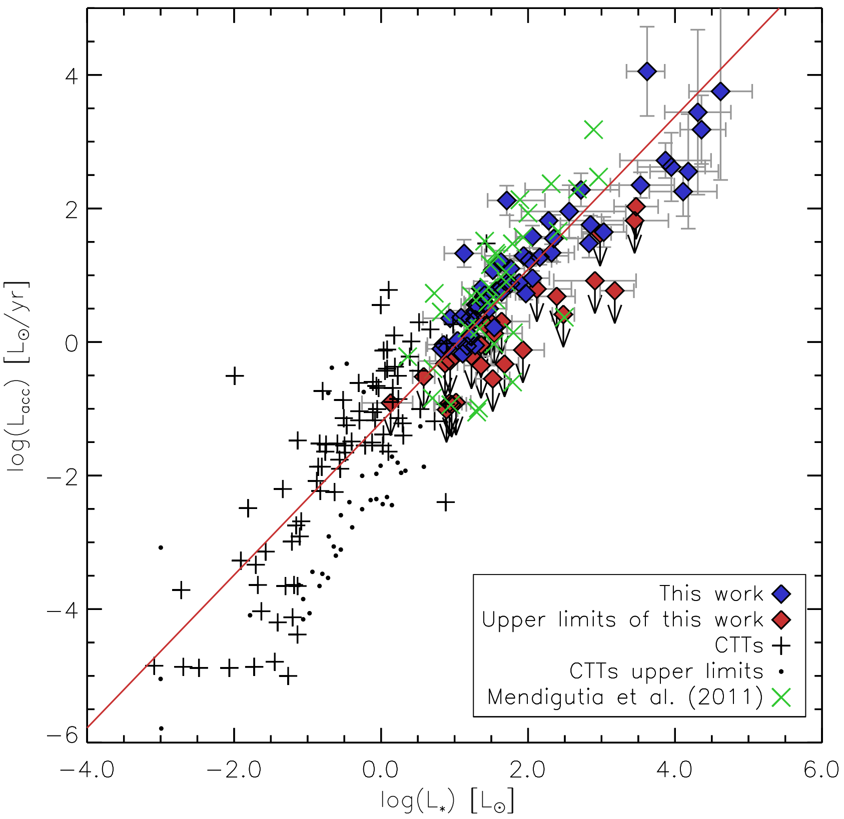

Figure 3.10: $L_{\rm acc}$ versus $L_\star$ is shown for each star in this work, along with additional HAeBe sources from Mendigutía *et al.* (2011a), and CTTs from Natta *et al.* (2006). A best fit is obtained of $L_{\rm acc} \propto \times L_\star^{1.13\pm0.03}$, which is plotted as a solid red line and excludes the upper limits.

A positive correlation between the two is also seen here of $L_{\rm acc} \propto L_\star^{1.13\pm0.03}$. This trend in the data shows a peak-to-peak variation of around 2 dex in $L_{\rm acc}$ throughout the luminosity range covered; this scatter is comparable to the scatter in $\dot{M}_{\rm acc}$ shown in Figure 3.8. These results will be discussed in detail in the following section.

In total, accretion rates, and therefore accretion luminosities, have been calculated for 81 stars in the sample. Their values are seen to agree with previous

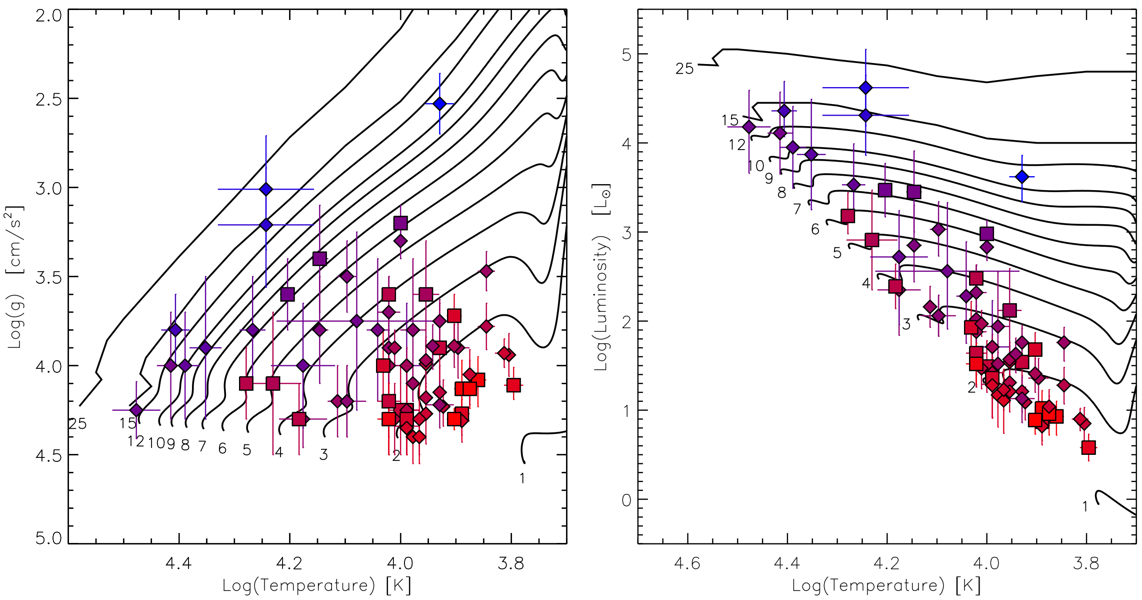

Figure 3.11: The sample is shown in both log(g) vs.log($T_{\rm eff}$, and log($L_\star$) vs. log($T_{\rm eff}$ space. In both panels the colour of the points reflect the strength of the accretion rate determined in each star; blue symbols are the strongest accretors while red ones are the weakest accretors. The squares denote objects where $\dot{M}_{\rm acc}$ is an upper limit. The PMS evolutionary mass tracks of Bressan *et al.* (2012) and Bernasconi & Maeder (1996) are also plotted as solid black lines and labelled according to mass.

literature estimates of accretion in HAeBes. The accretion rates obtained increase with both temperature and luminosity; a trend also seen in the literature for CTTs and HAeBes alike. A discussion of these results will now be presented.

3.4 Discussion

3.4.1 Overall Results

ΔD_B is clearly detected in 63 of the stars, while a further 25 stars have upper limits placed on them. The remaining 3 stars are seen to have a negative or zero

ΔD_B, the possible reasons for this in each star are now discussed. V590 Mon is found to have $\Delta D_B = 0$ within the errors, which is acceptable. PDS 281 has been listed previously as a possible evolved star (Vieira *et al.* 2003), as such it may not have any excess. HD 94509 has very narrow and deep absorption lines in its spectrum, which suggest it is a super-giant star. The KC-models used for determining log(g) is this work only go down to log(g)=2.5 for the temperature of this star, as such the stellar parameters derived earlier will not reflect the star being a possible super-giant. This super-giant nature is supported by past observations (Stephenson & Sanduleak 1971).

There are 7 objects for which the measured ΔD_B value cannot be reproduced though magnetospheric accretion shock-modelling, using the method we adopt. This is because the appropriate ΔD_B vs. $\dot{M}_{acc}$ curve calculated for each of the stars, based on its stellar parameters, cannot reach the observed ΔD_B before a 100% filling factor is achieved (see Figure 3.6 for the points at which a 100% filling factor is seen for different temperatures). Within this subset, 3 stars have a very large ΔD_B of > 0.85 (PDS 133, R Mon, and DG Cir), 3 have temperatures exceeding 20000 K (HD 141926, HD 53367, and HD 305298), while the final one, (HD 85567), lies in between these two scenarios having a strong ΔD_B value and has a mid-B spectral type. These stars are all HBes. In addition, there are 12 stars whose measured ΔD_B are modelled by filling factors of greater than 25% of the stellar surface. This is allowed, but it is an unusual occurrence under MA (Valenti *et al.* 1993; Long *et al.* 2011). This amounts to 9% of ΔD_B detections being non-reproducible though the adopted MA shock-modelling, with a further 15% having unusually high filling factors. This is a possible indication that MA may not be applicable in all HAeBes; particularly for stars with a large ΔD_B, or which have high temperatures i.e. the HBes. The remaining 76% can be fitted within the context of MA.

With accretion rates determined, the HR-diagram from Chapter 2 can be updated to show them, as is the case in Figure 3.11. The figure displays the stronger accretion rates in blue, while the weaker accretion rates are shown in red. Generally, it can be seen that the accretion rate is greater for the more massive stars. In addition, it also looks like the accretion rate decreases as the stars move closer to the main sequence for a given mass, which suggests that the accretion rate may decline with age. This shall now be explored further.

3.4.2 Age

Generally, for PMS stars, the higher the mass of the observed stars, the hotter and younger it will be (T_{eff} is roughly proportional to $M_{\star}$ for MS stars, and stars close to the ZAMS). As shown in chapter 2 there is an inverse relationship between the age and the temperature in a star; where increasing temperature results in younger ages.

The next step is to now look at age as a function of accretion rate, to see if $\dot{M}_{\mathrm{acc}}$ diminishes as the star grows older. Figure 3.12 shows how $\dot{M}_{\mathrm{acc}}$ changes with the age of a star. As the age increases the accretion rate diminishes, much like what has been seen for the temperature. A fit to the data provides a relationship of $\dot{M}_{\mathrm{acc}} \propto t^{-\eta}$, were t is the age in Myrs, and $\eta = 1.92 \pm 0.09$. The figure also shows the star split into separate mass bins too. A fit to just the HBes, where $M_{\star} > 3$ $\mathrm{M}_{\odot}$, obtains $\eta = 2.02 \pm 0.22$, which is similar to the result for all of the HAeBes. However, for the HAes alone in this work a much steeper relationship

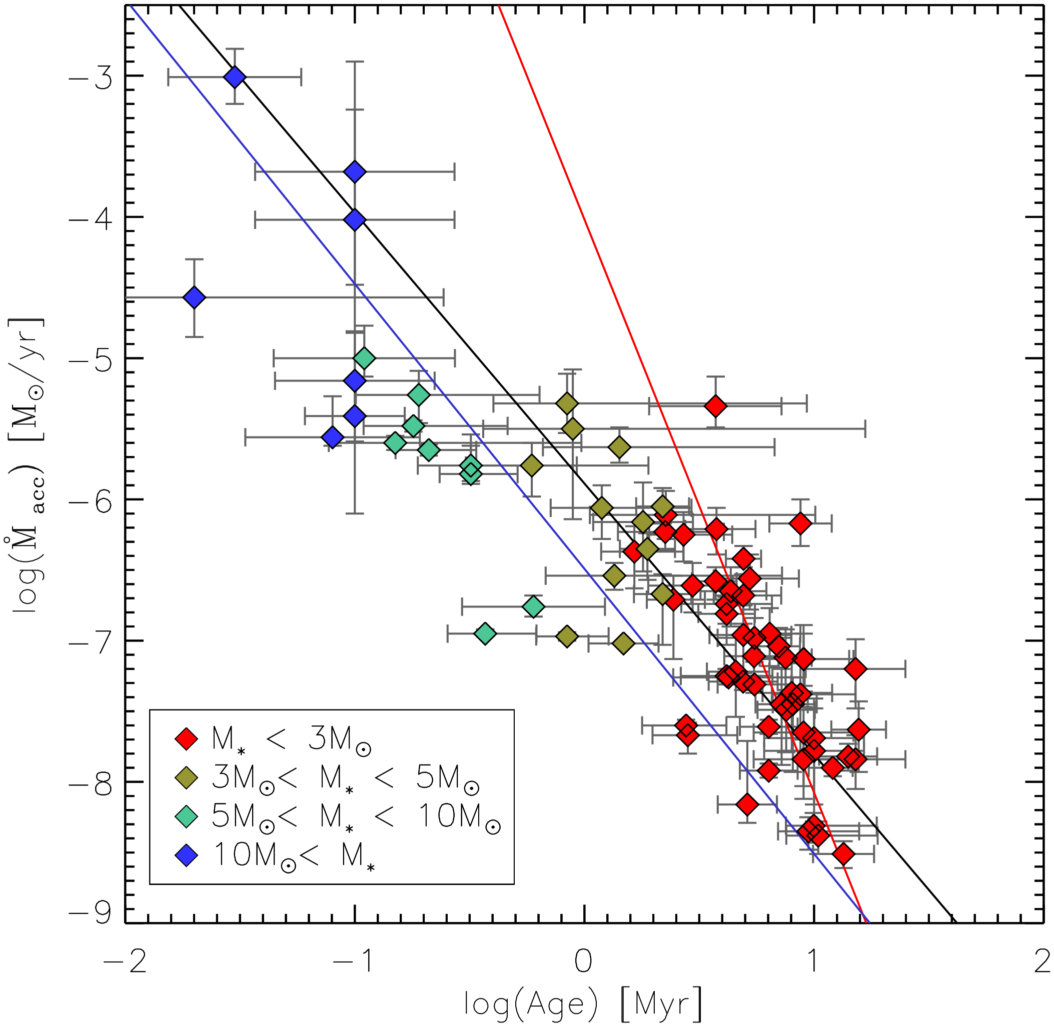

Figure 3.12: Plotted here are the derived accretion rates, from Table 3.1, against the age of the star, in a log-log plot. Various masses of stars have been colour coded and fitted in the figure. All of the HAes are shown in red (< 3 M$_\odot$), along with a fit to them of $\dot{M}_{\rm acc} \propto t^{-4.06\pm0.53}$; the HBes are all fitted with a blue line of $\dot{M}_{\rm acc} \propto t^{-2.02\pm0.22}$, while their colours correspond to the different mass bins they belong to. An overall fit to all of the HAeBes is shown in black of $\dot{M}_{\rm acc} \propto t^{-1.92\pm0.09}$.

is obtained of $\eta = 4.06 \pm 0.53$. The HAeBes as a whole here, and the separate HBe case, agree with the work of Mendigutía *et al.* (2012), where the authors obtain $\eta = 1.8$ for their HAeBe sample. For CTTs the relationship has been observed to cover a large range where $\eta = 1.5$–2.8 (Hartmann *et al.* 1998). This range encompasses the case for the HAeBes as a whole, and the HBes. However, more recent studies suggest that the relationship for CTTs is actually shallower than this of $\dot{M}_{\rm acc} \propto t^2$ (Sicilia-Aguilar *et al.* 2010; Caratti o Garatti *et al.* 2012), which suggests that there is a difference in the $\dot{M}_{\rm acc} \propto t^{-\eta}$ relationship between the CTTs and the HAeBes.

Overall, these relationships indicate that $\dot{M}_{\rm acc}$ could be an evolutionary property of HAeBes, which decreases as the star evolves; possibly accreting all of its disc material or dispersing its disc with time. Modelling of disc dispersion through photoevaporation suggests that the disc lifetimes are indeed shorter for more massive stars (Gorti & Hollenbach 2009). This offers an explanation for the steep exponent observed in the HAes, in which we could be observing the transition stage of disc dispersion as they approach the main sequence, resulting in a diminished accretion rate. The HBes, on the other hand, are younger and may not be dispersing their disc yet, which allows them to retain a more shallow relationship between $\dot{M}_{\rm acc}$ and age.

3.4.3 Accretion Rate vs. Stellar Parameters

Moving on from the age, the next natural questions are: how is $\dot{M}_{\rm acc}$ related to the stellar parameters of the star?; are they influenced by it or vice-versa? In Figure 3.13 a comparison is made between $\dot{M}_{\rm acc}$ and $T_{\rm eff}$. The scatter in

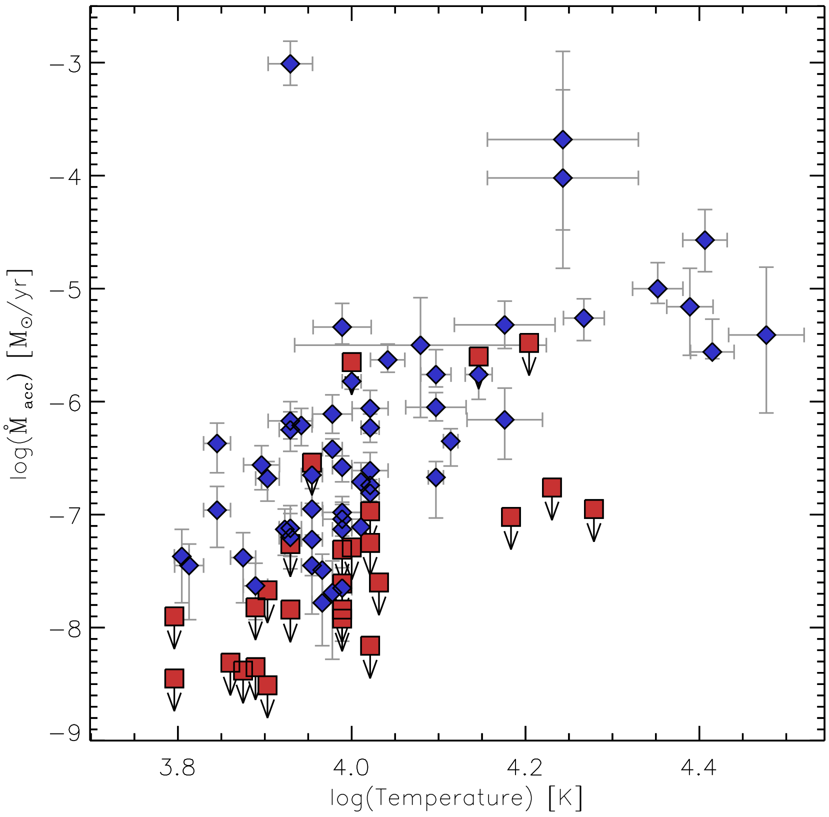

Figure 3.13: $\dot{M}_{\rm acc}$ is shown versus $T_{\rm eff}$ in a log-log plot here, where $\dot{M}_{\rm acc}$ appears to be increasing steadily with increasing temperature. The red squares denote upper limits. The outlier at $\log(\dot{M}_{\rm acc}) = -3.0$ and $\log(T_{\rm eff}) = 3.95$ is Z CMa.

$\dot{M}_{\rm acc}$ remains constant at about 2 orders of a magnitude. There is one object, Z CMa, which can be seen as an outlier from the general scatter. This star is cool, 8500 K, very massive, $M_\star = 11$ M$_\odot$, and has a very large Balmer Excess, $\Delta D_B = 1.05$. Its placement on the HR-diagram and PMS tracks puts it at a very early stage of evolution, in which it appears to be able to accrete at great rates of $\approx 10^{-3}\,{\rm M}_\odot\,{\rm yr}^{-1}$. The overall trend is that $\dot{M}_{\rm acc}$ increases steadily with temperature; the temperature of a star is generally proportional to its mass

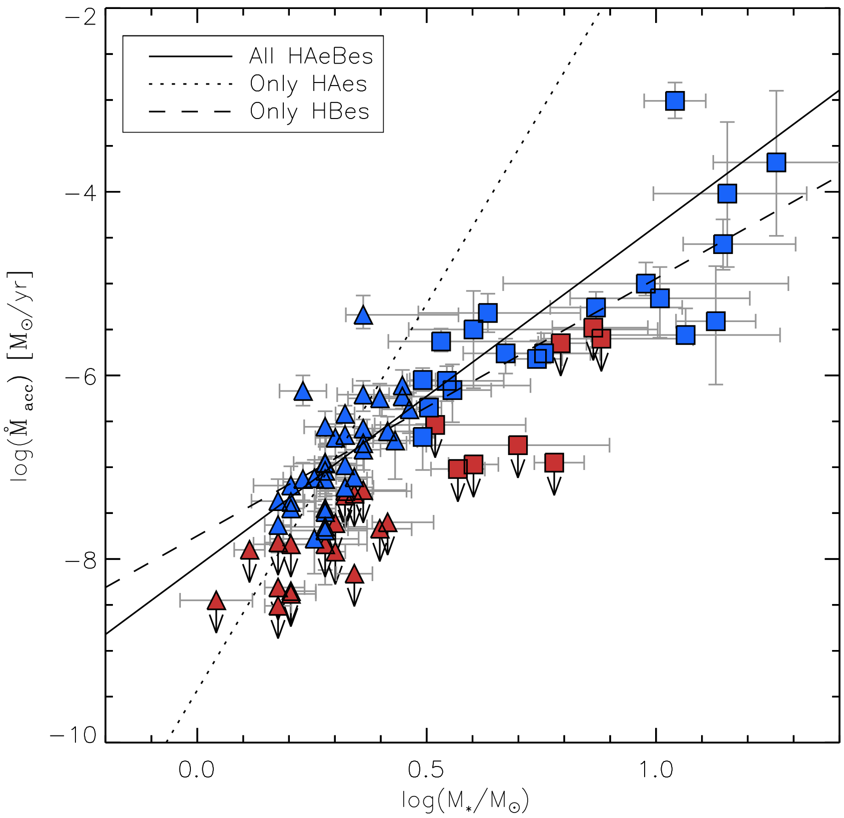

Figure 3.14: $\dot{M}_{\mathrm{acc}}$ versus $M_\star$ is plotted here, for all stars in which $\dot{M}_{\mathrm{acc}}$ could be determined. The stars are split into HAes (as triangles, where $M_\star < 3$ M$_\odot$) and HBes (as squares where $M_\star > 3$ M$_\odot$). Upper limits are denoted as the points in red with downward arrows from them. Separate fits are made to the HAes, HBes, and the group as a whole of the form $\dot{M}_{\mathrm{acc}} \propto M_\star^a$, where a is found to be 8.33 ± 1.34, 2.67 ± 0.34, and 3.48 ± 0.24, respectively . A discussion of the fits is provided in the text.

leading to the next relationship.

Figure 3.14 compares the $\log(\dot{M}_{\mathrm{acc}})$ vs. $\log(M_\star)$ relationship, along with a series of fits to the data. In the figure the stars are split into two groups, the HAes and the HBes, which comprise 60% and 40% respectively of the total sample (the split between the two regimes is made at 3 M$_\odot$). A best fit to the

HAes is made of $\dot{M}_{\rm acc} \propto M_\star^{8.42\pm1.37}$, while for the HBes a shallower relationship of $\dot{M}_{\rm acc} \propto M_\star^{2.82\pm0.39}$ is seen. An overall fit to the HAeBes is obtained of $\dot{M}_{\rm acc} \propto M_\star^{3.62\pm0.26}$, which lies between the HAe and HBe regime, and favours the HBe case, which covers a greater mass distribution. When considering the HAeBes as a whole, the relationship found between $\dot{M}_{\rm acc}$ and $M_\star$ has a larger exponent, ~1.5 greater, than in low mass PMS stars, where $\dot{M}_{\rm acc} \propto M_\star^{2.0\pm0.2}$ (Muzerolle *et al.* 2005; Natta *et al.* 2006). The trend we observe of a steeper relationship between accretion rate and stellar mass, over CTTs, agrees with the past findings of Mendigutía *et al.* (2011a), who obtained a relationship of $\dot{M}_{\rm acc} \propto M_\star^{4.6-5.2}$. Although, our findings for the HAeBes as a whole are about an order of magnitude shallower than Mendigutía *et al.* (2011a), this could be attributed to our sample containing more Herbig Be stars. Overall, it is apparent that HAeBes have higher accretion rates and a steeper relationship to $M_\star$ than CTTs. This could be due to HAeBes being younger stars, which are in earlier stages of accretion. The different relationships observed between HAes and HBes, could be due to the HAes crossing into a transitional disc phase, in which accretion rates may be lower (see the discussion above in Section 3.4.2). This is also possible due to the HAes having a longer stage of evolution compared to HBes.

Alternatively, luminosities can be compared against each other instead of masses; Figure 3.15 shows the luminosity plot of $\log(L_{\rm acc}/{\rm L}_\odot)$ vs. $\log(L_\star/{\rm L}_\odot)$. A best fit to all the HAeBes is found of $L_{\rm acc} \propto L_\star^{1.07\pm0.06}$. This fit is in agreement with the work of Mendigutía *et al.* (2011a), where these authors also found a shallower relationship for HAeBes of $L_{\rm acc} \propto L_\star^{1.2}$. As in the previous comparisons presented, when looking at the masses, the HAes and HBes are divided into two

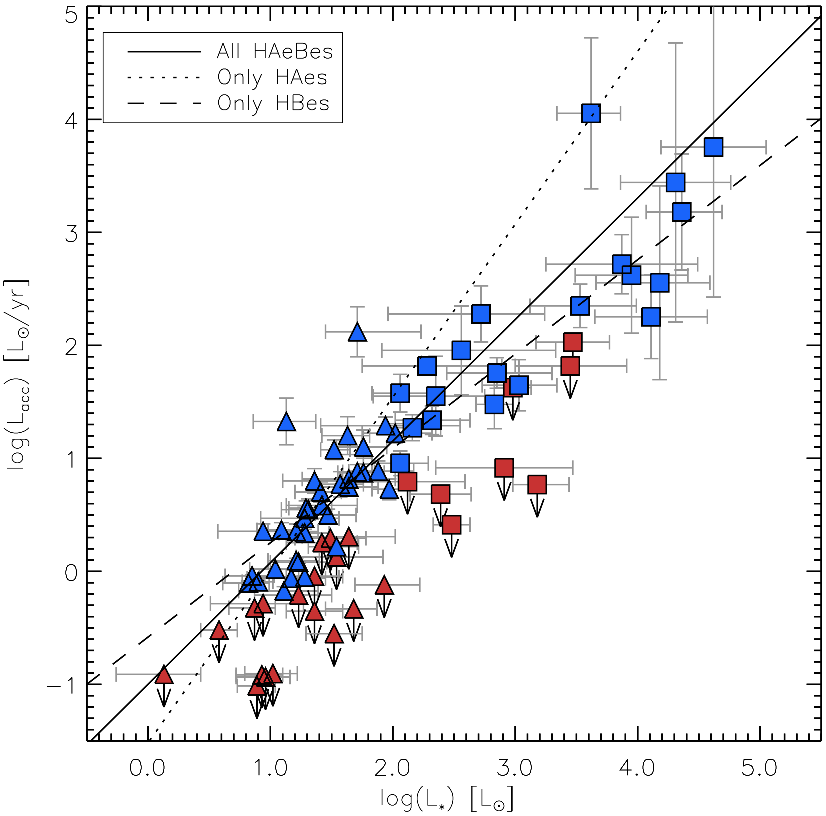

Figure 3.15: $L_{\rm acc}$ versus $L_\star$ is plotted here, for all stars in which $\dot{M}_{\rm acc}$ could be determined. The stars are split into HAes (as triangles, where $M_\star < 3$ M$_\odot$) and HBes (as squares where $M_\star > 3$ M$_\odot$). Upper limits are denoted as the points in red with downward arrows from them. Separate fits are made to the HAes, HBes, and the group as a whole of the form $L_{\rm acc} \propto L_\star^a$, where a is found to be 1.53 ± 0.14, 0.81 ± 0.12, and 1.07 ± 0.06, respectively . A discussion of the fits is provided in the text.

groups in the figure. A best fit to the HAes is obtained of $L_{\rm acc} \propto L_\star^{1.53\pm0.14}$, which agrees with the trends seen in CTTs of $L_{\rm acc} \propto L_\star^{1.5}$ (Natta *et al.* 2006; Tilling *et al.* 2008). The HBes, on the other hand, show a much shallower relationship of $L_{\rm acc} \propto L_\star^{0.84\pm0.13}$, this is turn shifts the weighting when looking at the HAeBes as a whole. The data is suggestive of $L_{\rm acc}$ being tightly correlated with $L_\star$, but the exact relationship changes in exponent as the stars cross into the HBe regime.

3.5 Conclusions

To conclude this chapter, work is presented of the largest spectroscopic survey into accretion rates in HAeBes to date, where the following results were found:

- A UV-excess is clearly detected in 63 stars of the sample, with upper limits placed on a further 25 stars. $\dot{M}_{\rm acc}$ is determined for these stars through modelling within the context of magnetospheric accretion. However, 7 of the ΔD_B detections cannot be reproduced in the context of magnetospheric accretion. These 7 stars are all HBe stars, often with very large ΔD_B values of > 0.85, or high temperatures exceeding 20000 K. This suggests a possible breakdown in the disc-accretion regime in HBes, particularly for early-type HBes.

- A clear trend is observed of $\dot{M}_{\rm acc}$ increasing as a function of stellar mass. The relationship obtained is a power law of the form: $\dot{M}_{\rm acc} \propto M_\star^{3.62\pm0.26}$. This is a steeper law than previously observed in CTTs, which is only $M_\star \propto \dot{M}_{\rm acc}^2$. We interpret this increased exponent, in the relationship between $\dot{M}_{\rm acc}$ and $M_\star$, for HAeBes as a possible combination of them being younger and therefore more active in formation than older CTTs. Deviations are seen between the HAes, where $\dot{M}_{\rm acc} \propto M_\star^{8.42\pm1.37}$, and the HBes, where $\dot{M}_{\rm acc} \propto M_\star^{2.82\pm0.39}$. An explanation could be that some of the HAes are crossing into a transitional disc phase, in which accretion rates may be lower for some of the stars.

- There is also a trend between the accretion luminosity and the stellar luminosity, which is found to be $L_{\text{acc}} \propto L_\star^{1.07\pm0.06}$ for the sample. This is lower than found in CTTs where $L_{\text{acc}} \propto L_\star^{1.5}$ (Natta *et al.* 2006; Tilling *et al.* 2008). However, for a subset of the HAes, the relationship is much closer to the CTTs case, we observe $L_{\text{acc}} \propto L_\star^{1.53\pm0.14}$. In contrast a shallower relation of $L_{\text{acc}} \propto L_\star^{0.84\pm0.13}$ is seen in the HBes. This demonstrates that the stellar luminosity of a star appears to be a good indicator of the accretion luminosity for a huge range of stellar luminosities, upto the HAe mass range, but there may be deviations in the HBe mass range.

- A final trend is seen in HAeBes between the age of the star and $\dot{M}_{\text{acc}}$, where the accretion rate decreases with increasing age of the form $\dot{M}_{\text{acc}} \propto t^{-\eta}$, with $\eta = 1.92 \pm 0.09$. This implies that the accretion rate decreases as stars approach the main sequence. The result is affected by the most massive stars, with the higher accretion rates, only being observable at young ages due to their quicker evolution. Similarly, the less massive stars have a longer PMS lifetime which could allow their accretion rate to diminish within this time; this could explain the change in the relationship for the HAes where $\eta = 4.06 \pm 0.53$. This suggests that $\dot{M}_{\text{acc}}$ decreases quicker for older HAeBe stars, perhaps as a consequence of disc dissipation. Overall, the younger objects are indeed accreting at a faster rate, while the rate diminishes with the age of the star.

The above points have led to three main findings. Firstly, the HAeBes display relationships in accretion which are similar but different to CTTs. $\dot{M}_{\text{acc}}$ is observed to have a steeper relationship with $M_\star$ than seen in CTTs, while L_{acc}

shows a shallower relationship with $L_\star$ than the CTTs case. Secondly, there are also notable differences within the HAeBe group; when separating the HAes and HBes. Most notably, the HAes display a much steeper relationship in $\dot{M}_{\rm acc}$ when related to both age and $M_\star$. In both cases the steepness of the relationship is approximately double that seen in HBes. Although, the HAes also display a $L_{\rm acc}$ relationship to $L_\star$ which is comparable to CTTs. The third, and final, finding is that multiple early-type HBes, and stars with an observable ΔD_B of > 0.85, cannot be modelled successfully though magnetospheric accretion. This suggests that there is a possible change in accretion mechanisms in these stars which requires further investigation. To further these findings, the next steps are to look at emission lines which are known tracers of accretion in CTTs and test their applicability in HAeBes. This will be presented in Chapter 4.

Chapter 4

Emission Lines as Accretion Diagnostics in Herbig Ae/Be Stars

4.1 Introduction

By their very nature, the Herbig Ae/Be stars are Pre-Main Sequence (PMS) and contain emission lines. Many of these lines are seen to be in common with those seen in Classical T Tauri stars (CTTs), which could mean that the origin of these lines is shared between the two classes of stars. It is not just the presence of common lines which is of interest, but specifically their luminosities and their profiles.

CTTs are thought to accrete via magnetospheric accretion (MA). In this scenario the disc is truncated by magnetic field lines, which also funnel the disc material onto the star via an accretion column. It has been shown that the accretion luminosity, derived from a UV-excess or line veiling, is correlated with the luminosities of the emission lines; this appears true for a large number of lines, such as Brγ, Hα, [O I]$_{\lambda 6300}$, and the Ca II IR-triplet (Muzerolle *et al.* 1998c; Calvet *et al.* 2004; Dahm 2008; Herczeg & Hillenbrand 2008; Rigliaco *et al.* 2012).

The various profiles of the spectral lines can also reveal details about the motions of the gas and the geometries of the emitting regions. One of the more simple profiles is that which contains the double peaked lines in emission, which are often signs of a rotating disc (e.g. Acke *et al.* 2005; Acke & van den Ancker 2006; Bagnoli *et al.* 2010). More complex lines like P-Cygni profiles have also been observed in CTTs and HAeBes, which are indicative of material outflowing from the star, such as in stellar winds (Finkenzeller & Mundt 1984), disc winds (Hartigan *et al.* 1995; Rigliaco *et al.* 2013), or even jets (Ellerbroek *et al.* 2011). The opposite of this is the inverse P-Cygni profile which represents infalling material (Hartmann *et al.* 1994) i.e. from material in an accretion column accreting onto the star (Calvet & Gullbring 1998; Muzerolle *et al.* 1998a). These in-fall signatures have been observed in CTTs and are consistent with their origin being from an accretion column, under the influence of MA (Muzerolle *et al.* 1998a; Edwards *et al.* 2006; Kurosawa *et al.* 2011)

To date, a few of the luminosity relationships for CTTs have been shown to also hold for HAeBes, with minor changes in coefficients (Mendigutía *et al.* 2011a). However, some authors suggest that the relationships may be breaking down towards the Herbig Be regime (see the Brγ relationship of Donehew & Brittain (2011)). Indeed, other works using spectropolarimetric observations also suggest that changes in the accretion mechanism may be taking place towards the early-Be stars (Vink *et al.* 2002, 2005). Therefore, it is critical to test a large number of known, and potential, accretion diagnostic lines for a large sample of HAeBe stars. These relationships allow the determination of accretion rates in stars where direct methods of measuring $\dot{M}_{\rm acc}$ cannot be used. In particular it is more difficult to obtain UV measurements than emission line measurements; emission lines can be measured at a variety of different wavelengths too. Therefore, these relationships open up possibilities for determining accretion rates with a limited set of data at a variety of wavelengths.

I present in this chapter the measurement of numerous emission lines across the entire sample of 91 HAeBes. The profiles and strengths of the lines are investigated, along with a determination of line luminosities using the stellar parameters determined in Chapter 2. These are then compared against the accretion rates determined in Chapter 3 in order to provide a critical assessment of the accretion luminosity versus line luminosity relationships in regards to HAeBes.

This Chapter is broken down as follows. Section 4.2 provides details on the sample and reduction of the data relevant to emission line measurements. Section 4.3 provides the methodology of measuring the lines and how determinations of line luminosities are made. Section 4.4 presents the data on the lines which have well established relationships between $L_{\rm acc}$ and $L_{\rm line}$ in CTTS; this section is broken down into subsections discussing each line. Section 4.5 analyses the less well established accretion tracing lines, along with some lines which are proposed as new diagnostics of accretion. Section 4.6 provides the discussion of the results. Section 4.7 provides the concluding remarks.

4.2 Observations and Data Reduction

Details on the sample selection and basic data reduction is contained in Section 2.2 of Chapter 2. Following on from that chapter knowledge has been gained of the stellar parameters. The sample contains 91 stars in total, out of these, 37 stars have a mass greater than $3\,\mathrm{M}_{\odot}$; the Herbig Be stars. The remaining stars are all HAes, with perhaps a few intermediate mass CTTs which straddle the mass boundary. This study provides the largest spectroscopic investigation into accretion of HAeBes to date. In additional, the spectral wavelength range covered in there stars is vastly superior to any other HAeBe investigation. The combination of these two allows the most robust statistical investigation into the emission lines in HAeBes to be performed to date, with numerous emission lines analysed contemporaneously against a direct tracer of accretion.

The range of accretion rates calculated in the previous chapter spans about 5 orders of magnitude from $\dot{M}_{\mathrm{acc}}= 10^{-8} - 10^{-3}\,\mathrm{M}_{\odot}\,\mathrm{yr}^{-1}$. This provides a range in accretion luminosities which spans a magnitude range of $L_{\mathrm{acc}}= 10^{-1.0} - 10^{-4.0}\,\mathrm{L}_{\odot}$. Such large ranges create good coverage in correlation studies involving L_{acc}, which is the main intention of this work. This will be done using the line luminosities, L_{line}.

One detail of data reduction which has not been mentioned in previous chapters is the removal of telluric line features. Telluric absorption features are present around the majority of the observable emission lines in the NIR, and also for a few cases in the VIS arm. Their removal is required in these regions in order to obtain accurate measurements of the line strengths. Normally a telluric standard star is used for correction, but these stars contain their own spectral features, which need

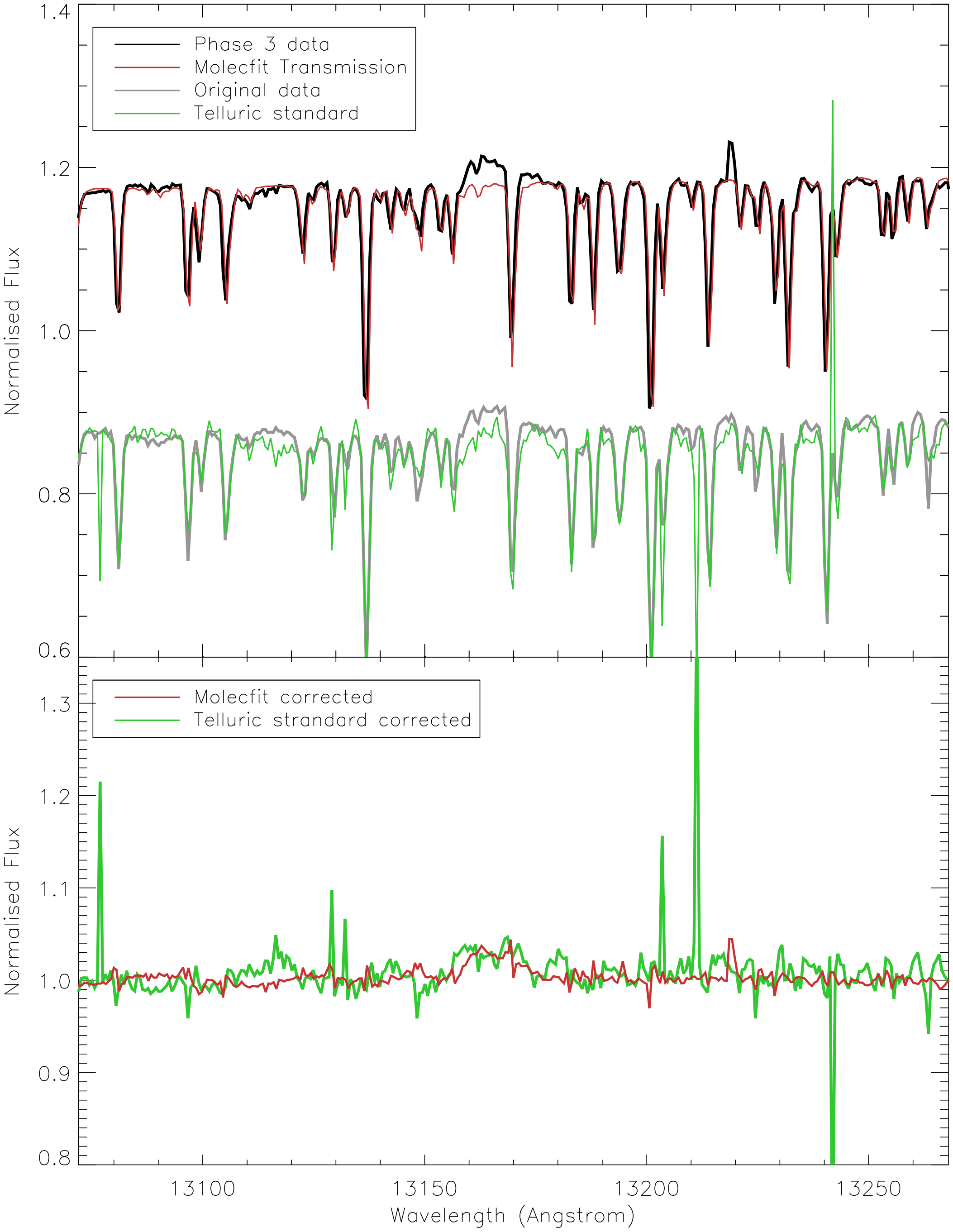

Figure 4.1: The top panel shows a portion of spectra for two data sets and the two methods of correcting, via either molecfit or the telluric standard. The bottom panel displays a comparison between the two methods of reduction. In this case it appear molecfit provides the better reduction.

to be accounted for. Therefore, correction is performed using the ESO Molecfit[1] telluric removal tool. This software provides an atmosphere transmission spectrum of the sky based upon the observatory conditions and the spectra observed. Tests are performed to see if this method of reduction is an improvement over using a telluric standard in Figure 4.1. In this figure two sets of data are shown. One set is from the initially observed spectra, which have been used in the previous chapters. The other is the "phase 3" data product, which is the same spectra but it has been reduced using a more recent version of the X-Shooter pipeline, and this has been done automatically by ESO. Comparisons between the two data sets shown that the phase 3 data has a slightly better SNR in the NIR arm, so it shall be used instead of the previous data where possible (a handful of objects are not available in the phase 3 data). The other two spectra plotted in the figure are the molecfit transmission and the telluric standard star spectrum, which are used with the phase 3 data and the original data respectively. The bottom panel shows the results of the correction; molecfit provides the better reduction. It should be noted that in the majority of cases the results are of comparable quality. Molecfit provides a better correction if the telluric SNR is low, and also when the target spectrum has a low SNR. Overall, the differences are minor and both approaches are suitable for equivalent width measurements. Since Molecfit shows a slight improvement over a standard telluric correction, it is performed on all spectral orders in each arm that contains telluric line features, and the results are used throughout the remainder of this chapter.

---

[1] http://www.eso.org/sci/software/pipelines/skytools/molecfit

4.3 Line Measurements

The observed strength of each emission line is recorded through the measurement of the equivalent width:

$$\mathrm{EW}_{\mathrm{obs}} = \int_a^b \frac{I_c - I_\lambda}{I_c}\mathrm{d}\lambda \tag{4.1}$$

Where a and b are the respective blue and red wavelength points which are summed over, I_λ is the intensity of the line at a particular wavelength, and I_c is the continuum intensity. In this work the choice is made to normalise the line such that the continuum level is at unity. This procedure is performed by selecting two continuum regions, one either side of the line. A best-fit is made to these regions using a straight line fit. The fit is applied to the observed spectra by dividing the spectra though by it; this results in the normalised spectra, where the continuum regions are now at unity as desired. $\mathrm{EW}_{\mathrm{obs}}$ is then calculated using Equation 4.1, with a and b chosen depending upon the width of the line. An emission line will produce a negative $\mathrm{EW}_{\mathrm{obs}}$, as it is above the continuum, while an absorption line will produce a positive $\mathrm{EW}_{\mathrm{obs}}$.

For the majority of the observable emission lines there will be a contribution to the observed spectrum from the underlying intrinsic absorption of the line, which is due to the star's photosphere. Figure 4.2 provides some example $\mathrm{EW}_{\mathrm{int}}$ values for some of the lines that will be measured as a function of temperature. It is apparent from the figure that $\mathrm{EW}_{\mathrm{int}}$ will be different for each star. $\mathrm{EW}_{\mathrm{obs}}$ is a combination of this intrinsic absorption from and true circumstellar emission, hence the true emission is actually stronger than $\mathrm{EW}_{\mathrm{cor}}$ would imply. A correction must be made for the intrinsic absorption. To obtain the corrected equivalent width, $\mathrm{EW}_{\mathrm{cor}}$, the intrinsic equivalent width, $\mathrm{EW}_{\mathrm{int}}$, must be subtracted from

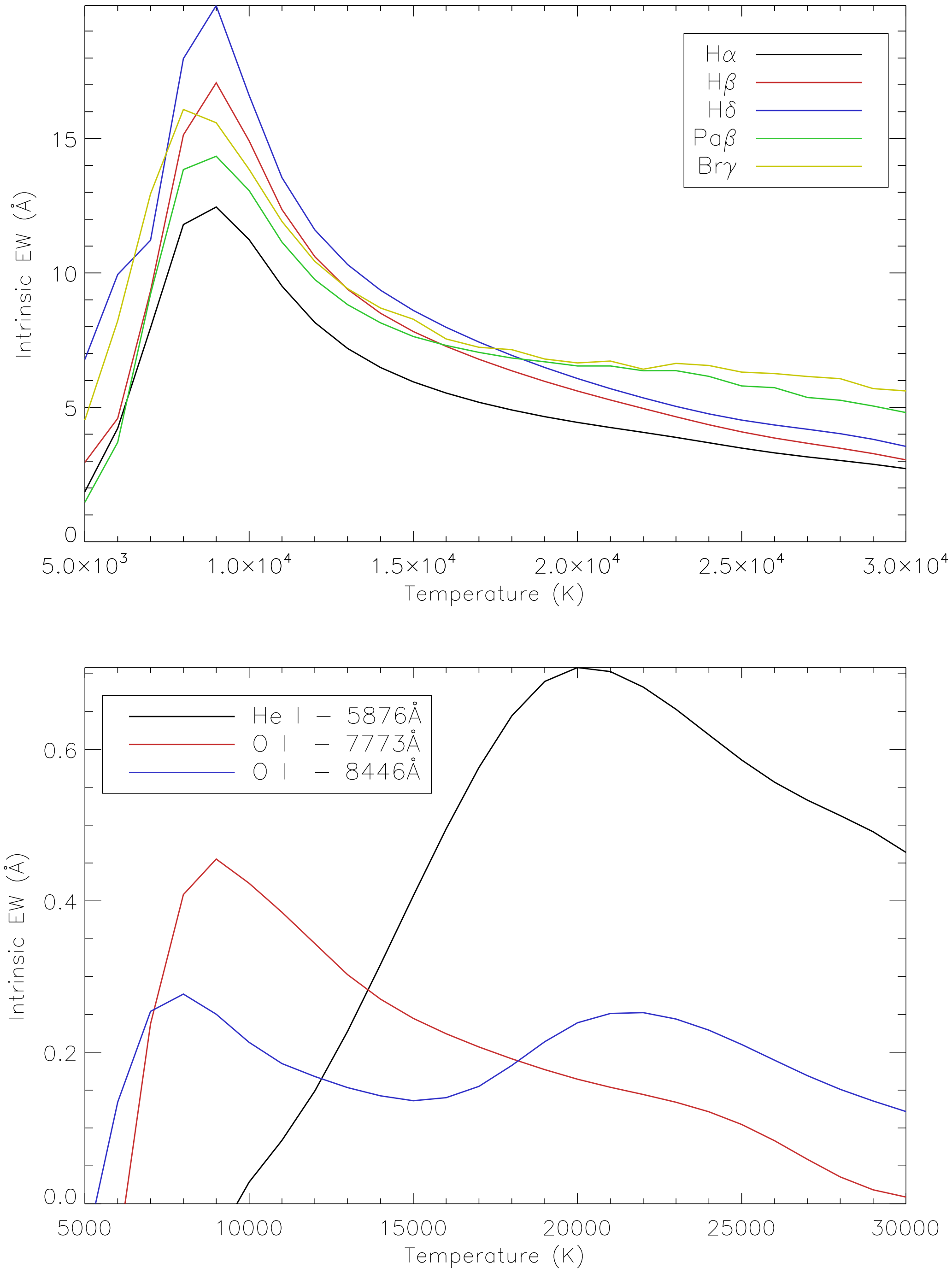

Figure 4.2: This figures displays the expected EW_{int} as a function of temperature. The top panel displays five different hydrogen lines, which can be seen to peak in absorption at $\sim 10000\,K$. The bottom panel shows three other lines which have much weaker EW_{int} values. The plot demonstrates that He I requires greater temperatures than the hydrogen lines to be excited, as its absorption peaks at $\sim 20000\,K$.

the observed:

$$\mathrm{EW_{cor}} = \mathrm{EW_{obs}} - \mathrm{EW_{int}} \tag{4.2}$$

The intrinsic strength of the line depends upon the temperature, surface gravity, and metallicity of the star in question (in all cases solar metallicity is adopted). The temperature and surface gravity of each star, which were determined in Chapter 2, are used to select an appropriate spectral model atmosphere. In this work the Munari set of Kurucz-Castelli models, KC-models, are used for lines with $\lambda < 10050\,\text{Å}$, due to their $1\,\text{Å}$ sampling (Munari *et al.* 2005). For longer wavelengths additional models are required; the older KC-models are used here (Kurucz 1993; Castelli & Kurucz 2004). For consistency, the same region of measurement used for $\mathrm{EW_{obs}}$ is used for measuring $\mathrm{EW_{int}}$. There are some lines in which no intrinsic absorption is present i.e. forbidden line transitions, and very high excitation lines. For these particular lines $\mathrm{EW_{cor}}$ is simply equal to $\mathrm{EW_{obs}}$.

These corrections are suitable for all lines which have a central wavelength of less than one micron. For wavelengths greater than this an additional correction needs to be made for the IR-excess of the star (if present). This is because the IR-excess is seen on top of the intrinsic absorption line and its continuum, modifying the continuum level, and effectively veiling the intrinsic absorption. This means that the subtraction of $\mathrm{EW_{int}}$ is no longer as straight-forward as in Equation 4.2. Instead, the following modification must be made:

$$\mathrm{EW_{cor}} = \mathrm{EW_{obs}} \times 10^{-0.4\Delta m_\lambda}\mathrm{EW_{int}} \tag{4.3}$$

where Δm_λ is the magnitude difference at a given wavelength between the observed, dereddened IR-magnitude and the intrinsic magnitude of a star of the same spectral type (the wavelength will be the wavelength of the line in question). The intrinsic magnitude is obtained by scaling a KC-model of the same stellar parameters to match the dereddened visible photometry of the star (scaling by distance to the star also works), and measuring the flux from the model at the wavelength in question. This is then converted into a magnitude. However, caution must be taken here as the models also have absorption lines present (after all, these were used to obtain $\mathrm{EW_{int}}$). So, to avoid making an underestimation in the flux, an interpolation of the continuum regions either side of the line is used to obtain the flux at the required wavelength. This is then converted into a magnitude to give the expected intrinsic magnitude. However, the observed magnitude at the wavelength in question is also required. This is obtained using photometry as the spectra is not flux calibrated, and contains many emission and absorption features at these wavelengths. The JHK photometry from 2MASS is used for this (Cutri *et al.* 2003; Skrutskie *et al.* 2006). The photometry is dereddened and converted into a flux by using the A_V values determined in Chapter 2. An interpolation is then made between the two photometric bands either side of the line centre to get the exact flux at the desired wavelength point. This is then converted into a magnitude to give the observed magnitude at the chosen wavelength. With both the observed and expected intrinsic magnitudes obtained, Δm_λ is found via the difference, meaning that $\mathrm{EW_{cor}}$ can now be calculated.

A consideration of errors needs to be made in all the above steps. The largest contribution to the errors is from the SNR of the spectra, as this affects the detection of the line and judgement of the continuum placement when measuring i.e. the fitting of the continuum regions. Since EW is a numerical calculation over a wavelength region, the error will be the extent of this region divided by the

SNR summed over: $\sigma_{\rm EWobs} = \Delta\lambda/{\rm SNR}$, where $\Delta\lambda$ is the wavelength region over which $\rm EW_{obs}$ is measured (i.e. a to b in Equation 4.1). However, the error on $\rm EW_{int}$ is also complicated by stellar parameters, metallicity, and the adopted set of models. For this reason a generous error of 10% is adopted for all $\rm EW_{int}$ which are calculated from the Munari set of KC-Models; an error of 20% is adopted for the NIR lines which are calculated from the lower resolution models. Errors in Δm_λ are low, due to the quality of the JHK photometry, and the relatively low errors in the stellar parameters (see Chapter 2). For this reason only the $\rm EW_{obs}$ and $\rm EW_{int}$ errors are considered in $\rm EW_{cor}$. With $\rm EW_{cor}$ established, a line flux, $F_{\rm line}$, can now be calculated by $F_{\rm line} = {\rm EW_{cor}} \times F_\lambda$, where F_λ is the continuum flux corresponding to the central wavelength of the line. For all lines with line centres $< 1\,\mu$m, F_λ is calculated from a KC-model in the same way the intrinsic magnitude was calculated earlier (except without the final magnitude conversion). For the lines with line centres $> 1\,\mu$m, an interpolation of the dereddened JHK photometry is performed in the same manner as was done for obtaining the IR-excess magnitude earlier, except a further step is required of converting this into a flux.

Expanding upon this, a line luminosity, $L_{\rm line}$, can also be calculated through use of the distance to the star: $L_{\rm line} = 4\pi D^2 F_{\rm line}$. The distance values adopted here are taken from Chapter 2. The $L_{\rm line}$ value takes into account both the error on the distance and the errors in the stellar parameters used to calculate $F_{\rm line}$. In total, $\rm EW_{obs}$, $\rm EW_{int}$, and $\rm EW_{cor}$ are calculated for a selected set of 32 different lines in the spectra. The lines were selected based on a combination of being observed previously in the literature, or the line has a high detection rate throughout the sample (preferably both).

4.4 Analysis of Established Accretion Tracers

Emission lines contain a wealth of information about a star and its environment. The line profiles alone can help disentangle in-falling and out-flowing material, and possibly the presence of a disc. In addition, the strengths of the line can provide information on how much energy is imparted due to processes such as accretion or heating.

To date many different lines have been used as proxies for measuring the accretion rate. Some of the most frequently used lines in the literature are: Hα, Paβ, Brγ, and [O I]$_{\lambda 6300}$. This is because the luminosity of these lines has been shown to correlate with the accretion luminosity, $L_{\rm acc}$ (Muzerolle *et al.* 1998c; Calvet *et al.* 2004; Dahm 2008; Herczeg & Hillenbrand 2008; Mendigutía *et al.* 2011a; Rigliaco *et al.* 2012). These relationships take the form of a power law where:

$$\log\left(\frac{L_{\rm acc}}{{\rm L}_\odot}\right) = A + B \times \log\left(\frac{L_{\rm line}}{{\rm L}_\odot}\right) \tag{4.4}$$

Such a relationship provides a useful tool for easily determining accretion luminosities in stars where it cannot normally be measured i.e. hot stars in which low accretion rates cannot be easily detected by a UV-excess. With knowledge of the stellar parameters, $L_{\rm acc}$ can then be converted into an accretion rate. The $L_{\rm acc}$ adopted and used throughout the rest of this chapter are obtained from the UV-excess measurements in Chapter 3.

Due to their frequent use and demonstrated relationship to accretion in CTTs, the lines in the literature, as mentioned above, shall be investigated first. The line profiles will also be investigated, as will the strengths of the lines as a function of temperature i.e. differences between HAes and HBes will be explored. Where possible, comparisons will be made with existing data on CTTs.

4.4.1 Hydrogen Lines – Hα, Paβ, and Brγ

Hydrogen is the most abundant element in stars, and as such is easily detected in their photosphere and circumstellar environments. Many transitions of the hydrogen recombination series are covered by X-shooter, specifically the Balmer, Paschen, and Brackett series. The strongest detectable line from each series is presented and analysed here.

4.4.1.1 H Alpha

The Hα line forms the lowest transition of the Balmer series, from n=3-2. Being such a low excitation line allows it to be seen as the strongest emission line in optical spectra of HAeBes. Indeed, its presence was used for the initial identification and classification of HAeBes (Herbig 1960), and has proved useful in detecting many more since then (Finkenzeller & Mundt 1984; Thé *et al.* 1994; Vieira *et al.* 2003). One of the largest works into analysing the Hα line in HAeBes was presented by Finkenzeller & Mundt (1984), where the authors found an approximate 2:1:1 ratio in the different line profiles seen in their sample between double peaked lines, single peaked lines, and P-Cygni lines respectively.

Figure 4.3 provides information on the Hα line profiles, the $L_{\rm acc}$ vs. $L_{\rm H\alpha}$ relationship, and a plot of EW$_{\rm cor}$ vs. $T_{\rm eff}$. The line profiles shown in the left panel are of 15 HAe stars and 15 HBe stars, in separate columns. The objects in the plot were selected randomly, and are in ascending temperature from bottom to top. The figure immediately highlights that this is a strong line, where the peak of the line reaches $\sim$ 8 times the continuum level in many cases, particularly

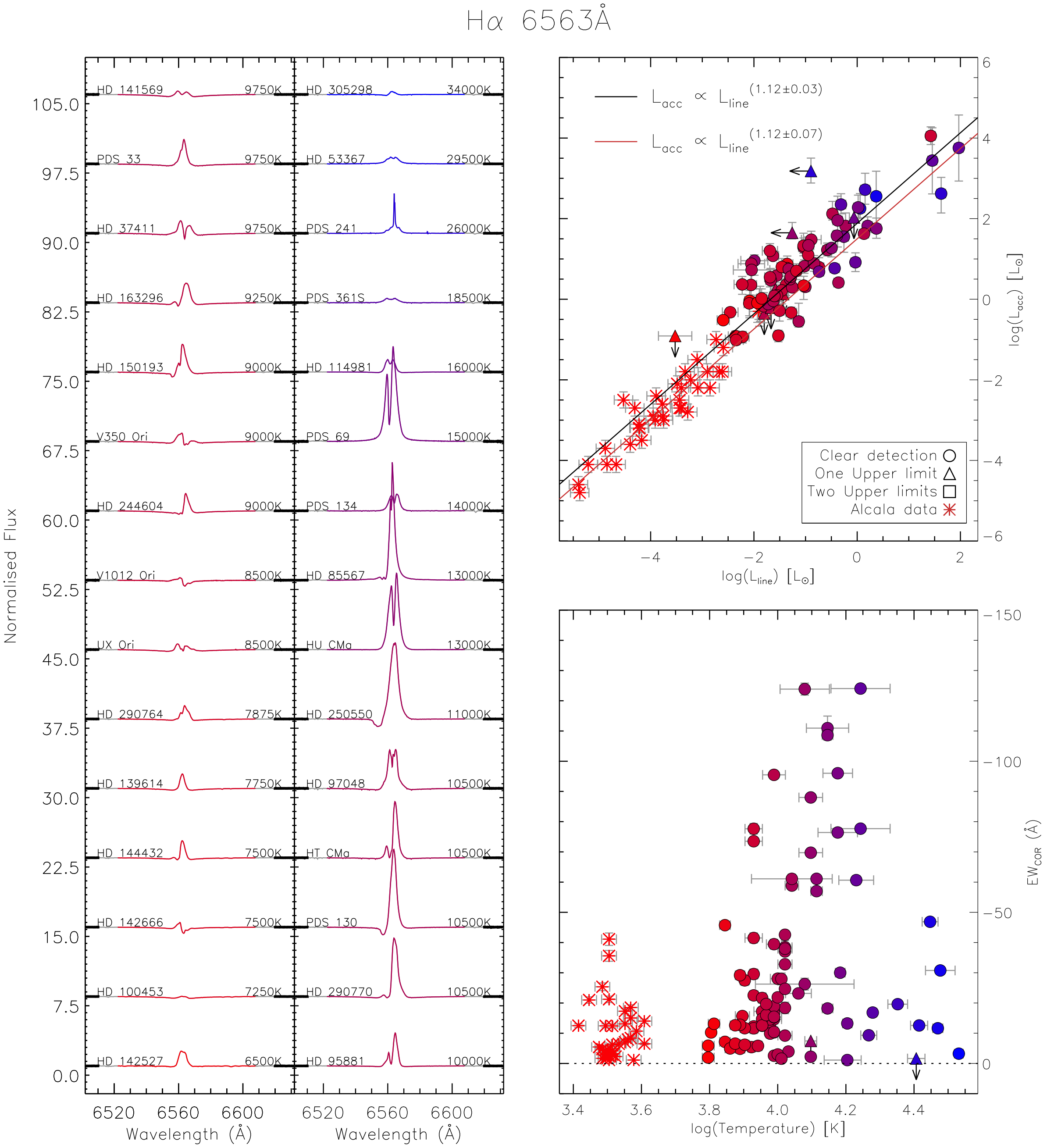

Figure 4.3: The left hand panel displays the line profiles of the HAes on the left, and the HBes on the right, with each column ascending in temperature from bottom to top. The top-right panel shows how the accretion luminosity is related to the line luminosity. The points are colour coded by temperature with red being cool, and blue being hot. A best fit to the data is shown as a solid black line. Where applicable, data on CTTs from (Alcalá *et al.* 2014) are shown along with their best fit. The bottom right panel shows the corrected equivalent width against the temperature of the star, where negative values are in emission. MWC 297 is omitted from this final plot for clarity as its strength is ∼ 600 Å.

for the HBes shown. The strengths of the lines are presented in the bottom right panel against the temperature of the star. $\mathrm{EW_{cor}}$ is seen to be greater than 25 Å in over a third of the sample, 35/91, with 18 of these displaying Hα line strengths greater than 50 Å. In general, the strength of Hα increases with temperature to a peak and then decreases again; the maximum occurs at ~ 14000 K.

The line profiles themselves show a range of complexities across all temperatures; single peaked, double peaked, and both regular and inverse P-Cygni profiles. Only two clear inverse P-Cygni profiles are present, with both of them belonging to HAes. This suggests material is infalling towards these stars, possibly from an accretion column. Meanwhile, classic P-Cygni profiles are seen predominately in the HBes stars (8 out of the 10 detections). Classic P-Cygni profiles are associated with outflowing material, such as a wind. Both of these line profiles are rare in the sample, with the majority of stars instead displaying either single or double peaked emission. The occurrence of these two profiles appears to be evenly distributed throughout the temperature range covered, with no obvious preference towards HAes or HBes.

The detection rate of Hα is very high, with it being present in 89 of the 91 stars, while the remaining 2 could have low levels of emission within the error margin. This quantity of detections allows a robust comparison between $L_{\rm line}$, determined in this chapter, against $L_{\rm acc}$, determined in the previous chapter. This comparison is shown in the top-right panel of Figure 4.3. A best fit to the data yields a power-law relationship of $L_{\rm acc} \propto L_{\rm line}^{1.12\pm0.03}$. This is in agreement with the CTTs plotted in the figure, and observed by Alcalá *et al.* (2014), who obtain a best-fit exponent of 1.12 ± 0.07. There is also further agreement with the CTTs studied by Herczeg & Hillenbrand (2008), where they obtain an exponent of 1.20 ± 0.11. However, the sample of CTTs observed by Rigliaco *et al.* (2012) does not agree with the results here, as the authors observe a higher exponent of 1.49 ± 0.05.

Hα is one of the few lines in HAeBes to already have a luminosity relationship previously determined. Mendigutía *et al.* (2011a) obtained a best-fit exponent for the case of 38 HAeBes to be 1.09 ± 0.16; a strong agreement is seen between this value and the one obtained in this work. Due to the high detection rate in this sample, and agreement of the $L_{\rm acc}$ vs. $L_{\rm line}$ relationship with the majority of previous works, Hα remains a good tracer of accretion, and accretion rate, for HAeBes; this shall be investigated further in Section 4.6.

4.4.1.2 Paschen Beta

Paschen β is the second lowest transition of the Paschen series. The lowest transition, Paα, lies in a wavelength region in which telluric line interference is extremely strong; the continuum is completely absorbed in some places, making corrections impossible. In a similar manner to Hα, line profiles of Paβ are shown in Figure 4.4, along with a $L_{\rm line}$ vs. $L_{\rm acc}$ comparison, and a line strength vs. temperature comparison too. The same trend of increasing line strength with temperature is seen for Paβ as was seen for Hα; in this case it peaks at $\sim 16000\,$K. However, despite the two lines arising from the same elemental species, many differences are observed in their line profiles. For Paβ only 6 clear double peaked profiles can be seen, with the majority occurring in HBes. The incidence of classical P-Cygni profiles is seen to be less than observed in Hα, while the number of inverse P-Cygni profiles has increased to 4 objects. The majority of lines are single peaked.

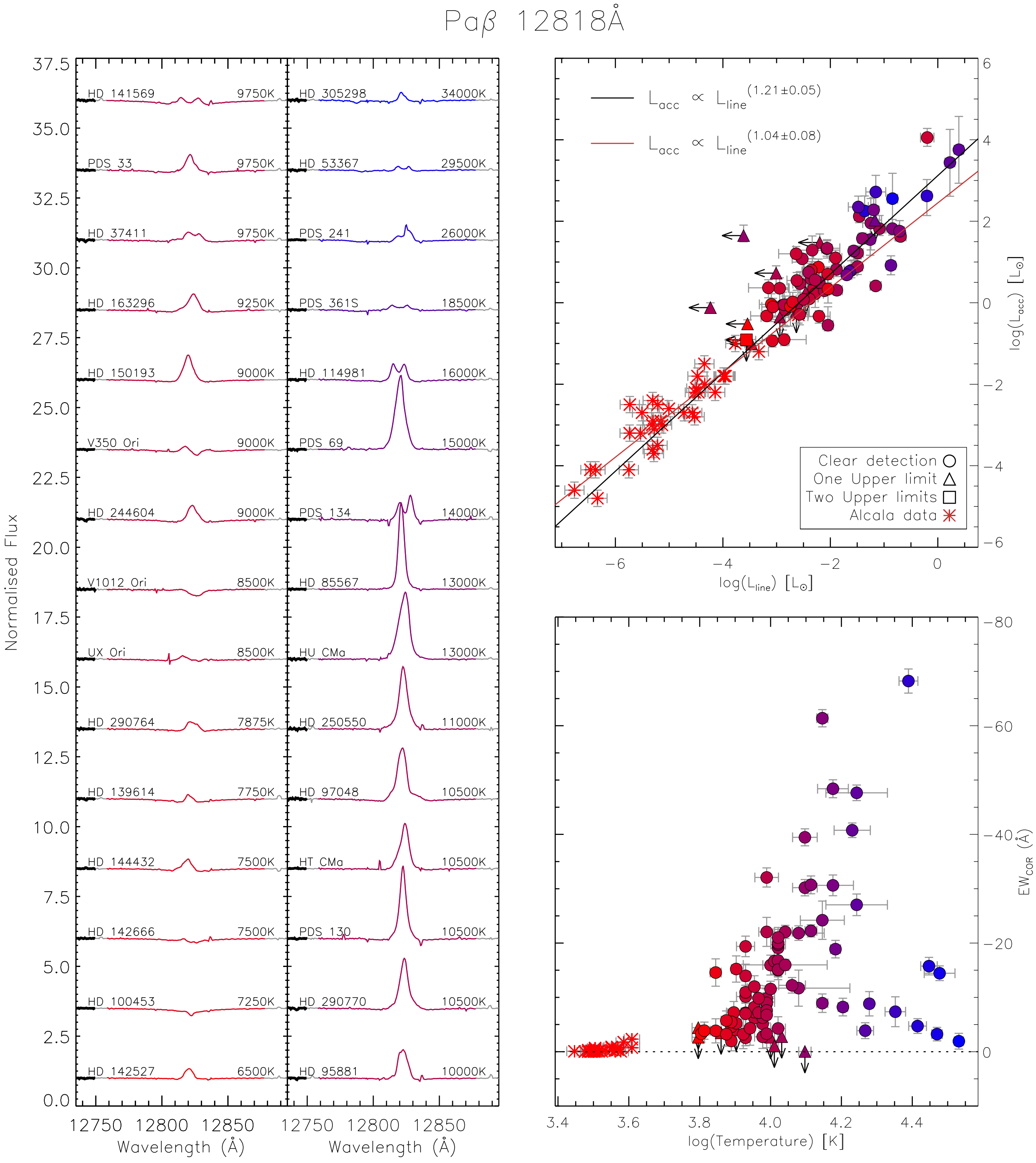

Figure 4.4: Same as Figure 4.3, but for the Paβ line.

The number of lines detected is 79, which is sufficient to provide a statistically sound comparison between L_{acc} and L_{line}. This plot is provided in the top-right of Figure 4.4, in which a best fitting relationship of $L_{\mathrm{acc}} \propto L_{\mathrm{line}}^{1.21\pm0.05}$ is obtained. As can be seen in the figure, this relationship is steeper than found previously in the sample of CTTs studied by Alcalá *et al.* (2014), where the exponent is 1.04 ± 0.08, but it remains close. However, their value is lower than most other studies of this line in CTTs, where the exponents have been observed to range from 1.14–1.49 (Muzerolle *et al.* 1998b; Gatti *et al.* 2008; Rigliaco *et al.* 2012). The relationship obtained in this work agrees with the lower bounds of the CTTs relationships, but there remains a large amount of scatter in the values for CTTs so far. This may be in part due to a selection effect in some of these works, as many studies concerning CTTs often focus on a particular star forming region (since CTTs are numerous in comparison to high mass stars). Therefore, an evolutionary factor may play a a larger role in the relationships obtained in those studies.

4.4.1.3 Brackett Gamma

The Brackett γ line exists at a longer wavelength than Paβ, and has been examined in many studies of CTTs (Muzerolle *et al.* 1998b; Calvet *et al.* 2004), and also in some HAeBes (Garcia Lopez *et al.* 2006; Mendigutía *et al.* 2011a). Recently, it has been observed that the strength of this line in HAeBes appears to be related to the nearby CO bandhead emission (Ilee *et al.* 2014). The CO bandhead traces regions close to the star, and its detection suggests that the stars are still actively accreting, due to its correlation with Brγ. Interferometric observations of this line have provided information about where the line originates from (Kraus *et al.*

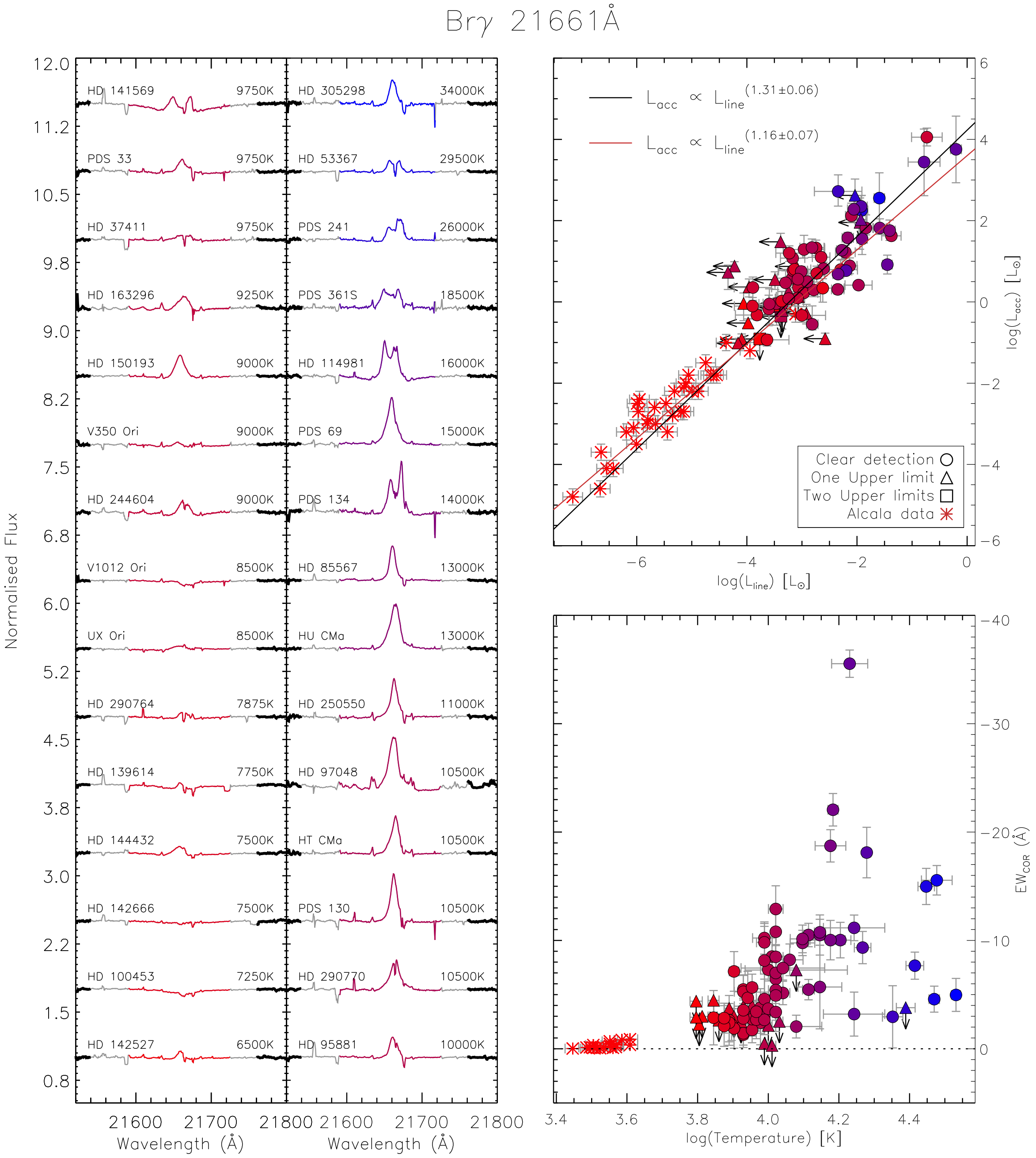

Figure 4.5: Same as Figure 4.3, but for the Brγ line.

2008), which is thought to be interior to the dust sublimation radius. However, the observations suggest that the Brγ in the majority of stars is more likely to be associated with a disc wind than an accretion column. Further interferometric investigations support this case by finding that Brγ also originates outside of the co-rotation radius in the HAe star HD 100546, and therefore cannot form from within an accretion column (Mendigutia *et al.*, submitted). This could be the case for all HAeBes, so the question is: would a relationship between L_{acc} and L_{line} still hold for a large set of HAeBes?

Figure 4.5 displays a series of line profiles and relations for Brγ which are analogous to Figures 4.3 and 4.4. The trends visible in the line profiles, the line luminosities, and $\mathrm{EW}_{\mathrm{cor}}$ display similarities to the two previous lines analysed; the line profiles in particular bear the most resemblance to the Paβ lines than the Hα lines. Detections are also fewer for Brγ, with only 69 emission lines detected, while the detection rate was 79 for Paβ and 89 for Hα. This decrease in detection from Hα to Paβ to Brγ is likely caused by two factors. Firstly, case-B recombination theory predicts that Brγ will be weaker than Paβ, which in turn is weaker than Hα (Osterbrock 1989); this explains the observed strengths. Secondly, a detection effect is also present due to the IR-excess. As the IR-excess strength increases, a line in the NIR will become more difficult to measure, because of the decreasing contrast between the IR-excess and the emission line. However, this second point is not particularly likely unless the emission line is quite weak. There is also the possibility that the lines originate from different regions.

The number of double peaked lines for Brγ remains around the same as seen in Paβ, while only one classical P-Cygni profile can be seen, and no inverse P-

Cygni profiles are present. The remainder of line profiles are are all single peaked emission lines (or in absorption).

Since the number of lines detected is still high, 69 in total, a robust comparison of L_{acc} vs. L_{line} can be made, and it is displayed in the top right panel of Figure 4.5. A best fit to the data is obtained of $L_{\mathrm{acc}} \propto L_{\mathrm{line}}^{1.31\pm0.06}$. This relationship is steeper than the two relationships obtained so far for Hα and Paβ; although the Paβ relationship lies within the errors of this one. Previously, exponents of the relationship have been observed to range from 0.9–1.26 in CTTs (Muzerolle *et al.* 1998b; Calvet *et al.* 2004), while in HAeBes is has been observed to be 0.91 ± 0.27 by Mendigutía *et al.* (2011a) and 0.90 ± 0.20 by Donehew & Brittain (2011). The errors allow the determination here to agree with the upper end of values found for CTTs, but it falls outside the error bounds for the previous determinations in HAeBes. In regards to the past works on HAeBes, the data set presented here includes ~ 3 times more HAeBes, including many more early HBe type stars. This may help to explain the observed differences between the samples as the most luminous and highly accreting stars in the sample are seen to be far into the top right corner.

The final section of Figure 4.5, in the bottom right hand panel, shows $\mathrm{EW}_{\mathrm{cor}}$ versus the temperature of the star. A large range in strengths can be seen, but the greatest absolute line strengths of $\mathrm{EW}_{\mathrm{cor}} = 40 - 70\,\text{Å}$ are observed only at around $\sim 16000 - 17000\,\mathrm{K}$. However, weaker line strengths of $\mathrm{EW}_{\mathrm{cor}} < 15\,\text{Å}$ can be seen at most temperatures. This behaviour is in agreement with the other two hydrogen lines analysed so far.

4.4.2 Oxygen – 7773, 8446 and forbidden 6300 Å

Measurements are made here of three different oxygen lines: one forbidden, and two which are not forbidden. Attention is first paid to the forbidden line at 6300 Å. This line has been observed in both CTTs and HAeBes alike (Cabrit *et al.* 1990; Boehm & Catala 1994). In the work by Boehm & Catala (1994) the authors observed this line in emission for 17 HAeBes and found the line to be symmetric and centred around the star's radial velocity in most cases. This was later confirmed for more HAeBes by Acke *et al.* (2005). These authors showed that the majority of the emission from this line is single peaked and centred on the stellar radial velocity, with most lines showing a FWHM $< 100\,\mathrm{km\,s^{-1}}$, and that double peaked line profiles are also seen with small separations. Their interpretation for group I HAeBes is that it originates from the surface of the rotating, flared, circumstellar disc, while the origin in group II HAeBes is less clear but may be from the inner gaseous disc. This scenario was extended to two more HAeBe stars by van der Plas *et al.* (2008), but the authors could not explain the observed emission profile for HD 135344B in either context, as the line suggests additional components other than sole emission from a disc. In Z CMa van den Ancker *et al.* (2004) observed this emission line to be composed of both a low velocity central line component and a high velocity line component on the blue side of the line; these two components are also both present in our spectrum of Z CMa.

Low velocity and high velocity components of $[\mathrm{O\ I}]_{\lambda 6300}$ have been observed by Natta *et al.* (2014) in multiple CTTs too. These authors observed a detection rate of 86%, 38 out of 44 stars, of which 12 were observed to also feature the

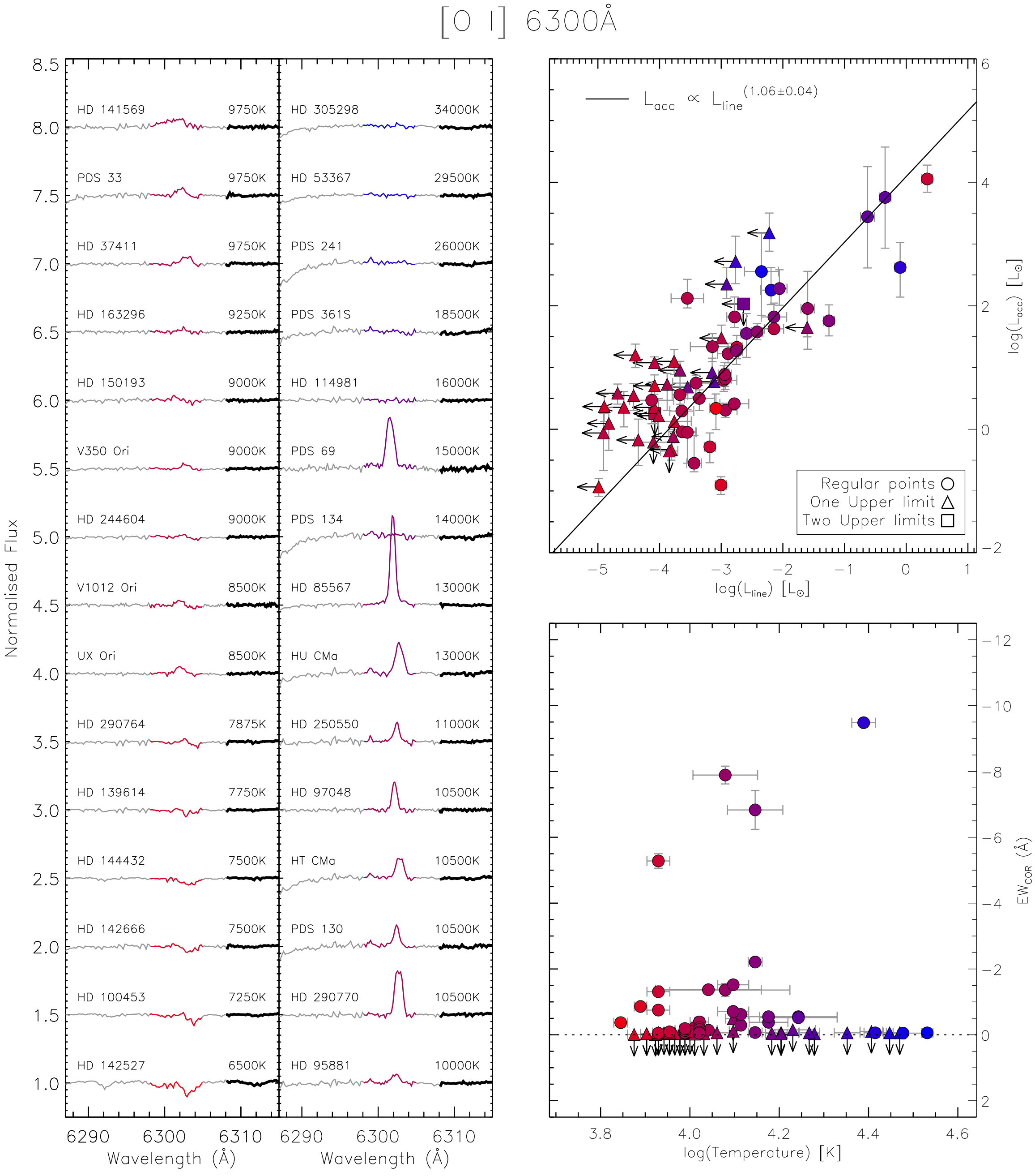

Figure 4.6: Same as Figure 4.3, but for the [O I] line at 6300Å.

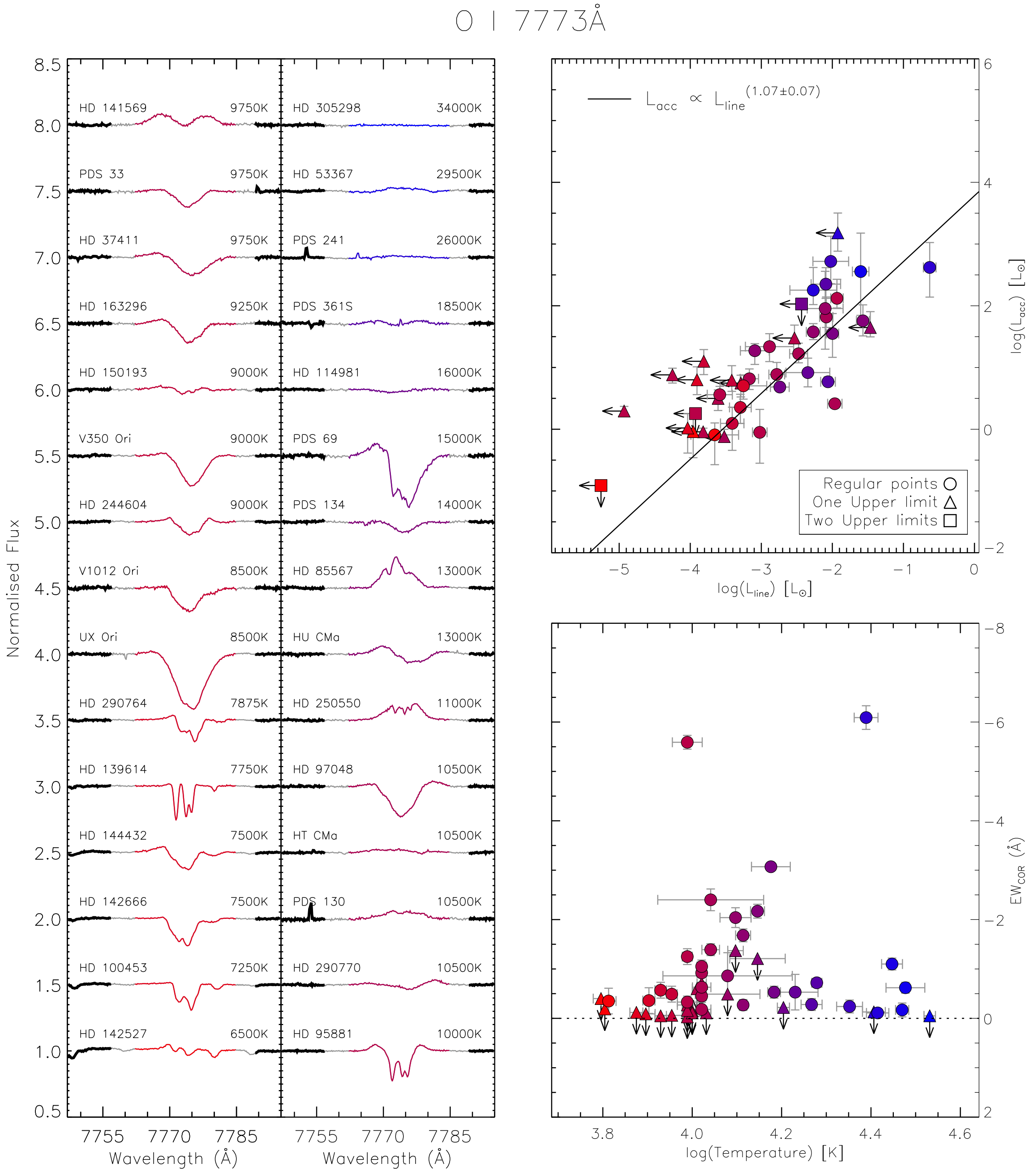

Figure 4.7: Same as Figure 4.3, but for the O I line at 7773Å.

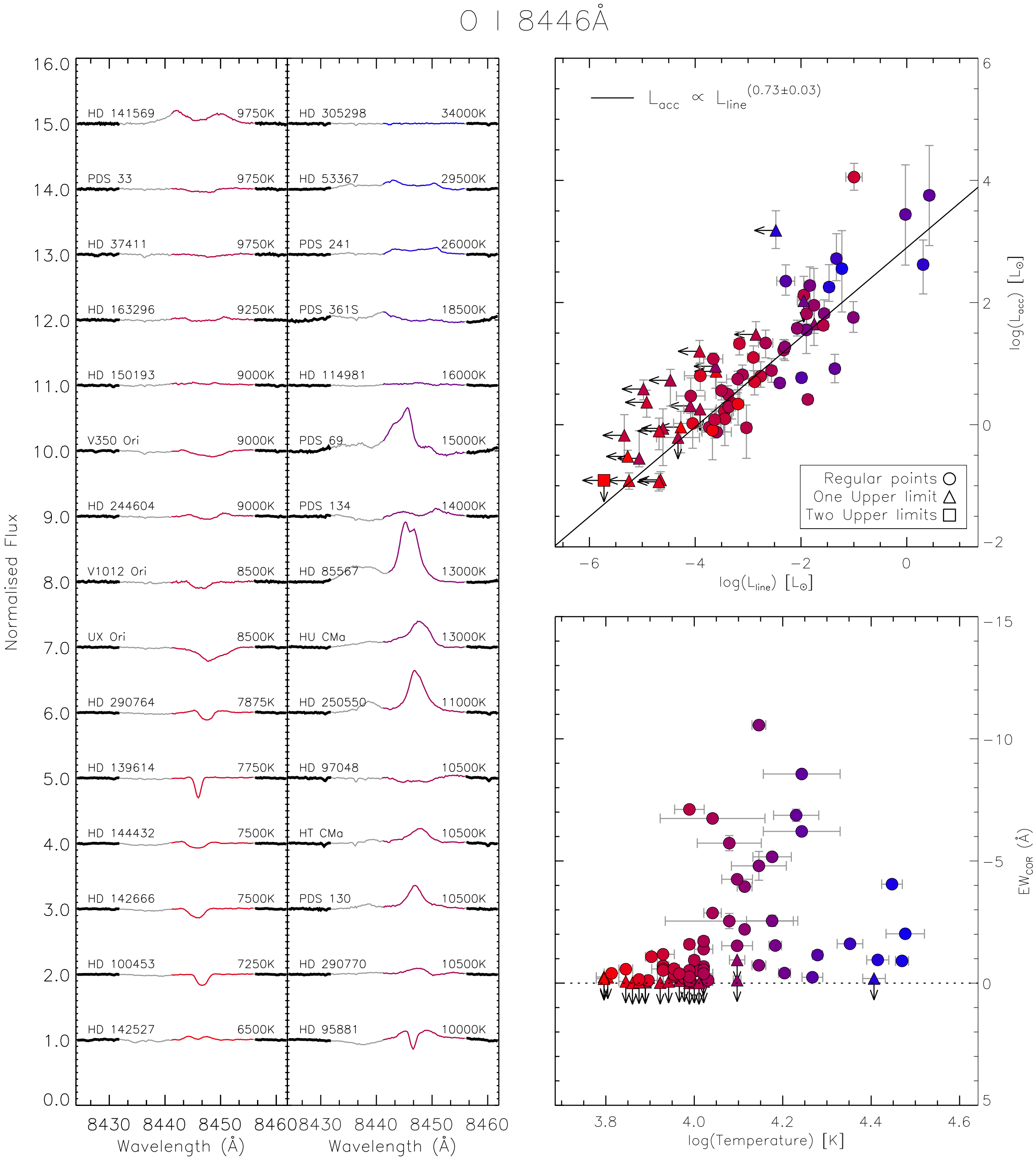

Figure 4.8: Same as Figure 4.3, but for the O I line at 8446Å.

high velocity component. Conversely, in HAeBes the detection rate of $[\text{O I}]_{\lambda6300}$ is lower, at only 52% (17 out of 33 stars Boehm & Catala 1994). This lower detection rate is confirmed by this work, where 44 out of the 91 stars see this line in emission – a detection rate of 48%. The high velocity component is thought to be arising from a jet, while the low velocity component has been theorised to come from a slow, neutral wind in CTTs (Rigliaco *et al.* 2013; Natta *et al.* 2014). High-resolution spectroscopic observations of two HAeBes by Acke & van den Ancker (2006) suggest that the origin of the low velocity component is from the dust disc, as the emission appear to coincide with the location of the dust disc. The medium resolution of our data is not sufficient to rule in favour of either scenario, although both possibilities are not mutually exclusive.

Dahm (2008) finds that $[\text{O I}]_{\lambda6300}$ is only present in CTTs which are actively accreting. In many of the studies of $[\text{O I}]_{\lambda6300}$, a relationship between L_{acc} and L_{line} has been observed. The top right panel of Figure 4.6 displays the L_{acc} vs. L_{line} plot for this line, where a best-fit is found of $L_{\text{acc}} \propto L_{\text{line}}^{1.06\pm0.04}$. This is in agreement with the HAeBes analysed by Mendigutía *et al.* (2011a), who find the exponent of the relationship to be 1.13 ± 0.14, and they note that the line luminosity appears to be decoupled with accretion variability; the line's origin is not closely linking to the accretion mechanism. However, for CTTs there is a large scatter in the relationship between different authors, with the exponent of the relationship having been listed as low as 0.96 (Herczeg & Hillenbrand 2008) and as high as 1.92 (Rigliaco *et al.* 2013). These differences may hint at the origin of the line not being uniform between samples. The effects of orientation may also play a role if its origin is from either inside the disc or from material outflowing from the disc.

The bottom right panel of Figure 4.6 displays the line strength as a function of stellar temperature. The line strength is quite weak in the majority of cases, where the absolute equivalent width is $< 1.0\,\text{Å}$ for 80% of the detections. No correlation is seen between the line strength and the temperature of the star.

The other two oxygen lines, at 7773 and 8446 Å, were selected as they have been observed in both CTTs and HAeBes to occasionally display line profiles typical of infalling material (Felenbok *et al.* 1988; Hamann & Persson 1992a,b; Muzerolle *et al.* 1998c). Detections of the 7773 Å line are fairly low with only 30 lines seen in emission, while there are 57 emission detections of the 8446 Å line. For the latter line, detections are weighted towards the hotter stars, of which 36 out of the 57 detections, 63%, are HBes ($T_{\rm eff} > 10000\,$K). The observed strength of this line is fairly low, as can be seen in the bottom right hand panel of Figure 4.8. Only 9 of the 57 stars have an absolute strength of $\text{EW}_{\text{cor}} > 5\,\text{Å}$, while only 2 stars have $\text{EW}_{\text{cor}} > 10\,\text{Å}$. The strongest lines are seen between 9500–18000 K. The stars with the stronger lines are generally seen to be HBe stars. A similar distribution in line strengths, with regards to temperature, is seen in the 7773 Å line. For this line, the line strengths are even weaker with only 2 stars having an absolute line strength of $\text{EW}_{\text{cor}} > 5\,\text{Å}$.

In general, there is a mix of line profiles present in both cases, as evidenced by the left hand panels in Figures 4.7 and 4.8. Many single peaked emission and absorption lines are present, while the number of stars with double peaked profiles are much less frequent. The majority of cases with absorption in both lines also appear to be fairly broad FWHM$> 50\,\text{km}\,\text{s}^{-1}$. In some of these the line profile is observed to be different between the two lines for the same star e.g. HU

CMa is seen to display an inverse P-Cygni profile for the 7773 Å line, while the 8446 Å is seen as single peaked emission. Therefore, an in-depth analysis of line profiles would be natural extension to this work in the future.

It has been noted previously in CTTs that when the 7773 Å line is seen in absorption, its absorption strength is often greater than the expected intrinsic strength of the line for the given temperature of the star (Hamann & Persson 1992a). For the 7773 Å line there are 39 clear absorption detections, with 22 of these displaying absorption greater than the intrinsic strength. A greater level of absorption than expected can be explained by an extended atmosphere or additional material between the star and our line of sight, likely circumstellar material. Conversely, the 8446 Å line is only seen in absorption in 12 cases, with just 2 of these being greater than the intrinsic absorption expected.

The cases for which the lines are seen in emission are converted to a luminosity and plotted against $L_{\rm acc}$ in the top right panels of Figures 4.7 and 4.8. The $L_{\rm acc}$ vs. $L_{\rm line}$ plot for the 7773 Å line can be best fit with a power law of the form $L_{\rm acc} \propto L_{\rm line}^{1.07\pm0.07}$. This is very similar to the case for the [O I]$_{\lambda6300}$ line, and some of the other lines analysed so far. The 8446 Å line, on the other hand, is best fit by $L_{\rm acc} \propto L_{\rm line}^{0.73\pm0.03}$, which has a much lower exponent than any of the other lines analysed so far. A shallower gradient indicates the line luminosity is increasing at a greater rate than $L_{\rm acc}$. Since the strongest emission was associated with HBes, the relationship suggests that they are more efficient producers of the 8446 Å line; this is a likely a consequence of the 8446 Å line being excited at higher energy levels (Hibbert *et al.* 1991).

4.4.3 Helium – 5876 and 10829 Å

Helium is often associated with O and B stars, as it requires high temperatures to be seen in either absorption or emission. In particular, He I peaks in absorption at around 20000 K. Despite this high temperature threshold, He I has been observed to be present in the much cooler CTTs, where it is often seen to display a variety of line profiles (Muzerolle *et al.* 1998c). This makes it an interesting line, and one which requires an additional source of energy to be seen in such cool stars. For CTTs it can be seen due to helium present in the accretion column, which is close to the star and can be excited by the UV-excess. In particular, the He I 5876 Å line has been seen as an inverse P-Cygni profile, suggestive of in-falling material in a hot region i.e. an accretion column (Muzerolle *et al.* 1998c). One key question is based on HAeBes being intrinsically hotter than CTTs, so will they display similar line profiles? The left hand panel of Figure 4.9 displays a selection of line profiles for the He I 5876 Å line. The majority of the line profiles displayed show some kind of absorption component; this is also true for the sample as a whole. Clear inverse P Cygni profiles can be seen in 14 of the HAes analysed, while only 5 can be seen in the HBes, 3 of which are borderline (between 10000–10500 K). On the other hand, only a few classical P-Cygni profiles can be seen for this line. Therefore, based on the large occurrence of inverse P-Cygni profiles, this suggests that the line's origin is from in-falling material, which could very well be an accretion column, particularly in the less massive stars.

Another helium line of interest lies in the NIR arm at 10829 Å. This line has been observed readily in CTTs, with many lines present in emission and absorption (Dupree *et al.* 2005; Edwards *et al.* 2006; Kwan *et al.* 2007). These

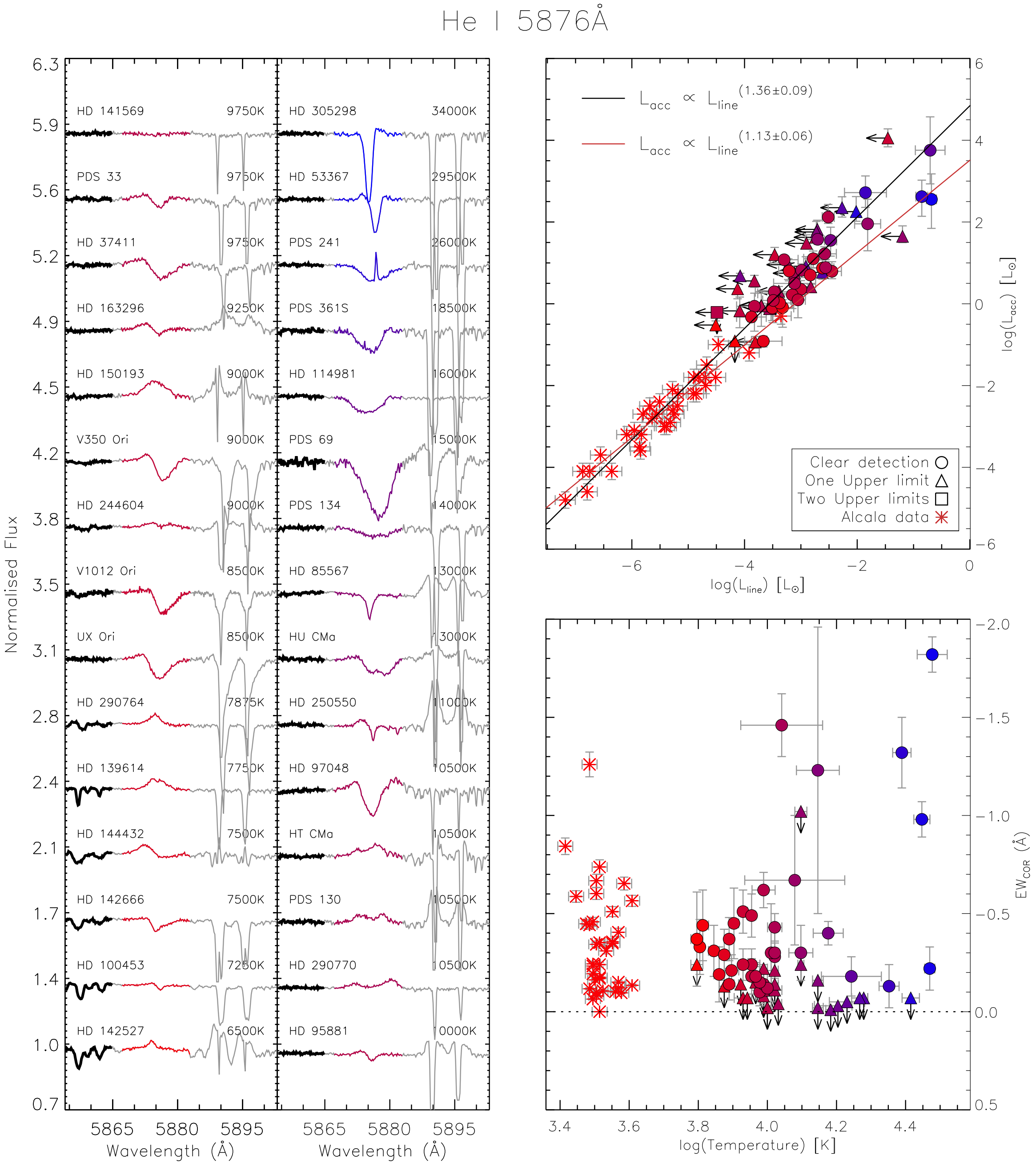

Figure 4.9: Same as Figure 4.3, but for the He I line at 5876Å.

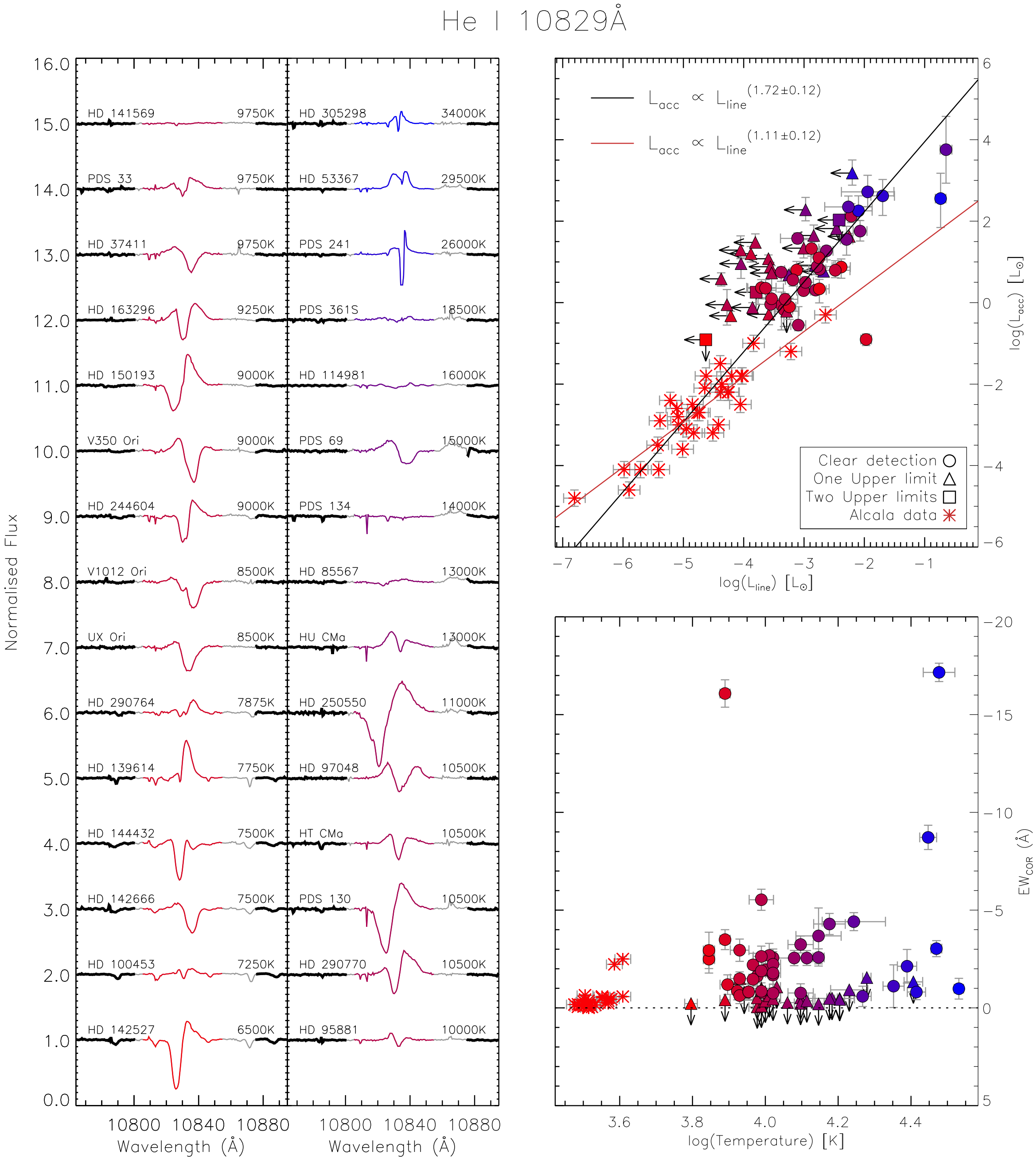

Figure 4.10: Same as Figure 4.3, but for the He I line at 10829Å.

profiles have been seen both in red shifted absorption, indicative of in-falling material, and in blue-shifted absorption, suggesting stellar winds as the origin, or even disc winds for the narrow absorption cases (Kurosawa & Romanova 2012). The orientation of the star plays a large role in the observations too, i.e. looking pole on, it is likely only the wind component will be seen, while the infall can only be seen at specific inclination angles (Edwards *et al.* 2006; Kurosawa & Romanova 2012).

Recently, observations by Cauley & Johns-Krull (2014) looked at this line in a large number of HAeBe stars and drew comparisons against CTTs. The authors found that the line profiles seen in HAes suggest that magnetospheric accretion is acting here, akin to CTTs, while for HBes it is not. This conclusion was based on the number of red shifted and blue shifted profiles seen in each mass category. They also did not see evidence for a disc-wind, narrow blue-shifted absorption, in the profiles they analysed. This is confirmed by the observations presented here, where there are 3 cases, out of 91 stars, which may be from a disc wind. One of these cases is HBe PDS 241, whose profile is displayed in the left hand panel of Figure 4.10. In this line there is also accompanying narrow redshifted emission, which can be seen in other line profiles of PDS 241, suggesting that its origin is likely from nebulosity around the star[1]. For the line profiles of the other two stars, PDS 133 and PDS 124, the narrow absorption is potentially still broad enough to be a stellar wind component. Inverse P-Cygni profiles are predominately observed in the HAes, and when present, they are often accompanied by the He I 5876 Å line also displaying an inverse P-Cygni profile. Generally, when they are seen together, the redshifted emission is stronger for the 10829 Å line e.g. see the

---

[1] This is supported by optical imaging of the star; see SIMBAD for an optical image

cases of V350 Ori, UX Ori, and HD 95881 in Figures 4.9 and 4.10.

Overall, the mix of line profiles observed for the two transitions suggests that they originate in a complex circumstellar region. To disentangle the exact origin of these lines, additional information about the possible system geometry is required, along with detailed modelling of winds and infall. Such an endeavour is beyond the scope of this chapter, as they goal here is to look at the statistics of the lines.

The L_{acc} vs. L_{line} comparisons are made for these two helium lines in the same manner as the other lines discussed so far. The first comparison is of the 5876 Å line and is shown in the top right hand panel of Figure 4.9. The best fit to the data is $L_{\mathrm{acc}} \propto L_{\mathrm{line}}^{1.36\pm0.09}$. This is similar to relationships obtained so far in CTTs, where the exponent in them has been calculated as 1.10 ± 0.23, 1.42 ± 0.08, and 1.46 ± 0.12 (Dahm 2008; Herczeg & Hillenbrand 2008; Fang *et al.* 2009). However, disagreement is seen with the value calculated by Rigliaco *et al.* (2012), which has a slightly larger exponent of 1.51 ± 0.03, placing it just outside of the uncertainty range. Disagreement is also seen between the fit presented here and the fit to CTTs by Alcalá *et al.* (2014), who, in contrast to the previous authors just mentioned, obtain a shallower exponent of 1.13 ± 0.06. Despite these disagreements, it can be seen in the L_{acc} vs. L_{line} plot of Figure 4.9 that the two most luminous lines of He I 5876 Å in this sample actually agree with the best fit of Alcalá *et al.* (2014). The best fit obtained to the HAeBes has a slope which lies between all previous relationships for CTTs, and agrees within the errors of the majority too.

The L_{acc} vs. L_{line} relationship, and best fit for the 10829 Å line, is shown in the top right panel of Figure 4.10, where the best fit to the data is found to be $L_{\mathrm{acc}} \propto L_{\mathrm{line}}^{1.72\pm0.12}$. This is much steeper than the exponent found for the 5876 Å line. At first it could be thought that the differing strengths of $\mathrm{EW_{cor}}$ between the lines may play a factor. The emission peak in the 10829 Å line is often higher than the 5876 Å line. However, conversion to a flux/luminosity depends upon the SED of the star, which for A and B type stars is always weaker around 10000 Å as opposed to 5000 Å, although the flux around 10000 Å can be slightly enhanced by an IR-excess. Therefore, despite the $\mathrm{EW_{cor}}$ of the 10829 Å line being stronger than the 5876 Å line in the majority of cases (two-thirds), its luminosity is weaker in half of the cases due to the laws of blackbody radiation. This allows the case of the steeper gradient observed for the 10829 Å line.

There is no overall trend seen between the line strength and the temperature of the star for either of the lines, as demonstrated in the bottom right panels of Figures 4.9 and 4.10. The distribution of strengths is seen to be scattered for CTTs and HAeBes alike – a probable consequence of the complex line profiles observed.

4.4.4 Calcium NIR Triplet

The calcium triplet consists of the lines at 8498, 8542, and 8662 Å, which are emitted from singly ionised calcium (Ca II). The lines have been observed in both CTTs and HAeBes, where they often display ratios between each other of 1:1:1 (Hamann & Persson 1992a,b; Boehm & Catala 1995; Rigliaco *et al.* 2012). Figure 4.11 provides a region of the NIR spectra which spans 8480–8720 Å, encompassing the entirety of the triplet and also the Paschen (14-3) transition. The cases in which the triplet is present in emission can be seen to display the typical 1:1:1 ratio previously observed in HAeBes and CTTs, meaning that it is likely

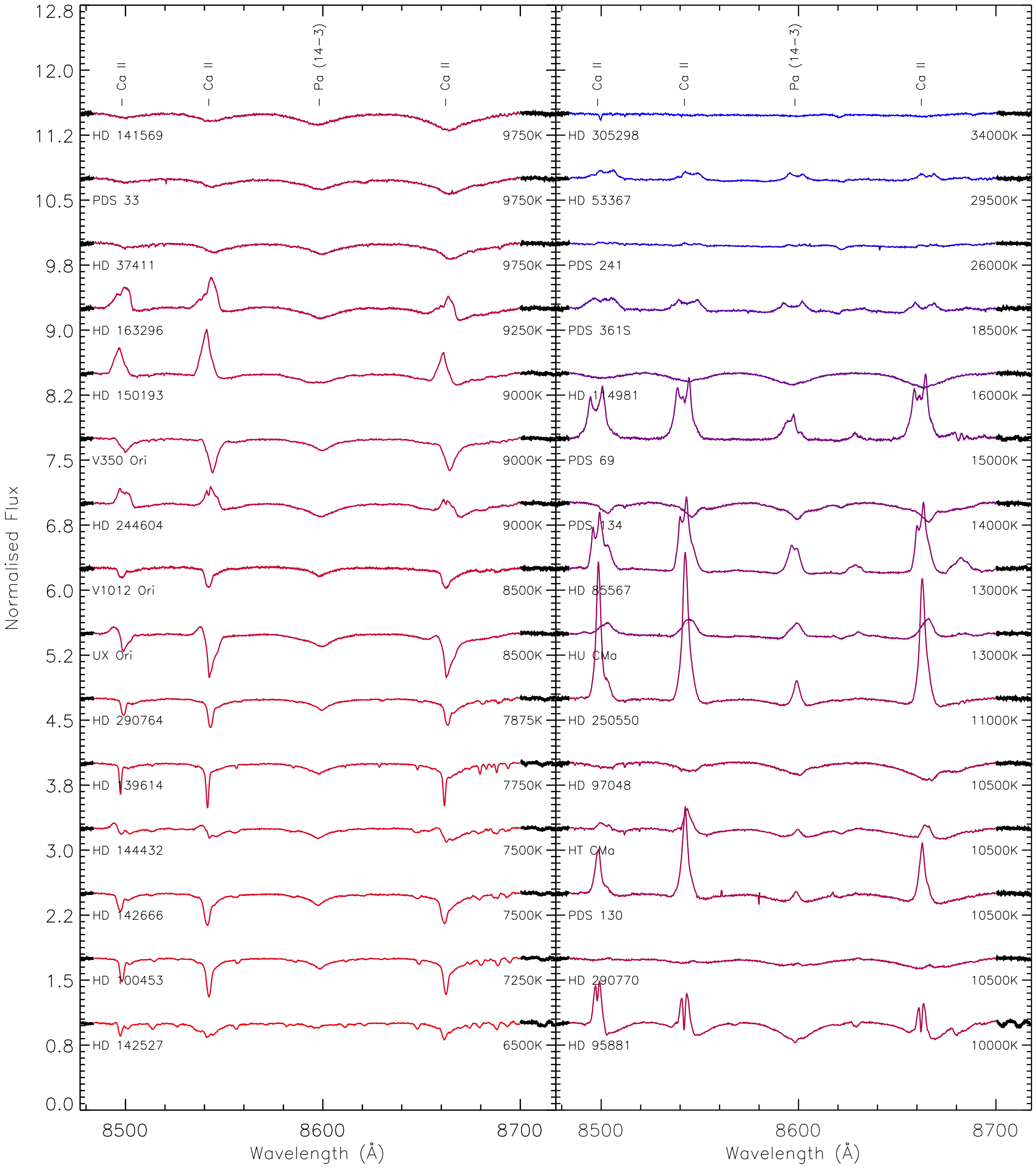

Figure 4.11: This figure displays a series of spectra spanning 8480–8720 Å. The region contains all three lines of the calcium II triplet (8498, 8542 and 8598 Å), along with four of the Paschen series hydrogen lines (three coincide with the Ca II triplet while the other is at 8598 Å). The triplet and the unblended Paschen line are labelled at the top. The spectra displayed are of the same stars displayed in Figures 4.3 to 4.10, with the HAes on the left and HBes on the right. Each column is ascending in temperature from bottom to top.

emitted from an optically thick region. The central wavelengths of the triplet are blended with the Paschen series. Therefore, to measure the strength of the line, corrections need to be made for the underlying absorption of the hydrogen line, which can be very broad and strong. For example, in Figure 4.11 the star HD 95881 demonstrates the broad wings of the Paschen lines in absorption with double peaked emission from the Ca II triplet superimposed on top of them. In this example the Pa(14-3) line is seen entirely in absorption. This line can serve as a useful indicator for the presence of the Ca II triplet e.g. for the cases of PDS 69 and HD 85567 there are four emission lines present, and it can be seen that the Pa (14-3) line is $\sim 2 - 3$ times weaker than the lines at the location of the Ca II triplet. This suggests that the triplet lines are a combination of both Ca II emission, and hydrogen emission. Meanwhile, for the cases of HD 53367 and PDS 361S, there are four emission lines present which are all of comparable strength, suggesting that they all belong to the Paschen series, and that there is no Ca II triplet emission.

Again, many different line profiles can been seen in the figure, such as inverse P-Cygni and double peaked lines, though the majority of lines are seen to be single peaked emission. This diversity in line profiles, much like the other lines discussed so far, suggests that the geometries and environments regarding the emission and absorption of this line are also complex. It is suspected that the emission from these lines occurs further out in the disc due to the low excitation energy of Ca II, where further out in the disc would be cooler. Emission also appears stronger in the HBes of the sample.

The triplet lines have also been used as accretion indicators in CTTs (Muzerolle *et al.* 1998c; Mohanty *et al.* 2005; Rigliaco *et al.* 2012; Costigan *et al.* 2012).

One of the latest studies by Costigan *et al.* (2012) showed that the triplet is variable, with accretion rates calculated from the line seen to change on average by ~ 0.83 dex over a time period of 15 months. Their work also suggests that accretion variability occurs on timescales of less than 25 days, providing an upper limit to the variability. In addition, further investigation by (Costigan *et al.* 2014) demonstrated than the variability does not occur significantly on a timescale of minutes or hours, but on days i.e. the variability appears to coincide with the rotation period.

The relationship between L_{acc} and L_{line} is presented for all 3 lines in Figure 4.12. The best fit for each of the lines is found to be: $L_{\mathrm{acc}} \propto L_{\mathrm{line}}^{0.82\pm0.04}$ for the 8498 Å line; $L_{\mathrm{acc}} \propto L_{\mathrm{line}}^{1.07\pm0.06}$ for the 8542 Å line; and $L_{\mathrm{acc}} \propto L_{\mathrm{line}}^{1.20\pm0.05}$ for the 8662 Å line. Interestingly, the exponent appears to be increasing with wavelength, with a total change of ~ 0.4 across the lines. This differs from the CTTs' case, where Alcalá *et al.* (2014) obtain the same exponent of 0.95 for all three lines. A possible cause for this change is the blending of the lines with the Paschen 13, 15, and 16 lines. Removal of the emission component of these lines has not been attempted, so if any emission is present it will contribute to the triplet, increasing their measured strengths, and hence luminosities. The strength of the lines in the Paschen series are seen to decrease towards the lower level transitions i.e. the strengths increase with wavelength. This means the contribution to the 8498 Å line from the Paschen series will be less than the contribution to the 8662 Å line. However, the trend of the exponent in the relationship increasing with wavelength actually suggests the opposite, as a higher exponent means that the correct accretion rate can be achieved with a lower line luminosity. Therefore, the exact cause of this increase remains unknown. The Ca II triplet may be a unique case, as it appears that the HAeBes are offset from the Ca II relationship seen for the CTTs. This will be investigated in the next section.

4.5 Additional Accretion Diagnostic Lines

Accretion tracers provide a method of inferring accretion rates for stars where direct methods of measurement $\dot{M}_{\rm acc}$ are difficult or impossible. i.e where it is much more difficult to obtain a UV-excess and model it to obtain an accretion rate. Emission lines are readily available at a variety of different wavelengths, and are easier to measure. Therefore, by establishing correlations between the accretion luminosity and line luminosity for a large series of lines, it opens up possibilities for researchers to infer accretion rates when using data sets with a limited wavelength range.

The advantage of the large wavelength range covered by X-Shooter is that it encompasses a huge range of emission lines, allowing many accretion diagnostic lines to be found. It also covers all these lines simultaneously to each other and the Balmer excess, which was used earlier for the accretion determinations. The simultaneity of the observations allows the lines to be safely compared against each other as there will be no variability effects between lines. A set of 24 emission lines have been chosen based on their frequency of detection in the sample, and they are presented in Figure 4.12. The figure shows the plots of $L_{\rm acc}$ vs. $L_{\rm line}$ for each of the 24 lines, along with a best fit to each one. Where possible, the data on CTTs from Alcalá *et al.* (2014) for the same lines are also included for comparison, along with their best fit. Overall, the plots appear to show a qualitative agreement in trends between the HAeBes and the CTTs, where $L_{\rm acc}$

is increasing proportionally to $L_{\rm line}$. However, the exact fits to the samples mostly show disagreement between the two on a quantitative level. In particular the Ca II triplet is fairly deviant as each of the best fitting lines for the HAeBes appears to be offset from the CTTs' case. As discussed in the previous section, these particular lines may be affected by the Paschen series. Most other disagreements are seen in the slope of the relationship, rather than the offset. The CTTs and HAeBes often agree in the transition region between them in the plots, and then grow more divergent towards the more luminous lines (i.e. the HBes). Exceptions to this correlation are the Ca II triplet, as mentioned, and a few of the higher order Paschen lines.

Table 4.1 provides the exact best fits for all of the $L_{\rm acc}$ vs. $L_{\rm line}$ relationships for easy reference; it also includes the fits from the previous section (bringing the total number of lines analysed to 32), and the best-fit cases for the CTTs analysed by Alcalá *et al.* (2014) for comparison. These relationships are compared visually in Figure 4.13, where each of the A and B values are plotted against their relevant line number (which happens to be in ascending wavelength order too). From the table and figure it can now be seen quantitatively that the relationships for CTTs do not agree with those with HAeBes on an individual line by line basis. In total, 80% of comparable lines do not agree with each other (16/20 lines). Additionally, the slope of the $L_{\rm acc}$ vs. $L_{\rm line}$ relationship, the B value, is found to have an average of $\bar{B} = 1.26 \pm 0.22$ in the HAeBes. This is steeper than the average seen in CTTs, which is $\bar{B} = 1.08 \pm 0.08$. Agreement is seen between the two, within the errors.

Further analysis of how B changes between lines and wavelengths can provide some further insight into the relationship between accretion and the emission

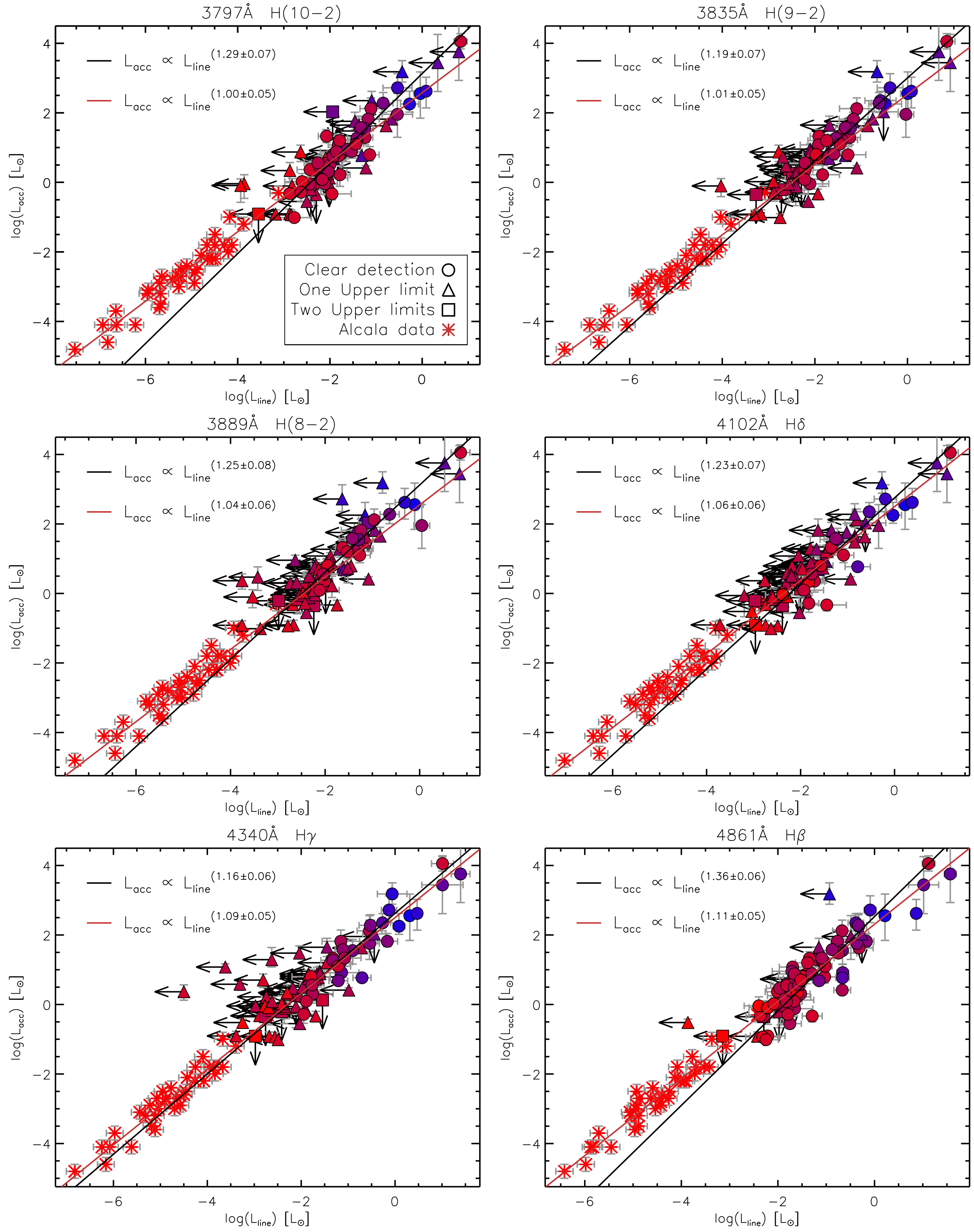

Figure 4.12: This figure shows the accretion luminosity, as calculated directly from the UV-excess in Chapter 3, against the line luminosities measured in this chapter. The first panel provides the legend for the points, and upper limits are marked with black arrows. The HAeBes are coloured according to their temperature (blue is hot; red is cold). A best-fit to the data is shown as a black line. Where applicable, the CTTs data from Alcalá *et al.* (2014) is also plotted for comparison, along with their best-fit in red.

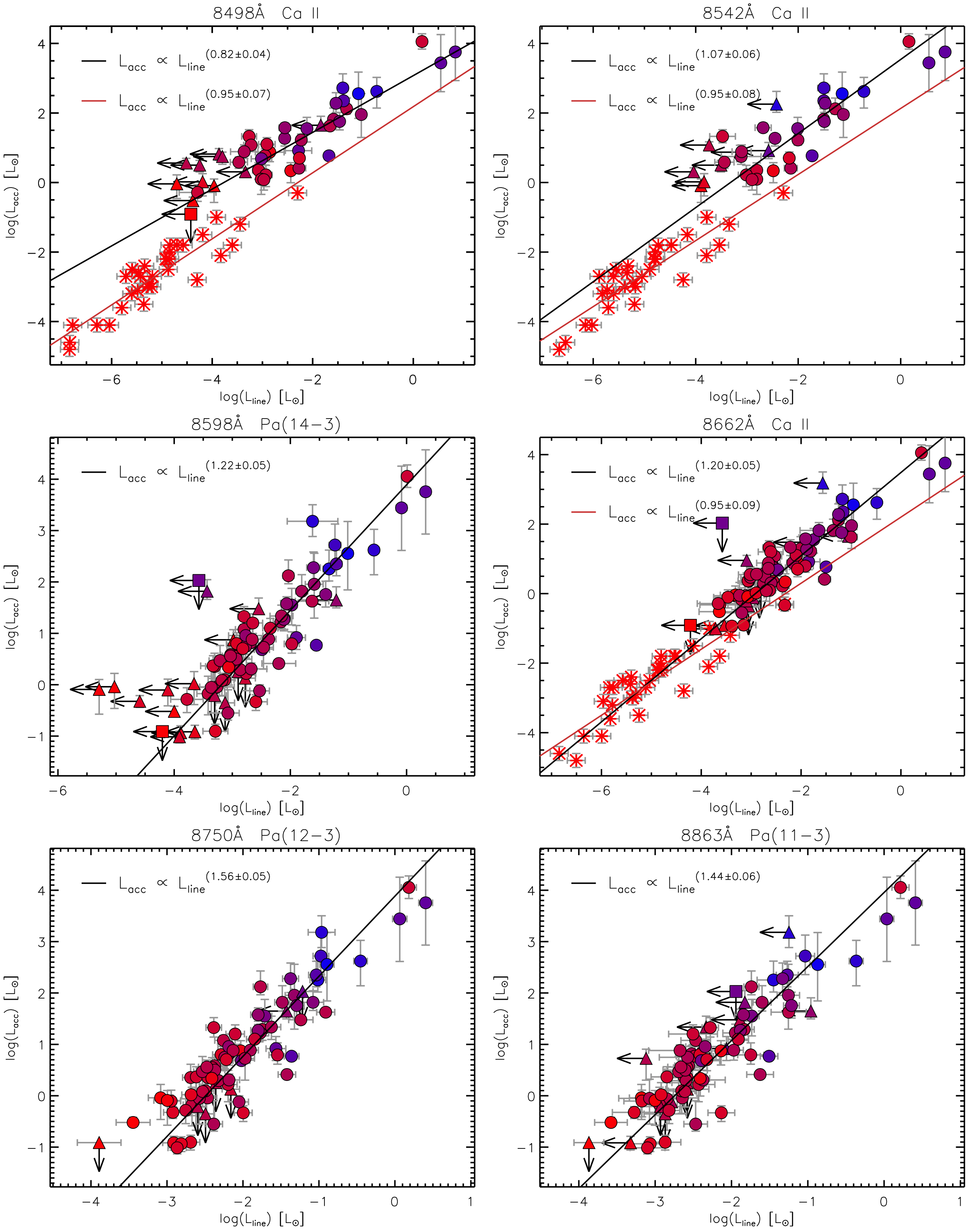

Figure 4.12: continued.

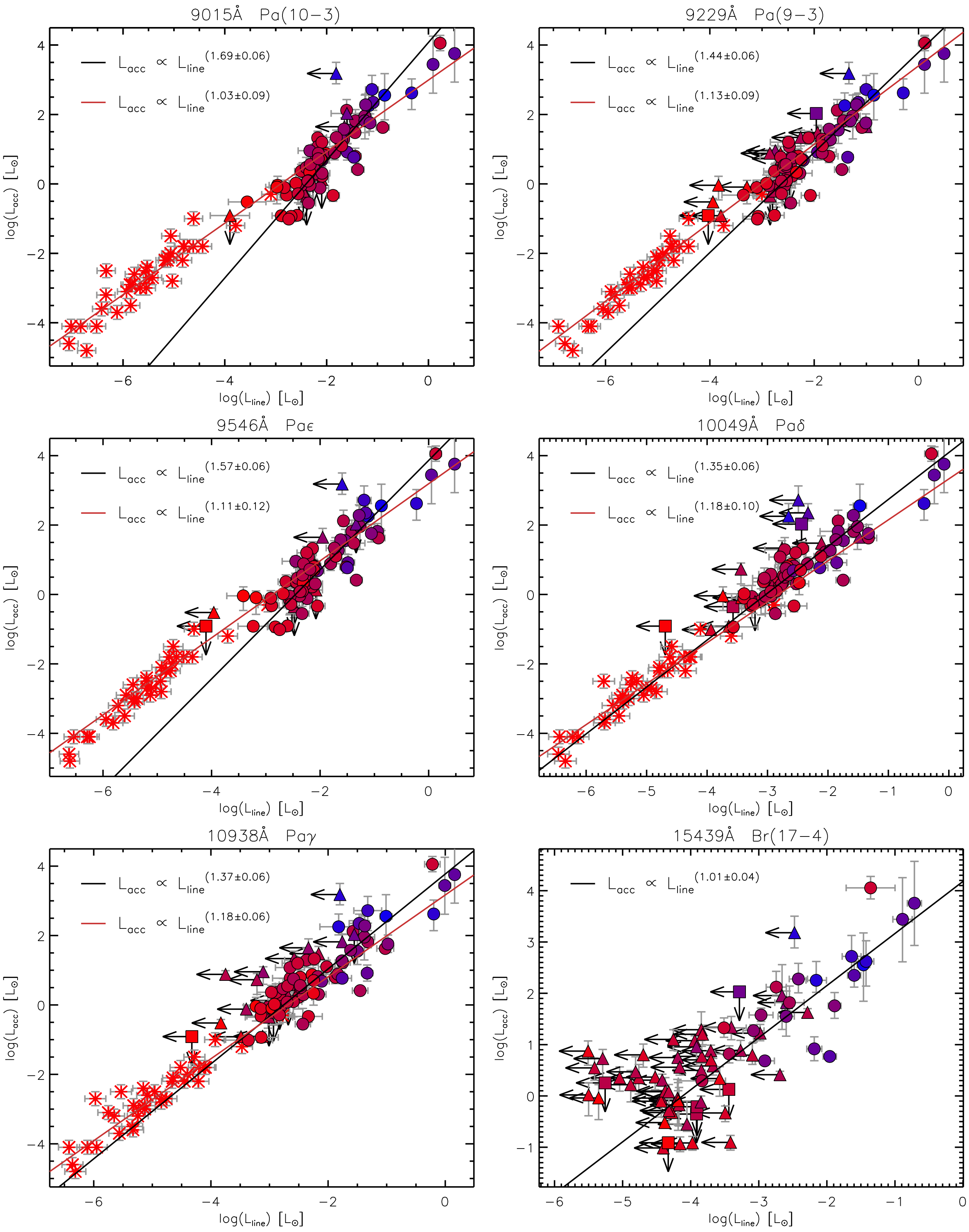

Figure 4.12: continued.

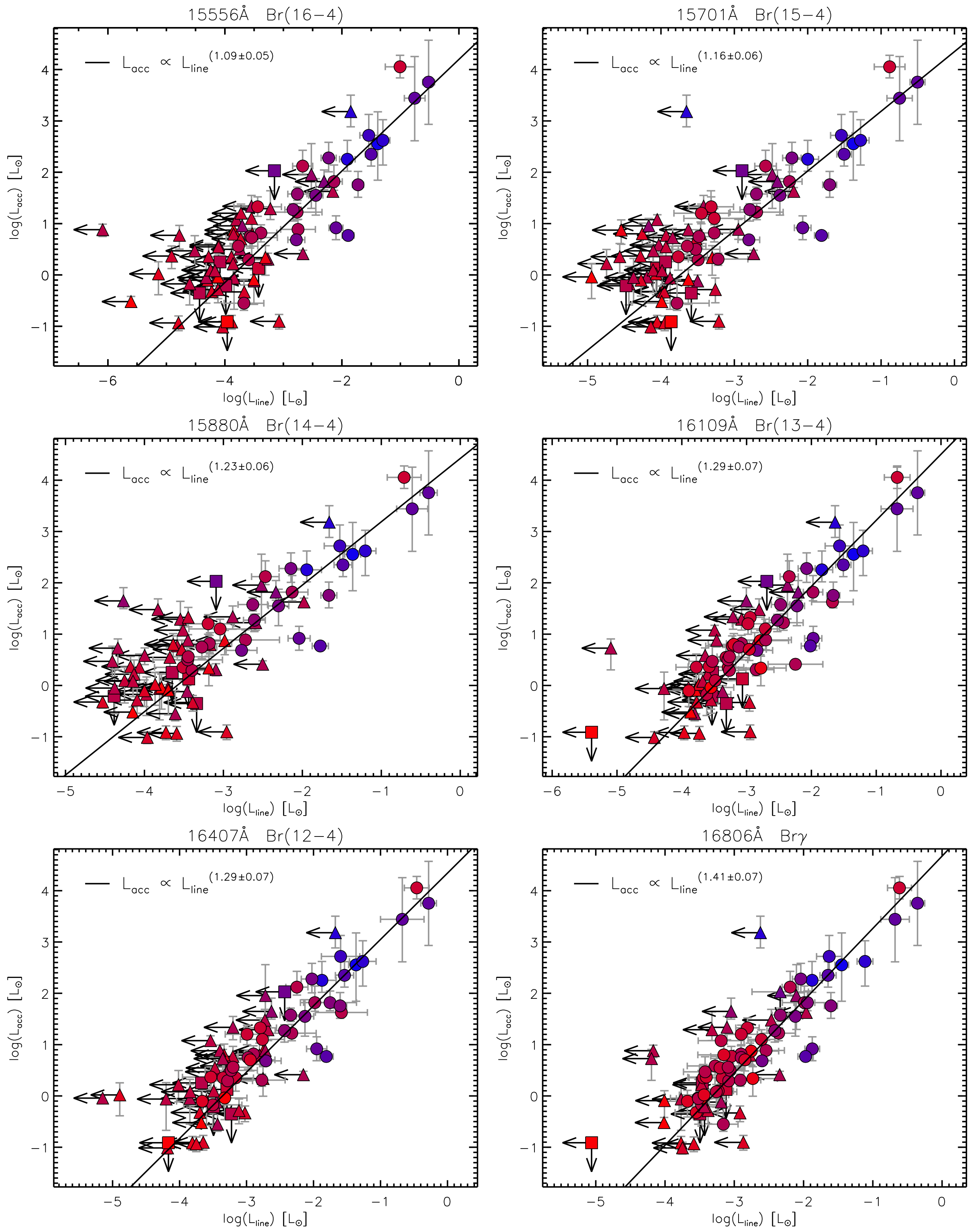

Figure 4.12: continued.

Table 4.1: This table0 displays all of the luminosity relationships plotted in Figures 4.3 to 4.12. The best-fit slope and intercept are provided in columns 6 and 7, while the numbers of emission lines used in their calculation are provided in column 4. For comparison the best-fit parameters for CTTs by Alcalá *et al.* (2014) are provided in the last two columns.

Line	λ	Line	No.	No.	This work		Alcalá *et al.* (2014)	
No.	(Å)		Detections	Limits	$A \pm \sigma_A$	$B \pm \sigma_{\mathrm{B}}$	A $\pm \sigma_A$	$B \pm \sigma_B$
1	3797	H(10-2)	59	31	3.13 ± 0.12	1.29 ± 0.07	2.58 ± 0.27	1.00 ± 0.05
2	3835	H(9-2)	36	48	3.00 ± 0.12	1.19 ± 0.07	2.53 ± 0.27	1.01 ± 0.05
3	3889	H(8-2)	22	60	3.12 ± 0.15	1.25 ± 0.08	2.55 ± 0.29	1.04 ± 0.06
4	4102	Hδ	25	66	2.75 ± 0.11	1.23 ± 0.07	2.50 ± 0.28	1.06 ± 0.06
5	4340	Hγ	39	52	2.62 ± 0.09	1.16 ± 0.06	2.50 ± 0.25	1.09 ± 0.05
6	4861	Hβ	81	10	2.53 ± 0.08	1.36 ± 0.06	2.31 ± 0.23	1.11 ± 0.05
7	5876	He I	36	26	4.84 ± 0.27	1.36 ± 0.09	3.51 ± 0.30	1.13 ± 0.06
8	6300	[O I]	44	32	4.09 ± 0.13	1.06 ± 0.04	-	-
9	6563	Hα	89	2	1.88 ± 0.04	1.12 ± 0.03	1.50 ± 0.26	1.12 ± 0.07
10	7773	O I	30	20	3.78 ± 0.20	1.07 ± 0.07	3.91 ± 0.51	1.16 ± 0.09
11	8446	O I	57	20	2.90 ± 0.08	0.73 ± 0.03	-	-
12	8498	Ca II	41	12	3.07 ± 0.10	0.82 ± 0.04	2.18 ± 0.38	0.95 ± 0.07
13	8542	Ca II	34	10	3.54 ± 0.14	1.07 ± 0.06	2.13 ± 0.42	0.95 ± 0.08
14	8598	Pa(14-3)	74	15	3.89 ± 0.12	1.22 ± 0.05	-	-
15	8662	Ca II	79	11	3.48 ± 0.11	1.20 ± 0.05	2.20 ± 0.43	0.95 ± 0.09
16	8750	Pa(12-3)	90	1	3.88 ± 0.11	1.56 ± 0.05	-	-
17	8863	Pa(11-3)	78	13	3.96 ± 0.13	1.44 ± 0.06	-	-
18	9015	Pa(10-3)	87	4	4.07 ± 0.13	1.69 ± 0.06	2.99 ± 0.49	1.03 ± 0.09
19	9229	Pa(9-3)	73	17	3.79 ± 0.13	1.44 ± 0.06	3.40 ± 0.47	1.13 ± 0.09
20	9546	Paϵ	86	5	3.86 ± 0.12	1.57 ± 0.06	3.19 ± 0.58	1.11 ± 0.12
21	10049	Paδ	66	17	4.09 ± 0.14	1.35 ± 0.06	3.33 ± 0.47	1.18 ± 0.10
22	10829	He I	41	27	5.67 ± 0.34	1.72 ± 0.12	2.62 ± 0.57	1.11 ± 0.12
23	10938	Paγ	75	16	3.77 ± 0.13	1.37 ± 0.06	3.17 ± 0.31	1.18 ± 0.06
24	12818	Paβ	79	8	3.12 ± 0.10	1.21 ± 0.05	2.45 ± 0.39	1.04 ± 0.08
25	15439	Br(17-4)	28	59	4.18 ± 0.15	1.01 ± 0.04	-	-
26	15556	Br(16-4)	33	55	4.20 ± 0.16	1.09 ± 0.05	-	-
27	15701	Br(15-4)	37	51	4.35 ± 0.17	1.16 ± 0.06	-	-
28	15880	Br(14-4)	33	56	4.42 ± 0.18	1.23 ± 0.06	-	-
29	16109	Br(13-4)	52	38	4.50 ± 0.18	1.29 ± 0.07	-	-
30	16407	Br(12-4)	44	46	4.34 ± 0.19	1.29 ± 0.07	-	-
31	16806	Br(11-4)	61	29	4.67 ± 0.19	1.41 ± 0.07	-	-
32	21661	Brγ	69	18	4.23 ± 0.16	1.31 ± 0.06	3.60 ± 0.38	1.16 ± 0.07

lines. In particular the Balmer and Brackett series lines show an increasing B value as the energy level transitions get lower i.e. B is increasing with wavelength. This trend is also evident in the Balmer series for the CTTs; no CTTs data is present for a Brackett series comparison. This could be an optical depth effect. However, the Paschen series does not follow such a trend. The scatter of the points are higher for this series too, in both HAeBes and CTTs. This gives the appearance of B looking roughly constant, although in this work there appears to be a decline around Paγ and Paβ.

Overall, it appears that the relationship between $L_{\rm acc}$ and $L_{\rm line}$, for all lines, is well correlated in HAeBes, although the slope is slightly enhanced over the set of CTTs analysed by Alcalá *et al.* (2014). Caution should be noted in the use of the Ca II triplet, due to Paschen blending. Caution is also advised in the use of the He I and O I lines, as their complex line profiles suggest various origins, some of which may not be associated with accretion. More importantly, the actual line profiles themselves can lead to incorrect luminosities due to multiple components.

4.6 Discussion

Since all of the emission lines appear to be correlated with the accretion luminosity it is worth discussing which lines serve as the "best" tracers of accretion i.e. most reliably detected and likely associated directly with accretion. That way the best lines can be prioritised in future observations.

In Table 4.2 all 32 lines are presented along with details of the number of emission line detections. The other columns of the table are split into different categories based upon emission detection and UV-excess detection. The total

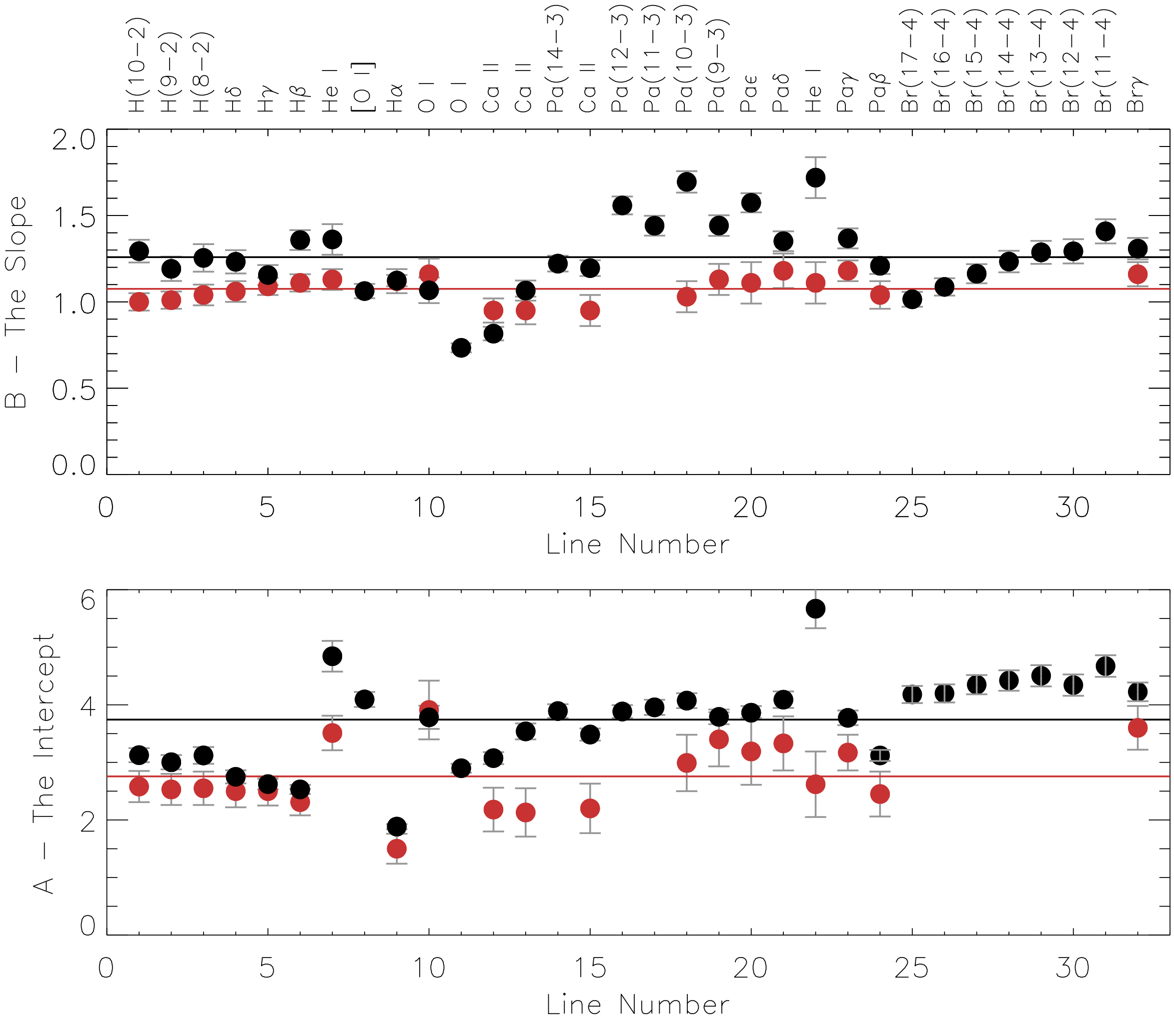

Figure 4.13: The slope and intercept values describing the best-fits to the L_{acc} vs. L_{line} relationships for each line, which are recorded in 4.12, are plotted above in black. The slopes are in the top panel and the intercepts are in the bottom panel. A solid black line denotes the mean values, which are $\bar{B} = 1.26 \pm 0.22$ and $\bar{A} = 3.74 \pm 0.78$. The values for CTTs obtained by Alcalá *et al.* (2014) are also plotted here in red; their mean values are $\bar{B} = 1.08 \pm 0.08$ and $\bar{A} = 2.76 \pm 0.60$.

Table 4.2: This table details all of the measured emission lines, along with their respective number of detections. The final four columns denote the four categories into which each star of the sample can belong to for a given line; their descriptions are provided in the text. 'Emis' denotes emission, and ΔD_B denotes a UV-excess detection.

Line Number	λ (Å)	Line	Emission Lines Detected	No. of stars which match the criteria			
				Emis - Y ΔD_B - Y	Emis - N ΔD_B - N	Emis - Y ΔD_B - Y	Emis - N ΔD_B - N
1	3797	H(10-2)	59	46	17	13	15
2	3835	H(9-2)	36	33	30	3	25
3	3889	H(8-2)	22	22	41	0	28
4	4102	Hδ	25	21	42	4	24
5	4340	Hγ	39	30	33	9	19
6	4861	Hβ	81	58	5	23	5
7	5876	He I	36	30	33	6	22
8	6300	[O I]	44	31	32	13	15
9	6563	Hα	89	61	2	28	0
10	7773	O I	30	26	37	4	24
11	8446	O I	57	43	20	14	14
12	8498	Ca II	41	35	28	6	22
13	8542	Ca II	34	32	31	2	26
14	8598	Pa(14-3)	74	56	7	18	10
15	8662	Ca II	79	58	5	21	7
16	8750	Pa(12-3)	90	62	1	28	0
17	8863	Pa(11-3)	78	57	6	21	7
18	9015	Pa(10-3)	87	61	2	26	2
19	9229	Pa(9-3)	73	52	11	21	7
20	9546	Paϵ	86	61	2	25	3
21	10049	Paδ	66	49	14	17	11
22	10829	He I	41	34	29	7	21
23	10938	Paγ	75	55	8	20	8
24	12818	Paβ	79	57	6	22	6
25	15439	Br(17-4)	28	23	40	5	23
26	15556	Br(16-4)	33	28	35	5	23
27	15701	Br(15-4)	37	31	32	6	22
28	15880	Br(14-4)	33	28	35	5	23
29	16109	Br(13-4)	52	44	19	8	20
30	16407	Br(12-4)	44	36	27	8	20
31	16806	Br(11-4)	61	50	13	11	17
32	21661	Brγ	69	50	13	19	9

accretion rate detection is defined as all of the HAeBes for which a UV-excess, referred to as a Balmer excess ΔD_B, was clearly measured in the previous chapter. There are 63 stars which match this criteria. This includes the 7 stars in which an accretion rate could not be determined within the context of MA. Their inclusion is due to the measured ΔD_B likely being associated with accretion, although the exact method and rate of accretion has not been established.

The two categories, of emission and accretion, can be divided into two outcomes for each case, a yes and a no. This gives a total of four categories in which a star can lie e.g. a star may have a particular line in emission, but no ΔD_B was detected in the star. Upper limits on both the Balmer excess detection and the accretion rates are grouped into their respective *no detection* categories.

Table 4.2 is presented visually in Figure 4.14. The figure shows each line broken down into percentages for the four separate categories, with the total being 100% i.e the whole sample. In the figure there is clear division at 31% due to the detection of the Balmer excess occupying the upper 69% of the figure. This division is due to the detection of ΔD_B remaining constant for a star across all lines, as it is independent of the line measurement. The detection of the emission lines does change for the same star on a line to line basis, resulting in the various divisions in the plot. The four different categories provide a lot of information about each line.

1. The first category is where both emission and excess are detected, and is represented by the green segments in the diagram. This category measures if the line is a good one to one tracer of accretion i.e. excess is present and so is the emission line - good tracer. Examples of good tracers are Hα, Brγ, and Paβ as their emission detections fall predominately in this category.

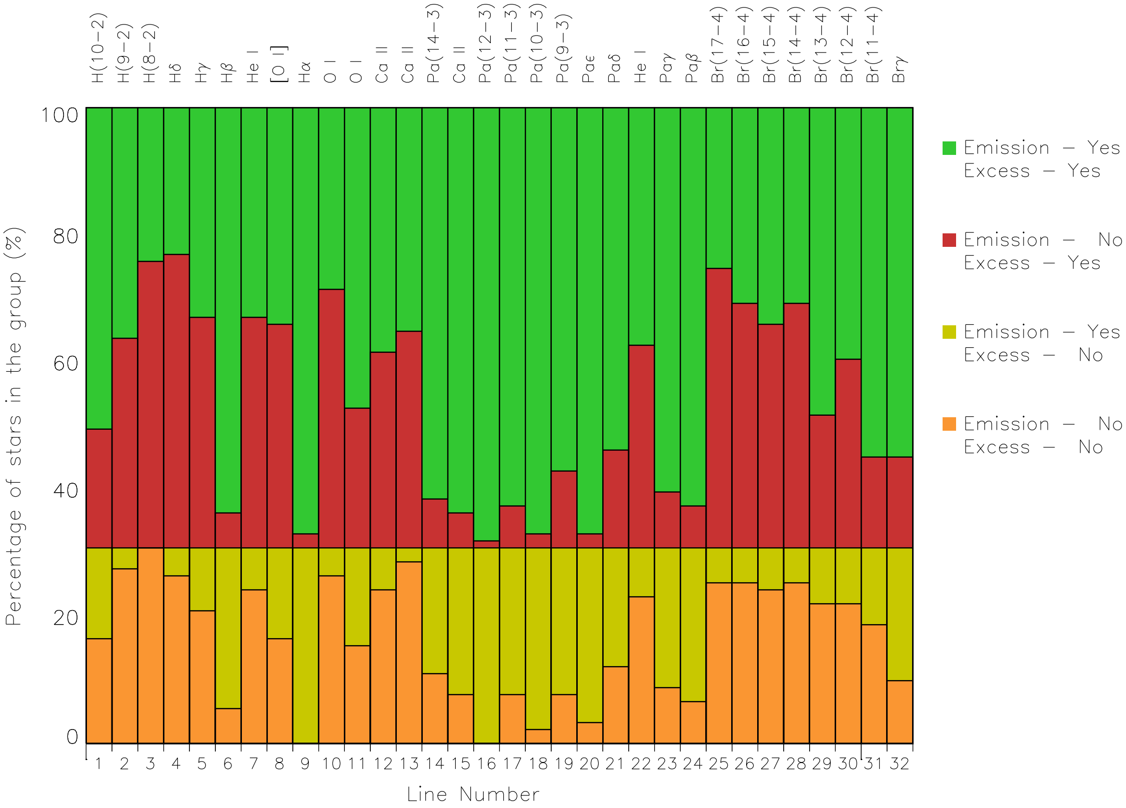

Figure 4.14: This figure presents for each line in turn, the whole HAeBe sample divided up into different categories based on whether an emission line was, or was not detected, and on whether ΔD_B could, or could not, be measured in Chapter 3. Details on the meanings of each category are provided in the text.

2. The second category measures how poor a tracer the line is. This category is shown in red and is where there has been a clear excess detected, and therefore accretion rate, but there is no corresponding emission line detection. An example of this is the oxygen 7773 Å line, in which the majority of ΔD_B detections have no corresponding emission line detection.

3. The third category denotes the objects in which emission is detected, but no excess is visible (shown in yellow in the figure). Interpretation of this category can be as either a good or poor tracer for two different reasons. Arguments as a poor tracer follow a "Red-Herring" approach, where the

emission present is considered to not actually be associated with accretion, since no excess is detected. This can then lead to false identifications of accretion through the L_{acc} vs. L_{line} relationship. However, arguments for this category being a good tracer assume that the emission present is sensitive to accretion, and therefore more readily detectable than an excess. This allows the L_{acc} vs. L_{line} relationship to be used to infer an accretion luminosity. The data in the table, and the percentages shown in the figure appear to favour the later argument. This is because as the green percentage increases, which is said to be a good accretion tracer, so does this category.

4. The fourth and final category is shown in orange and is generally a redundant category, stating that there is no emission and no excess detected i.e. the stars are not accreting and therefore no signatures of accretion are present. The category may reflect situations in which both the excess and emission lines lie below the detection limits of the methods used here. Due to there being no detection, anything in this category cannot be used as a tracer of accretion.

The findings in the table and figure highlight that the already established accretion tracing relationships are good ones. Namely, Hα, Brγ, and Paβ are all predominately in the green. They also have large percentages of detection in the yellow category; yes to emission, no to ΔD_B. This suggests that the emission lines may be tracing accretion which is below the detection limits of the Balmer excess method.

To test this, Hα is analysed. To do this, L_{line} is converted into L_{acc} using the relationship for Hα obtained in this work. This is performed only on the stars in

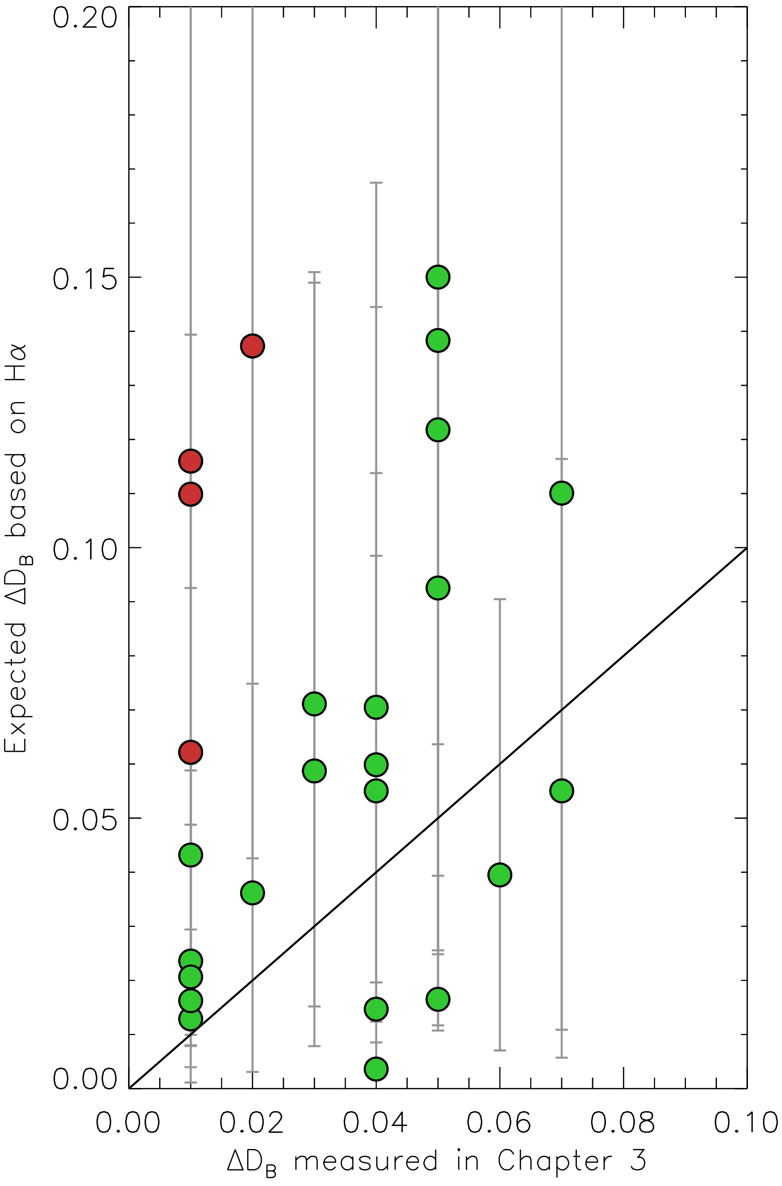

Figure 4.15: This figure shows the expected Balmer excess based on the strength of Hα against the stars in which only an upper limit could be placed on their UV-excess in chapter 3. The green points are stars which show agreement between the line strength and actual Balmer excess given the errors. Details of how the theoretical ΔD_B is calculated are given in the text.

which an upper limit could be placed on the strength of the Balmer excess (25 stars, see Chapter 3). The Hα calculated $L_{\rm acc}$ is then converted into $\dot{M}_{\rm acc}$ using the stellar parameters determined in Chapter 2. This, in turn, can be used to infer ΔD_B values which should theoretically be detected for the corresponding line strengths observed. The theoretical excess is calculated via the ΔD_B vs. $\dot{M}_{\rm acc}$ curves seen in Figure 3.6 of Chapter 3. The results of this are shown in Figure 4.15. In the figure the points which lie below the solid black line are ones where the upper limits of the measured ΔD_B from the UV-excess are greater than the ΔD_B values theorised by the Hα lines i.e. the accretion rate inferred by the line agrees with the upper limits. However, the points above the line shown the opposite situation; here the Hα line states that the accretion rate is higher than the upper limits would suggest, and that they should be detectable though UV-excess measurements. It is important to note that the errors on the excesses derived from Hα are largely due to the multiple conversions involved in going from the relationships to an actual excess, along with added uncertainties from various stellar parameters. These allow many of the theoretical excess to lie below the upper limits; and can therefore be deemed acceptable. All of the points where the Hα line predicts an excess which falls below the upper limits, within the errors, are marked as green points in the figure; they comprise 84% of the upper limits. There remain four points in which the predicted excesses are definitely greater than the observed upper limits on the excess. The upper limits on these particular stars are placed at only 0.02 mag, which may actually be an underestimate. Two of the stars were low temperature and required a distance to be adopted for calculation of stellar parameters; this could lead to incorrect surface gravities and hence excess measurements. However, these stars may actually have no accretion associated with them and the Hα emission could be due to another source e.g. it could be emission from a regular Be star disc if the star was misclassified. Overall, the figure demonstrates that the "yes in emission, no in excess" criteria serves as a good tracer indicator, meaning that Hα appears to be a good accretion tracer. The line luminosity can be safely used to determine the accretion rate.

Returning to Figure 4.14 there are also lines which appear to be poor tracers of accretion. In particular the Brackett series appears to get worse as an accretion tracer towards the higher order transitions, although Brγ itself appears to be a good tracer. Such a decline is likely because of the decreasing strength in emission towards the shorter wavelengths; which is supported by the green/red ratio changing between successive orders (with a slight hiccup around Br 12-4). Inversely, the Balmer series begins to improve again towards higher transition lines after Hδ. A possible explanation for this is because of the UV-excess veiling the lines. In veiling, the lines are filled in slightly by excess emission, which decreases their observed absorption profiles and gives then an $\mathrm{EW_{obs}}$ closer to 0. Then, after correction for the intrinsic absorption, which will be now be bigger than the observed line, an $\mathrm{EW_{cor}}$ is obtained in emission. This explanation is plausible, as towards higher orders the UV-excess gets stronger and $\mathrm{EW_{int}}$ gets weaker.

As for lines which are weighted more towards being poor tracers, like the O I 7773 Å and the He I 5876 Å lines, one possible explanation for their poor nature is that the definition of a line being in emission used in this work is an absolute one i.e. the strength is computed though summation over the whole line. This means that complex profiles where there is both absorption and emission present may not be classed as in emission by this definition, as the opposing profile contributions can cancel each other out in extreme situation (or at least the net emission/absorption will be drastically altered). In such cases some stars may be found to have no emission detection despite the clear presence of an inverse P-Cygni profile. Therefore, when considering accretion in HAeBes analysis of line profiles, line strengths, and UV-excesses where possible, should all be used together to reach a consensus.

A final point is made here on the emission lines which are detected less frequently, and take up a large fraction of the "no emission detected, UV-excess detected" part of Figure 4.14. Despite them being technically poor tracers from a detection point of view, when they are detected they are nearly entirely seen to be correlated with a UV-excess. This, along with all of the relationships tested and fitted, suggests that all lines are correlated to the accretion luminosity. Since $L_{\rm acc}$ is strongly correlated to $L_\star$ too, it is possible that the relationships seen here are in fact just a consequence of the star's own stellar luminosity (Boehm & Catala 1995) which shall be explored and discussed in detail in an up-coming paper by Mendigutía et al. (2015, in prep).

4.7 Conclusion

This Chapter has focussed on expanding our understanding of relationships between $L_{\rm acc}$ and $L_{\rm line}$ in HAeBes, and how these relate to CTTs. The following key points are found:

- Relationships are obtained between $L_{\rm acc}$ and $L_{\rm line}$ for 32 different emission lines. In all cases a best fit is made to these lines, with the average correlation being $L_{\text{acc}} \propto L_{\text{line}}^{1.26 \pm 0.22}$. This is found to be in agreement with the CTTs observed by (Alcalá *et al.* 2014) where the average is $L_{\text{acc}} \propto L_{\text{line}}^{1.08 \pm 0.08}$. Overall, the relationship is measured to be steeper in HAeBes than in CTTs, and could therefore be even steeper in MYSOs.

- On an individual line basis, variations are seen in the $L_{\text{acc}} \propto L_{\text{line}}$ relationship between CTTs and HAeBes. 80% of the lines in common between the two samples are found to not agree with each other within their error margins. Therefore, this suggests that there are differences in the production of emission lines between the two. However, a large level of scatter has been observed in the line relationships of CTTs, suggesting that these differences may also be related to the actual sample compared against.

- An assessment of the reliability of each line as an accretion tracer has been performed though a comparison between the rates of emission line detection and UV-excess detection. Confirmation is found that the accretion tracers for CTTs, like Hβ, Hα, Paβ and Brγ, are also reliable tracers of accretion in HAeBe stars. Additionally, a few other lines are found to be possibly poor tracers based on their low levels of emission line detection e.g. [O I]$_{\lambda 6300}$ and He I 5876 Å. However, when these lines are detected they are nearly always associated with a UV-excess

- The sheer number of objects and emission lines analysed here provide robust relationships between accretion luminosity and line luminosity for an exceptional wavelength coverage, which opens up new diagnostics of accretion in the *J*-band. These relationships provide a useful tool for future work of accretion in both HAeBes and CTTs alike.

As a final remark, it appears that whenever emission lines are detected in HAeBes, that their luminosities are always correlated with the accretion luminosity of the star.

Chapter 5

Conclusions

This thesis has focused upon providing a statistical and investigation into the spectroscopic properties of Herbig Ae/Be stars. In particular, derivations of the stellar properties and accretion rates were the two key objectives in this research. This chapter provides a summary of the findings within this thesis, along with a look at the future challenges which await in this field of research.

5.1 Summary

The Herbig Ae/Be stars act as a bridge between the numerous and reasonably well understood low-mass CTTs, to the rare and deeply embedded MYSOs. HAeBes are optically visible stars, which makes them ideal objects for studying up to the MYSO mass range. This is the main reason these stars were selected for this study.

Knowledge is first required about the stellar parameters of the HAeBes in order to determine accretion rates and emission line luminosities. They are also required if any general comparisons are to be made between CTTs and MYSOs.

In this study the properties of 91 HAeBes are assessed using medium resolution spectra covering a wavelength rage from $\sim 3000 - 25000\,\text{Å}$. This is one of the largest spectroscopic studies to date, covering a huge wavelength range.

Chapter 1 provided a method of determining the temperature, surface gravity, reddening, luminosity, mass, radius, age, *and* distance to the majority of HAeBes in a consistent and homogeneous fashion (distances were adopted

This was done through spectral typing using medium resolution X-Shooter spectra. Specifically, the temperature, $T_{\rm eff}$, and surface gravity, log(g), of each star was calculated by comparing the broad absorption wings of the hydrogen Balmer series to model spectra. The absorption wings are sensitive to both $T_{\rm eff}$ and log(g), making them ideal for determining accurate spectral types. The remaining stellar parameters were determined through a combination of optical photometry and placing the stars on PMS tracks. There were a few exceptions to this method: the first were stars with $T_{\rm eff} < 9000\,\text{K}$, below which there is a degeneracy in determining log(g) from model atmospheres, so a distance had to be adopted to these stars; the others are stars with such strong emission lines that that even the broad wings used for analysis can no longer be seen. All remaining stellar parameters were calculated by placing the stars on a log(g) vs. $T_{\rm eff}$ plot, or an HR-diagram, and then properties were extracted from the PMS tracks plotted along side. Some of the previously adopted distances were revised, as they produced unfeasible results which yielded unlikely placements on the HR-diagram i.e. some of the adopted distances caused the calculated radii for these stars to be less than solar for stars much hotter than the Sun, which suggests that the distance adopted was underestimated.

By using the same instrument, and the same method throughout, the parameters are obtained in a homogeneous fashion for the majority of the stars. There are exceptions for low temperature stars, and stars with exceptionally strong emission lines. In general, the approach makes comparison within the sample more accurate than the case of adopting parameters from various literature sources. Comparisons against previous values in the literature are in agreement, which supports the methodology used here.

Chapter 3 focused on the calculation of accretion rates, ($\dot{M}_{\rm acc}$) – a crucial piece of information in understanding how HAeBes evolve. $\dot{M}_{\rm acc}$ was obtained by first making measurements of the UV-excess across the Balmer jump region. This was done by measuring the amount of excess flux that is seen on top of the underlying photosphere, referred to as the Balmer excess, ΔD_B. Such an excess is thought to be produced due to magnetospheric accretion taking place, at least in CTTs. Within the context of MA the truncated disc material is accreted though a column onto the star via the magnetic field lines. The material falls at speeds close to free-fall and shocks the photosphere upon impact. This shock produces X-rays which thermalise the surroundings, and in turn are visible as a hotspot on the surface, giving rise to a UV-excess. This excess was clearly detected in 63 stars of the sample, with an upper limit placeable on a further 25 stars; $\dot{M}_{\rm acc}$ was then derived for these stars within the context of magnetospheric accretion. However, 7 of the ΔD_B detections were not reproducible in this context. These 7 stars are all HBe stars, often with very large ΔD_B values of > 0.85, or high temperatures exceeding 20000 K. This suggests a possible breakdown in the disc-accretion regime in HBes, particularly for early-type HBes.

The HAeBes for which $\dot{M}_{\rm acc}$ was successfully determined were investigated further, to see how $\dot{M}_{\rm acc}$ changes as a function of mass and luminosity. Interestingly the HAes and HBes behaved differently from each other. In the mass comparisons, a relationship for the HAes was obtained of $\dot{M}_{\rm acc} \propto M_{\star}^{8.42\pm1.37}$, while in the HBes it was found to be much less steep, $\dot{M}_{\rm acc} \propto M_{\star}^{2.82\pm0.39}$. In CTTs this relationship is shallower again, being $M_{\star} \propto \dot{M}_{\rm acc}^{2.0}$ (Muzerolle *et al.* 2005; Natta *et al.* 2006). However, when comparing the accretion luminosity to the stellar luminosity it was found that the HAes and CTTs are in agreement with each other - their respective relationships are $L_{\rm acc} \propto L_{\star}^{1.53\pm0.14}$ and $L_{\rm acc} \propto L_{\star}^{1.5}$ (Natta *et al.* 2006; Tilling *et al.* 2008), while the HBes showed a much shallower relationship $L_{\rm acc} \propto L_{\star}^{0.84\pm0.13}$.

In order to better understand these various relationships, the ages of the HAeBes were examined too. It was found that the relationship between $\dot{M}_{\rm acc}$ and age varies between the HAe and HBe regime, with the relationship being of the form $\dot{M}_{\rm acc} \propto t^{-\eta}$. The exponent here for the HBes is $\eta = 2.02 \pm 0.09$, while for HAes it is steeper, with $\eta = 4.06 \pm 0.53$. This result is expected to be influenced by the most massive stars, which have the higher accretion rates, and are only observable at small ages due to their quicker evolution. Similarly, the less massive stars have a longer PMS lifetime which could allow their accretion rate to diminish with this time; this could perhaps explain the change in the relationship. In general, this result may indicate that $\dot{M}_{\rm acc}$ decreases quicker for older HAeBe stars. However, in CTTs it has been observed that $\eta \sim 2$ (Sicilia-Aguilar *et al.* 2010; Caratti o Garatti *et al.* 2012). This suggests that there is a change taking place between the CTTs to HAes mass boundary, and also between the HAes and HBes.

Overall, these relationships indicate that $\dot{M}_{\rm acc}$ is an evolutionary property of

HAeBes, which decreases as the star evolves, possibly accreting all of its disc material or dispersing it with time. Modelling of disc dispersion through photoevaporation suggests that the disc lifetimes are indeed shorter for more massive stars (Gorti & Hollenbach 2009). This offers an explanation for the steep exponent observed in the HAes, in which we could be observing the transition stage of disc dispersion as they approach the main sequence, resulting in a decreased accretion rate. The HBes, on the other hand, are always younger and may not have existed long enough for disc dispersal so really get going, which allows them to retain a more shallow relationship between $\dot{M}_{\rm acc}$ and age, making them appear similar to CTTs.

An unanswered question remains here, which is why does $L_{\rm acc}$ show similarites between CTTs and HAes, but not between CTTs and HBes? This was investigated in Chapter 4 by analysing $L_{\rm acc}$ with respect to the line luminosities, $L_{\rm line}$. It has been established in CTTs that $L_{\rm acc}$ is correlated with $L_{\rm line}$ for various lines (Muzerolle *et al.* 1998c; Calvet *et al.* 2004; Dahm 2008; Herczeg & Hillenbrand 2008; Mendigutía *et al.* 2011a; Rigliaco *et al.* 2012). This has also been shown to be true for a few lines in HAeBes too (Garcia Lopez *et al.* 2006; Mendigutía *et al.* 2011a). So, comparisons were made here of $L_{\rm acc}$ as a function of $L_{\rm line}$ for 32 different emission lines in total. It was found that the already established accretion tracers in CTTs also work well in HAeBes. For the HAeBes a mean slope of 1.26 ± 0.22 is obtained for the $L_{\rm acc}$ vs. $L_{\rm line}$ relationship, while for CTTs an exponent of 1.08 ± 0.08 is seen. They are in agreement. However, on a line to line basis, the exponent of this relationship is observed to disagree in 80% of the 24 lines in common. The CTTs and HAeBes are seen to agree with each around the boundary between them, but as $L_{\rm line}$ increases, the corresponding $L_{\rm acc}$ becomes more deviant i.e. L_{acc} increases at a faster rate, resulting in a steeper exponent to the slope, which occurs towards the HBe mass regime. Overall, it has been observed that all lines appear to be correlated with the accretion luminosity . This is a similar behaviour to the L_{acc} vs. $L_\star$ situation observed in Chapter 3. In a sense, this means that all lines are good tracers. Considering this universal agreement and the trend with $L_\star$, it appears that the underlying relationship between L_{line} and L_{acc} is perhaps solely due to the stellar photosphere.

In summary the chapters within this thesis have found:

- Stellar parameter determinations for the entire sample, the majority following the same methodology.

- Accretion rates are measured directly from a UV-excess within the context of magnetospheric accretion, although some Herbig Be stars cannot be modeled with this context.

- Relationships with various stellar parameters and accretion rates appear to deviate between the CTTs, HAe, and HBe groups.

- The accretion rate is observed to diminish with age, suggesting that the decrease is an evolutionary effect. The relationship is observed to be steeper in HAes than HBes.

- Accretion luminosity versus line luminosity relationships are established for 32 different emission lines. Many of these are new diagnostics both for HAeBes, and for CTTs. Deviations are observed from the CTTs towards the early-type HBes.

5.2 Future Work

There have been many exciting developments in the the field of PMS stars lately, particularly in regards to the Herbig Ae/Be stars. Despite this, there remain many questions about their circumstellar environments, how they accrete, and their relation to CTTs and MYSOs. This thesis has provided information which helps towards a better understanding of these relations, but more work is required. This section will provide information on the topics that still need to be addressed in this field, along with future extensions to the work presented in this thesis.

Applicability of Magnetospheric Accretion

Magnetospheric accretion has been convincingly demonstrated as a viable form of accretion in CTTs (Calvet & Gullbring 1998; Muzerolle *et al.* 1998a; Gullbring *et al.* 2000; Muzerolle *et al.* 2001; Kurosawa *et al.* 2011; Ingleby *et al.* 2013). It has also been shown to be applicable in some HAeBes too (Mendigutía *et al.* 2011a; Donehew & Brittain 2011; Pogodin *et al.* 2012). However, their applicability has been brought into question by one or two stars which could not be modelled in this context (Mendigutía *et al.* 2011a). This thesis has demonstrated that MA does hold in the majority of HAeBes, so their formation, accretion rates, and evolution may be similar to CTTs. However, there were 7 stars in the sample where clear UV-excess detection could not be modelled within the context of MA. All of these were HBe objects with either a high temperature, a large excess, or both. There were also numerous HAeBes which required accretion columns to take up more than 25% of the total stellar surface, in order to reproduce the observed UV-excesses. These above points suggest that there is perhaps a breakdown of MA in HAeBes, particularly at high masses. Therefore, efforts should be made to try and either prove or rule-out MA in HAeBes. This means probing as close to the star as possible through interferometry or polarisation techniques in order to try to resolve the effects of an accretion column, or even the column itself.

Thoughts should also be taken into consideration about an alternative method of accretion in HAeBes. One method could be a boundary-layer model, which has been shown to be applicable in a sample of HAeBes (Blondel & Djie 2006). The boundary-layer model involves the disc extending right down to the stellar surface, where kinetic energy is lost through small, oblique shocks. This energy is radiated away in a boundary layer around the star, of a given thickness, giving rise to a UV-excess (Bertout *et al.* 1988). For this theory to be tested, detailed UV observations are required.

Herbig Ae/Be circumstellar geometry

HAeBes are known to have circumstellar discs around them, as this has been inferred from polarisation measurements (Vink *et al.* 2002, 2005) and direct observations (McCaughrean & O'dell 1996; Grady *et al.* 2001). In recent years there have been observations of CO in the discs of HAeBes which are well explained by gaps in the discs (van der Plas *et al.* 2009, 2015; Maaskant *et al.* 2013; Ilee *et al.* 2014). This is one example of our understanding about the geometry of the circumstellar material around HAeBes improving. Further knowledge has been obtained on where the Brγ line originates from too, which is thought to be interior to the dust sublimation radius (Kraus *et al.* 2008). Further interferometric investigations confirm this, and also find that it can originate outside of the co-rotation radius, in the case of the HAe star HD 100546, which suggests that it is not formed from within an accretion column (Mendigutia *et al.*, submitted).

Another example of improved understanding, as of late, is that observations were made of the outflow material produced by the HAeBe star HD 163296 (Ellerbroek *et al.* 2014). The authors noted that the visible clumps are perpendicular to the disc and can provide information about the outflow history, where the velocities and collimation observed support outflow production though a magneto-centrifugal jet. Furthermore, no dust is detected in the outflows suggesting that the launching occurs within the dust sublimation radius. It would be ideal in future observations to probe closer in to confirm the jet launching mechanism, while observations of more HAeBe systems showing outflows would be greatly welcome.

Line profiles can provide an insight into the geometry too, but the profiles can be complicated by many components (see the discussion of the O I and He I lines in Chapter 4). Variability also plays a factor in such observations, which makes multi-epoch observations necessary to assess how the line profile is changing (if at all). Observations of line profiles would serve as a helpful tool alongside other observational techniques to help confirm findings. Additionally, more dedicated modelling of the complex line profiles would help in understanding their origins (e.g. Muzerolle *et al.* 1998a; Kurosawa *et al.* 2011; Kurosawa & Romanova 2012)

Overall, a greater understanding of the geometries in HAeBes are required in order to disentangle potential disc winds, accretion columns, and outflows.

Extreme Emission Line Objects

As presented in this work there are a number of HAeBes which have a large amount of strong emission lines in their spectra, and no photospheric absorption features. It was not possible to obtain spectral types of these objects from the spectra in this work, so their stellar parameters remain less certain as a result. These particular stars are fascinating ones, as they may represent some of the earliest stages of evolution in these stars. They often have large UV-excess and high line luminosities, both of which are indicative of high accretion rates; high accretion rates are typically attributed to the stars being massive and young. Some of these stars may indeed be bordering the MYSO mass range and can provide a better insight into PMS stars as a function of mass. In order to obtain a better understanding of these stars, more observations are required at different wavelengths. This will allow us to see if line profiles remain the same throughout, or if there are perhaps some indicators at other wavelengths of outflows, winds, and even accretion.

Line Luminosity Relationship

This work has helped to confirm that the many established $L_{\rm line}$ relationships to $L_{\rm acc}$ in CTTs are also present in HAeBes. However, the exact relationships differ from each other more than expected than if they share similar line origin. This ties back to the geometry, that greater knowledge of where the emitting regions are within the circumstellar environment are needed. This will also help in solving why $L_{\rm line}$ remains correlated with $L_{\rm acc}$ over many orders of magnitude.

Recently, two NIR lines at $11.32\,\mu$m and $12.37\,\mu$m have been presented as potential accretion tracers in CTTs, as the luminosities of the lines correlate with the accretion luminosity (Rigliaco *et al.* 2015). It may be the case that these lines will also trace accretion in HAeBes, but more importantly they may provide a way of investigating accretion in more deeply embedded stars, specifically the MYSOs.

5.3 Final Remarks

To conclude, this thesis presents the culmination of one of the largest dedicated spectroscopic surveys into Herbig Ae/Be stars to date, with the results providing robust stellar parameters, mass accretion rates, and many line luminosity relationships for the sample. It is found that the HAeBes display many properties similar to CTTs, however there are also breaks in these general trends between them; it appears that CTTs, HAes, and HBes all behave differently from each other to some degree. In particular, evidence has been presented that magnetospheric accretion may be breaking down in the Herbig Be mass range.

References

Ababakr, K.M., Fairlamb, J.R., Oudmaijer, R.D. & van den Ancker, M.E. (2015). Spectroscopy and Linear Spectropolarimetry of the Early Herbig Be Stars PDS 27 and PDS 37. MNRAS*, submitted*. 34, 61, 65, 66

Acke, B. & van den Ancker, M.E. (2006). Resolving the disk rotation of HD 97048 and HD 100546 in the [O I] 6300 Å line: evidence for a giant planet orbiting HD 100546. A&A, **449**, 267–279. 120, 144

Acke, B., van den Ancker, M.E. & Dullemond, C.P. (2005). [O I] 6300 Å emission in Herbig Ae/Be systems: Signature of Keplerian rotation. A&A, **436**, 209–230. 120, 140

Alcalá, J.M., Natta, A., Manara, C.F., Spezzi, L., Stelzer, B., Frasca, A., Biazzo, K., Covino, E., Randich, S., Rigliaco, E., Testi, L., Comerón, F., Cupani, G. & D'Elia, V. (2014). X-shooter spectroscopy of young stellar objects. IV. Accretion in low-mass stars and substellar objects in Lupus. A&A, **561**, A2. 16, 132, 133, 136, 151, 155, 156, 157, 158, 162, 163, 164, 173

Alecian, E., Wade, G.A., Catala, C., Grunhut, J.H., Landstreet, J.D., Bagnulo, S., Böhm, T., Folsom, C.P., Marsden, S. & Waite,

I. (2013). A high-resolution spectropolarimetric survey of Herbig Ae/Be stars - I. Observations and measurements. MNRAS, **429**, 1001–1026. 22, 79

Alexander, R., Pascucci, I., Andrews, S., Armitage, P. & Cieza, L. (2014). The Dispersal of Protoplanetary Disks. *Protostars and Planets VI*, 475–496. 20

Alexander, R.D. & Armitage, P.J. (2009). Giant Planet Migration, Disk Evolution, and the Origin of Transitional Disks. ApJ, **704**, 989–1001. 20

Alves, J.F., Lada, C.J. & Lada, E.A. (2001). Internal structure of a cold dark molecular cloud inferred from the extinction of background starlight. Nature, **409**, 159–161. 6

Alves de Oliveira, C., Schneider, N., Merín, B., Prusti, T., Ribas, Á., Cox, N.L.J., Vavrek, R., Könyves, V., Arzoumanian, D., Puga, E., Pilbratt, G.L., Kóspál, Á., André, P., Didelon, P., Men'shchikov, A., Royer, P., Waelkens, C., Bontemps, S., Winston, E. & Spezzi, L. (2014). Herschel view of the large-scale structure in the ¡ASTROBJ¿Chamaeleon¡/ASTROBJ¿ dark clouds. A&A, **568**, A98. 5

Andersen, J., Lindgren, H., Hazen, M.L. & Mayor, M. (1989). The pre-main-sequence binary system AK Scorpii. A&A, **219**, 142–150. 34

Andre, P., Ward-Thompson, D. & Barsony, M. (1993). Submillimeter continuum observations of Rho Ophiuchi A - The candidate protostar VLA 1623 and prestellar clumps. ApJ, **406**, 122–141. 12

André, P., Men'shchikov, A., Bontemps, S., Könyves, V., Motte, F., Schneider, N., Didelon, P., Minier, V., Saraceno, P., Ward-Thompson, D., di Francesco, J., White, G., Molinari, S., Testi, L., Abergel, A., Griffin, M., Henning, T., Royer, P., Merín, B., Vavrek, R., Attard, M., Arzoumanian, D., Wilson, C.D., Ade, P., Aussel, H., Baluteau, J.P., Benedettini, M., Bernard, J.P., Blommaert, J.A.D.L., Cambrésy, L., Cox, P., di Giorgio, A., Hargrave, P., Hennemann, M., Huang, M., Kirk, J., Krause, O., Launhardt, R., Leeks, S., Le Pennec, J., Li, J.Z., Martin, P.G., Maury, A., Olofsson, G., Omont, A., Peretto, N., Pezzuto, S., Prusti, T., Roussel, H., Russeil, D., Sauvage, M., Sibthorpe, B., Sicilia-Aguilar, A., Spinoglio, L., Waelkens, C., Woodcraft, A. & Zavagno, A. (2010). From filamentary clouds to prestellar cores to the stellar IMF: Initial highlights from the Herschel Gould Belt Survey. A&A, **518**, L102. 5

Arzoumanian, D., André, P., Didelon, P., Könyves, V., Schneider, N., Men'shchikov, A., Sousbie, T., Zavagno, A., Bontemps, S., di Francesco, J., Griffin, M., Hennemann, M., Hill, T., Kirk, J., Martin, P., Minier, V., Molinari, S., Motte, F., Peretto, N., Pezzuto, S., Spinoglio, L., Ward-Thompson, D., White, G. & Wilson, C.D. (2011). Characterizing interstellar filaments with Herschel in IC 5146. A&A, **529**, L6. 5

Avedisova, V. (2000). Catalogue of Galactic Star-Forming Regions. Observational Data. *Baltic Astronomy*, **9**, 569–572. 34

BACCIOTTI, F., RAY, T.P., MUNDT, R., EISLÖFFEL, J. & SOLF, J. (2002). Hubble Space Telescope/STIS Spectroscopy of the Optical Outflow from DG Tauri: Indications for Rotation in the Initial Jet Channel. ApJ, **576**, 222–231. 10

BAGNOLI, T., VAN LIESHOUT, R., WATERS, L.B.F.M., VAN DER PLAS, G., ACKE, B., VAN WINCKEL, H., RASKIN, G. & MEERBURG, P.D. (2010). An Inner Gaseous Disk Around the Herbig Be Star MWC 147. ApJL, **724**, L5–L8. 120

BAINES, D., OUDMAIJER, R.D., MORA, A., EIROA, C., PORTER, J.M., MERÍN, B., MONTESINOS, B., DE WINTER, D., COLLIER CAMERON, A., DAVIES, J.K., DEEG, H.J., FERLET, R., GRADY, C.A., HARRIS, A.W., HOARE, M.G., HORNE, K., LUMSDEN, S.L., MIRANDA, L.F., PENNY, A. & QUIRRENBACH, A. (2004). The pre-main-sequence binary HK Ori: spectro-astrometry and EXPORT data. MNRAS, **353**, 697–704. 34

BAINES, D., OUDMAIJER, R.D., PORTER, J.M. & POZZO, M. (2006). On the binarity of Herbig Ae/Be stars. MNRAS, **367**, 737–753. 37

BALBUS, S.A. & HAWLEY, J.F. (1991). A powerful local shear instability in weakly magnetized disks. I - Linear analysis. II - Nonlinear evolution. ApJ, **376**, 214–233. 10

BANERJEE, R., PUDRITZ, R.E. & ANDERSON, D.W. (2006). Supersonic turbulence, filamentary accretion and the rapid assembly of massive stars and discs. MNRAS, **373**, 1091–1106. 7

Bania, T.M. & Lyon, J.G. (1980). OB stars and the structure of the interstellar medium - Cloud formation and effects of different equations of state. ApJ, **239**, 173–192. 3

Basri, G. & Batalha, C. (1990). Hamilton echelle spectra of young stars. I - Optical veiling. ApJ, **363**, 654–669. 15

Bate, M.R., Bonnell, I.A. & Bromm, V. (2003). The formation of a star cluster: predicting the properties of stars and brown dwarfs. MNRAS, **339**, 577–599. 8

Beccari, G., Spezzi, L., De Marchi, G., Paresce, F., Young, E., Andersen, M., Panagia, N., Balick, B., Bond, H., Calzetti, D., Carollo, C.M., Disney, M.J., Dopita, M.A., Frogel, J.A., Hall, D.N.B., Holtzman, J.A., Kimble, R.A., McCarthy, P.J., O'Connell, R.W., Saha, A., Silk, J.I., Trauger, J.T., Walker, A.R., Whitmore, B.C. & Windhorst, R.A. (2010). Progressive Star Formation in the Young Galactic Super Star Cluster NGC 3603. ApJ, **720**, 1108–1117. 10

Beltrán, M.T., Sánchez-Monge, Á., Cesaroni, R., Kumar, M.S.N., Galli, D., Walmsley, C.M., Etoka, S., Furuya, R.S., Moscadelli, L., Stanke, T., van der Tak, F.F.S., Vig, S., Wang, K.S., Zinnecker, H., Elia, D. & Schisano, E. (2014). Filamentary structure and Keplerian rotation in the high-mass star-forming region G35.03+0.35 imaged with ALMA. A&A, **571**, A52. 17

Beristain, G., Edwards, S. & Kwan, J. (2001). Helium Emission from Classical T Tauri Stars: Dual Origin in Magnetospheric Infall and Hot Wind. ApJ, **551**, 1037–1064. 67

Bernasconi, P.A. & Maeder, A. (1996). About the absence of a proper zero age main sequence for massive stars. A&A, **307**, 829–839. 47, 71, 106

Bertout, C. (1989). T Tauri stars - Wild as dust. ARA&A, **27**, 351–395. 15

Bertout, C., Basri, G. & Bouvier, J. (1988). Accretion disks around T Tauri stars. ApJ, **330**, 350–373. 15, 182

Beuther, H., Kainulainen, J., Henning, T., Plume, R. & Heitsch, F. (2011). The Coalsack near and far. A&A, **533**, A17. 5

Blandford, R.D. & Payne, D.G. (1982). Hydromagnetic flows from accretion discs and the production of radio jets. MNRAS, **199**, 883–903. 10

Blondel, P.F.C. & Djie, H.R.E.T.A. (2006). Modeling of PMS Ae/Fe stars using UV spectra. A&A, **456**, 1045–1068. 182

Boehm, T. & Catala, C. (1994). Forbidden lines in Herbig Ae/Be stars: the [O I](1F) 6300.31A and 6363.79A lines. I. Observations and qualitative analysis. A&A, **290**, 167–175. 140, 144

Boehm, T. & Catala, C. (1995). Rotation, winds and active phenomena in Herbig Ae/Be stars. A&A, **301**, 155. 152, 172

Bonnell, I.A. & Bate, M.R. (2002). Accretion in stellar clusters and the collisional formation of massive stars. MNRAS, **336**, 659–669. 11

Bonnell, I.A., Bate, M.R., Clarke, C.J. & Pringle, J.E. (1997). Accretion and the stellar mass spectrum in small clusters. MNRAS, **285**, 201–208. 11

Bontemps, S., Andre, P., Terebey, S. & Cabrit, S. (1996). Evolution of outflow activity around low-mass embedded young stellar objects. A&A, **311**, 858–872. 12

Bontemps, S., André, P., Könyves, V., Men'shchikov, A., Schneider, N., Maury, A., Peretto, N., Arzoumanian, D., Attard, M., Motte, F., Minier, V., Didelon, P., Saraceno, P., Abergel, A., Baluteau, J.P., Bernard, J.P., Cambrésy, L., Cox, P., di Francesco, J., di Giorgo, A.M., Griffin, M., Hargrave, P., Huang, M., Kirk, J., Li, J., Martin, P., Merín, B., Molinari, S., Olofsson, G., Pezzuto, S., Prusti, T., Roussel, H., Russeil, D., Sauvage, M., Sibthorpe, B., Spinoglio, L., Testi, L., Vavrek, R., Ward-Thompson, D., White, G., Wilson, C., Woodcraft, A. & Zavagno, A. (2010). The Herschel first look at protostars in the Aquila rift. A&A, **518**, L85. 5

Bouvier, J., Alencar, S.H.P., Harries, T.J., Johns-Krull, C.M. & Romanova, M.M. (2007). Magnetospheric Accretion in Classical T Tauri Stars. *Protostars and Planets V*, 479–494. 21, 79

Brand, J. & Wouterloot, J.G.A. (1995). IRAS sources beyond the solar circle. V. Properties of far-outer Galaxy molecular clouds. A&A, **303**, 851. 2

Bressan, A., Marigo, P., Girardi, L., Salasnich, B., Dal Cero, C., Rubele, S. & Nanni, A. (2012). PARSEC: stellar tracks and isochrones with the PAdova and TRieste Stellar Evolution Code. MNRAS, **427**, 127–145. 25, 47, 71, 106

Brittain, S.D., Najita, J.R., Carr, J.S., Liskowsky, J., Troutman, M.R. & Doppmann, G.W. (2013). High-resolution Near-infrared Spectroscopy of HD 100546. II. Analysis of Variable Rovibrational CO Emission Lines. ApJ, **767**, 159. 20, 78

Cabrit, S., Edwards, S., Strom, S.E. & Strom, K.M. (1990). Forbidden-line emission and infrared excesses in T Tauri stars - Evidence for accretion-driven mass loss? ApJ, **354**, 687–700. 140

Calvet, N. & Gullbring, E. (1998). The Structure and Emission of the Accretion Shock in T Tauri Stars. ApJ, **509**, 802–818. 15, 78, 96, 97, 98, 120, 181

Calvet, N., Muzerolle, J., Briceño, C., Hernández, J., Hartmann, L., Saucedo, J.L. & Gordon, K.D. (2004). The Mass Accretion Rates of Intermediate-Mass T Tauri Stars. ApJ, **128**, 1294–1318. 16, 80, 120, 130, 136, 139, 179

Canto, J., Rodriguez, L.F., Calvet, N. & Levreault, R.M. (1984). Stellar winds and molecular clouds - Herbig Be and AE type stars. ApJ, **282**, 631–640. 34

Caratti o Garatti, A., Garcia Lopez, R., Antoniucci, S., Nisini, B., Giannini, T., Eislöffel, J., Ray, T.P., Lorenzetti, D. & Cabrit, S. (2012). POISSON project. II. A multi-wavelength spectroscopic and photometric survey of young protostars in L 1641. A&A, **538**, A64. 110, 178

CARDELLI, J.A., CLAYTON, G.C. & MATHIS, J.S. (1989). The relationship between infrared, optical, and ultraviolet extinction. ApJ, **345**, 245–256. 46, 82, 86

CARMONA, A., VAN DEN ANCKER, M.E., AUDARD, M., HENNING, T., SETIAWAN, J. & RODMANN, J. (2010). New Herbig Ae/Be stars confirmed via high-resolution optical spectroscopy. A&A, **517**, A67. 34

CARRUTHERS, G.R. (1970). Rocket Observation of Interstellar Molecular Hydrogen. ApJL, **161**, L81. 2

CASASSUS, S., VAN DER PLAS, G., M, S.P., DENT, W.R.F., FOMALONT, E., HAGELBERG, J., HALES, A., JORDÁN, A., MAWET, D., MÉNARD, F., WOOTTEN, A., WILNER, D., HUGHES, A.M., SCHREIBER, M.R., GIRARD, J.H., ERCOLANO, B., CANOVAS, H., ROMÁN, P.E. & SALINAS, V. (2013). Flows of gas through a protoplanetary gap. Nature, **493**, 191–194. 21

CASTELLI, F. & KURUCZ, R.L. (2004). *New Grids of ATLAS9 Model Atmospheres, ArXiv Astrophysics e-prints, arXiv:astro-ph/0405087*. 39, 127

CATALA, C., ALECIAN, E., DONATI, J.F., WADE, G.A., LANDSTREET, J.D., BÖHM, T., BOURET, J.C., BAGNULO, S., FOLSOM, C. & SILVESTER, J. (2007). The magnetic field of the pre-main sequence Herbig Ae star HD 190073. A&A, **462**, 293–301. 22, 79

CAULEY, P.W. & JOHNS-KRULL, C.M. (2014). Diagnosing Mass Flows around Herbig Ae/Be Stars Using the He I λ10830 Line. ApJ, **797**, 112. 22, 79, 150

Cesaroni, R., Galli, D., Neri, R. & Walmsley, C.M. (2014). Imaging the disk around IRAS 20126+4104 at subarcsecond resolution. A&A, **566**, A73. 17

Chabrier, G. (2003). Galactic Stellar and Substellar Initial Mass Function. PASP, **115**, 763–795. 7

Charbonneau, P. & MacGregor, K.B. (2001). Magnetic Fields in Massive Stars. I. Dynamo Models. ApJ, **559**, 1094–1107. 79

Cidale, L., Zorec, J. & Tringaniello, L. (2001). BCD spectrophotometry of stars with the B[e] phenomenon. I. Fundamental parameters. A&A, **368**, 160–174. 34

Clark, P.C. & Bonnell, I.A. (2005). The onset of collapse in turbulently supported molecular clouds. MNRAS, **361**, 2–16. 8

Close, L.M., Follette, K.B., Males, J.R., Puglisi, A., Xompero, M., Apai, D., Najita, J., Weinberger, A.J., Morzinski, K., Rodigas, T.J., Hinz, P., Bailey, V. & Briguglio, R. (2014). Discovery of Hα Emission from the Close Companion inside the Gap of Transitional Disk HD 142527. ApJL, **781**, L30. 20, 78

Colombo, D., Hughes, A., Schinnerer, E., Meidt, S.E., Leroy, A.K., Pety, J., Dobbs, C.L., García-Burillo, S., Dumas, G., Thompson, T.A., Schuster, K.F. & Kramer, C. (2014). The PdBI Arcsecond Whirlpool Survey (PAWS): Environmental Dependence of Giant Molecular Cloud Properties in M51. ApJ, **784**, 3. 3

Commerçon, B., Hennebelle, P. & Henning, T. (2011). Collapse of Massive Magnetized Dense Cores Using Radiation Magnetohydrodynamics: Early Fragmentation Inhibition. ApJL, **742**, L9. 11

Costigan, G., Scholz, A., Stelzer, B., Ray, T., Vink, J.S. & Mohanty, S. (2012). LAMP: the long-term accretion monitoring programme of T Tauri stars in Chamaeleon I. MNRAS, **427**, 1344–1362. 154, 155

Costigan, G., Vink, J.S., Scholz, A., Ray, T. & Testi, L. (2014). Temperaments of young stars: rapid mass accretion rate changes in T Tauri and Herbig Ae stars. MNRAS, **440**, 3444–3461. 155

Coulson, I.M. & Walther, D.M. (1995). SAO 206462 - a solar-type star with a dusty, organically rich environment. MNRAS, **274**, 977–986. 34

Crutcher, R.M. (2012). Magnetic Fields in Molecular Clouds. ARA&A, **50**, 29–63. 4

Currie, T., Muto, T., Kudo, T., Honda, M., Brandt, T.D., Grady, C., Fukagawa, M., Burrows, A., Janson, M., Kuzuhara, M., McElwain, M.W., Follette, K., Hashimoto, J., Henning, T., Kandori, R., Kusakabe, N., Kwon, J., Mede, K., Morino, J.i., Nishikawa, J., Pyo, T.S., Serabyn, G., Suenaga, T., Takahashi, Y., Wisniewski, J. & Tamura, M. (2014). Recovery of the Candidate Protoplanet HD 100546 b with Gemini/NICI and Detection of Additional (Planet-induced?) Disk Structure at Small Separations. ApJL, **796**, L30. 20, 78

Cutri, R.M., Skrutskie, M.F., van Dyk, S., Beichman, C.A., Carpenter, J.M., Chester, T., Cambresy, L., Evans, T., Fowler, J., Gizis, J., Howard, E., Huchra, J., Jarrett, T., Kopan, E.L., Kirkpatrick, J.D., Light, R.M., Marsh, K.A., McCallon, H., Schneider, S., Stiening, R., Sykes, M., Weinberg, M., Wheaton, W.A., Wheelock, S. & Zacarias, N. (2003). *2MASS All Sky Catalog of point sources.*. NASA/IPAC Infrared Science Archive. 128

Dahm, S.E. (2008). A Spectroscopic Examination of Accretion Diagnostics for Near Solar Mass Stars in IC 348. ApJ, **136**, 521–547. 16, 120, 130, 144, 151, 179

Dahm, S.E. & Simon, T. (2005). The T Tauri Star Population of the Young Cluster NGC 2264. ApJ, **129**, 829–855. 34, 61, 73

Dawson, J.R., McClure-Griffiths, N.M., Kawamura, A., Mizuno, N., Onishi, T., Mizuno, A. & Fukui, Y. (2011). Supershells as Molecular Cloud Factories: Parsec Resolution Observations of H I and ^{12}CO(J = 1-0) in GSH 287+04-17 and GSH 277+00+36. ApJ, **728**, 127. 3

de Winter, D., van den Ancker, M.E., Maira, A., Thé, P.S., Djie, H.R.E.T.A., Redondo, I., Eiroa, C. & Molster, F.J. (2001). A photometric catalogue of southern emission-line stars. A&A, **380**, 609–614. 34, 45

de Wit, W.J., Testi, L., Palla, F. & Zinnecker, H. (2005). The origin of massive O-type field stars: II. Field O stars as runaways. A&A, **437**, 247–255. 11

de Zeeuw, P.T., Hoogerwerf, R., de Bruijne, J.H.J., Brown, A.G.A. & Blaauw, A. (1999). A HIPPARCOS Census of the Nearby OB Associations. ApJ, **117**, 354–399. 34, 54, 61, 72

Dobbs, C.L. & Pringle, J.E. (2013). The exciting lives of giant molecular clouds. MNRAS, **432**, 653–667. 3

Dodson-Robinson, S.E. & Salyk, C. (2011). Transitional Disks as Signposts of Young, Multiplanet Systems. ApJ, **738**, 131. 20

Donati, J.F., Jardine, M.M., Gregory, S.G., Petit, P., Bouvier, J., Dougados, C., Ménard, F., Collier Cameron, A., Harries, T.J., Jeffers, S.V. & Paletou, F. (2007). Magnetic fields and accretion flows on the classical T Tauri star V2129 Oph. MNRAS, **380**, 1297–1312. 15

Donehew, B. & Brittain, S. (2011). Measuring the Stellar Accretion Rates of Herbig Ae/Be Stars. ApJ, **141**, 46. 21, 64, 78, 79, 80, 81, 83, 92, 103, 120, 139, 181

Drew, J.E., Busfield, G., Hoare, M.G., Murdoch, K.A., Nixon, C.A. & Oudmaijer, R.D. (1997). MWC 297, B1.5Ve: a zero-age main-sequence star in the Aquila Rift. MNRAS, **286**, 538–548. 34

Duchêne, G. (2015). Herbig AeBe stars: multiplicity and consequences. Ap&SS, **355**, 291–301. 37

Dunkin, S.K., Barlow, M.J. & Ryan, S.G. (1997). High-resolution spectroscopy of Vega-like stars - I. Effective temperatures, gravities and photospheric abundances. MNRAS, **286**, 604–616. 34

Dupree, A.K., Brickhouse, N.S., Smith, G.H. & Strader, J. (2005). A Hot Wind from the Classical T Tauri Stars: TW Hydrae and T Tauri. ApJL, **625**, L131–L134. 147

Edwards, S., Fischer, W., Hillenbrand, L. & Kwan, J. (2006). Probing T Tauri Accretion and Outflow with 1 Micron Spectroscopy. ApJ, **646**, 319–341. 120, 147, 150

Ellerbroek, L.E., Kaper, L., Bik, A., de Koter, A., Horrobin, M., Puga, E., Sana, H. & Waters, L.B.F.M. (2011). The Intermediate-mass Young Stellar Object 08576nr292: Discovery of A Disk-Jet System. ApJL, **732**, L9. 120

Ellerbroek, L.E., Podio, L., Dougados, C., Cabrit, S., Sitko, M.L., Sana, H., Kaper, L., de Koter, A., Klaassen, P.D., Mulders, G.D., Mendigutía, I., Grady, C.A., Grankin, K., van Winckel, H., Bacciotti, F., Russell, R.W., Lynch, D.K., Hammel, H.B., Beerman, L.C., Day, A.N., Huelsman, D.M., Werren, C., Henden, A. & Grindlay, J. (2014). Relating jet structure to photometric variability: the Herbig Ae star HD 163296. A&A, **563**, A87. 183

Elmegreen, B.G. (1979). Gravitational collapse in dust lanes and the appearance of spiral structure in galaxies. ApJ, **231**, 372–383. 3

Elmegreen, B.G. & Lada, C.J. (1977). Sequential formation of subgroups in OB associations. ApJ, **214**, 725–741. 10

Fang, M., van Boekel, R., Wang, W., Carmona, A., Sicilia-Aguilar, A. & Henning, T. (2009). Star and protoplanetary disk properties in Orion's suburbs. A&A, **504**, 461–489. 151

Feigelson, E.D. & Kriss, G.A. (1981). Discovery of three X-ray luminous pre-main-sequence stars. ApJL, **248**, L35–L38. 14

Felenbok, P., Czarny, J., Catala, C. & Praderie, F. (1988). Neutral oxygen in Herbig AE stars. A&A, **201**, 247–258. 145

Field, G.B. & Saslaw, W.C. (1965). A Statistical Model of the Formation of Stars and Interstellar Clouds. ApJ, **142**, 568. 3

Finkenzeller, U. (1985). Rotational velocities, spectral types, and forbidden lines of Herbig Ae/Be stars. A&A, **151**, 340–348. 34

Finkenzeller, U. & Mundt, R. (1984). The Herbig Ae/Be stars associated with nebulosity. A&AS, **55**, 109–141. 19, 34, 120, 131

Franco, G.A.P. (1990). The interstellar medium in the solar vicinity - Analysis of the distribution of colour excesses E(b-y) towards 10 selected areas. A&A, **227**, 499–514. 34

Fukagawa, M., Tamura, M., Itoh, Y., Kudo, T., Imaeda, Y., Oasa, Y., Hayashi, S.S. & Hayashi, M. (2006). Near-Infrared Images of Protoplanetary Disk Surrounding HD 142527. ApJL, **636**, L153–L156. 34, 61

Gahm, G.F. & Malmort, A.M. (1980). A study of stars in southern dust clouds with bright nebulosities. A&A, **82**, 295–304. 34, 64

Garcia Lopez, R., Natta, A., Testi, L. & Habart, E. (2006). Accretion rates in Herbig Ae stars. A&A, **459**, 837–842. 21, 136, 179

Garrison, L.M., Jr. (1978). Observational studies of the Herbig Ae/Be stars. III - Spectrophotometry. ApJ, **224**, 535–545. 78, 81

Gatti, T., Natta, A., Randich, S., Testi, L. & Sacco, G. (2008). Accretion properties of T Tauri stars in σ Orionis. A&A, **481**, 423–432. 136

Ghosh, P. & Lamb, F.K. (1979). Accretion by rotating magnetic neutron stars. II - Radial and vertical structure of the transition zone in disk accretion. ApJ, **232**, 259–276. 15, 21, 79

Girart, J.M., Beltrán, M.T., Zhang, Q., Rao, R. & Estalella, R. (2009). Magnetic Fields in the Formation of Massive Stars. *Science*, **324**, 1408–. 9

Goldreich, P. & Lynden-Bell, D. (1965). II. Spiral arms as sheared gravitational instabilities. MNRAS, **130**, 125. 3

Goodwin, S.P., Nutter, D., Kroupa, P., Ward-Thompson, D. & Whitworth, A.P. (2008). The relationship between the prestellar core mass function and the stellar initial mass function. A&A, **477**, 823–827. 8

Gorti, U. & Hollenbach, D. (2009). Photoevaporation of Circumstellar Disks By Far-Ultraviolet, Extreme-Ultraviolet and X-Ray Radiation from the Central Star. ApJ, **690**, 1539–1552. 110, 179

Grady, C.A., Polomski, E.F., Henning, T., Stecklum, B., Woodgate, B.E., Telesco, C.M., Piña, R.K., Gull, T.R., Boggess, A., Bowers, C.W., Bruhweiler, F.C., Clampin, M., Danks, A.C., Green, R.F., Heap, S.R., Hutchings, J.B., Jenkins, E.B., Joseph, C., Kaiser, M.E., Kimble, R.A., Kraemer, S., Lindler, D., Linsky, J.L., Maran, S.P., Moos, H.W., Plait, P., Roesler, F., Timothy, J.G. & Weistrop, D. (2001). The Disk and Environment of the Herbig Be Star HD 100546. ApJ, **122**, 3396–3406. 19, 182

Graham, J.A. (1970). The space distribution of the OB stars in Carina. ApJ, **75**, 703–717. 34

Gray, R.O. & Corbally, C.J. (1993). A search for Lambda Bootis stars in OB associations. ApJ, **106**, 632–636. 34

Gray, R.O. & Corbally, C.J. (1998). The Incidence of lambda Boötis Stars via an Extension of the MK Spectral Classification System to Very Young A-Type Stars. ApJ, **116**, 2530–2535. 34

Guetter, H.H. (1979). Photometric studies of stars in ORI OB1 /belt/. ApJ, **84**, 1846–1857. 34

Guimarães, M.M., Alencar, S.H.P., Corradi, W.J.B. & Vieira, S.L.A. (2006). Stellar parameters and evidence of circumstellar activity for a sample of Herbig Ae/Be stars. A&A, **457**, 581–589. 34, 43

Gullbring, E., Hartmann, L., Briceno, C. & Calvet, N. (1998). Disk Accretion Rates for T Tauri Stars. ApJ, **492**, 323. 15, 78

Gullbring, E., Calvet, N., Muzerolle, J. & Hartmann, L. (2000). The Structure and Emission of the Accretion Shock in T Tauri Stars. II. The Ultraviolet-Continuum Emission. ApJ, **544**, 927–932. 15, 78, 80, 181

Hamann, F. & Persson, S.E. (1992a). Emission-line studies of young stars. I - The T Tauri stars. II - The Herbig Ae/Be stars. ApJS, **82**, 247–283. 145, 146, 152

Hamann, F. & Persson, S.E. (1992b). Emission-Line Studies of Young Stars. II. The Herbig Ae/Be Stars. ApJS, **82**, 285. 68, 145, 152

Hartigan, P., Edwards, S. & Ghandour, L. (1995). Disk Accretion and Mass Loss from Young Stars. ApJ, **452**, 736. 15, 120

Hartmann, L., Hewett, R. & Calvet, N. (1994). Magnetospheric accretion models for T Tauri stars. 1: Balmer line profiles without rotation. ApJ, **426**, 669–687. 120

Hartmann, L., Calvet, N., Gullbring, E. & D'Alessio, P. (1998). Accretion and the Evolution of T Tauri Disks. ApJ, **495**, 385. 110

Hennemann, M., Motte, F., Schneider, N., Didelon, P., Hill, T., Arzoumanian, D., Bontemps, S., Csengeri, T., André, P., Konyves, V., Louvet, F., Marston, A., Men'shchikov, A., Minier, V., Nguyen Luong, Q., Palmeirim, P., Peretto, N., Sauvage, M., Zavagno, A., Anderson, L.D., Bernard, J.P., Di Francesco, J., Elia, D., Li, J.Z., Martin, P.G., Molinari, S., Pezzuto, S., Russeil, D., Rygl, K.L.J., Schisano, E., Spinoglio, L., Sousbie, T., Ward-Thompson,

D. & White, G.J. (2012). The spine of the swan: a Herschel study of the DR21 ridge and filaments in Cygnus X. A&A, **543**, L3. 6

Henshaw, J.D., Caselli, P., Fontani, F., Jiménez-Serra, I., Tan, J.C. & Hernandez, A.K. (2013). Complex, quiescent kinematics in a highly filamentary infrared dark cloud. MNRAS, **428**, 3425–3442. 6

Herbig, G.H. (1960). The Spectra of Be- and Ae-TYPE Stars Associated with Nebulosity. ApJS, **4**, 337. 18, 131

Herbig, G.H. (2005). IX Ophiuchi: A High-Velocity Star Near a Molecular Cloud. ApJ, **130**, 815–824. 34

Herbst, W. & Racine, R. (1976). R-associations. V. Monoceros R2. ApJ, **81**, 840–844. 34

Herbst, W. & Shevchenko, V.S. (1999). A Photometric Catalog of Herbig AE/BE Stars and Discussion of the Nature and Cause of the Variations of UX Orionis Stars. ApJ, **118**, 1043–1060. 34

Herczeg, G.J. & Hillenbrand, L.A. (2008). UV Excess Measures of Accretion onto Young Very Low Mass Stars and Brown Dwarfs. ApJ, **681**, 594–625. 16, 80, 120, 130, 133, 144, 151, 179

Herczeg, G.J., Cruz, K.L. & Hillenbrand, L.A. (2009). Measuring Tiny Mass Accretion Rates Onto Young Brown Dwarfs. ApJ, **696**, 1589–1599. 80

Hernández, J., Calvet, N., Briceño, C., Hartmann, L. & Berlind, P. (2004). Spectral Analysis and Classification of Herbig Ae/Be Stars. ApJ, **127**, 1682–1701. 26, 34, 56

Hernández, J., Calvet, N., Hartmann, L., Briceño, C., Sicilia-Aguilar, A. & Berlind, P. (2005). Herbig Ae/Be Stars in nearby OB Associations. ApJ, **129**, 856–871. 34

Heyer, M.H., Carpenter, J.M. & Snell, R.L. (2001). The Equilibrium State of Molecular Regions in the Outer Galaxy. ApJ, **551**, 852–866. 2

Hibbert, A., Biemont, E., Godefroid, M. & Vaeck, N. (1991). E1 transitions of astrophysical interest in neutral oxygen. *Journal of Physics B: Atomic, Molecular and Optical Physics*, **24**, 3943. 146

Hill, T., Motte, F., Didelon, P., Bontemps, S., Minier, V., Hennemann, M., Schneider, N., André, P., Men'shchikov, A., Anderson, L.D., Arzoumanian, D., Bernard, J.P., di Francesco, J., Elia, D., Giannini, T., Griffin, M.J., Könyves, V., Kirk, J., Marston, A.P., Martin, P.G., Molinari, S., Nguyen Luong, Q., Peretto, N., Pezzuto, S., Roussel, H., Sauvage, M., Sousbie, T., Testi, L., Ward-Thompson, D., White, G.J., Wilson, C.D. & Zavagno, A. (2011). Filaments and ridges in Vela C revealed by Herschel: from low-mass to high-mass star-forming sites. A&A, **533**, A94. 6

Hillenbrand, L.A. & Hartmann, L.W. (1998). A Preliminary Study of the Orion Nebula Cluster Structure and Dynamics. ApJ, **492**, 540–553. 11

Hilton, J. & Lahulla, J.F. (1995). Distance measurements of LYNDS galactic dark nebulae. A&AS, **113**, 325. 34

Hinkley, S., Hillenbrand, L., Oppenheimer, B.R., Rice, E.L., Pueyo, L., Vasisht, G., Zimmerman, N., Kraus, A.L., Ireland, M.J., Brenner, D., Beichman, C., Dekany, R., Roberts, J.E., Parry, I.R., Roberts, L.C., Jr., Crepp, J.R., Burruss, R., Wallace, J.K., Cady, E., Zhai, C., Shao, M., Lockhart, T., Soummer, R. & Sivaramakrishnan, A. (2013). High-resolution Infrared Imaging and Spectroscopy of the Z Canis Majoris System during Quiescence and Outburst. ApJL, **763**, L9. 64

Hollenbach, D. & McKee, C.F. (1979). Molecule formation and infrared emission in fast interstellar shocks. I Physical processes. ApJS, **41**, 555–592. 3

Hollenbach, D., Johnstone, D., Lizano, S. & Shu, F. (1994). Photoevaporation of disks around massive stars and application to ultracompact H II regions. ApJ, **428**, 654–669. 20

Houk, N. (1982). *Michigan Catalogue of Two-dimensional Spectral Types for the HD stars. Volume 3. Declinations -40 to -26*. 34

Houk, N. & Cowley, A.P. (1975). *University of Michigan Catalogue of two-dimensional spectral types for the HD stars. Volume I.*. University of Michigan. 34

Houk, N. & Smith-Moore, M. (1988). *Michigan Catalogue of Two-dimensional Spectral Types for the HD Stars. Volume 4, Declinations -26 to -12*. 34

Hubrig, S., Stelzer, B., Schöller, M., Grady, C., Schütz, O., Pogodin, M.A., Curé, M., Hamaguchi, K. & Yudin, R.V. (2009). Searching for a link between the magnetic nature and other observed properties of Herbig Ae/Be stars and stars with debris disks. A&A, **502**, 283–301. 22, 79

Ilee, J.D., Fairlamb, J., Oudmaijer, R.D., Mendigutía, I., van den Ancker, M.E., Kraus, S. & Wheelwright, H.E. (2014). Investigating the inner discs of Herbig Ae/Be stars with CO bandhead and Brγ emission. MNRAS, **445**, 3723–3736. 20, 78, 136, 182

Ingleby, L., Calvet, N., Herczeg, G., Blaty, A., Walter, F., Ardila, D., Alexander, R., Edwards, S., Espaillat, C., Gregory, S.G., Hillenbrand, L. & Brown, A. (2013). Accretion Rates for T Tauri Stars Using Nearly Simultaneous Ultraviolet and Optical Spectra. ApJ, **767**, 112. 15, 16, 78, 80, 181

Isella, A. (2006). *Interferometric observations of pre-main sequence disks*. Ph.D. thesis, Universitá degli Studi di Milano, Facoltaà di Scienze Matematiche, Fisiche e Naturali. 13

Jackson, J.M., Finn, S.C., Chambers, E.T., Rathborne, J.M. & Simon, R. (2010). The "Nessie" Nebula: Cluster Formation in a Filamentary Infrared Dark Cloud. ApJL, **719**, L185–L189. 5

Jenniskens, P. & Desert, F.X. (1994). A survey of diffuse interstellar bands (3800-8680 A). A&AS, **106**, 39–78. 54

Johns-Krull, C.M. (2007). The Magnetic Fields of Classical T Tauri Stars. ApJ, **664**, 975–985. 15, 21, 79

JOHNS-KRULL, C.M., VALENTI, J.A., HATZES, A.P. & KANAAN, A. (1999a). Spectropolarimetry of Magnetospheric Accretion on the Classical T Tauri Star BP Tauri. ApJL, **510**, L41–L44. 15

JOHNS-KRULL, C.M., VALENTI, J.A. & KORESKO, C. (1999b). Measuring the Magnetic Field on the Classical T Tauri Star BP Tauri. ApJ, **516**, 900–915. 15

JOHNSTONE, D., WILSON, C.D., MORIARTY-SCHIEVEN, G., JONCAS, G., SMITH, G., GREGERSEN, E. & FICH, M. (2000). Large-Area Mapping at 850 Microns. II. Analysis of the Clump Distribution in the ρ Ophiuchi Molecular Cloud. ApJ, **545**, 327–339. 6, 7

JOY, A.H. (1945). T Tauri Variable Stars. ApJ, **102**, 168. 14

KAHN, F.D. (1974). Cocoons around early-type stars. A&A, **37**, 149–162. 17

KAINULAINEN, J. & TAN, J.C. (2013). High-dynamic-range extinction mapping of infrared dark clouds. Dependence of density variance with sonic Mach number in molecular clouds. A&A, **549**, A53. 6

KENYON, S.J. & HARTMANN, L. (1995). Pre-Main-Sequence Evolution in the Taurus-Auriga Molecular Cloud. ApJS, **101**, 117. 51, 54

KLESSEN, R.S., HEITSCH, F. & MAC LOW, M.M. (2000). Gravitational Collapse in Turbulent Molecular Clouds. I. Gasdynamical Turbulence. ApJ, **535**, 887–906. 8

KOENIGL, A. (1991). Disk accretion onto magnetic T Tauri stars. ApJL, **370**, L39–L43. 15, 21, 79, 97

Könyves, V., André, P., Men'shchikov, A., Schneider, N., Arzoumanian, D., Bontemps, S., Attard, M., Motte, F., Didelon, P., Maury, A., Abergel, A., Ali, B., Baluteau, J.P., Bernard, J.P., Cambrésy, L., Cox, P., di Francesco, J., di Giorgio, A.M., Griffin, M.J., Hargrave, P., Huang, M., Kirk, J., Li, J.Z., Martin, P., Minier, V., Molinari, S., Olofsson, G., Pezzuto, S., Russeil, D., Roussel, H., Saraceno, P., Sauvage, M., Sibthorpe, B., Spinoglio, L., Testi, L., Ward-Thompson, D., White, G., Wilson, C.D., Woodcraft, A. & Zavagno, A. (2010). The Aquila prestellar core population revealed by Herschel. A&A, **518**, L106. 7

Koyama, H. & Inutsuka, S.I. (2000). Molecular Cloud Formation in Shock-compressed Layers. ApJ, **532**, 980–993. 3

Kraus, S., Hofmann, K.H., Benisty, M., Berger, J.P., Chesneau, O., Isella, A., Malbet, F., Meilland, A., Nardetto, N., Natta, A., Preibisch, T., Schertl, D., Smith, M., Stee, P., Tatulli, E., Testi, L. & Weigelt, G. (2008). The origin of hydrogen line emission for five Herbig Ae/Be stars spatially resolved by VLTI/AMBER spectro-interferometry. A&A, **489**, 1157–1173. 136, 182

Kroupa, P. (2001). On the variation of the initial mass function. MNRAS, **322**, 231–246. 7

Krumholz, M.R. & McKee, C.F. (2005). A General Theory of Turbulence-regulated Star Formation, from Spirals to Ultraluminous Infrared Galaxies. ApJ, **630**, 250–268. 17

KUROSAWA, R. & ROMANOVA, M.M. (2012). Line formation in the inner winds of classical T Tauri stars: testing the conical-shell wind solution. MNRAS, **426**, 2901–2916. 150, 183

KUROSAWA, R., ROMANOVA, M.M. & HARRIES, T.J. (2011). Multidimensional models of hydrogen and helium emission line profiles for classical T Tauri stars: method, tests and examples. MNRAS, **416**, 2623–2639. 16, 67, 78, 120, 181, 183

KURUCZ, R.L. (1993). *SYNTHE spectrum synthesis programs and line data*. Cambridge, MA: Smithsonian Astrophysical Observatory. 39, 127

KWAN, J., EDWARDS, S. & FISCHER, W. (2007). Modeling T Tauri Winds from He I λ10830 Profiles. ApJ, **657**, 897–915. 147

LADA, C.J. (1987). Star formation - From OB associations to protostars. In M. Peimbert & J. Jugaku, eds., *Star Forming Regions*, vol. 115 of *IAU Symposium*, 1–17. 12, 13

LARSON, R.B. (1969). Numerical calculations of the dynamics of collapsing proto-star. MNRAS, **145**, 271. 8

LARSON, R.B. (1981). Turbulence and star formation in molecular clouds. MNRAS, **194**, 809–826. 6

LEVENHAGEN, R.S. & LEISTER, N.V. (2006). Spectroscopic analysis of southern B and Be stars. MNRAS, **371**, 252–262. 34

LIZANO, S. & SHU, F.H. (1989). Molecular cloud cores and bimodal star formation. ApJ, **342**, 834–854. 4

Loinard, L., Torres, R.M., Mioduszewski, A.J. & Rodríguez, L.F. (2008). A Preliminary VLBA Distance to the Core of Ophiuchus, with an Accuracy of 4%. ApJL, **675**, L29–L32. 34, 61

Long, M., Romanova, M.M., Kulkarni, A.K. & Donati, J.F. (2011). Global 3D simulations of disc accretion on to the classical T Tauri star BP Tauri. MNRAS, **413**, 1061–1071. 107

Lumsden, S.L., Hoare, M.G., Urquhart, J.S., Oudmaijer, R.D., Davies, B., Mottram, J.C., Cooper, H.D.B. & Moore, T.J.T. (2013). The Red MSX Source Survey: The Massive Young Stellar Population of Our Galaxy. ApJS, **208**, 11. 16

Maaskant, K.M., Honda, M., Waters, L.B.F.M., Tielens, A.G.G.M., Dominik, C., Min, M., Verhoeff, A., Meeus, G. & van den Ancker, M.E. (2013). Identifying gaps in flaring Herbig Ae/Be disks using spatially resolved mid-infrared imaging. Are all group I disks transitional? A&A, **555**, A64. 20, 182

Maaskant, K.M., Min, M., Waters, L.B.F.M. & Tielens, A.G.G.M. (2014). Polycyclic aromatic hydrocarbon ionization as a tracer of gas flows through protoplanetary disk gaps. A&A, **563**, A78. 20

Magnani, L., Blitz, L. & Mundy, L. (1985). Molecular gas at high Galactic latitudes. ApJ, **295**, 402–421. 2

Malfait, K., Waelkens, C., Waters, L.B.F.M., Vandenbussche, B., Huygen, E. & de Graauw, M.S. (1998). The spectrum of the young star

HD 100546 observed with the Infrared Space Observatory. A&A, **332**, L25–L28. 34

Mannings, V. & Sargent, A.I. (1997). A High-Resolution Study of Gas and Dust around Young Intermediate-Mass Stars: Evidence for Circumstellar Disks in Herbig Ae Systems. ApJ, **490**, 792–802. 19

Manoj, P., Bhatt, H.C., Maheswar, G. & Muneer, S. (2006). Evolution of Emission-Line Activity in Intermediate-Mass Young Stars. ApJ, **653**, 657–674. 56, 62, 64

Maschberger, T. (2013). On the function describing the stellar initial mass function. MNRAS, **429**, 1725–1733. 7

Masunaga, H., Miyama, S.M. & Inutsuka, S.I. (1998). A Radiation Hydrodynamic Model for Protostellar Collapse. I. The First Collapse. ApJ, **495**, 346. 9

McCaughrean, M.J. & O'dell, C.R. (1996). Direct Imaging of Circumstellar Disks in the Orion Nebula. ApJ, **111**, 1977. 19, 182

McCray, R. & Kafatos, M. (1987). Supershells and propagating star formation. ApJ, **317**, 190–196. 3

McGregor, P.J., Harrison, T.E., Hough, J.H. & Bailey, J.A. (1994). Infrared Polarimetry in the Chamaeleon-I Dark Cloud. MNRAS, **267**, 755. 5

McKee, C.F. & Ostriker, E.C. (2007). Theory of Star Formation. ARA&A, **45**, 565–687. 8

McKee, C.F. & Tan, J.C. (2002). Massive star formation in 100,000 years from turbulent and pressurized molecular clouds. Nature, **416**, 59–61. 11

McKee, C.F. & Tan, J.C. (2003). The Formation of Massive Stars from Turbulent Cores. ApJ, **585**, 850–871. 11

Meeus, G., Waters, L.B.F.M., Bouwman, J., van den Ancker, M.E., Waelkens, C. & Malfait, K. (2001). ISO spectroscopy of circumstellar dust in 14 Herbig Ae/Be systems: Towards an understanding of dust processing. A&A, **365**, 476–490. 19, 77

Mendigutia, I., de Wit, W.J., Oudmaijer, R.D., Fairlamb, J.R., D., C.A., J.D., I. & R.G., V. (????). High resolution Brγ spectro-interferometry of the transitional Herbig Ae/Be star HD 100546: A Keplerian gaseous disc inside the inner rim. 138, 183

Mendigutía, I., Calvet, N., Montesinos, B., Mora, A., Muzerolle, J., Eiroa, C., Oudmaijer, R.D. & Merín, B. (2011a). Accretion rates and accretion tracers of Herbig Ae/Be stars. A&A, **535**, A99. 21, 78, 79, 80, 92, 96, 98, 103, 104, 105, 113, 120, 130, 134, 136, 139, 144, 179, 181

Mendigutía, I., Eiroa, C., Montesinos, B., Mora, A., Oudmaijer, R.D., Merín, B. & Meeus, G. (2011b). Optical spectroscopic variability of Herbig Ae/Be stars. A&A, **529**, A34. 45

Mendigutía, I., Mora, A., Montesinos, B., Eiroa, C., Meeus, G., Merín, B. & Oudmaijer, R.D. (2012). Accretion-related properties of Herbig Ae/Be stars. Comparison with T Tauris. A&A, **543**, A59. 110

Mendigutía, I., Brittain, S., Eiroa, C., Meeus, G., Montesinos, B., Mora, A., Muzerolle, J., Oudmaijer, R.D. & Rigliaco, E. (2013). Accretion Variability of Herbig Ae/Be Stars Observed by X-Shooter HD 31648 and HD 163296. ApJ, **776**, 44. 21, 45, 79, 81, 84

Mendigutía, I., Fairlamb, J., Montesinos, B., Oudmaijer, R.D., Najita, J.R., Brittain, S.D. & van den Ancker, M.E. (2014). Stellar Parameters and Accretion Rate of the Transition Disk Star HD142527 from X-Shooter. ApJ, **790**, 21. 21, 79

Men'shchikov, A., André, P., Didelon, P., Könyves, V., Schneider, N., Motte, F., Bontemps, S., Arzoumanian, D., Attard, M., Abergel, A., Baluteau, J.P., Bernard, J.P., Cambrésy, L., Cox, P., di Francesco, J., di Giorgio, A.M., Griffin, M., Hargrave, P., Huang, M., Kirk, J., Li, J.Z., Martin, P., Minier, V., Miville-Deschênes, M.A., Molinari, S., Olofsson, G., Pezzuto, S., Roussel, H., Russeil, D., Saraceno, P., Sauvage, M., Sibthorpe, B., Spinoglio, L., Testi, L., Ward-Thompson, D., White, G., Wilson, C.D., Woodcraft, A. & Zavagno, A. (2010). Filamentary structures and compact objects in the Aquila and Polaris clouds observed by Herschel. A&A, **518**, L103. 5

Mestel, L. & Spitzer, L., Jr. (1956). Star formation in magnetic dust clouds. MNRAS, **116**, 503. 9

Miller, G.E. & Scalo, J.M. (1979). The initial mass function and stellar birthrate in the solar neighborhood. ApJS, **41**, 513–547. 7

Miroshnichenko, A.S., Gray, R.O., Vieira, S.L.A., Kuratov, K.S. & Bergner, Y.K. (1999). Observations of recently recognized candidate Herbig Ae/Be stars. A&A, **347**, 137–150. 34

Miroshnichenko, A.S., Gray, R.O., Klochkova, V.G., Bjorkman, K.S. & Kuratov, K.S. (2004). Fundamental parameters and evolutionary state of the Herbig Ae star candidate HD 35929. A&A, **427**, 937–944. 34

Modigliani, A., Goldoni, P., Royer, F., Haigron, R., Guglielmi, L., François, P., Horrobin, M., Bristow, P., Vernet, J., Moehler, S., Kerber, F., Ballester, P., Mason, E. & Christensen, L. (2010). The X-shooter pipeline. In *Society of Photo-Optical Instrumentation Engineers (SPIE) Conference Series*, vol. 7737 of *Society of Photo-Optical Instrumentation Engineers (SPIE) Conference Series*. 37

Mohanty, S., Jayawardhana, R. & Basri, G. (2005). The T Tauri Phase Down to Nearly Planetary Masses: Echelle Spectra of 82 Very Low Mass Stars and Brown Dwarfs. ApJ, **626**, 498–522. 154

Molinari, S., Swinyard, B., Bally, J., Barlow, M., Bernard, J.P., Martin, P., Moore, T., Noriega-Crespo, A., Plume, R., Testi, L., Zavagno, A., Abergel, A., Ali, B., Anderson, L., André, P., Baluteau, J.P., Battersby, C., Beltrán, M.T., Benedettini, M., Billot, N., Blommaert, J., Bontemps, S., Boulanger, F., Brand, J., Brunt, C., Burton, M., Calzoletti, L., Carey, S., Caselli, P., Cesaroni, R., Cernicharo, J., Chakrabarti, S., Chrysostomou, A., Cohen, M., Compiegne, M., de Bernardis, P., de Gasperis, G., di Giorgio, A.M., Elia, D., Faustini, F., Flagey, N., Fukui, Y., Fuller, G.A., Ganga, K., Garcia-Lario, P., Glenn, J., Goldsmith, P.F., Griffin, M., Hoare, M., Huang, M., Ikhenaode, D., Joblin, C., Joncas, G., Juvela, M., Kirk, J.M., Lagache, G., Li, J.Z., Lim, T.L., Lord, S.D., Marengo, M., Marshall, D.J., Masi, S., Massi, F., Matsuura, M., Minier, V., Miville-Deschênes, M.A., Montier, L.A., Morgan, L., Motte, F., Mottram, J.C., Müller, T.G., Natoli, P., Neves, J., Olmi, L., Paladini, R., Paradis, D., Parsons, H., Peretto, N., Pestalozzi, M., Pezzuto, S., Piacentini, F., Piazzo, L., Polychroni, D., Pomarès, M., Popescu, C.C., Reach, W.T., Ristorcelli, I., Robitaille, J.F., Robitaille, T., Rodón, J.A., Roy, A., Royer, P., Russeil, D., Saraceno, P., Sauvage, M., Schilke, P., Schisano, E., Schneider, N., Schuller, F., Schulz, B., Sibthorpe, B., Smith, H.A., Smith, M.D., Spinoglio, L., Stamatellos, D., Strafella, F., Stringfellow, G.S., Sturm, E., Taylor, R., Thompson, M.A., Traficante, A., Tuffs, R.J., Umana, G., Valenziano, L., Vavrek, R., Veneziani, M., Viti, S., Waelkens, C., Ward-Thompson, D., White, G., Wilcock, L.A., Wyrowski, F., Yorke, H.W. & Zhang, Q. (2010). Clouds, filaments, and protostars: The Herschel Hi-GAL Milky Way. A&A, **518**, L100. 7

Montesinos, B., Eiroa, C., Mora, A. & Merín, B. (2009). Parameters of Herbig Ae/Be and Vega-type stars. A&A, **495**, 901–917. 26, 42, 55

Mora, A., Merín, B., Solano, E., Montesinos, B., de Winter, D., Eiroa, C., Ferlet, R., Grady, C.A., Davies, J.K., Miranda, L.F., Oudmaijer, R.D., Palacios, J., Quirrenbach, A., Harris, A.W., Rauer, H., Collier Cameron, A., Deeg, H.J., Garzón, F., Penny, A., Schneider, J., Tsapras, Y. & Wesselius, P.R. (2001). EXPORT: Spectral classification and projected rotational velocities of Vega-type and pre-main sequence stars. A&A, **378**, 116–131. 26, 34, 62

Motte, F., Andre, P. & Neri, R. (1998). The initial conditions of star formation in the rho Ophiuchi main cloud: wide-field millimeter continuum mapping. A&A, **336**, 150–172. 7

Mottram, J.C., Hoare, M.G., Urquhart, J.S., Lumsden, S.L., Oudmaijer, R.D., Robitaille, T.P., Moore, T.J.T., Davies, B. & Stead, J. (2011). The Red MSX Source survey: the bolometric fluxes and luminosity distributions of young massive stars. A&A, **525**, A149. 16

Mouschovias, T.C. (1974). Static Equilibria of the Interstellar Gas in the Presence of Magnetic and Gravitational Fields: Large-Scale Condensations. ApJ, **192**, 37–50. 4

Mouschovias, T.C. (1987). Star formation in magnetic interstellar clouds. I - Interplay between theory and observations. II - Basic theory. In G.E. Morfill & M. Scholer, eds., *NATO ASIC Proc. 210: Physical Processes in Interstellar Clouds*, 453–489. 4

Mouschovias, T.C. & Paleologou, E.V. (1979). The angular momentum problem and magnetic braking - an exact time-dependent solution. ApJ, **230**, 204–222. 9

MOUSCHOVIAS, T.C. & SPITZER, L., JR. (1976). Note on the collapse of magnetic interstellar clouds. ApJ, **210**, 326. 4

MUNARI, U., SORDO, R., CASTELLI, F. & ZWITTER, T. (2005). An extensive library of 2500 10 500 Å synthetic spectra. A&A, **442**, 1127–1134. 39, 127

MUZEROLLE, J., CALVET, N. & HARTMANN, L. (1998a). Magnetospheric Accretion Models for the Hydrogen Emission Lines of T Tauri Stars. ApJ, **492**, 743. 15, 78, 120, 181, 183

MUZEROLLE, J., HARTMANN, L. & CALVET, N. (1998b). A Brgamma Probe of Disk Accretion in T Tauri Stars and Embedded Young Stellar Objects. ApJ, **116**, 2965–2974. 16, 136, 139

MUZEROLLE, J., HARTMANN, L. & CALVET, N. (1998c). Emission-Line Diagnostics of T Tauri Magnetospheric Accretion. I. Line Profile Observations. ApJ, **116**, 455–468. 120, 130, 145, 147, 154, 179

MUZEROLLE, J., CALVET, N. & HARTMANN, L. (2001). Emission-Line Diagnostics of T Tauri Magnetospheric Accretion. II. Improved Model Tests and Insights into Accretion Physics. ApJ, **550**, 944–961. 16, 78, 181

MUZEROLLE, J., D'ALESSIO, P., CALVET, N. & HARTMANN, L. (2004). Magnetospheres and Disk Accretion in Herbig Ae/Be Stars. ApJ, **617**, 406–417. 21, 79, 80, 83, 96, 98, 99

MUZEROLLE, J., LUHMAN, K.L., BRICEÑO, C., HARTMANN, L. & CALVET, N. (2005). Measuring Accretion in Young Substellar Objects: Approaching the Planetary Mass Regime. ApJ, **625**, 906–912. 16, 113, 178

MYERS, A.T., MCKEE, C.F., CUNNINGHAM, A.J., KLEIN, R.I. & KRUMHOLZ, M.R. (2013). The Fragmentation of Magnetized, Massive Star-forming Cores with Radiative Feedback. ApJ, **766**, 97. 11

MYERS, P.C. (2011). Star Formation in Dense Clusters. ApJ, **743**, 98. 6

NAKANO, T. (1989). Magnetic braking of the rotation of molecular cloud cores. MNRAS, **241**, 495–505. 9

NAKANO, T. & NAKAMURA, T. (1978). Gravitational Instability of Magnetized Gaseous Disks 6. , **30**, 671–680. 4

NARAYANAN, D., KRUMHOLZ, M., OSTRIKER, E.C. & HERNQUIST, L. (2011). The CO-H_2 conversion factor in disc galaxies and mergers. MNRAS, **418**, 664–679. 2

NARAYANAN, D., KRUMHOLZ, M.R., OSTRIKER, E.C. & HERNQUIST, L. (2012). A general model for the CO-H_2 conversion factor in galaxies with applications to the star formation law. MNRAS, **421**, 3127–3146. 2

NATTA, A., TESTI, L., MUZEROLLE, J., RANDICH, S., COMERÓN, F. & PERSI, P. (2004). Accretion in brown dwarfs: An infrared view. A&A, **424**, 603–612. 16

NATTA, A., TESTI, L. & RANDICH, S. (2006). Accretion in the ρ-Ophiuchi pre-main sequence stars. A&A, **452**, 245–252. 16, 104, 105, 113, 114, 116, 178

NATTA, A., TESTI, L., ALCALÁ, J.M., RIGLIACO, E., COVINO, E., STELZER, B. & D'ELIA, V. (2014). X-shooter spectroscopy of young stellar objects. V. Slow winds in T Tauri stars. A&A, **569**, A5. 140, 144

Oka, T., Hasegawa, T., Sato, F., Tsuboi, M., Miyazaki, A. & Sugimoto, M. (2001). Statistical Properties of Molecular Clouds in the Galactic Center. ApJ, **562**, 348–362. 2

Oort, J.H. (1954). Outline of a theory on the origin and acceleration of interstellar clouds and O associations. , **12**, 177. 3

Osterbrock, D.E. (1989). *Astrophysics of gaseous nebulae and active galactic nuclei*. University Science Books, California. 138

Oudmaijer, R.D., Palacios, J., Eiroa, C., Davies, J.K., de Winter, D., Ferlet, R., Garzón, F., Grady, C.A., Collier Cameron, A., Deeg, H.J., Harris, A.W., Horne, K., Merín, B., Miranda, L.F., Montesinos, B., Mora, A., Penny, A., Quirrenbach, A., Rauer, H., Schneider, J., Solano, E., Tsapras, Y. & Wesselius, P.R. (2001). EXPORT: Optical photometry and polarimetry of Vega-type and pre-main sequence stars. A&A, **379**, 564–578. 45

Palau, A., Fuente, A., Girart, J.M., Estalella, R., Ho, P.T.P., Sánchez-Monge, Á., Fontani, F., Busquet, G., Commerçon, B., Hennebelle, P., Boissier, J., Zhang, Q., Cesaroni, R. & Zapata, L.A. (2013). Early Stages of Cluster Formation: Fragmentation of Massive Dense Cores down to ˜ 1000 AU. ApJ, **762**, 120. 11

Palla, F. & Stahler, S.W. (1993). The Pre-Main-Sequence Evolution of Intermediate-Mass Stars. ApJ, **418**, 414. 17

Papaloizou, J.C.B. & Lin, D.N.C. (1995). Theory Of Accretion Disks I: Angular Momentum Transport Processes. ARA&A, **33**, 505–540. 10

Parker, E.N. (1966). The Dynamical State of the Interstellar Gas and Field. ApJ, **145**, 811. 4

Peretto, N., André, P., Könyves, V., Schneider, N., Arzoumanian, D., Palmeirim, P., Didelon, P., Attard, M., Bernard, J.P., Di Francesco, J., Elia, D., Hennemann, M., Hill, T., Kirk, J., Men'shchikov, A., Motte, F., Nguyen Luong, Q., Roussel, H., Sousbie, T., Testi, L., Ward-Thompson, D., White, G.J. & Zavagno, A. (2012). The Pipe Nebula as seen with Herschel: formation of filamentary structures by large-scale compression? A&A, **541**, A63. 6

Peretto, N., Fuller, G.A., Duarte-Cabral, A., Avison, A., Hennebelle, P., Pineda, J.E., André, P., Bontemps, S., Motte, F., Schneider, N. & Molinari, S. (2013). Global collapse of molecular clouds as a formation mechanism for the most massive stars. A&A, **555**, A112. 6

Pérez, M.R., McCollum, B., van den Ancker, M.E. & Joner, M.D. (2008). The enigmatic young object: Walker 90/V590 Monocerotis. A&A, **486**, 533–544. 34

Pilbratt, G.L., Riedinger, J.R., Passvogel, T., Crone, G., Doyle, D., Gageur, U., Heras, A.M., Jewell, C., Metcalfe, L., Ott, S. & Schmidt, M. (2010). Herschel Space Observatory. An ESA facility for far-infrared and submillimetre astronomy. A&A, **518**, L1. 5

Pineda, J.E., Rosolowsky, E.W. & Goodman, A.A. (2009). The Perils of Clumpfind: The Mass Spectrum of Substructures in Molecular Clouds. ApJL, **699**, L134–L138. 7

Pogodin, M.A., Hubrig, S., Yudin, R.V., Schöller, M., González, J.F. & Stelzer, B. (2012). Measuring the mass accretion rates of Herbig Ae/Be stars with X-shooter. *Astronomische Nachrichten*, **333**, 594–612. 21, 45, 79, 80, 92, 181

Polychroni, D., Schisano, E., Elia, D., Roy, A., Molinari, S., Martin, P., André, P., Turrini, D., Rygl, K.L.J., Di Francesco, J., Benedettini, M., Busquet, G., di Giorgio, A.M., Pestalozzi, M., Pezzuto, S., Arzoumanian, D., Bontemps, S., Hennemann, M., Hill, T., Könyves, V., Men'shchikov, A., Motte, F., Nguyen-Luong, Q., Peretto, N., Schneider, N. & White, G. (2013). Two Mass Distributions in the L 1641 Molecular Clouds: The Herschel Connection of Dense Cores and Filaments in Orion A. ApJL, **777**, L33. 6

Pon, A., Johnstone, D. & Heitsch, F. (2011). Modes of Star Formation in Finite Molecular Clouds. ApJ, **740**, 88. 7

Price, D.J. & Bate, M.R. (2007). The impact of magnetic fields on single and binary star formation. MNRAS, **377**, 77–90. 11

Pringle, J.E. (1981). Accretion discs in astrophysics. ARA&A, **19**, 137–162. 10

Pudritz, R.E. & Norman, C.A. (1983). Centrifugally driven winds from contracting molecular disks. ApJ, **274**, 677–697. 10

Quanz, S.P., Amara, A., Meyer, M.R., Kenworthy, M.A., Kasper, M. & Girard, J.H. (2013). A Young Protoplanet Candidate Embedded in the Circumstellar Disk of HD 100546. ApJL, **766**, L1. 20, 78

REID, M.A., WADSLEY, J., PETITCLERC, N. & SILLS, A. (2010). Measuring the Clump Mass Function in the Age of SCUBA2, Herschel, and ALMA. ApJ, **719**, 561–575. 7

REID, M.J., MENTEN, K.M., ZHENG, X.W., BRUNTHALER, A., MOSCADELLI, L., XU, Y., ZHANG, B., SATO, M., HONMA, M., HIROTA, T., HACHISUKA, K., CHOI, Y.K., MOELLENBROCK, G.A. & BARTKIEWICZ, A. (2009). Trigonometric Parallaxes of Massive Star-Forming Regions. VI. Galactic Structure, Fundamental Parameters, and Noncircular Motions. ApJ, **700**, 137–148. 69

REIPURTH, B. & ZINNECKER, H. (1993). Visual binaries among pre-main sequence stars. A&A, **278**, 81–108. 34

RIGLIACO, E., NATTA, A., TESTI, L., RANDICH, S., ALCALÀ, J.M., COVINO, E. & STELZER, B. (2012). X-shooter spectroscopy of young stellar objects. I. Mass accretion rates of low-mass T Tauri stars in σ Orionis. A&A, **548**, A56. 80, 120, 130, 134, 136, 151, 152, 154, 179

RIGLIACO, E., PASCUCCI, I., GORTI, U., EDWARDS, S. & HOLLENBACH, D. (2013). Understanding the Origin of the [O I] Low-velocity Component from T Tauri Stars. ApJ, **772**, 60. 120, 144

RIGLIACO, E., PASCUCCI, I., DUCHENE, G., EDWARDS, S., ARDILA, D.R., GRADY, C., MENDIGUTÍA, I., MONTESINOS, B., MULDERS, G.D., NAJITA, J.R., CARPENTER, J., FURLAN, E., GORTI, U., MEIJERINK, R. & MEYER, M.R. (2015). Probing Stellar Accretion with Mid-infrared Hydrogen Lines. ApJ, **801**, 31. 185

Roberts, W.W. (1969). Large-Scale Shock Formation in Spiral Galaxies and its Implications on Star Formation. ApJ, **158**, 123. 3

Rosolowsky, E. (2005). The Mass Spectra of Giant Molecular Clouds in the Local Group. PASP, **117**, 1403–1410. 3

Sadavoy, S.I., Di Francesco, J., André, P., Pezzuto, S., Bernard, J.P., Maury, A., Men'shchikov, A., Motte, F., Nguy ên-Lu'o'ng, Q., Schneider, N., Arzoumanian, D., Benedettini, M., Bontemps, S., Elia, D., Hennemann, M., Hill, T., Könyves, V., Louvet, F., Peretto, N., Roy, A. & White, G.J. (2014). Class 0 Protostars in the Perseus Molecular Cloud: A Correlation Between the Youngest Protostars and the Dense Gas Distribution. ApJL, **787**, L18. 12

Salpeter, E.E. (1955). The Luminosity Function and Stellar Evolution. ApJ, **121**, 161. 7, 71

Sánchez-Monge, Á., Cesaroni, R., Beltrán, M.T., Kumar, M.S.N., Stanke, T., Zinnecker, H., Etoka, S., Galli, D., Hummel, C.A., Moscadelli, L., Preibisch, T., Ratzka, T., van der Tak, F.F.S., Vig, S., Walmsley, C.M. & Wang, K.S. (2013). A candidate circumbinary Keplerian disk in G35.20-0.74 N: A study with ALMA. A&A, **552**, L10. 17

Sanduleak, N. & Stephenson, C.B. (1973). Low-dispersion spectra and galactic distribution of various interesting strong-emission-line objects in the southern Milky Way. ApJ, **185**, 899–913. 64

Sargent, A.I. & Beckwith, S. (1987). Kinematics of the circumstellar gas of HL Tauri and R Monocerotis. ApJ, **323**, 294–305. 14

Shetty, R., Glover, S.C., Dullemond, C.P. & Klessen, R.S. (2011). Modelling CO emission - I. CO as a column density tracer and the X factor in molecular clouds. MNRAS, **412**, 1686–1700. 2

Shevchenko, V.S., Ezhkova, O.V., Ibrahimov, M.A., van den Ancker, M.E. & Tjin A Djie, H.R.E. (1999). The stellar composition of the star formation region CMa R1 - I. Results from new photometric and spectroscopic classifications. MNRAS, **310**, 210–222. 34, 61, 72

Shu, F., Najita, J., Ostriker, E., Wilkin, F., Ruden, S. & Lizano, S. (1994). Magnetocentrifugally driven flows from young stars and disks. 1: A generalized model. ApJ, **429**, 781–796. 15, 21, 79, 97

Shu, F.H. (1977). Self-similar collapse of isothermal spheres and star formation. ApJ, **214**, 488–497. 8

Sicilia-Aguilar, A., Henning, T. & Hartmann, L.W. (2010). Accretion in Evolved and Transitional Disks in CEP OB2: Looking for the Origin of the Inner Holes. ApJ, **710**, 597–612. 110, 178

Simon, T., Ayres, T.R., Redfield, S. & Linsky, J.L. (2002). Limits on Chromospheres and Convection among the Main-Sequence A Stars. ApJ, **579**, 800–809. 79

Skrutskie, M.F., Cutri, R.M., Stiening, R., Weinberg, M.D., Schneider, S., Carpenter, J.M., Beichman, C., Capps, R., Chester, T., Elias, J., Huchra, J., Liebert, J., Lonsdale, C., Monet, D.G., Price, S., Seitzer, P., Jarrett, T., Kirkpatrick, J.D., Gizis, J.E., Howard, E., Evans, T., Fowler, J., Fullmer, L., Hurt, R., Light, R., Kopan, E.L., Marsh, K.A., McCallon, H.L., Tam, R., Van Dyk, S. & Wheelock, S. (2006). The Two Micron All Sky Survey (2MASS). ApJ, **131**, 1163–1183. 128

Smith, R.J., Glover, S.C.O., Bonnell, I.A., Clark, P.C. & Klessen, R.S. (2011). A quantification of the non-spherical geometry and accretion of collapsing cores. MNRAS, **411**, 1354–1366. 6

Solomon, P.M., Sanders, D.B. & Scoville, N.Z. (1979). Giant molecular clouds in the Galaxy - The distribution of CO-13 emission in the galactic plane. ApJL, **232**, L89–L93. 2

Solomon, P.M., Rivolo, A.R., Barrett, J. & Yahil, A. (1987). Mass, luminosity, and line width relations of Galactic molecular clouds. ApJ, **319**, 730–741. 2

Stephenson, C.B. & Sanduleak, N. (1971). Luminous stars in the Southern Milky Way. *Publications of the Warner & Swasey Observatory*, **1**, 1. 34, 107

Strom, S.E., Strom, K.M., Yost, J., Carrasco, L. & Grasdalen, G. (1972). The Nature of the Herbig Ae- and Be-TYPE Stars Associated with Nebulosity. ApJ, **173**, 353. 25

Tafalla, M., Myers, P.C., Caselli, P. & Walmsley, C.M. (2004). On the internal structure of starless cores. I. Physical conditions and the distribution of CO, CS, N_2H^+, and NH_3 in L1498 and L1517B. A&A, **416**, 191–212. 6

TESTI, L. & SARGENT, A.I. (1998). Star Formation in Clusters: A Survey of Compact Millimeter-Wave Sources in the Serpens Core. ApJL, **508**, L91–L94. 7

THÉ, P.S., DE WINTER, D. & PEREZ, M.R. (1994). A new catalogue of members and candidate members of the Herbig Ae/Be (HAEBE) stellar group. A&AS, **104**, 315–339. 19, 35, 131

TILLING, I., CLARKE, C.J., PRINGLE, J.E. & TOUT, C.A. (2008). Disc evolution and the relationship between L_{acc} and L_* in T Tauri stars. MNRAS, **385**, 1530–1534. 114, 116, 178

TJIN A DJIE, H.R.E., THE, P.S., ANDERSEN, J., NORDSTROM, B., FINKENZELLER, U. & JANKOVICS, I. (1989). The variable Herbig AE star HR 5999. VIII - Spectroscopic observations 1975-1985 and correlations with simultaneous photometry. A&AS, **78**, 1–24. 34

TJIN A DJIE, H.R.E., VAN DEN ANCKER, M.E., BLONDEL, P.F.C., SHEVCHENKO, V.S., EZHKOVA, O.V., DE WINTER, D. & GRANKIN, K.N. (2001). The stellar composition of the star formation region CMa R1 - II. Spectroscopic and photometric observations of nine young stars. MNRAS, **325**, 1441–1457. 34

TOOMRE, A. (1964). On the gravitational stability of a disk of stars. ApJ, **139**, 1217–1238. 3

UCHIDA, Y. & SHIBATA, K. (1985). Magnetodynamical acceleration of CO and optical bipolar flows from the region of star formation. , **37**, 515–535. 15

Urquhart, J.S., Morgan, L.K., Figura, C.C., Moore, T.J.T., Lumsden, S.L., Hoare, M.G., Oudmaijer, R.D., Mottram, J.C., Davies, B. & Dunham, M.K. (2011). The Red MSX Source survey: ammonia and water maser analysis of massive star-forming regions. MNRAS, **418**, 1689–1706. 16, 69

Valenti, J.A., Basri, G. & Johns, C.M. (1993). T Tauri stars in blue. ApJ, **106**, 2024–2050. 15, 107

Valenti, J.A., Johns-Krull, C.M. & Linsky, J.L. (2000). An IUE Atlas of Pre-Main-Sequence Stars. I. Co-added Final Archive Spectra from the SWP Camera. ApJS, **129**, 399–420. 34

van den Ancker, M.E., de Winter, D. & Tjin A Djie, H.R.E. (1998). HIPPARCOS photometry of Herbig Ae/Be stars. A&A, **330**, 145–154. 34

van den Ancker, M.E., Bouwman, J., Wesselius, P.R., Waters, L.B.F.M., Dougherty, S.M. & van Dishoeck, E.F. (2000). ISO spectroscopy of circumstellar dust in the Herbig Ae systems AB Aur and HD 163296. A&A, **357**, 325–329. 19

van den Ancker, M.E., Blondel, P.F.C., Tjin A Djie, H.R.E., Grankin, K.N., Ezhkova, O.V., Shevchenko, V.S., Guenther, E. & Acke, B. (2004). The stellar composition of the star formation region CMa R1 - III. A new outburst of the Be star component in Z CMa. MNRAS, **349**, 1516–1536. 34, 64, 140

van der Plas, G., van den Ancker, M.E., Fedele, D., Acke, B., Dominik, C., Waters, L.B.F.M. & Bouwman, J. (2008). The structure of protoplanetary disks surrounding three young intermediate mass stars. I. Resolving the disk rotation in the [OI] 6300 Å line. A&A, **485**, 487–495. 140

van der Plas, G., van den Ancker, M.E., Acke, B., Carmona, A., Dominik, C., Fedele, D. & Waters, L.B.F.M. (2009). Evidence for CO depletion in the inner regions of gas-rich protoplanetary disks. A&A, **500**, 1137–1141. 19, 78, 182

van der Plas, G., van den Ancker, M.E., Waters, L.B.F.M. & Dominik, C. (2015). The structure of disks around Herbig Ae/Be stars as traced by CO ro-vibrational emission. A&A, **574**, A75. 20, 78, 182

van Dishoeck, E.F. & Black, J.H. (1988). The photodissociation and chemistry of interstellar CO. ApJ, **334**, 771–802. 3

van Leeuwen, F. (2007). Validation of the new Hipparcos reduction. A&A, **474**, 653–664. 34, 61, 73

Van Loo, S., Butler, M.J. & Tan, J.C. (2013). Kiloparsec-scale Simulations of Star Formation in Disk Galaxies. I. The Unmagnetized and Zero-feedback Limit. ApJ, **764**, 36. 4

Vernet, J., Dekker, H., D'Odorico, S., Kaper, L., Kjaergaard, P., Hammer, F., Randich, S., Zerbi, F., Groot, P.J., Hjorth, J., Guinouard, I., Navarro, R., Adolfse, T., Albers, P.W., Amans, J.P., Andersen, J.J., Andersen, M.I., Binetruy, P., Bristow, P., Castillo, R., Chemla, F., Christensen, L., Conconi, P., Conzelmann, R., Dam, J., de Caprio, V., de Ugarte Postigo, A., Delabre, B., di Marcantonio, P., Downing, M., Elswijk, E., Finger, G., Fischer, G., Flores, H., François, P., Goldoni, P., Guglielmi, L., Haigron, R., Hanenburg, H., Hendriks, I., Horrobin, M., Horville, D., Jessen, N.C., Kerber, F., Kern, L., Kiekebusch, M., Kleszcz, P., Klougart, J., Kragt, J., Larsen, H.H., Lizon, J.L., Lucuix, C., Mainieri, V., Manuputy, R., Martayan, C., Mason, E., Mazzoleni, R., Michaelsen, N., Modigliani, A., Moehler, S., Møller, P., Norup Sørensen, A., Nørregaard, P., Péroux, C., Patat, F., Pena, E., Pragt, J., Reinero, C., Rigal, F., Riva, M., Roelfsema, R., Royer, F., Sacco, G., Santin, P., Schoenmaker, T., Spano, P., Sweers, E., Ter Horst, R., Tintori, M., Tromp, N., van Dael, P., van der Vliet, H., Venema, L., Vidali, M., Vinther, J., Vola, P., Winters, R., Wistisen, D., Wulterkens, G. & Zacchei, A. (2011). X-shooter, the new wide band intermediate resolution spectrograph at the ESO Very Large Telescope. A&A, **536**, A105. 35

Vieira, S.L.A., Corradi, W.J.B., Alencar, S.H.P., Mendes, L.T.S., Torres, C.A.O., Quast, G.R., Guimarães, M.M. & da Silva, L. (2003). Investigation of 131 Herbig Ae/Be Candidate Stars. ApJ, **126**, 2971–2987. 19, 34, 35, 37, 61, 64, 65, 67, 107, 131

Vink, J.S., Drew, J.E., Harries, T.J. & Oudmaijer, R.D. (2002). Probing the circumstellar structure of Herbig Ae/Be stars. MNRAS, **337**, 356–368. 19, 120, 182

Vink, J.S., Drew, J.E., Harries, T.J., Oudmaijer, R.D. & Unruh, Y. (2005). Probing the circumstellar structures of T Tauri stars and their relationship to those of Herbig stars. MNRAS, **359**, 1049–1064. 19, 120, 182

WADE, G.A., DROUIN, D., BAGNULO, S., LANDSTREET, J.D., MASON, E., SILVESTER, J., ALECIAN, E., BÖHM, T., BOURET, J.C., CATALA, C. & DONATI, J.F. (2005). Discovery of the pre-main sequence progenitors of the magnetic Ap/Bp stars? A&A, **442**, L31–L34. 22, 79

WADE, G.A., BAGNULO, S., DROUIN, D., LANDSTREET, J.D. & MONIN, D. (2007). A search for strong, ordered magnetic fields in Herbig Ae/Be stars. MNRAS, **376**, 1145–1161. 22, 79

WARD-THOMPSON, D., KIRK, J.M., ANDRÉ, P., SARACENO, P., DIDELON, P., KÖNYVES, V., SCHNEIDER, N., ABERGEL, A., BALUTEAU, J.P., BERNARD, J.P., BONTEMPS, S., CAMBRÉSY, L., COX, P., DI FRANCESCO, J., DI GIORGIO, A.M., GRIFFIN, M., HARGRAVE, P., HUANG, M., LI, J.Z., MARTIN, P., MEN'SHCHIKOV, A., MINIER, V., MOLINARI, S., MOTTE, F., OLOFSSON, G., PEZZUTO, S., RUSSEIL, D., SAUVAGE, M., SIBTHORPE, B., SPINOGLIO, L., TESTI, L., WHITE, G., WILSON, C., WOODCRAFT, A. & ZAVAGNO, A. (2010). A Herschel study of the properties of starless cores in the Polaris Flare dark cloud region using PACS and SPIRE. A&A, **518**, L92. 5

WHEELWRIGHT, H.E., OUDMAIJER, R.D. & GOODWIN, S.P. (2010). The mass ratio and formation mechanisms of Herbig Ae/Be star binary systems. MNRAS, **401**, 1199–1218. 37

WHITTET, D.C.B., ed. (2003). *Dust in the galactic environment*. 54

Whittet, D.C.B., Kirrane, T.M., Kilkenny, D., Oates, A.P., Watson, F.G. & King, D.J. (1987). A study of the Chamaeleon dark cloud and T-association. I - Extinction, distance and membership. MNRAS, **224**, 497–512. 34

Whittet, D.C.B., Gerakines, P.A., Carkner, A.L., Hough, J.H., Martin, P.G., Prusti, T. & Kilkenny, D. (1994). A Study of the Chamaeleon-I Dark Cloud and T-Association - Part Six - Interstellar Polarization Grain Alignment and Magnetic Field. MNRAS, **268**, 1. 5

Wilson, R.W., Jefferts, K.B. & Penzias, A.A. (1970). Carbon Monoxide in the Orion Nebula. ApJL, **161**, L43. 2

Zhang, Y., Tan, J.C., De Buizer, J.M., Sandell, G., Beltran, M.T., Churchwell, E., McKee, C.F., Shuping, R., Staff, J.E., Telesco, C. & Whitney, B. (2013). A Massive Protostar Forming by Ordered Collapse of a Dense, Massive Core. ApJ, **767**, 58. 11

Zinnecker, H. & Yorke, H.W. (2007). Toward Understanding Massive Star Formation. ARA&A, **45**, 481–563. 71